University of Algarve

Physics Department

Signal Processing Laboratory

Application of Ocean Acoustic Tomography to the estimation of internal tides on the continental platform

Orlando Camargo Rodríguez

University of Algarve, Faro

December 2000

University of Algarve

Faculty of Science and Technology

Application of Ocean Acoustic Tomography to the estimation of internal tides on the continental platform

Orlando Camargo Rodríguez

Physics Department

Signal Processing Laboratory (SiPLAB)

Ph.D. Thesis in the scientific field
of Geophysics

December 2000

To Leo and Lali...
and to my parents.

“De pronto, sin ningún anuncio, su actividad febril se interrumpió y fue substituida por una especie de fascinación. Estuvo varios días como hechizado, repitiendose a sí mismo en voz baja un sartal de asombrosas conjeturas, sin dar crédito a su propio entendimiento. Por fin, un martes de diciembre, a la hora del almuerzo, soltó de un golpe toda la carga de su tormento. Los niños habian de recordar por el resto de su vida la augusta solemnidad con que su padre se sentó a la cabecera de la mesa, temblando de fiebre, desvastado por la prolongada vigilia y por el encono de su imaginación y les reveló su descubrimiento:

–La tierra es redonda como una naranja.”

Gabriel Garcia Marquez

Cien años de Soledad

Agradecimentos

Gostaria de agradecer em primeiro lugar aos meus colegas do SiPLAB, Mário Jesus, João António Silva, Nelson Martins, Cristiano Lopes e Cristiano Soares, pela excelente atmosfera de trabalho nas instalações do SiPLAB. Foram inúmeras as horas –e as bicas– que partilhei com eles, discutindo sobre Linux, filtros de Kalman, comunicações submarinas, wavelets, distribuições tempo-frequência e Algoritmos Genéticos. Em relação a este último ponto quero agradecer especialmente ao Cristiano Soares pelos seus conselhos, e pelo tempo que tão gentilmente dispensou para testar algumas hipóteses preliminares relacionadas com a aplicação dos Algoritmos Genéticos na inversão tomográfica. Quero agradecer igualmente a minha esposa e ao meu filho pelo seu apoio incondicional, pela paciência inesgotável e o calor de família que mostraram durante tantos fins de semana roubados à vida familiar, e que ocupei a redigir e a melhorar alguns dos capítulos desta tese. Em último lugar quero agradecer ao meu orientador científico, Prof.D. Sérgio Jesus, pelos potentes meios de computação do SiPLAB, constantemente disponíveis, pela extraordinária experiência adquirida no decorrer deste trabalho de investigação, pelas sugestões e críticas construc-tivas, e pelo seguimento constante do trabalho de doutoramento. E sobretudo, pela sua amizade.

Abstract

This thesis discusses the application of the methods of Ocean Acoustic Tomography to monitorize and invert the variations of internal tides in coastal environments. The material of this thesis starts with a detailed theoretical description of the propagation of internal tides, in the linear and non-linear cases. That discussion allows one to introduce the concept of Hydrostatic Normal Modes (HNMs) and shows, in particular, that the HNMs form a complete orthogonal basis to represent the fields of pressure, current, temperature, sound speed and salinity. Furthermore, ray-tracing simulations allow one to predict the effects of variations of waveguide geometry, and sound speed, on the temporal arrivals of the acoustic signal. The simulations allow also to develop a robust strategy of tomographic inversion, which is tested first with simulated data, and then with real acoustic data from the INTIMATE'96 experiment. Finally, this dissertation shows that the methods of Ocean Acoustic Tomography can be efficiently applied to monitorize and invert the propagation of the internal tide in a coastal environment, allowing to achieve a high degree of accuracy in the tomographic inversion.

Resumo

Esta tese discute a aplicação dos métodos da Tomografia Acústica Oceanográfica à monitorização e consequente inversão das marés internas em ambientes costeiros. O material desta tese começa por descrever em detalhe o modelo teórico de propagação das marés internas, nos casos linear e não-linear. Esta discussão permite introduzir o conceito de Modos Normais Hidrostáticos (MNHs). Mostra-se, em particular, que os MNHs constituem uma base ortogonal completa para representar os campos de pressão, corrente, temperatura, velocidade do som e salinidade. Seguidamente, recorrendo a simulações, discutem-se os efeitos das variações geométricas e ambientais, nas chegadas temporais do sinal. As simulações permitem desenvolver uma estratégia robusta de inversão tomográfica, a qual é inicialmente testada em dados simulados, e é então aplicada aos dados reais da experiência INTIMATE'96. Mostra-se, de forma consistente, que os métodos da Tomografia Acústica Oceanográfica podem ser aplicados eficientemente na monitorização e inversão da maré interna, permitindo alcançar um alto grau de precisão tomográfica.

Table of contents

List of Figures

Notation

Latin Alphabet

Scalars

$\hat{\mathcal{A}}$	Estimator of the amplitudes of the HNMs
a_j	Weighted amplitude of the emitted signal
a_s	Saline contraction coefficient
a_T	Thermal expansion coefficient of water
C_{ps}	Specific heat of water (constant pressure and salinity)
$c(z,r,t), c(z,t), c$	General (perturbed) sound speed profile
$c_0(z), c_0$	Background (reference) sound speed profile
c_v	Specific heat of water (constant volume)
D	Maximal depth (bottom depth)
d	Modal parameter of nonlinearity
$\hat{\mathcal{E}}$	Bartlett estimator (narrowband case)
$\hat{\mathcal{E}}_{inc}$	Incoherent Bartlett estimator (broadband case)
f	Linear frequency
f_c	Coriolis frequency
g	Gravitational acceleration
$h(t)$	Channel impulse response
i	Imaginary unit ($i = \sqrt{-1}$)
j, l, m	Indices
k	Wavenumber
k_j	Eigenvalue associated with the normal mode Z_j
k_T	Thermal conductivity of water
k_x, k_y	Components of $\mathbf{k}_h$
L	Number of "snapshots"
L	Number of layers
$N(z)$	Brunt-Väiasällä frequency
N_f	Number of frequencies
N	Number of sensors
n	Noise
P_m	Weigth of the HNM of index m in δc ($m = 1, 2, 3$)
p	Pressure (time domain)
p_0	Fluid pressure in the equilibrium state

p'	Pressure perturbations ($p' = p - p_0$)
$p(t, z_r)$	Acoustic pressure at depth z_r
p_m	Modal amplitude of pressure
$\hat{p}$	Pressure (frequency domain)
$\hat{p}(f, z_r), \hat{p}(z_r)$	Narrowband component of the Fourier transfrom of $p(t, z_r)$
Q_T	External sources of heat
R	Horizontal distance of transmission
r	Horizontal distance
$r(t, z_r)$	Temporal signal received on the hydrophone at depth z_r
r	Rank of the observation matrix
S	Salinity
S_0	Salinity in the equilibrium state (mean salinity profile)
$\hat{S}(\omega)$	Source spectrum
s	Dimensionless parameter of modal nonlinearity
$s(t), s(t, z_s)$	Emitted signal at depth z_s
s_j	Lenght of the eigenray Γ_j
T	Temperature
T_0	Temperature in the state of equilibrium (mean temperature profile)
T	Number of eigenrays or arrivals
$\hat{\mathcal{T}}$	Estimator of the bottom depth
t	Time
(u, v, w)	Current vector components along the x, y and z axes
(u_m, v_m, w_m)	Modal amplitudes of u, v e w
$\hat{\mathcal{X}}$	Estimator of proximity between true and estimated solutions
x, y	Orthogonal components of the horizontal plane
$Z_j(z)$	Acoustic normal mode
z	Vertical component (depth)
$\{z_l\}$	Discretization grid in depth
z_r	Hydrophone depth
z_s	Acoustic source depth

Vectors and Matrices

$\mathbf{a}^{\mathsf{t}}$	Transpose of vector (or matrix) **a**
$\mathbf{a}^{*}$	Transpose conjugated of vector (or matrix) **a**
$\mathbf{E}$	Observation matrix
$\mathbf{g}$	Vector of gravity acceleration
$\mathbf{i}, \mathbf{j}, \mathbf{k}$	Versors along the x, y and z axes
$\mathbf{k}_h$	Horizontal wavenumber component (internal waves, linear-rotational case)
$\mathbf{n}$	Noise vector
$\mathbf{P}$	Regularization matrix
$\hat{\mathbf{p}}$	Normalized vector of observed acoustic pressure (narrowband case)
$\hat{\mathbf{p}}_m$	Normalized vector of modeled acoustic pressure (narrowband case)
$\mathbf{U}$	Current vector
$\mathbf{U}_h$	Horizontal component of **U**
$\boldsymbol{\mathcal{U}}_m$	Nonlinear modal amplitude of $\mathbf{U}_h$
$\mathbf{u}_1$	"Identity" vector ($\mathbf{u}_1 = [\ 1\ 1\ \ldots\ 1\ ]^{\mathsf{t}}$)
$\mathbf{x}$	Vector of sound speed perturbations ("true" solution)
$\mathbf{x}^{\#}$	Estimated value of **x** (estimated solution)
$\mathbf{y}$	Vector of delays
$\mathbf{y}'$	Vector of delays with temporal perturbations $\boldsymbol{\delta}\mathbf{y}$ ($\mathbf{y}' = \mathbf{y} + \boldsymbol{\delta}\mathbf{y}$)
$\mathbf{y}_j$	Vector of delays in the hydrophone j
$\boldsymbol{\delta}\mathbf{y}$	Temporal perturbations of arrival times

Greek Alphabet

Scalars

α_m	Modal amplitudes of temperature, sound speed and salinity
$\tilde{\alpha}_m, \tilde{\beta}_m$	Parameters of the Korteweg-de Vries equation
$\delta(t)$	Dirac "delta" function

η_m	Nonlinear vertical displacement of the HNM of index m
Ω	Frequency of earth rotation
ω	Radial frequency ($\omega = 2\pi f$)
$\tilde{\omega}$	Internal waves frequency
$\Psi_m(z), \phi_m(z)$	Hydrostatic Normal Modes (HNMs)
$\tilde{\Psi}_m(z), \tilde{\phi}_m(z)$	Nonhydrostatic Normal Modes
ρ	Fluid density
ρ_0	Fluid density in the equilibrium state
ρ'	Density perturbations ($\rho' = \rho - \rho_0$)
ρ_m	Modal density amplitude
φ	Geographic latitude
τ	Arrival time corresponding to $c(z,r,t)$
τ_0	Arrival time corresponding to $c_0(z)$
$\Delta\tau$	Arrival time perturbation ($\Delta\tau = \tau - \tau_0$)
τ_r	Relative temporal arrival ($\tau_r = \tau - \tau_{ref}$)
τ_{ref}	Reference arrival
θ	Angle of propagation of the internal tide
ϑ	Geographic latitude

Vectors and Matrices

$\boldsymbol{\alpha}$	Vector of amplitudes of the HNMs
$\boldsymbol{\alpha}^{\#}$	Estimated value of $\boldsymbol{\alpha}$
$\boldsymbol{\Omega}$	Earth rotation vector
$\boldsymbol{\Psi}$	Regularization matrix of the HNMs
$\boldsymbol{\tau}$	Vector of absolute arrivals, corresponding to $c(z,r,t)$
$\boldsymbol{\tau}_0$	Vector of absolute arrivals, corresponding to $c_0(z)$
$\boldsymbol{\tau}_r$	Vector of relative arrivals ($\boldsymbol{\tau}_r = \boldsymbol{\tau} - \boldsymbol{\tau}_{ref}$)
$\boldsymbol{\tau}_{ref}$	Vector of reference arrivals ($\boldsymbol{\tau}_{ref} = \tau_{ref}\mathbf{u}_1$)
$\boldsymbol{\tau}^p$, $\boldsymbol{\tau}_0^p$	Paired arrivals
$\boldsymbol{\theta}$	Vector of parameters in the search space
$\boldsymbol{\theta}_0$	Vector of searched parameters

Special Symbols

∇	"Nabla" operator
∇_h	Horizontal component of ∇
$\langle \ldots \rangle$	Mean value operator
$\langle \ldots \vert \ldots \vert \ldots \rangle$	Functional inner product operator ($\langle \ldots \vert 1 \vert \ldots \rangle = \langle \ldots \vert \ldots \rangle$)
$\dfrac{D}{Dt}$	Total derivative operator
$*$	Convolution operator
$\vert\vert \ldots \vert\vert$	Vector norm
$\times$	Vector product
$\cdot$	Inner product

Abreviatures

BCs	Boundary Conditions
CTD	Conductivity-Temperature-Depth
EOFs	Empirical Orthogonal Functions
HNMs	Hydrostatic Normal Modes
INTIMATE	INternal Tide Investigation by Means of Acoustic Tomography Experiments
LFM	Linear Frequency Modulation
MFP	Matched-Field Processing
MFT	Matched-Field Tomography
SLP	Sturm-Liouville Problem
SNR	Signal to Noise Ratio
SVD	Singular Value Decomposition
VLA	Vertical Line Array
XBT	Expendable bathythermograph

Chapter 1

Introduction

The concept of "tide" is usually associated with the rise and fall of the sea level, which takes place approximately every twelve hours [1]. Generally speaking tides correspond to a particular case of gravity waves, which propagation depends on the relative positions of the Moon and the Sun [2]. In this way tidal waves propagate along the planet inducing the movement of the oceanic masses, with the particularity that their movement is constrained by the presence of continents. As any other type of oscillatory motion tides can be characterized in terms of energy, according to the intensity of oscillations of the sea level. In general, the motion of the oceanic masses takes place uniformly, so the surfaces of constant density and pressure oscillate in phase, and there is no mixing of the water located close to the surface, with the water located at higher depths. Therefore, the density and temperature distributions remain almost constant along time. However, when the tidal wave propagates from the deep ocean to a shallow water region (for instance, towards the coast) there is a significant concentration of the tidal energy in the shallower channel of propagation. That concentration of energy can give rise to the mixing of the water masses located at different depths, and therefore induces temporal variations of the water column density and temperature. Since those variations take place in the interior of the water column they are known, generally, as “internal tides” [3], in contrast with the usually observed tide, which is often called as “surface tide”. From the physical point of view internal tides correspond to a particular case of internal waves, in resonance with the surface tide. Both surface and internal tides have a significant impact in the coastal habitats, due, in particular, to the phenonema of sediment transport and redistribution of plankton populations, which are associated to the propagation of both types of tides. In this sense, monitoring the internal tide constitutes a task of significant importance for the management of coastal resources. The technical means involved nowadays in that type of monitoring involve the usage of “intrusive” techniques, like CTDs, XBTs, ADCPs, thermistor chains, etc. [1]. Those techniques are not only expensive to use, but they are also “constrained” in the sense that they provide only local measurements of the water column properties. If the acquisition of oceanographic data involves the usage of a significant amount of technical resources the situation becomes unfeasible for the monitoring of a large zone along the coast. For this reason (and many others) internal tides had not been studied in a consistent manner.

Ocean Acoustic Tomography [3]–[5] constitutes an alternative to the standard, “intrusive”, methods. The technique, proposed originally by Walter Munk and Carl Wunsch, is inspired in biomedicine and sysmology and consists in the utilization of a net of acoustic sources/receivers, along the borders of a particular oceanic area, to invert (i.e., to determine) the sound speed field within the interior of the considered area. The tomographic inversion takes advantage of the sensitivity of the acoustic signals to the variations, in time and space, of the sound speed field (and, as will be shown later, of the temperature field) within the interior of the monitorized area. Since Ocean Acoustic Tomography was proposed, in the beginning of the seventies, it has been used as an effective alternative to the classical methods for the monitoring of ocean environments. In this sense, a significant number of studies dedicated to tomographic inversion, in different ocean environments, had been developed, starting with the "classic" case of deep water (with transmission and reception distances of the order of hundreds, and even thousands, of kilometers) [6]–[8], until the case of the continental platform and coastal –shallow water– areas, with typical depths less than 200 m [9, 10]. In a closer temporal perspective some experiments on acoustic shallow water tomography have been performed in Portuguese waters, through the development of the INTIMATE project, which will be discussed in detail in Chapter 3.

One of the most interesting aspects (although not explored yet) of Ocean Acoustic Tomography is related to its application to the monitoring (and further inversion) of internal tides in coastal areas [11, 12]. Acoustic tomography monitoring, and inversion, of the internal tide would involve a reduced set of human and technical resources, in addition to the fact that it would provide important information that could be used to improve the management of coastal resources. From the point of view of the forward problem, i.e., from the point of view of acoustic propagation through a sound speed field perturbed by an internal tide, there is a significant amount of observations (to be discussed in section 2.5) which show the sensitivity of acoustic signals to the propagation of internal tides. Nevertheless, from the point of view of the inverse problem, i.e., considering the problem of determining the internal tide from the variations of the acoustic signal, there is an evident lack of experimental studies. In fact, at the scale of coastal habitats, the transmission distances are of the order of tens of kilometers, and it is not clear how to adapt "classical" tomography, characteristic of deep-water propagation scenarios, to the case of coastal (shallow-water) regions. That adaptation should take into account both the specific characteristics of the *environment* that one pretends to monitor, and the particular characteristics of the *phenomenon* that one intends to invert. These two particularities are strongly remarked by *Munk et al.*, during the discussion of the inverse problem, in [5].

This dissertation will develop a detailed discussion of the application of acoustic tomography to the monitoring, and further inversion, of the internal tide. The discussion will take advantage of an intensive analysis of the physical model of propagation of internal tides, which will be discussed in detail in Chapter 2. The main objective of this Chapter will consist in identifying the most important aspects of the theoretical model, to be incorporated into the tomographic inversion. Chapter 2 will allow one also to introduce a logical structure of interconnections between the propagation problems of acoustics and internal tides, by introducing also some of the fundamental concepts of underwater acoustic propagation and signal processing. Some concepts introduced in Chapter 2 will simplify the discussion of the acoustic and oceanographic data, acquired during the tomography sea trial INTIMATE'96, which will be described in Chapter 3. The concepts introduced in Chapters 2 and 3 will allow to introduce a robust parameterization of the sound speed profile, to be discussed in the first part of Chapter 4. Furthermore, the second part of Chapter 4 will be dedicated to simulations of acoustic propagation, in the case of geometric and environmental variations of the propagation channel, which will allow to clearly identify the perturbations on the acoustic signal, induced by the surface and internal tides. The results of this Chapter, together with the discussion of the theoretical model related to the propagation of internal tides, will allow to develop a tomography scheme, which will be tested initially through simulations, in Chapter 5, and on real data of the INTIMATE'96 sea trial. The results of these tests will be discussed in Chapter 6 and the conclusions will be presented in Chapter 7.

The discussion presented in this dissertation will allow to clearly identify the fundamental factors that make possible to develop a robust inversion of internal tides, and will also show the feasibility and robustness of the methods of Ocean Acoustic Tomography, based on arrival times, for the monitoring of internal tides. Finally, this dissertation will show the high accuracy of inversion, that those methods can achieve.

Chapter 2

Internal and surface tides

The concept of "tide" is usually associated to the rise and fall of the sea level, which in most of the coastal zones has a period of approximately twelve hours. At some locations one can find deviations from this value, with tides that can achieve a periodicity up to 25 hours. The rise and fall of the sea level is the most obvious characteristic to most part of observers, which explains the existence of tidal records since the beginnings of navigation. It is also quite significant that in the thirteen century it already existed a compilation of empirical techniques for the prediction of tides, which were based on the observation of the motion of the Moon. Nevertheless, the driving phenomenon is related to the horizontal currents of the tides, since the rise and fall of the water masses are the main consequence of the convergence or divergence of the currents, when the flux of water moves towards to the coast or away from it. It should be remarked that the phenomenon of tides is not exclusive of the masses of water that form the oceans, since the mass of the Earth and the different layers of the atmosphere are affected also by the gravitational forces that originate the ocean tides, although the corresponding oscillations for the Earth and the atmosphere are of reduced amplitude. Taking into account the particular characteristics of the tides one can notice that they correspond to a *barotropic* phenomenon, which means that, independently of the phase and height of the ocean tide, the different "layers" that constitute the water column displace in phase, keeping a parallel alignment between the surfaces of constant pressure (known as "isobars"), the surface of the ocean, and the surfaces of constant density (known as "isopycnics"). However, when the tide propagates from an environment of deep waters (as in the case of the open ocean), to an environment of shallow waters (towards the coastline), there is a significant concentration of tidal energy in a channel of smaller depth, giving rise to the mixing of the different layers, which were initially homogeneous. That mixing originates variations of the water column density, where the isopycnics loose the parallel alignment with the isobars and the ocean surface. A system under those conditions is known as *baroclinic*. In the case of the *baroclinic* tide one can observe a periodic variation of the water column temperature, which takes place with the same frequency as the rise and fall of the water level. Taking into account that all those variations occur within the water column (which explains the reason why the baroclinic tides started to be systematically studied at the beginning of the XX century) the baroclinic tide is usually known as the "internal tide", in contrast with the usual barotropic tide, which is generally termed as the "surface tide". In this Chapter some fundamental concepts will be introduced, that will then be used extensively along the remaining Chapters.

2.1 Surface tides

The surface tides are a consequence of the variation of the gravitational forces, induced by the Sun and the Moon, over the masses of water of our planet, as the two celestial bodies change their position in relation to the Earth.

Although of weak intensity, when compared with the gravity force from the side of the

Earth(in a ratio of one to one million) the tidal components that act along the surface of our planet are strong enough to induce the motion of the water masses of the oceans.

Depending on the combined rotation of the Sun and the Moon one obtains a sum of periodical oscillations (see Table 2.1), where the main component corresponds to the *semidiurnal*, denoted with the symbol M_2, having a period of 12.42 hours. The first eight terms on Table 2.1 contribute approximately to 90% of the total of tidal oscillations at any point of the Earth. Altimetry data of the sea surface, obtained using satellites, show in particular that in the proximity of the Portuguese coast the M_2 tidal component propagates Northward, from the South Atlantic [13].

The formulation of the gravitation theory by Isaac Newton in 1687 allowed the development of the first simplified mathematical model of barotropic tides, which is known in nowadays as the Theory of the Equilibrium Tides [2]. Despite the fact that the model allowed to accurately derive some of the general characteristics of the observed tides it also predicted that the tidal oscillations in the antipodes of the earth globe should be in phase. This prediction do not match the systematic observations acquired in numerous locations at the Earth surface. One century later, in 1776, the French mathematician Pierre-Simon Laplace reformulated the tide problem, in a model that nowadays is termed as the Dynamic Theory of the Tides [1]. Within the context of this theory the barotropic tides correspond to waves induced by the periodic fluctuation of the gravitational forces, of the Moon and the Sun, acting on the water masses of the Earth. Essentially, Laplace's theory reformulated the problem of tide prediction by relating an external periodical force, known *apriori*, with the motion of the oceanic waters. This problem can be treated properly in the case of an earth globe covered entirely with a water mass of uniform depth, but becomes extremely complex

	Symbol	*Velocity* (degrees/hour)	*Period* (h)	*C.R.*
Semidiurnal components				
Principal lunar	M_2	28.98410	12.42	100.0
Principal solar	S_2	30.00000	12.00	46.6
Larger elliptic lunar	N_2	28.43973	12.66	19.2
Lunisolar semidiurnal	K_2	30.08214	11.97	12.7
Larger elliptic solar	T_2	29.95893	12.01	2.7
Smaller elliptic lunar	L_2	29.52848	12.19	2.8
Lunar elliptic 2nd. order	$2N_2$	27.89535	12.91	2.5
Larger lunar evectional	ν_2	28.51258	12.63	3.6
Minor lunar evectional	λ_3	29.45563	12.22	0.7
Variational	μ_2	27.96821	12.87	3.1
Diurnal components				
Diurnal lunisolar	K_l	15.04107	23.93	58.4
Principal lunar diurnal	O_l	13.94304	25.82	41.5
Principal solar diurnal	P_l	14.95893	24.07	19.4
Larger lunar elliptic	Q_1	13.39866	26.87	7.9
Smaller lunar elliptic	M_l	14.49205	24.84	3.3
Small lunar elliptic	J_l	15.58544	23.10	3.3
Long-period components				
Lunar fortnightly	M_f	1.09803	327.67	17.2
Lunar monthly	M_m	0.54437	661.30	9.1
Solar semiannual	S_{sa}	0.08214	2191.43	8.0

Table 2.1: Principal tidal harmonic components. The C.R. (*Coefficient Ratio*) is the ratio of the amplitudes $\times$ 100, related to the M_2 component.

in the case of oceans with variable topography, and where the planetary circulation of the oceanic masses is constrained by the presence of the continents. Beyond those constraints a realistic treatment of the problem should include the fact that each of the basins can be characterized by a particular set of physical parameters, and will respond to the action of the external force with its own set of characteristic frequencies. In this case an appropriate treatment of the problem will be only possible using numerical solutions of the Laplace's model, using computers. Some models of this type are available in the Internet[1].

A simpler technique to predict tides was introduced by Lord Kelvin in 1870 [2], and involves a satisfactory degree of accuracy. Kelvin's technique is based on the usage of an annual set of tide measurements at a particular location. The set of measurements allow to identify the "weights" of the different periodic components, that contribute to the tidal oscillation at the considered location. The information of those weights could be passed to an analogical "computer", made of different gears. In this computer the motion of the first gear was transmitted to the last one through an ingenuous set of secondary gears, with different diameters. The relative positions of the secondary gears depended on the weights of the different components, and the rotations of the last gear showed progressively the phases and amplitudes of the expected tides. From a mathematical point of view Kelvin's machine reproduced mechanically the sum of the most important tidal components, for the location where the set of annual measurements was acquired. Nowadays, computers substituted the gears of Kelvin's machine, although a significant part of the tidal tables made by the Hydrographic Services around the world is still based on the method introduced by Kelvin or on some variant of it.

[1] See, for instance, *http://podaac.jpl.nasa.gov/cdrom/tide/Document/html/models.htm.*

2.2 Internal tides

One of the particularities of the barotropic tide that propagates over the continental platform corresponds to the generation of *internal tides*, i.e., of internal waves, predominantly *semidiurnals*, which propagate on the continental platform. In contrast with the open sea, where the spectrum of internal waves obeys the Garret-Munk distribution [14], the semidiurnal internal waves that propagate in coastal environments exhibit a spectrum dominated by the frequency of the barotropic semidiurnal tide [9].

In general, the internal tides are a consequence of the interaction between the barotropic tide and the variable topography of the sea bottom, as in the case of propagation over sea mountains and canyons [15, 16], or over the continental slope [17, 18]. Despite the numerous studies dedicated to this problem (see, for instance, [17]–[22]) the exact mechanism of this interaction (and the mechanism of the process of generation) is still not understood.

In particular, the propagation of internal tides in coastal environments leads to the oscillation of the thermocline [1] in phase with the variations of the surface tide. The internal tides can lead also to small variations of the sea level, which can be detected using satellite SAR[2] images. Those images allow one to detect the bands of organic matter associated to the propagation of internal tides. In most cases those bands follow the topography of the sea bottom [13, 23, 24]. Together with the observations of linear waves the SAR images, associated to the study of temperature data taken at different locations of the earth globe, revealed the generation on the continental platform (and further propagation) of wave packets of non-linear solitary waves commonly known as *solitons*, which are energetically associated to the internal tide [25]–[28]. This type of phenomenon has a significant importance from the

[2] *Synthetic Aperture Radar.*

theoretical and practical points of view, due to the fact that there is a complete mathematical description of the propagation problem [29]–[31], but not of the generation problem for the particular case of internal tides [15, 21, 32].

Together with surface tides internal tides play an important role in the coastal habitats due to their effects in the biological activities as, for instance, in the redistribution of nutrients, fish shoals, and plankton populations [33], or due to the phenomena of sediment transport which are associated to both types of tide [34].

As will be discussed in section 2.5 there is a significant amount of experimental evidence, showing the sensitivity of acoustic signals to the propagation of the internal tide. In some cases the investigation of this problem led to important results. However, one can notice the absence of an homogeneous perspective in the analysis of this matter, with different studies embracing *apriori* different cases regarding hydrostatic, non-hydrostatic, linear and non-linear approximations. This heterogeneity makes it difficult to properly understand both the acoustic and oceanographic problems. To minimize the difficulties the following section will be dedicated to the discussion of the theoretical background regarding the internal tides, by describing, as briefly and detailed as possible, the three most important theoretical cases: the linear rotationless hydrostatic case, the linear rotational non-hydrostatic case, and the non-linear rotationless case.

2.3 Internal waves: theoretical background

In general, the motion of a fluid obeys to the set of Navier-Stokes equations [14, 35], which include the terms of viscosity and friction. These terms play a minor role in the motion of the oceanic masses of water, allowing one to introduce the following equation for the motion of a fluid [36]:

$$\rho\frac{\partial \mathbf{U}}{\partial t} + \rho\left(\mathbf{U}\cdot\nabla\right)\mathbf{U} + 2\rho\mathbf{\Omega}\times\mathbf{U} = -\nabla p + \rho\mathbf{g}\ , \tag{2.1}$$

where $\mathbf{U} = (u, v, w)$ represents the velocity of the fluid particles, p represents the fluid pressure, ρ corresponds to its density, t represents the time coordinate, $\mathbf{\Omega}$ corresponds to the vector of angular rotation of the Earth and $\mathbf{g} = -\mathbf{k}g$, with g representing the acceleration of free fall in the gravity field of the Earth, ($g = 9.8$ m/s^2). In Eq.(2.1) ∇ represents the "nabla" operator: $\nabla = \mathbf{i}\partial/\partial x + \mathbf{j}\partial/\partial y + \mathbf{k}\partial/\partial z$. In general the terms to the left of the equality sign in Eq.(2.1) describe the motion of the fluid particles within a non-inertial frame of reference and in the absence of viscosity. The terms to the right of the sign describe the combined action of the external fields of the pressure and gravity forces. Eq.(2.1) can be simplified further by introducing the *Boussinesq approximation* [35], which states that the perturbations in density, $\rho' = \rho - \rho_0$, play a second order role in the calculations of the terms to the left of Eq.(2.1). In this way one can substitute in those terms, without loss of generality, the total density, ρ, by the equilibrium density, ρ_0. However, the same reasoning is not valid for the terms to the right of the equation. Therefore, according to the Boussinesq approximation, one can rewrite Eq.(2.1) as

$$\rho_0\frac{\partial \mathbf{U}}{\partial t} + 2\rho_0\mathbf{\Omega}\times\mathbf{U} + \rho_0\left(\mathbf{U}\cdot\nabla\right)\mathbf{U} = -\nabla p + \rho\mathbf{g}\ . \tag{2.2}$$

Eq.(2.2) is insufficient to develop a complete analysis of the motion of the oceanic masses. In addition to that equation one can show that the velocity and density of the fluid particles are related to each other through the *Continuity equation* [37]:

$$\frac{1}{\rho}\frac{D\rho}{Dt} + \nabla\cdot\mathbf{U} = 0\ , \tag{2.3}$$

where the operator of the total derivative is defined as

$$\frac{D}{Dt} \equiv \frac{\partial}{\partial t} + \mathbf{U} \cdot \nabla \ . \tag{2.4}$$

Eq.(2.3) can be splitted in two independent equations applying the *incompressibility condition*:

$$\frac{D\rho}{Dt} = 0 \ , \tag{2.5}$$

where the first of the equations corresponds to

$$\nabla \cdot \mathbf{U} = \frac{\partial u}{\partial x} + \frac{\partial v}{\partial y} + \frac{\partial w}{\partial z} = 0 \ , \tag{2.6}$$

while the second, in its full form, is given by:

$$\frac{D\rho}{Dt} = \frac{\partial \rho}{\partial t} + u\frac{\partial \rho}{\partial x} + v\frac{\partial \rho}{\partial y} + w\frac{\partial \rho}{\partial z} = 0 \ . \tag{2.7}$$

Neglecting the non-linear terms $u\partial\rho/\partial x$ and $v\partial\rho/\partial y$ in Eq.(2.7), taking into account that $\rho = \rho_0(z) + \rho'$, and considering that $w\partial\rho/\partial z \approx w d\rho_0/dz$, one can obtain the following expression:

$$\frac{\partial \rho'}{\partial t} + w\frac{d\rho_0}{dz} \ = \ \frac{\partial \rho'}{\partial t} - N^2\frac{\rho_0}{g}w = \ 0 \ \ . \tag{2.8}$$

where N^2 is known as the *buoyancy frequency* (or the *Brunt-Väiasällä frequency*) [36]:

$$N^2 = -\frac{g}{\rho_0}\frac{d\rho_0}{dz} \ . \tag{2.9}$$

The buoyancy frequency corresponds to the frequency of natural oscillations of a fluid element, when that element is in the state of small amplitude harmonic motion along the vertical axis. Taking into account that $N(z)$ depends on the gradient of the equilibrium density, ρ_0, the dependency of the buoyancy frequency on depth constitutes a fundamental indicator of the environment stratification and of its stable equilibrium. Furthermore, the buoyancy profile imposes an upper limit (known as the *cuttoff frequency*) to the interval of natural frequencies of the water column.

The system of equations Eq.(2.2), Eq.(2.6) and Eq.(2.8), constitutes the starting point for the discussion, in sections 2.3.1, 2.3.2 and 2.3.3, of the three more relevant cases of the propagation of internal waves.

2.3.1 Hydrostatic linear case ($\Omega = 0$)

The simplest case of propagation of internal waves corresponds to the hydrostatic linear rotationless case. First, let one admit the validity of the *hydrostatic approximation* [36] for the density and pressure of the water column:

$$\frac{\partial p}{\partial z} + \rho g = 0 \; . \tag{2.10}$$

This approximation implies automatically that $\partial w/\partial t = 0$, which corresponds to making the vertical component of Eq.(2.2) equal to zero. Furthermore, let one neglect in Eq.(2.2) the non-linear and rotational terms:

$$(\mathbf{U} \cdot \nabla)\, \mathbf{U} \approx \mathbf{0} \;\; \text{and} \;\; \mathbf{\Omega} \times \mathbf{U} \approx \mathbf{0} \; . \tag{2.11}$$

In this way, based on the approximations (2.10) and (2.11), and after rearranging some of the terms, one can obtain the following components of Eq.(2.2):

$$\frac{\partial u}{\partial t} = -\frac{1}{\rho_0}\frac{\partial p}{\partial x} \; , \quad \text{and} \quad \frac{\partial v}{\partial t} = -\frac{1}{\rho_0}\frac{\partial p}{\partial y} \; . \tag{2.12}$$

It can be shown that the fields of currents, density perturbations and pressure, that satisfy the system of equations Eq.(2.6), Eq.(2.8), and the pair of equations (2.12), can be represented in terms of expansions on a basis of Hydrostatic Normal Modes (HNMs) Ψ_m and ϕ_m [31]:

$$\begin{aligned} w &= \sum_m w_m \Psi_m(z) \; , \quad (u, v) = D \sum_m (u_m, v_m)\, \phi_m(z) \; , \\ \rho' = \rho_0 \frac{N^2}{g} &\sum_m \rho_m \Psi_m(z) \; , \quad p = \rho_0 \sum_m p_m \phi_m(z) \; , \end{aligned} \tag{2.13}$$

where D represents the water column depth, and the modal amplitudes u_m, v_m, w_m, ρ_m and p_m depend on the horizontal coordinates (x, y), and on time t. The HNMs are related through the equation $\phi_m = d\Psi_m/dz$, where the functions Ψ_m correspond to the solutions of a Sturm-Liouville Problem (hereafter, SLP) [38]:

$$\frac{d^2\Psi_m}{dz^2} + \frac{N^2}{C_m^2}\Psi_m = 0 \tag{2.14}$$

+ Boundary Conditions (BCs).

In Eq.(2.14) the coefficients C_m represent the propagation velocity of linear hydrostatic internal waves in a rotationless environment. From the mathematical point of view the SLP guarantees the existence of a complete system of eigenfunctions Ψ_m, with orthogonal properties:

$$\langle \Psi_m \left| N^2 \right| \Psi_n \rangle = 0 \quad \text{when } m \neq n \ ; \tag{2.15}$$

in Eq.(2.15) the "inner product" $\langle f_1 \left| f_2 \right| f_3 \rangle$ is defined as

$$\langle f_1 \left| f_2 \right| f_3 \rangle = \int_0^D f_1 f_2 f_3 \ dz \ . \tag{2.16}$$

Moreover, the coefficients C_m^{-2} correspond to the eigenvalues of the functions Ψ_m. For an arbitrary choice of BCs the orthogonality of the eigenfunctions Ψ_m does not imply the orthogonality of their derivatives, ϕ_m. However, for the particular case of homogeneous BCs, on bottom and surface:

$$\Psi_m(0) = \Psi_m(D) = 0 \ , \tag{2.17}$$

one obtains that

$$\langle \phi_m \mid \phi_n \rangle = 0 \ , \tag{2.18}$$

where $\langle f_1 \mid f_2 \rangle = \langle f_1 \left| 1 \right| f_2 \rangle$. Furthermore, on the basis of the inner products (2.15) and (2.18), one can show the validity of the following relationships:

$$\begin{aligned}
\langle \Psi_m \left| N^2 \right| \Psi_m \rangle &= C_m^2 \langle \phi_m \mid \phi_m \rangle \ , \\
\langle \Psi_m \left| N^2 \right| \phi_m \rangle &= \frac{1}{2} C_m^2 \langle \phi_m \left| \phi_m \right| \phi_m \rangle \ , \\
\langle \Psi_m \left| \frac{d\phi_m}{dz} \right| \phi_m \rangle &= -\frac{1}{2} \langle \phi_m \left| \phi_m \right| \phi_m \rangle \ , \\
\langle \Psi_m \left| N^2 \right| \phi_m^2 \rangle &= -\frac{1}{3} C_m^2 \ \phi_m^3 \Big|_0^D \ .
\end{aligned} \tag{2.19}$$

From the physical point of view one can expect that the modal amplitudes p_m, ρ_m, ... w_m, will exhibit an oscillating behaviour. It should be remarked that the set of expansions (2.13) do not constrain in any particular manner the analytic choice of those amplitudes. However, the consistency of the system of equations (2.6), (2.8), (2.10) and (2.12)[3] implies the following linear interdependency of those amplitudes:

$$\begin{aligned}
&D\left(\frac{\partial u_m}{\partial x} + \frac{\partial v_m}{\partial y} \right) + w_m = 0 \ , \quad && \frac{\partial \rho_m}{\partial t} - w_m = 0 \ , \\
&D \frac{\partial u_m}{\partial t} = -\frac{\partial p_m}{\partial x} \ , && D \frac{\partial v_m}{\partial t} = -\frac{\partial p_m}{\partial y} \ , \\
&\frac{p_m}{C_m^2} - \rho_m = 0 \ .
\end{aligned} \tag{2.20}$$

In this way, by imposing a particular set of periodic conditions on a particular amplitude, one will define automatically the particular analytic structure of the other modal amplitudes.

It should be remarked that the hydrostatic linear rotationless case can be analytically extended in order to consider the presence of a mean gradient of the velocity components u and v (see, for instance, [39, 40]). The description of that case, which is of significant importance from a theoretical point of view, would exceed the objectives of this discussion and will not be considered.

[3] Including the approximation $\partial p/\partial z \approx \rho_0 \sum_m p_m d\phi_m/dz$.

2.3.2 Non-hydrostatic linear case ($\Omega \neq 0$)

Neglecting non-linear terms in Eq.(2.1)

$$(\mathbf{U} \cdot \nabla)\, \mathbf{U} \approx \mathbf{0} \,, \tag{2.21}$$

considering that $p' = p - p_0$, and constraining the hydrostatic approximation to the equilibrium terms (i.e., considering that $dp_0/dz + \rho_0 g = 0$), one can obtain the following system of equations:

$$\begin{aligned} \left(\frac{\partial u}{\partial t} - f_c v\right) &= -\frac{1}{\rho_0}\frac{\partial p'}{\partial x} \,, \\ \left(\frac{\partial v}{\partial t} + f_c u\right) &= -\frac{1}{\rho_0}\frac{\partial p'}{\partial y} \,, \\ \left(\frac{\partial w}{\partial t}\right) &= -\frac{1}{\rho_0}\frac{\partial p'}{\partial z} - \frac{\rho'}{\rho_0} g \,. \end{aligned} \tag{2.22}$$

In system (2.22) the parameter $f_c = 2\Omega \sin\vartheta$ is known as the *Coriolis frequency* [14] and ϑ corresponds to the geographic latitude; the Coriolis frequency plays an important role in the study of the motion of a fluid within a rotating system of reference.

The solutions of the system of equations (2.6), (2.8) and (2.22) for the fields of current components, and perturbations of pressure and density, can be represented again under the form of orthogonal expansions [14]:

$$\begin{aligned} w &= \sum_m w_m \tilde{\Psi}_m(z) \,, & (u, v) &= \sum_m (u_m, v_m)\, \tilde{\phi}_m(z) \,, \\ \rho' &= \rho_0 N^2 \sum_m \rho_m \tilde{\phi}_m(z) \,, & p' &= \rho_0 \sum_m p_m \tilde{\phi}_m(z) \,, \end{aligned} \tag{2.23}$$

where $\tilde{\phi}_m = d\tilde{\Psi}_m/dz$; the *non-hydrostatic* normal modes $\tilde{\Psi}_m$ are, again, eigenfunctions of a SLP of the following form:

$$\frac{d^2\tilde{\Psi}_m}{dz^2} + \left(k_h^2\right)_m \frac{N^2 - \tilde{\omega}^2}{\tilde{\omega}^2 - f_c^2}\tilde{\Psi}_m = 0 \quad + \quad \text{BCs} \quad , \tag{2.24}$$

which guarantees the orthogonal properties of the modes $\tilde{\Psi}_m$:

$$\langle \tilde{\Psi}_m \left| \frac{N^2 - \tilde{\omega}^2}{\tilde{\omega}^2 - f_c^2} \right| \tilde{\Psi}_n \rangle = 0 \quad \text{with } m \neq n \,. \tag{2.25}$$

In Eq.(2.24) $\tilde{\omega}$ corresponds to the frequency of the internal waves, and k_h represents the horizontal component of the wavenumber vector. Denoting as θ the direction of propagation of internal waves one obtains that

$$\mathbf{k}_h = \mathbf{i}k_x + \mathbf{j}k_y \quad \text{and} \quad k_x = k_h \cos\theta \ , \ k_y = k_h \sin\theta \ . \tag{2.26}$$

In contrast to the hydrostatic linear case the consistency of the system of equations (2.6), (2.8) and (2.22) depends on the constraint

$$(\ p_m \ , \ \rho_m \ , \ u_m \ , \ v_m \ , \ w_m \ ) \sim \exp\left[i\left(k_x x + k_y y - \tilde{\omega} t\right)\right] \ , \tag{2.27}$$

which imposes the particular application of expansions (2.23) to the case of plane-wave propagation.

2.3.3 Non-linear case ($\Omega = 0$)

The theoretical treatment of the non-linear rotationless case involves a significant number of approximations, in both cases of an environment with constant density [29, 30] or with complex stratification [31]. In general, the presence of rotation terms, $\mathbf{\Omega} \times \mathbf{U}$, in the system of equations (2.2) makes cumbersome a detailed theoretical study of the problem. In this way, the study of the rotational non-linear case is usually accomplished with the help of numerical models [15], which allow one to conclude, in particular, that the rotation of the system of reference imposes severe limitations to the stability of internal non-linear wave packets [32].

The main purpose of this section will consist in the theoretical analysis of Eq.(2.2), but neglecting only the rotation terms, $\mathbf{\Omega} \times \mathbf{U}$. That analysis will allow one to obtain the fundamental equation of internal non-linear solitary waves, commonly know as *solitons*. The material described in this section will follow (with some minor changes in notation) the derivation shown in [31].

First, let one introduce the following notation

$$\mathbf{U}_h = \mathbf{i}u + \mathbf{j}v \quad \text{and} \quad \nabla_h = \mathbf{i}\frac{\partial}{\partial x} + \mathbf{j}\frac{\partial}{\partial y} \ . \tag{2.28}$$

Therefore, Eq.(2.6) can be rewritten in the following form:

$$\nabla_h \cdot \mathbf{U}_h + \frac{\partial w}{\partial z} = 0 \ . \tag{2.29}$$

On the other side, by neglecting the horizontal terms in Eq.(2.7):

$$\left(\mathbf{U}_h \cdot \nabla_h\right) \rho \approx \mathbf{0} \ , \tag{2.30}$$

and rearranging terms, it is possible to obtain the following equation:

$$\frac{\partial \rho'}{\partial t} + w\frac{d\rho}{dz} = -w\frac{\partial \rho'}{\partial z} \ . \tag{2.31}$$

Furthermore, rejecting in Eq.(2.2) the non-linear terms of small magnitude

$$\left(\rho'\frac{\partial \mathbf{U}_h}{\partial t} \ , \ \rho'\frac{\partial w}{\partial t} \ , \rho\left(\mathbf{U}_h \cdot \nabla_h\right) w \ , \ w\frac{\partial w}{\partial z}\right) \approx \mathbf{0} \ , \tag{2.32}$$

and terms of higher order non-linearity

$$\rho\left(\mathbf{U}_h \cdot \nabla_h\right) \mathbf{U}_h \approx \mathbf{0} \ , \tag{2.33}$$

one can obtain the following system of equations:

$$\begin{aligned} \rho_0\frac{\partial \mathbf{U}_h}{\partial t} + \nabla_h p' &= -\left[\rho'\frac{\partial \mathbf{U}_h}{\partial t} + \rho_0 w\frac{\partial \mathbf{U}_h}{\partial z} + \rho_0\left(\mathbf{U}_h \cdot \nabla_h\right) \mathbf{U}_h\right] \ , \\ \frac{\partial p'}{\partial z} + \rho' g &= -\rho_0\frac{\partial w}{\partial t} \ . \end{aligned} \tag{2.34}$$

Using the HNMs introduced in section (2.3.1) it is possible to represent the non-linear fields of current components, density and pressure, for the system of equations (2.29), (2.31), and the pair (2.34), under the form of the following set of expansions:

$$\begin{aligned} \mathbf{U}_h = D \sum_m \boldsymbol{\mathcal{U}}_m \phi_m \ , \quad \rho' &= N^2 \sum_m A_m \rho_m \Psi_m \ , \\ p' = \rho_0 \sum_m B_m p_m \phi_m \ , \quad w &= \frac{\partial \xi}{\partial t} + \nabla_h \cdot (\mathbf{U}_h \xi) \ , \end{aligned} \tag{2.35}$$

where A_m and B_m represent dimensional constants that guarantee the consistency of the corresponding equations, and

$$\xi = \sum_m \eta_m \Psi_m \ . \tag{2.36}$$

In Eq.(2.36) ξ represents, in general, the surfaces of constant density (or isopycnics) of the non-linear case. Neglecting modal coupling, and taking advantage of the orthogonal properties of the HNMs (equations (2.15), (2.18) and system (2.19)) one can calculate the modal amplitudes $\boldsymbol{\mathcal{U}}_m$, ρ_m, p_m and η_m, as will be shown in the following paragraphs.

First, regarding equation (2.29), one can notice that

$$\langle \nabla_h \cdot \mathbf{U}_h + \frac{\partial w}{\partial z} \mid \phi_m \rangle = \langle \nabla_h \cdot \mathbf{U}_h \mid \phi_m \rangle + \langle \frac{\partial w}{\partial z} \mid \phi_m \rangle = 0 \ . \tag{2.37}$$

The first term corresponds to

$$\langle \nabla_h \cdot \mathbf{U}_h \mid \phi_m \rangle = D \nabla_h \cdot \boldsymbol{\mathcal{U}}_m \langle \phi_m \mid \phi_m \rangle \ , \tag{2.38}$$

while the second term can be calculated through the expression

$$\begin{aligned} \langle \frac{\partial w}{\partial z} \mid \phi_m \rangle &= \langle \frac{\partial}{\partial z} \left[\frac{\partial \xi}{\partial t} + \nabla_h \cdot (\mathbf{U}_h \xi) \right] \mid \phi_m \rangle = \\ &= \langle \frac{\partial^2 \xi}{\partial z \partial t} \mid \phi_m \rangle + \langle \frac{\partial}{\partial z} \left[\nabla_h \cdot (\mathbf{U}_h \xi) \right] \mid \phi_m \rangle = \\ &= \frac{\partial \eta_m}{\partial t} \langle \phi_m \mid \phi_m \rangle + \frac{1}{2} D \nabla_h \cdot (\boldsymbol{\mathcal{U}}_m \eta_m) \, \langle \phi_m \, | \phi_m | \, \phi_m \rangle \ . \end{aligned} \tag{2.39}$$

Joining terms (2.38) and (2.39) one can conclude that

$$\frac{\partial \eta_m}{\partial t} + D \nabla_h \cdot \boldsymbol{\mathcal{U}}_m + \frac{1}{2} s \nabla_h \cdot (\boldsymbol{\mathcal{U}}_m \eta_m) = 0 \ , \tag{2.40}$$

where $s = D\langle\phi_m\,|\phi_m|\,\phi_m\rangle/\langle\phi_m \mid \phi_m\rangle$ corresponds to a dimensionless parameter, representative of modal non-linearity.

For Eq.(2.31) it can be found that:

$$\langle\frac{\partial\rho'}{\partial t}+\frac{d\rho_0}{dz}w \mid \Psi_m\rangle = \langle\frac{\partial\rho'}{\partial t} \mid \Psi_m\rangle + \langle\frac{d\rho_0}{dz}\,|w|\,\Psi_m\rangle = -\langle\frac{\partial\rho'}{\partial z}\,|w|\,\Psi_m\rangle \ ; \tag{2.41}$$

rejecting again the terms of higher non-linearity one gets the following pair of approximations:

$$\langle\frac{d\rho_0}{dz}\,|w|\,\Psi_m\rangle \approx \langle\frac{d\rho_0}{dz}\left|\frac{\partial\xi}{\partial t}\right|\Psi_m\rangle \ , \tag{2.42}$$

and

$$\langle\frac{\partial\rho'}{\partial z}\,|w|\,\Psi_m\rangle \approx \langle\frac{\partial\rho'}{\partial z}\left|\frac{\partial\xi}{\partial t}\right|\Psi_m\rangle \ . \tag{2.43}$$

Using once more the inner product properties one can show that

$$\begin{aligned}
\langle\frac{\partial\rho'}{\partial t} \mid \Psi_m\rangle &= C_m^2 A_m\frac{\partial\rho_m}{\partial t}\langle\phi_m \mid \phi_m\rangle \ , \\
\langle\frac{d\rho_0}{dz}\left|\frac{\partial\xi}{\partial t}\right|\Psi_m\rangle &\approx -\frac{\rho_0}{g}C_m^2\frac{\partial\eta_m}{\partial t}\langle\phi_m \mid \phi_m\rangle \ , \\
\langle\frac{\partial\rho'}{\partial z}\left|\frac{\partial\xi}{\partial t}\right|\Psi_m\rangle &\approx \frac{1}{2}C_m^2 A_m\rho_m\frac{\partial\eta_m}{\partial t}\langle\phi_m\,|\phi_m|\,\phi_m\rangle \ ;
\end{aligned} \tag{2.44}$$

combining the terms of the system (2.44) one concludes that

$$gA_m\frac{\partial\rho_m}{\partial t} = \rho_0\left(\frac{\partial\eta_m}{\partial t}+\frac{1}{2D}s\eta_m\frac{\partial\eta_m}{\partial t}\right) \ , \tag{2.45}$$

which together with an homogeneous system of initial conditions can be rewritten as

$$gA_m\rho_m = \rho_0\left(\eta_m+\frac{s}{4D}\eta_m^2\right) \ . \tag{2.46}$$

For the second equation of the system (2.34) one can see that

$$\langle\frac{\partial p'}{\partial z}+\rho' g \mid \Psi_m\rangle = \langle\frac{\partial p'}{\partial z} \mid \Psi_m\rangle + \langle\rho' g \mid \Psi_m\rangle = -\langle\rho_0\left|\frac{\partial^2\xi}{\partial t^2}\right|\Psi_m\rangle \ ; \tag{2.47}$$

where the term $\partial w/\partial t$ can be approximated as $\partial^2\xi/\partial t^2$. For each of the previous terms one can get the followings expressions

$$\begin{aligned}
\langle \frac{\partial p'}{\partial z} \mid \Psi_m\rangle &\approx -\rho_0 B_m p_m \langle \phi_m \mid \phi_m\rangle \ , \\
g\langle \rho' \mid \Psi_m\rangle &= gC_m^2 A_m \rho_m \langle \phi_m \mid \phi_m\rangle \ , \\
\langle \rho_0 \left| \frac{\partial^2 \xi}{\partial t^2} \right| \Psi_m\rangle &\approx -\rho_0 \frac{\partial^2 \eta_m}{\partial t^2} \langle \Psi_m \mid \Psi_m\rangle \ ;
\end{aligned} \tag{2.48}$$

grouping back the three previous terms, according to Eq.(2.47), it follows that

$$\rho_0 B_m p_m = gC_m^2 A_m \rho_m + \rho_0 d D^2 \frac{\partial^2 \eta_m}{\partial t^2} \ , \tag{2.49}$$

where $d = D^{-2}\langle \Psi_m \mid \Psi_m\rangle / \langle \phi_m \mid \phi_m\rangle$. Furthermore, equations (2.46) and (2.49) can be joined into a single expression, of the following form:

$$p_m = \frac{C_m^2}{B_m}\left(\eta_m + \frac{s}{4D}\eta_m^2\right) + d\frac{D^2}{B_m}\frac{\partial^2 \eta_m}{\partial t^2} \ . \tag{2.50}$$

Finally, for the third equation of the system (2.34) one can verify that

$$\begin{aligned}
&\langle \rho_0 \frac{\partial \mathbf{U}_h}{\partial t} + \nabla_h p' \mid \phi_m\rangle = \langle \rho_0 \left| \frac{\partial \mathbf{U}_h}{\partial t} \right| \phi_m\rangle + \langle \nabla_h p' \mid \phi_m\rangle = \\
&= -\langle \rho' \frac{\partial \mathbf{U}_h}{\partial t} + \rho_0 w \frac{\partial \mathbf{U}_h}{\partial z} + \rho_0 \left(\mathbf{U}_h \cdot \nabla_h\right) \mathbf{U}_h \mid \phi_m\rangle = \\
&= -\langle \rho' \left| \frac{\partial \mathbf{U}_h}{\partial t} \right| \phi_m\rangle - \langle \rho_0 \left| w \frac{\partial \mathbf{U}_h}{\partial z} \right| \phi_m\rangle - \langle \rho_0 \left| \left(\mathbf{U}_h \cdot \nabla_h\right) \mathbf{U}_h \right| \phi_m\rangle \ ;
\end{aligned} \tag{2.51}$$

for each term of the previous equation one can use the following approximations:

$$\langle \rho_0 \left| \frac{\partial \mathbf{U}_h}{\partial t} \right| \phi_m\rangle \approx \rho_0 \langle \frac{\partial \mathbf{U}_h}{\partial t} \mid \phi_m\rangle = \rho_0 D \frac{\partial \boldsymbol{\mathcal{U}}_m}{\partial t}\langle \phi_m \mid \phi_m\rangle \ , \tag{2.52}$$

$$\begin{aligned}
&\langle \nabla_h p' \mid \phi_m\rangle \approx \rho_0 C_{3m} \nabla_h p_m \langle \phi_m \mid \phi_m\rangle = \\
&= \rho_0 c_m^2 \nabla_h \eta_m \langle \phi_m \mid \phi_m\rangle - \frac{1}{2} s \rho_0 \eta_m \frac{\partial \boldsymbol{\mathcal{U}}_m}{\partial t}\langle \phi_m \mid \phi_m\rangle \\
&\quad + \rho_0 d D^2 \nabla_h \frac{\partial^2 \eta_m}{\partial t^2}\langle \phi_m \mid \phi_m\rangle \ ,
\end{aligned} \tag{2.53}$$

and

$$\langle\rho' \left|\frac{\partial \mathbf{U}_h}{\partial t}\right| \phi_m\rangle = -\frac{1}{3}C_m^2 D\rho_m \frac{\partial \boldsymbol{\mathcal{U}}_m}{\partial t}\ \phi_m^3\Big|_0^D \ ; \tag{2.54}$$

This term can be neglected and further ignored without any loss of generality [31]. Going further:

$$\langle\rho_0 \left|w\frac{\partial \mathbf{U}_h}{\partial z}\right| \phi_m\rangle \approx \langle\rho_0 \left|\frac{\partial \xi}{\partial t}\frac{\partial \mathbf{U}_h}{\partial z}\right| \phi_m\rangle \approx$$

$$\approx -\frac{1}{2}D\rho_0\frac{\partial \eta_m}{\partial t}\boldsymbol{\mathcal{U}}_m\langle\phi_m\left|\phi_m\right|\phi_m\rangle \ , \tag{2.55}$$

and

$$\langle\rho_0 \left|\left(\mathbf{U}_h\cdot\nabla_h\right)\mathbf{U}_h\right| \phi_m\rangle \approx \langle\rho_0 \left|\left(\mathbf{U}_h\cdot\nabla_h\right)\mathbf{U}_h\right| \phi_m\rangle \approx$$

$$\approx \rho_0 D^2\left(\boldsymbol{\mathcal{U}}_m\cdot\nabla_h\right)\boldsymbol{\mathcal{U}}_m\langle\phi_m\left|\phi_m\right|\phi_m\rangle \ ; \tag{2.56}$$

joining together the inner products obtained from Eq.(2.51), and rearranging the terms of the respective equation, one obtains that

$$\frac{\partial \boldsymbol{\mathcal{U}}_m}{\partial t} + \frac{C_m^2}{D}\nabla_h\eta_m + s\left(\boldsymbol{\mathcal{U}}_m\cdot\nabla_h\right)\boldsymbol{\mathcal{U}}_m$$

$$-\frac{s}{2D}\frac{\partial}{\partial t}\left(\eta_m\boldsymbol{\mathcal{U}}_m\right) + dD\nabla_h\frac{\partial^2\eta_m}{\partial t^2} = 0 \ ; \tag{2.57}$$

The equations (2.40) and (2.57) form the pair of *Boussinesq equations* ([30],[31]) for the case of a stratified fluid. The Boussinesq equations constitute an important preliminary stage in the study of soliton propagation.

In order to simplify the upcoming analysis, one will consider that the non-linear perturbation propagates along the x axis. Therefore, the equations (2.40) and (2.57) can be rewritten as

$$\frac{\partial \eta_m}{\partial t} + D\frac{\partial \mathcal{U}_m}{\partial x} + \frac{1}{2}s\frac{\partial}{\partial x}\left(\mathcal{U}_m\eta_m\right) = 0 \ , \tag{2.58}$$

and

$$\frac{\partial \mathcal{U}_m}{\partial t} + \frac{C_m^2}{D}\frac{\partial \eta_m}{\partial x} + s\mathcal{U}_m\frac{\partial u_m}{\partial x} - \frac{s}{2D}\frac{\partial}{\partial t}\left(\eta_m\mathcal{U}_m\right) + dD\frac{\partial^3\eta_m}{\partial t^2\partial x} = 0 \ ; \tag{2.59}$$

the velocity term can be eliminated by considering that [30]:

$$\mathcal{U}_m = \frac{C_m}{D}\eta_m + \frac{1}{4}s\frac{C_m}{D^2}\eta_m^2 + \frac{1}{2}dDC_m\frac{\partial^2\eta_m}{\partial x^2}\ , \tag{2.60}$$

where $\partial/\partial t \approx -C_m\partial/\partial x$; rejecting terms of higher non-linearity and substituting the above expression, into Eq.(2.58), one obtains, for the modal vertical displacement, η_m, that:

$$\frac{\partial\eta_m}{\partial t} + C_m\frac{\partial\eta_m}{\partial x} + \tilde{\alpha}_m\eta_m\frac{\partial\eta_m}{\partial x} + \tilde{\beta}_m\frac{\partial^3\eta_m}{\partial x^3} = 0 \tag{2.61}$$

where

$$\tilde{\alpha}_m = \frac{3}{2}s\frac{C_m}{D} \quad \text{and} \quad \tilde{\beta}_m = \frac{1}{2}dD^2C_m\ ; \tag{2.62}$$

Eq.(2.61) is known as the *Korteweg-de Vries equation* [29], and constitutes the starting point for the theoretical (or numerical) study of propagation of soliton packets[4]. Eq.(2.61) admits particular analytic solutions in terms of the hyperbolic secant, or of "dnoidal" Jacobi functions [39]. In both solutions the characteristic width of the soliton packets, and its phase velocity, depend on the pair of constants (2.62). However, regarding the spatial and temporal structure of the soliton packets, the analytic solutions of hyperbolic secant and dnoidal functions exhibit different behaviours, since in the first case the shape of the soliton packet remains constant in time and space, while in the second case one verifies a temporal and spatial evolution of the packet [41, 42].

2.3.4 Temperature perturbations

As previously remarked in section 2.2 one of the main effects of internal tide propagation corresponds to the oscillation of the thermocline at the semidiurnal frequency. However, from the tomography point of view, the system formed by equations (2.2), (2.6) and (2.8),

[4]It should be remarked that the substitution of Eq.(2.60) into Eq.(2.59) allows once again to obtain the Korteweg-de Vries equation, for the non-linear modal amplitude $\mathcal{U}_m$.

does not provide a clear physical basis for the analysis of temperature perturbations of the water column. In order to include the temperature within the context of the propagation problem of internal waves it becomes necessary to add a system of thermodynamic equations, relating the field of currents, $\mathbf{U}$, to the temperature field, T. By analogy with the general scheme illustrated in [43], one can consider the following thermodynamic equation [35]:

$$\frac{D}{Dt}(\rho c_v T) = \nabla \cdot (k_T \nabla T) + Q_T \ , \tag{2.63}$$

where c_v represents the specific heat of the water column, k_T corresponds to the thermal fluid conductivity, and Q_T represents the external sources of heat. Taking $(k_T, Q_T) = 0$, and considering both density and specific heat as constants, one can obtain the following expansion for the temperature perturbations (see the appendix of [41], which is included in Appendix II):

$$T - T_0(z) = \frac{dT_0}{dz} \sum_m \alpha_m(x,y,t)\Psi_m(z) \ ; \tag{2.64}$$

in this equation α_m represents the modal amplitude of temperature. Eq.(2.64) represents the starting point to relate the oceanographic problem of propagation of internal tides with the acoustic problem of tomographic inversion.

2.3.5 Salinity perturbations

In contrast with the temperature field, linearly related to the field of sound velocity, the salinity distribution, S, is not a common object of discussion within the context of the tomography problem. However, since the salinity field obeys to the differential equation [35]:

$$\frac{DS}{Dt} = \nabla \cdot (K_S \nabla S) + Q_S \ , \tag{2.65}$$

which has a structure similar to the one of Eq.(2.63), one can admit the following orthogonal expansion for the salinity:

$$S - S_0(z) = \frac{dS_0}{dz}\sum_m \alpha_m(x,y,t)\Psi_m(z) \ . \tag{2.66}$$

The validity of this expansion will be discussed in Chapter 6.

2.4 Underwater acoustic waves

The propagation of acoustic waves at sea plays an important role in many theoretical and practical problems, such as the localization of underwater acoustic sources, the characterization of bottom properties, underwater communications, identification of the emitted signal, or tomography, among many others. The fundamental equation for the propagation of acoustic linear waves can be derived from Eqs.(2.1) and (2.3), by neglecting the non-linear and rotation terms (Eq.(2.11)). On the basis of thermodynamic relationships, and considering variations of first order in the water column salinity and entropy, one can obtain the *Wave Equation* for the acoustic pressure, p [14, 44]:

$$\nabla^2 p = \frac{1}{c^2}\frac{\partial^2 p}{\partial t^2} \ , \tag{2.67}$$

where c represents the propagation velocity of linear acoustic waves (sound velocity in the water column). A direct measurement of c can be accomplished with the help of velocimeters, which provide information with an accuracy of 0.3 m/s. Alternatively, one can measure the water temperature, T, and salinity, S, at different depths, z, and calculate the sound velocity profile using empirical expressions, as, for instance, using Mackenzie's expansion [45]:

$$\begin{aligned} c \;=\; & 1448.96 + 4.591 \times T - 5.304 \times 10^{-2}T^2 + 2.374 \times 10^{-4}T^3 + \\ & +1.304 \times (S - 35) + 1.630 \times 10^{-2}z + 1.675 \times 10^{-7}z^2 + \end{aligned}$$

$$+1.025 \times T\,(35 - S) - 7.139 \times 10^{-13} T z^3 \ . \tag{2.68}$$

In the previous expansion the values of temperature, salinity and depth, should be specified, respectively, in Celsius degrees, parts per thousands, and meters. It should be remarked that in shallow water the predominant contribution corresponds to the one of the linear term of temperature. This linear relationship (in a first approximation) between T and c will be extremely important in the parameterization of the sound velocity profile, which will be discussed in section 4.1.3.

For a narrowband acoustic signal one can assume that $p(t) = \hat{p}e^{-i\omega t}$, where i represents the imaginary unit ($i = \sqrt{-1}$). Replacing this expression into Eq.(2.67) one can obtain the *Helmholtz Equation*:

$$\nabla^2 \hat{p} + \frac{\omega^2}{c^2}\hat{p} = 0 \ . \tag{2.69}$$

The previous equation constitutes the starting point for the analysis of propagation of acoustics signals within the water column. For a broadband signal the solution of Eq.(2.69), for each component ω of the frequency spectrum, allows one to calculate $p(t)$ through a Fourier synthesis.

The direct numerical solution of Eq.(2.69) involves intensive calculations on a computer. To reduce significantly the time of calculations one can apply analytic approximations that simplify the Helmholtz Equation. One approximation corresponds to the *Method of Ray Tracing* [46], which introduces in a natural fashion the concepts of *eigenrays*, Γ, and of *travel times*, (or simply *arrival times*), τ. The eigenrays correspond to trajectories which obey to the Snell's Law (related to the Principle of Minimal Time [47]) and connect the acoustic source to the hydrophone. The arrival time for a particular eigenray can be obtained by calculating the path integral

$$\tau = \int_{\Gamma} \frac{ds(z,r)}{c} \ , \tag{2.70}$$

where ds corresponds to the differential of the eigenray at the (z,r) position. Furthermore, the acoustic pressure would correspond to [46]

$$\hat{p} = \hat{p}_0 \sum_{j=1}^{\mathsf{T}} \frac{1}{4\pi s_j} \exp\left(i\omega\tau_j\right) \tag{2.71}$$

where $\hat{p}_0$ represents the amplitude of the emitted signal, T corresponds to the number of eigenrays, and s_j represents the length of the eigenray Γ_j:

$$s_j = \int_{\Gamma_j} d\Gamma_j \ . \tag{2.72}$$

In general Ray Tracing methods are applied in the cases where the wavelength of the acoustic signal, λ, is much less than the waveguide depth, D:

$$\lambda \ll D \ . \tag{2.73}$$

Although less accurate than other analytic approximations the Ray Tracing methods are the fastest.

Another approximation corresponds to the *Method of Normal Modes* [46, 48], when the method of separation of variables is applied to solve Eq.(2.69), thus giving a solution of the type

$$\hat{p} = \hat{p}_0 \sum_{j=1}^{\infty} \left(\frac{2\pi}{k_j r}\right)^{1/2} Z_j(z_s) Z_j(z) \exp\left(i k_j r\right) \ , \tag{2.74}$$

where z_s represents the acoustic source depth, k_j corresponds to the eigenvalue associated to the acoustic normal mode Z_j, which can be calculated by solving a SLP of the following form:

$$\frac{d^2 Z_j}{dz^2} + \left(\frac{\omega^2}{c^2} - k_j^2\right) Z_j = 0 \quad + \quad \text{BCs} \ . \tag{2.75}$$

It can be shown that the first normal modes correspond to those that contribute more to the structure of the acoustic field, so the expansion (2.74) can be accurately approximated keeping only some of the first terms [48].

One interesting aspect of the solution (2.71) consists in that one can calculate the acoustic pressure in the time domain through the Fourier synthesis analytically. In fact, by denoting the acoustic source spectrum as $\hat{S}(\omega)$, one obtains that [46]

$$\begin{aligned} p(t) &= \frac{1}{2\pi}\int\limits_{-\infty}^{\infty} \hat{p}\hat{S}(\omega)\exp(-i\omega t)\,d\omega = \\ &= \hat{p}_0\sum_{j=1}^{\mathsf{T}}\frac{1}{4\pi s_j}\int\limits_{-\infty}^{\infty}\hat{S}(\omega)\exp\left[-i\omega\left(t-\tau_j\right)\right] = \\ &= \hat{p}_0\sum_{j=1}^{\mathsf{T}}\frac{1}{4\pi s_j}s\left(t-\tau_j\right) = \\ &= \sum_{j=1}^{\mathsf{T}} a_j s\left(t-\tau_j\right)\ , \end{aligned} \tag{2.76}$$

where $a_j = \hat{p}_0\left(4\pi s_j\right)^{-1}$ and $s(t)$ represents the signal emitted by the source. Eq.(2.76) indicates that the received signal can be represented at the acoustic hydrophone as a sum of "replicas" of the emitted signal, weighted by the amplitudes a_j, and delayed by the arrival times, τ_j. However, from the point of view of signal processing, the received signal corresponds to the convolution of the emitted signal with the *impulse response* of the propagation channel, $h(t)$ [49]:

$$p(t) = h(t) * s(t)\ . \tag{2.77}$$

Therefore, by combining Eq.(2.77) with Eq.(2.76) one can conclude that the channel impulse response can be represented as a sum of Dirac functions, $\delta(t)$, weighted with the amplitudes a_j, and delayed with the arrivals τ_j:

$$h(t) = \sum_{j=1}^{\mathsf{T}} a_j\delta\left(t-\tau_j\right)\ . \tag{2.78}$$

This analytic approximation to the channel impulse response will be referred to during the discussion of the pre-processing of acoustic data, in section 3.3.4.

2.5 Internal tide effects on acoustic signals

The previous sections have been dedicated to the discussion of the theoretical aspects of internal tides and wave propagation, and also of linear acoustic wave propagation. As indicated in sections 2.3.4 and 2.3.5 internal waves affect the distributions of temperature and salinity, which in turn will affect the sound velocity field, c. These variations will also affect (in a non-linear way) the received signal at the hydrophone. Therefore, the propagation of internal tides in coastal zones will be reflected in the perturbations of the acoustic signal, that propagates through the respective field of sound velocity. This section will present a brief description of some of the references which discuss this problem, both at the level of simulations and observations.

For the deep water case the effects of internal tides on the propagation of acoustic signals had been referred to since the beginnings of the 70s [50]. Since then the number of references has increased, covering the case of coastal waters as well. Those studies reveal, in particular, the sensitivity of reciprocal acoustic transmissions (i.e., with emission and reception systems which switch functions alternatively) to the semidiurnal variations of underwater currents [51], and also to the significant fluctuations that internal tides induce in the signal-to-noise ratio [52]. Additionally, internal tides had been indicated as responsible by the temporal compression and dilation, at large distances, and at roughly the semidiurnal period, of the arrival patterns[5] of the emitted and received signals [53]. The effects of internal tides on the

[5] The "arrival pattern" of the emitted and received signals corresponds to an estimator of the channel impulse response. This preliminary definition will be discussed in detail during the description of the acoustic data pre-processing of the INTIMATE'96 sea trial.

performance of matched-field estimators have been discussed on synthetic data within the context of the source localization problem [54, 55]. Moreover, the study developed in [11] is concerned to the impact of thermocline oscillations in the propagation of acoustic signals in continental platform waters, and tries to identify some of the preliminary conditions that would make feasible the tomographic inversion of the internal tide.

Chapter 3

The INTIMATE project

The INTIMATE project (INternal Tide Investigation by Means of Acoustic Tomography Experiments)[1] was developed as a preliminary study, focusing the application of the methods of Ocean Acoustic Tomography to the monitoring, and further inversion, of internal tides. The main motivation for this study is related to the importance of internal tides in coastal habitats (already referenced in section 2.2), and also with the existence of a significant amount of observations, indicating the sensitivity of acoustic signals to the environmental perturbations induced by internal tides. The INTIMATE project involved the collaboration of the *Universidade do Algarve* (UALG, in Faro), the *Instituto Hidrográfico* (IH, in Lisbon), the *Service Hydrographique et Oceanographique de la Marine/Centre Militaire Oceanographique* (SHOM/CMO, in Brest, France), and the *New Jersey Institute of Technologie* (NJIT, in New Jersey, USA), and has been an innovative platform for the development of instrumental, theoretical, and computational techniques, oriented to a field of research which is poorly known in Portugal, but that has been developing intensively beyond frontiers, not only among the state members of the European Community, but also in Canada and United States. One of the fundamental achievements of the INTIMATE project was the development of the first tomography sea trial in Portuguese waters (the INTIMATE'96 experiment),

[1] *Url:* http://w3.ualg.pt/~sjesus/intimate.html.

which was further followed by the INTIMATE'98, in the Bay of Biscay and, more recently, by the INTIMATE'00, in the Bay of Setúbal. Of these three sea trials the INTIMATE'96 experiment is the one that had received more attention within the context of the project, leading to a significant number of publications in conferences and scientific journals. In this way, the detailed study of the acoustic and oceanographic data acquired during this sea trial helped the INTIMATE team to consolidate fundamental aspects of the general problem of acoustic tomography of internal tides. The preliminary knowledge acquired will simplify the future processing of the data gathered during the second and third tomography experiments.

3.1 The INTIMATE'96 sea trial

The INTIMATE'96 sea trial took place during June of 1996, near the town of Nazaré (see Fig.3.1). The experimental site was chosen based on previous studies developed by IH, which indicated the experimental area as a potential candidate for the generation, (and further propagation) of internal tides. The INTIMATE'96 experiment constitutes the first sea trial of acoustic tomography developed in Portuguese waters. During the six days of the experiment (from June 13 to 18) the research vessels BO D'ENTRECASTEAUX (SHOM), and NRP ANDROMEDA (IH), proceeded with the acquisition of navigation, bathymetry, current, temperature, CTD[2], and acoustic data, according to a schedule of activities previously defined. During the phase regarding the acoustics transmissions the French vessel carried an acoustic source (see Fig.3.2). The description of the emitted signal can be found in section 3.3.1. The acoustic signals were received on a vertical line array (hereafter VLA), belonging to the NATO SACLANT Undersea Research Center (La Spezia, Italy). The VLA

[2] *Conductivity-Temperature-Depth* [3]. However, a significant part of the instrumentation, formally known as CTD, allows nowadays to measure a wider set of parameters.

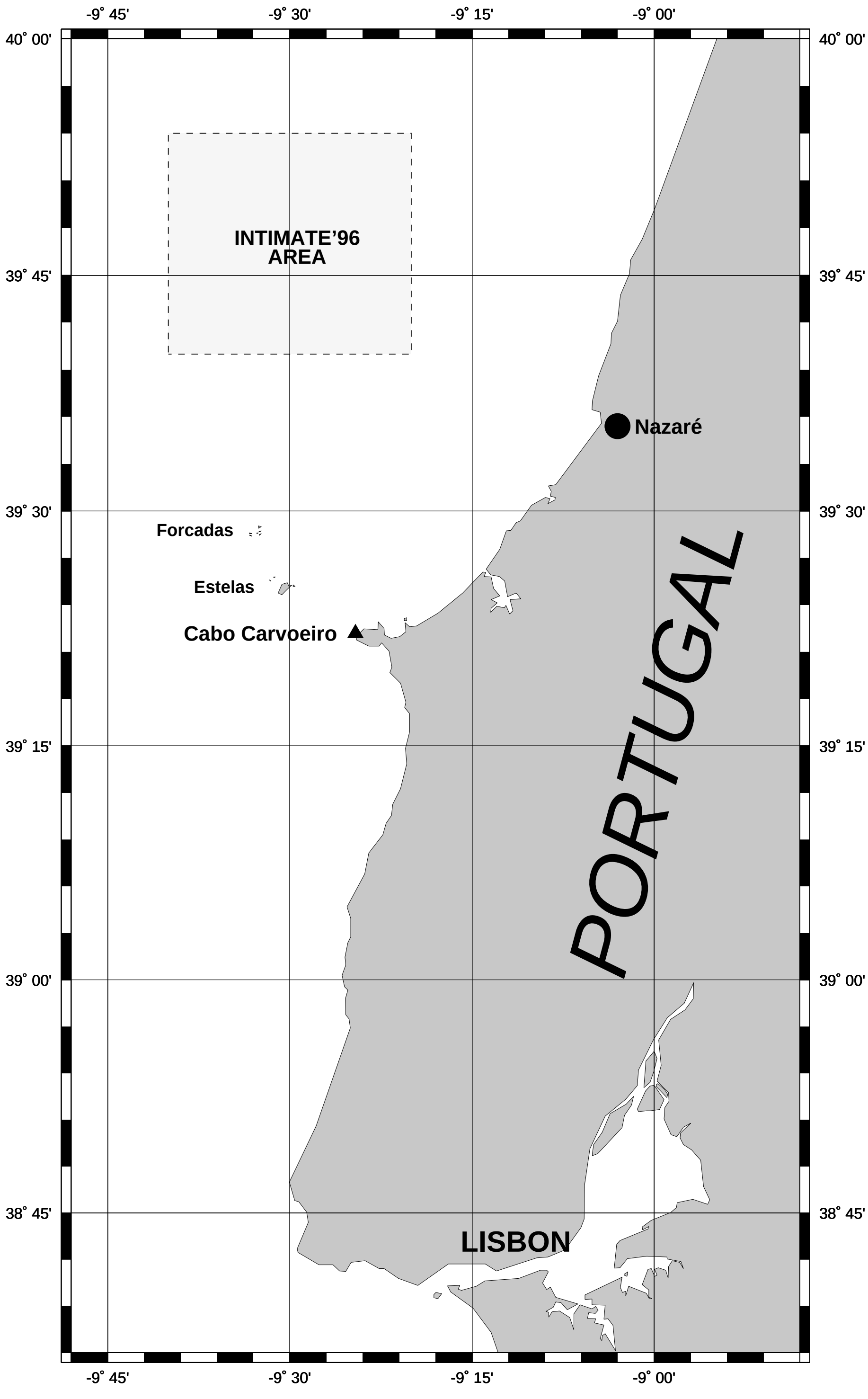

Figure 3.1: Geographic location of the area reserved for the INTIMATE'96 sea trial.

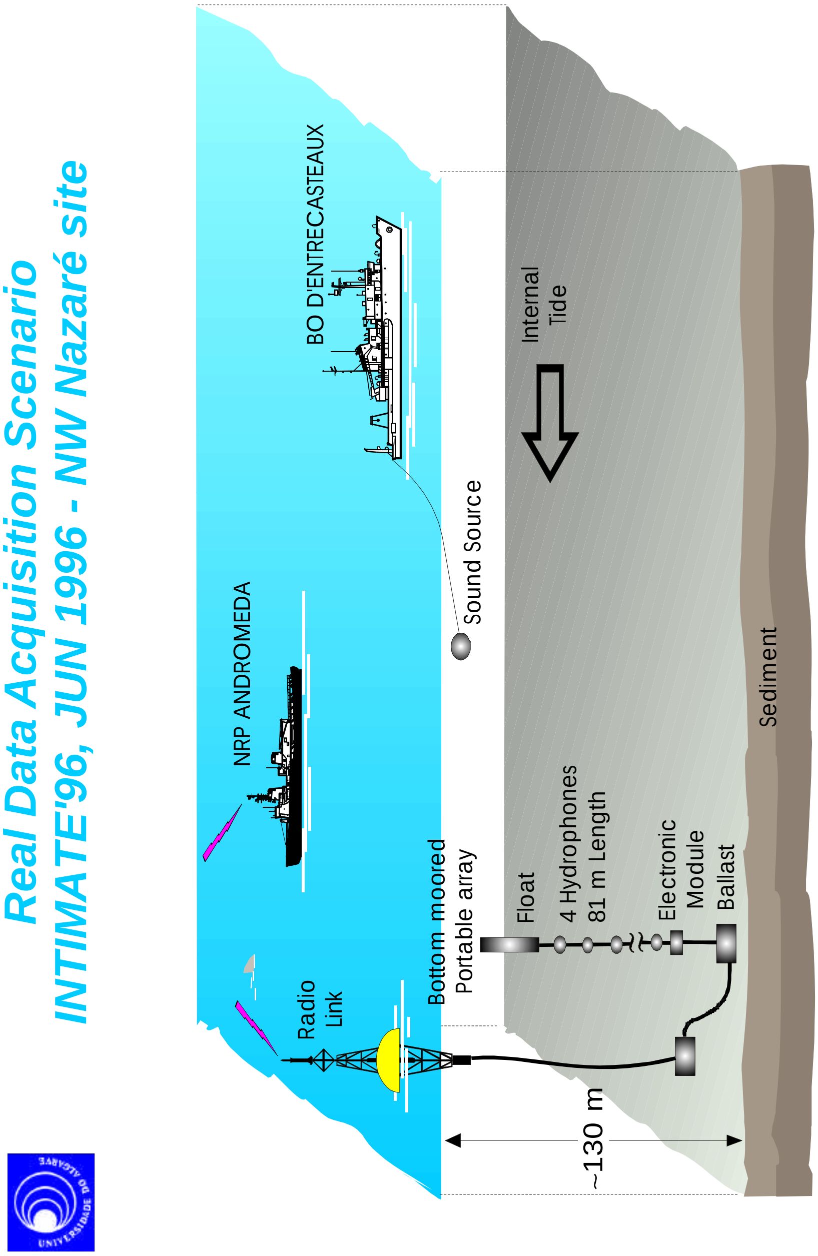

Figure 3.2: Experimental strategy of the INTIMATE'96 sea trial.

was composed of an electronic system and 4 hydrophones (see Fig.3.2). The received signals were transmitted through a radio link from the VLA to the NRP ANDROMEDA, and was sampled at a frequency of 6kHz, and further recorded on VHS tapes. Each tape contained approximately three hours of acoustic data. All the acoustic data were recorded after the end of the sea trial in CD-ROM support at the SiPLAB. Each set of three hours with acoustic transmissions (formally known as a "Tape"), was recorded in groups ("runs") with 300 seconds of duration. Each run contained 37 records (formally called as "pings", or "snapshots") of the received signal in each of the 4 hydrophones. The preliminary description of the set of oceanographic and acoustic data can be found in the internal report [56], written by the INTIMATE team. Despite the fact that this report constitutes a source of fundamental information for the starting development of a particular strategy of tomographic inversion (which will be discussed in section 5.2), the report also develops an independent analysis of the two data sets. That independent approach is a natural consequence of the temporal proximity between the end of the tomography sea trial and the redaction of the report. In order to update the analytic overview of the data referenced above, the two sets of oceanographic and acoustic data will be discussed once more in sections 3.2 and 3.3, with the natural care of avoiding any kind of superposition.

3.2 Oceanographic data

During the sea trial an intensive acquisition of oceanographic (temperature, pressure, etc.) data was accomplished . The discussion of these data will be developed in the following sections by grouping different measurements in pairs mutually related. To simplify the description of the temporal variations of the oceanographic data it will be introduced a "Julian" time scale, with the convention that the normal date 1996/06/13/00:00h corresponds to the Julian date 165.0.

3.2.1 Bathymetry, geology and acoustic transmission geometry

The direct acquisition of geological bottom samples and uniboom surveys, accomplished by the two oceanographic teams on board the vessels BO D'ENTRECASTEAUX and NRP ANDROMEDA, revealed a bottom structure with the predominance of a layer of fine sand, with a thickness between 0.5 and 1 m, lying upon a substrate of silty clay. As indicated by geoacoustic reference studies ([57]–[59]), the sediment structure can be characterized with the following parameters:

Mean density,	ρ,	$\approx$	1.98 g/cm^3.
Compressional speed,	c,	$\approx$	1750 m/s.
Attenuation,		$\approx$	0.8 dB/λ.

The bathymetry data, acquired by the IH and the CMO, indicates variations in bottom depth, along the longitudinal axis, between 150 and 130 meters. On the other side, those data indicate that the bottom depth remains constant along the latitudinal axis (see Fig.3.3, the set of continuous lines indicates the navigation of the BO D'ENTRECASTEAUX during the transmissions), although near the continental slope –partially seen on the left side of the figure– one can notice a slight inclination of the isobaths, with a slope $\theta \approx 15°$ related to the vertical axis. This orientation of the continental slope suggests that the direction of internal tide propagation corresponds to $\theta \approx 15°$, relative to the horizontal axis, which implies the anisotropy of the temperature field along the horizontal and vertical axes. As will be discussed in section 4.1.2 this direction of propagation will be consistent with the phase difference of actual current data acquired in the proximity of the VLA.

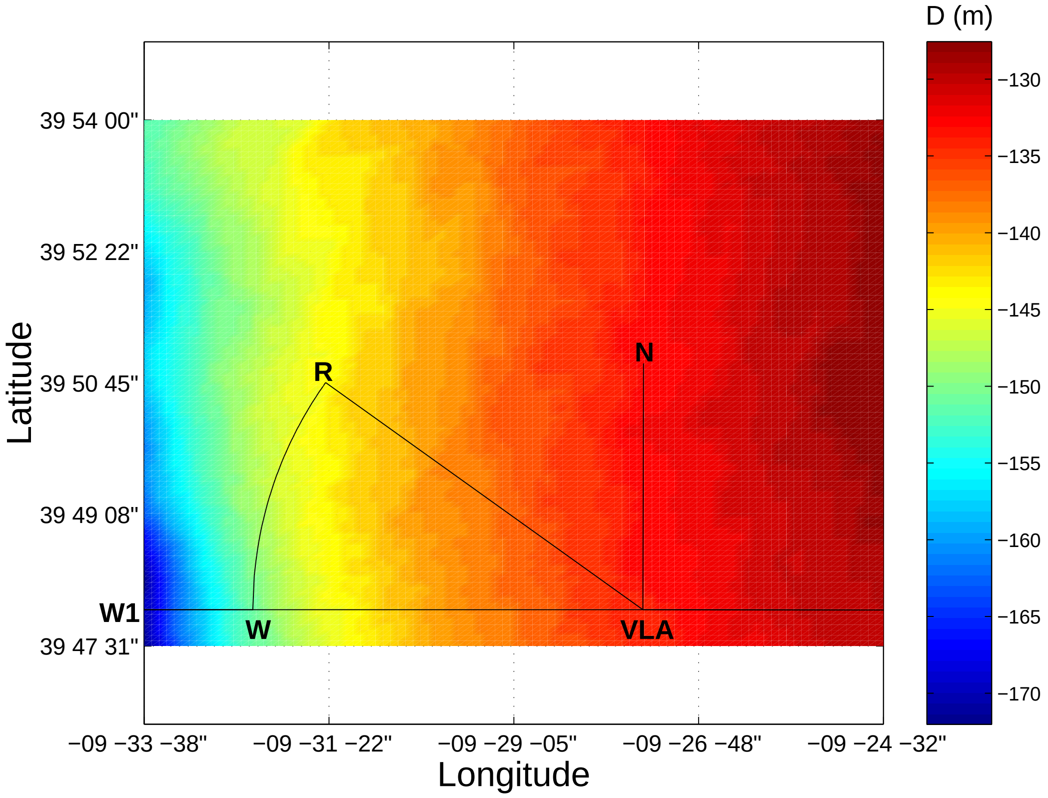

Figure 3.3: General bathymetry of the INTIMATE'96 area and geometry of acoustic transmissions.

3.2.2 Water column pressure and salinity

The water column pressure and salinity data correspond to 34 CTD-IH records. As was discussed in Chapter 2 the comparison of these two types of water column characteristics provides a concrete perspective of the baroclinic conditions of the monitorized environment. The comparison of pressure and salinity data (see Fig.3.4) allow one to verify that the isobaths remain constant along time, while the isopycnics are clearly dominated by the propagation of the internal tide, exhibiting semidiurnal oscillations in amplitude, with maximal values achieving approximately 10 meters. This comparison makes it clear the predominance of the semidiurnal baroclinic tide in the area that the experimental team intended to acoustically monitorize during the tomography sea trial.

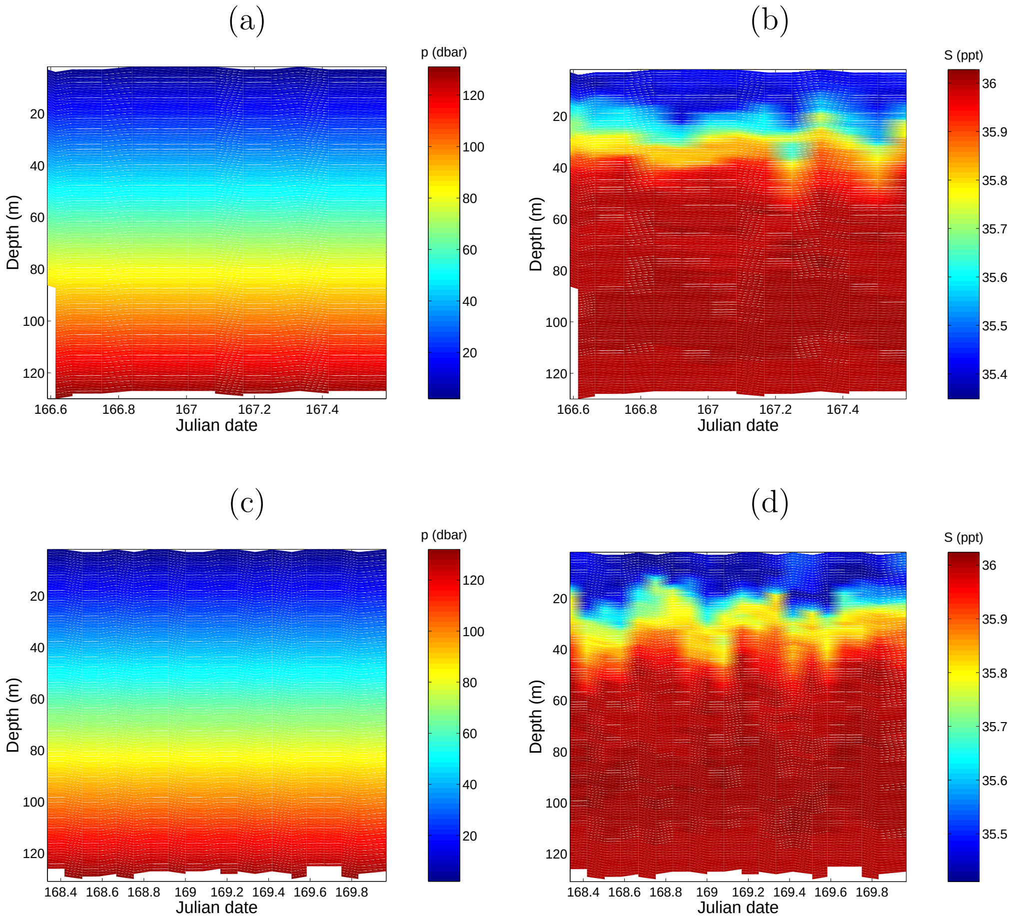

Figure 3.4: CTD-IH data: pressure, p (cases (a) and (c)), and salinity, S (cases (b) and (d)).

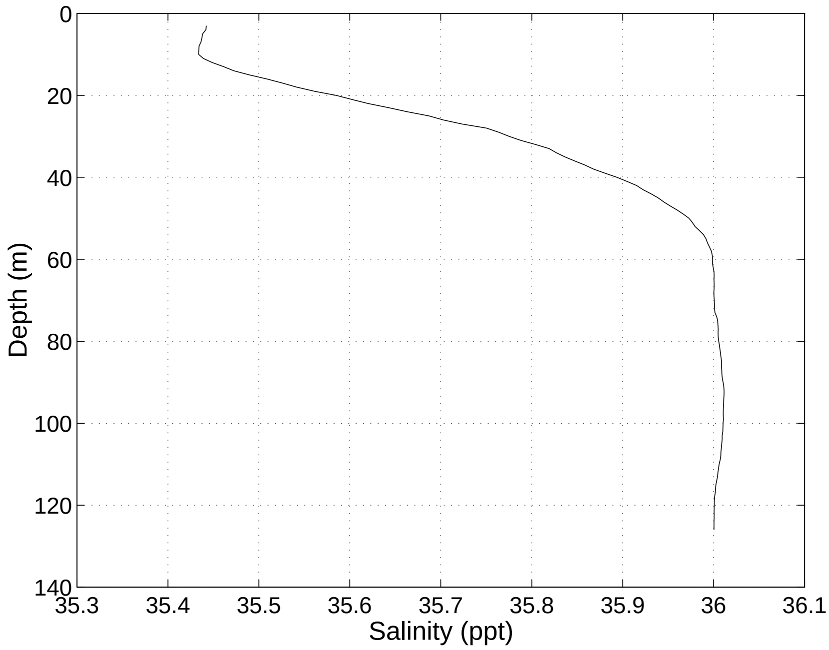

Figure 3.5: CTD-IH, mean salinity profile, $S_0(z)$.

3.2.3 Temperature

The temperature data corresponds to 34 CTD-IH records, 680 records of a thermistor chain at the position (39.7917°N , 9.4503°W) and 73 XBT[3] records, made by CMO. The XBT data were acquired at different locations of the monitorized area, with a slight concentration of records at fixed locations "N" and "W", at distances of 5.6 and 6.5 km, respectively, relative to the location of the VLA (see Fig.3.3). On the other side, the acquisition of CTD and thermistor chain data took place in the proximity of the VLA.

The CTD records have a depth resolution $\Delta z \approx 1$ meter, and were acquired at different time instants along days 14 to 17 (see Fig.3.6). The thermistor chain data, with a depth resolution $\Delta z \approx 5$ meters[4], and were acquired at regular intervals of 10 minutes, along days 13 to 18 (see Fig.3.7). In both cases the temperature field shows clearly semidiurnal variations of temperature, which are induced by the propagation of the internal tide. The mean temperature profile, $T_0(z)$ (see Fig.3.8), exhibits an exponential-like decay in depth, and differs significantly of the usual representations of a water column constituted by a reduced number of layers, with different densities, and with a thermocline which can be easily identified. In fact, it is difficult to identify clearly in figures 3.6 and 3.7 the presence of a thermocline, and this fact makes it evident the complex stratification of the monitorized water column. This particularity of the mean temperature profile constitutes an important indicator of the continuous density variations in depth, which should be included in the context of the inversion scheme. It will be shown in Chapter 5 that the stratification leads to the calculation of the HNMs, and that these theoretical modes allow one to parametrize

[3] *Expendable bathythermograph.*

[4] In fact the thermistor records at depths 48 and 76 m were eliminated from the analysis, since they indicated unrealistic values of temperature.

the variations of temperature and sound velocity. Moreover, in that Chapter will be also shown that the HNMs can be used to regularize the problem of tomographic inversion.

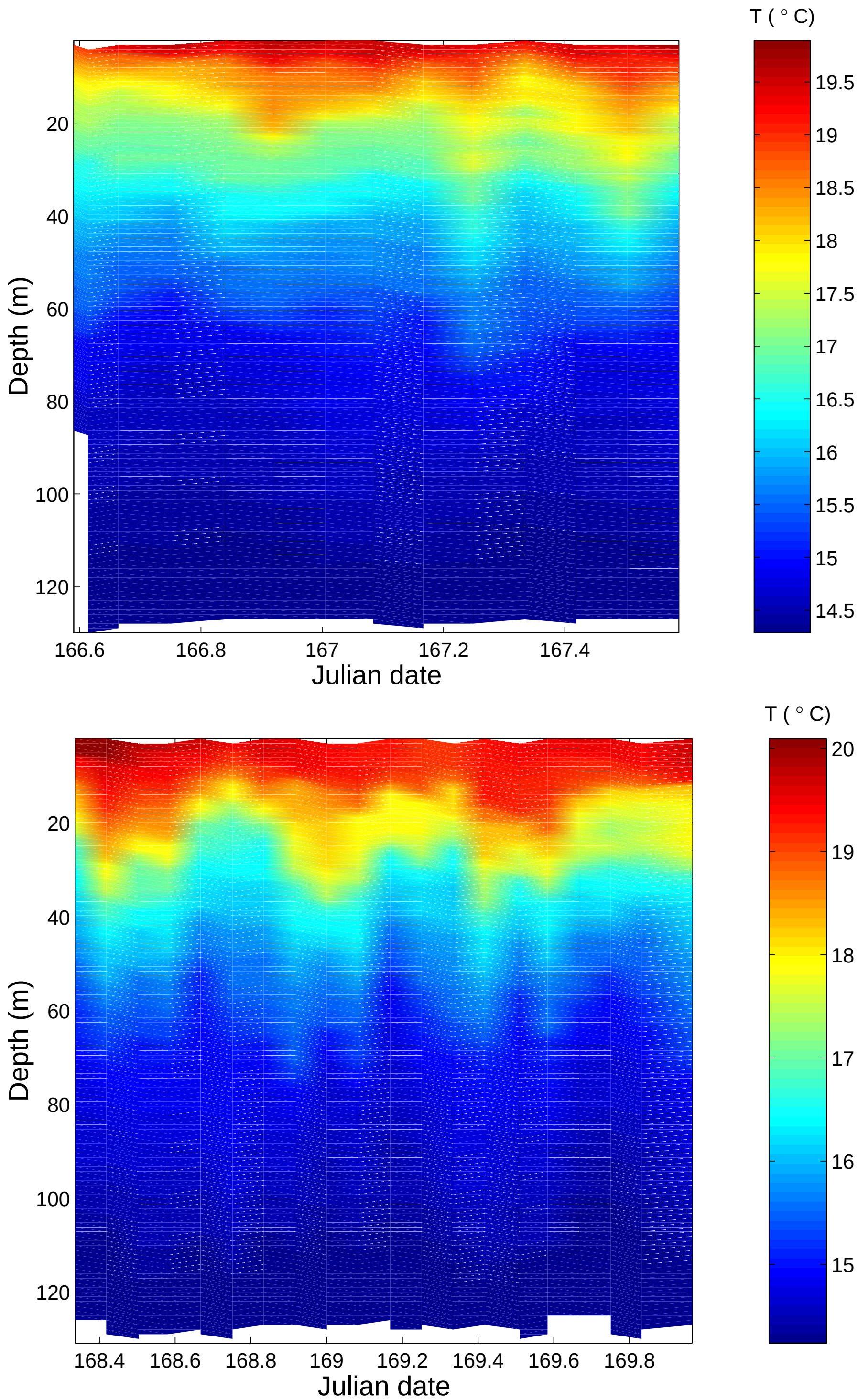

Figure 3.6: CTD-IH temperature data, T.

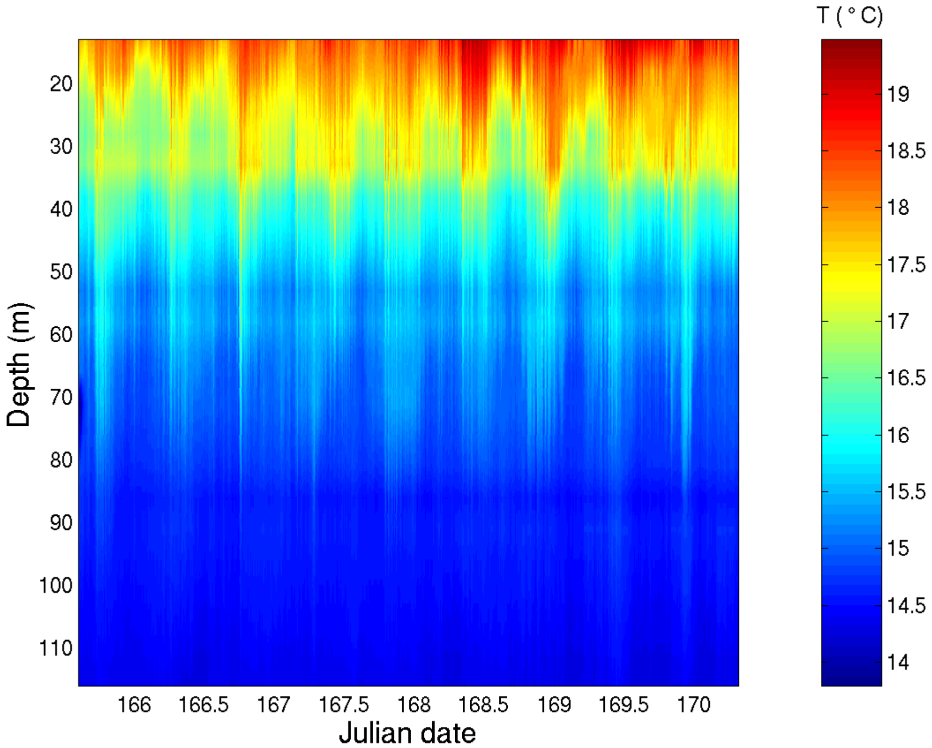

Figure 3.7: TERM-CMO temperature data, T.

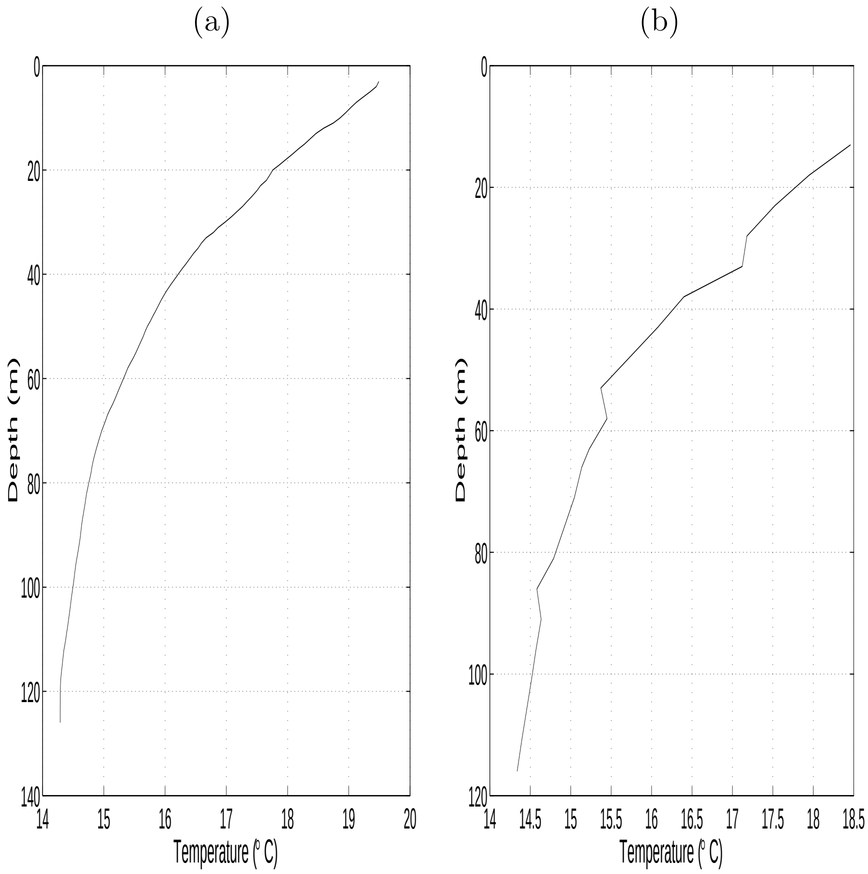

Figure 3.8: Mean temperature profiles CTD-IH (a) and TERM-CMO (b).

3.2.4 Currents

The ADCP[5] CMO data contain 678 records of current components u, v and w[6]. The records started 1996/06/13/15:20h and ended in 1996/06/18/08:10h. The ADCP system was located at the position (39.7917°N , 9.4673°W), and operated at a frequency of 300 kHz, with a sampling period of 10 minutes, and a depth resolution of 4 meters. The current records exhibit amplitudes of oscillation around 40 cm/s, and make evident the semidiurnal variation of the current components (see Fig.3.9 for the case of the u component, the variations of v exhibit a similar pattern).

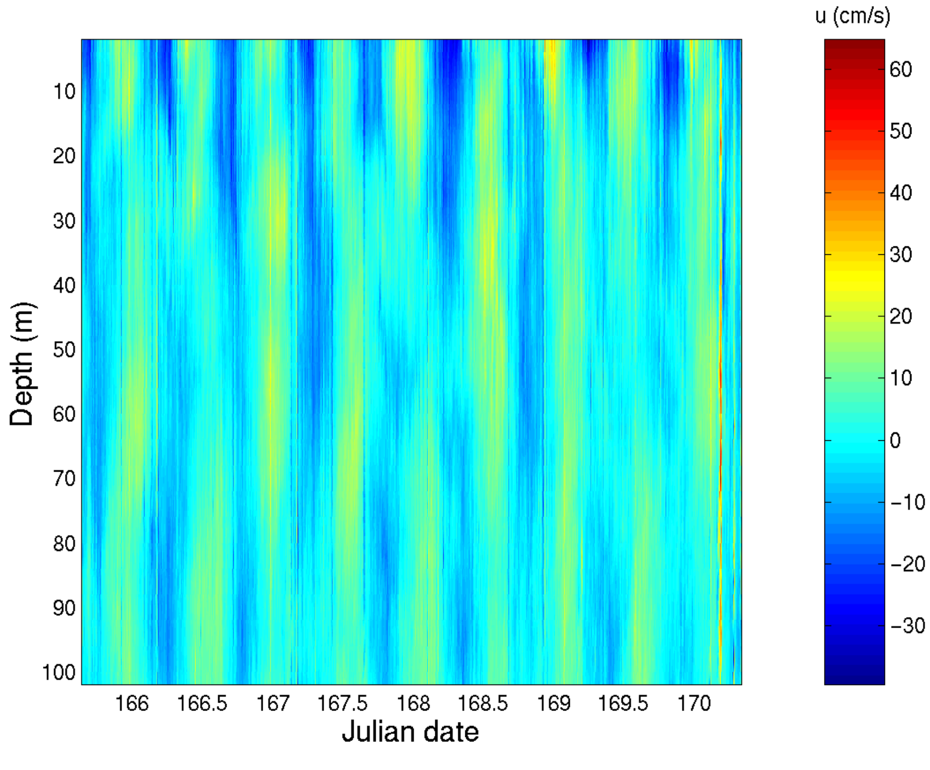

Figure 3.9: ADCP-CMO current data, u.

[5] *Acoustic Doppler Current Profiler.*

[6] This last set of records was contaminated with a high level of noise, making it impossible to include them in the analysis.

3.2.5 The buoyancy profile

The calculation of hydrostatic and non-hydrostatic modes can be accomplished by calculating the mean buoyancy profile from CTD-IH data. However, from the tomographic point of view, it is more interesting to explore the relationship [14, 36]

$$N^2 = g\left[a_T\frac{dT_0}{dz} + a_T^2 g\frac{T_0}{C_{ps}} - a_s\frac{dS_0}{dz}\right] \ , \tag{3.1}$$

where $a_T = 2.4110^{-4}\,(^\circ\mathrm{C})^{-1}$ and $C_{ps} = 3994\mathrm{J}\,(\mathrm{kg}^\circ\mathrm{C})^{-1}$. Eq.(3.1) allows one to calculate $N(z)$ from the temperature and salinity profiles, T_0 and S_0, respectively, reducing the information involved in the tomography scheme. By eliminating the vertical gradient of salinity, S, (i.e., admitting that the vertical variation of salinity can be neglected) one obtains an expression that depends only on the temperature, T_0, and that can be used to calculate the theoretical modes HNMs referred above. The validity of the suggested approximation can be verified through the comparison between the mean profile, calculated from direct measurements of buoyancy data, and the profiles calculated from both salinity and temperature mean profiles, and from the temperature profile only (see Fig.3.10).

3.2.6 Sound velocity

The CTD-IH data contain also sound velocity records, which are very important for a confrontation of the inverted and expected results. The semidiurnal variations of the sound velocity field (see Fig.3.11) reproduce the pattern already exhibited by Fig.3.6. This similarity between the temperature and the sound velocity fields is not surprising. In fact, as discussed in section 2.4, the empirical expansion of Mackenzie (see Eq.(2.68)) allow one to notice, in a first approximation, the predominance in an shallow water environment of the linear term related to the temperature. As will be discussed in section 4.1.3 this linear ap-

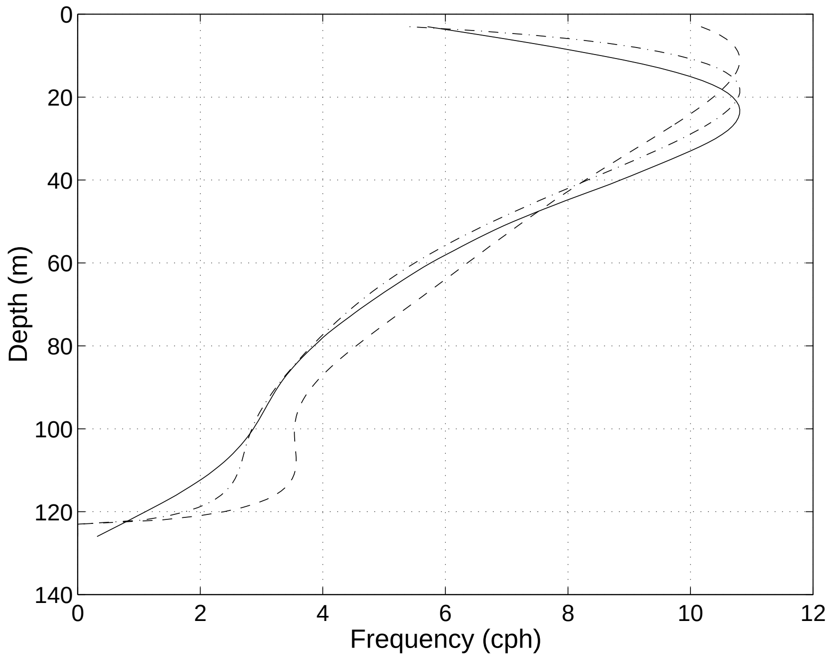

Figure 3.10: CTD-IH, buoyancy profiles $N(z)$: mean of measured profiles (continuous line), estimated profile from mean temperature and salinity (dot-dash line) and estimated profile from mean temperature only (dashed line).

proximation will be extremely important in order to parametrize the sound velocity profile, $c(z)$.

The mean profile $c_0(z)$ (see Fig.3.12), as the mean temperature profile, $T_0(z)$, exhibits a negative depth gradient, which acoustically implies a refractive action on the propagating signal, forcing it to be reflected repeatedly on the bottom. This issue will be discussed in more detail in Chapters 4 and 5 dedicated, respectively, to the inverse and forward problems.

3.3 Acoustic data

3.3.1 Acoustic source and emitted signal

As commented previously the acoustic source was carried by the French vessel BO D'ENTRECASTEAUX, and was most of the time at an average depth $z_s = 90$ meters. The acoustic source corresponded to a model of transducer designed by the French institutions DCN and ERAMER, and emitted a broadband signal, with a duration of 2 seconds, a repetition rate

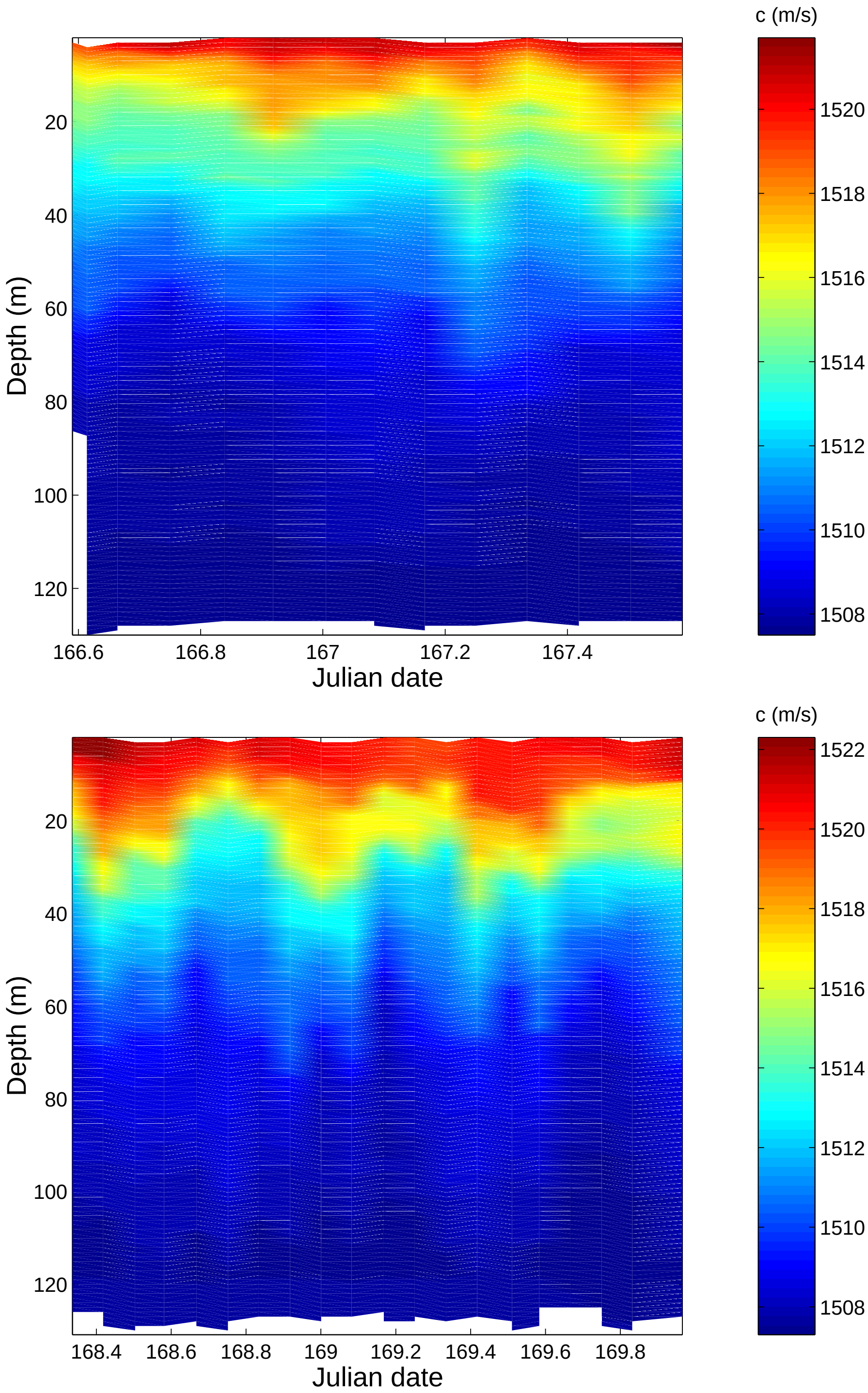

Figure 3.11: CTD-IH sound velocity data, c.

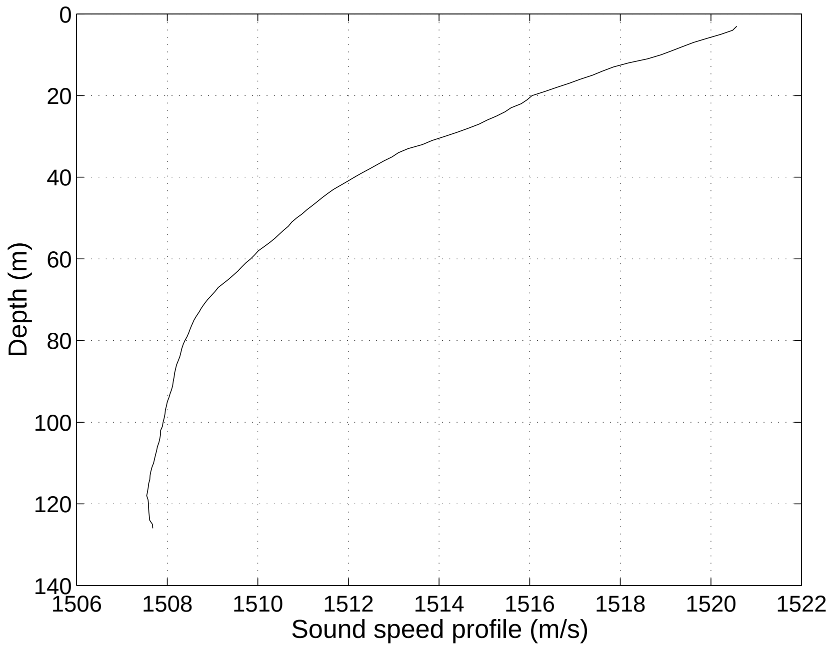

Figure 3.12: CTD-IH mean sound velocity profile, $c_0(z)$.

of 8 seconds, and a linearly modulated frequency, $f(t) = \alpha t + f_0$, where $f(0) = 300$ Hz and $f(2\text{s}) = 800$ Hz.

3.3.2 Receiving system

The VLA was constituted by 4 hydrophones, at average depths of 35, 75, 105 and 115 m and was located at geographic position (39.7995°N , 9.4583°W). It was found at the end of the experiment that the hydrophone at 75 m was flooded with salt water, making it impossible to use the corresponding set of received signals in the tomographic inversion. The other three hydrophones will be hereafter named as hydrophone 1, hydrophone 2 and hydrophone 3. As will be shown in Chapter 5 an array geometry with only three hydrophones imposes severe limitations to the degree of accuracy of the tomography results. Another important issue corresponded to the problem of arrival *synchronization*. The acquisition system was designed in order to include a signal of reduced duration and large amplitude (usually known as a "spike") at the moment of signal emission by the acoustic source. The presence of the spike in the received signal would indicate the instant of signal emission and would allow one to accurately determine the absolute arrival times, τ. However, the processing of the received signals, searching for the presence of the spikes in the acoustic data, revealed frequent discontinuities in their record [60]. The lack of regularity in the presence of the spikes makes it impossible to develop an absolute datation of the received signals. This issue will be discussed again in Chapter 6, which will be dedicated to the discussion of the tomographic inversion of acoustic data.

3.3.3 Events

The continuous lines illustrated in Fig.3.3 indicate the navigation of the BO D'ENTRECASTEAUX during the acoustic transmissions. The transmissions, hereafter called as "Events", can be classified in the following way:

- Event 0: set of transmissions along the N–VLA axis, while the BO D'ENTRECASTEAUX approached to the N position. This set of transmissions was developed exclusively for the testing of the transmission and reception systems. Event 0 started at 1996/06/14, 7:36 h.

- Event I: set of transmissions along of the N–VLA axis, with a constant water column depth $D \approx 135$ m, and a constant horizontal distance of transmission $R \approx 5.6$ km. Event I covers the acoustic transmissions from Tape 4 until Tape 10. This Event started at 1996/06/14, 17:19 h.

- Event II: set of transmissions along of the N–VLA and R–VLA axes, R–W radial and W–W1 axis, with simultaneous variations in the horizontal distance of transmissions, R, and depth, D, along the horizontal propagation distance r. Event II covers the acoustic transmissions from Tape 11 until Tape 15, and started at 1996/06/16, 7:18 h.

- Event III: set of transmissions along of the W–VLA axis, with a variation of the water column depth, D, between 150 and 130 meters, and a constant horizontal distance $R \approx 6.5$ km. Event III covers the acoustic transmissions from Tape 16 until Tape 24. This Event started at 1996/06/16, 22:16 h.

3.3.4 Acoustic data pre-processing

One of the preliminary stages in the analysis of the acoustic transmissions consisted in the calculation of the arrival patterns, Π, of the emitted and received signals, respectively $s(t, z_s)$ and $r(t, z_r)$. The arrival pattern corresponds to an estimate of the channel impulse response, $h(t)$. In a perfect waveguide (and as previously discussed in section 2.4) $h(t)$ corresponds to a sum of Dirac delta functions, delayed and weighted with a set of delays and amplitudes, which depend on the propagation channel. The distribution of Dirac delta functions in the reception window allows one to determine the acoustic arrivals, which in the language of signal processing implies that an arrival pattern constitutes an estimator of the temporal arrivals. In the real case $s(t, z_s)$ has a finite bandwidth, Δf, which imposes a temporal resolution $\sim (\Delta f)^{-1}$ to the arrival pattern. Therefore, the arrival pattern Π, instead of corresponding to a sum of delayed and weighted Dirac delta functions (with zero width), will correspond approximately to a sum of delayed and weighted "sinc"[7] functions, with a temporal width $\Delta t \approx (\Delta f)^{-1}$.

The pre-processing scheme of acoustic data, aiming to the calculation of the mean arrival patterns, is illustrated in Fig.3.13. That pre-processing involved the usage of classical signal processing techniques (intercorrelation, Hilbert transform, signal envelope) which will not be

[7]The "sinc" function is defined as $\mathrm{sinc}(x) = \sin(\pi x) / (\pi x)$

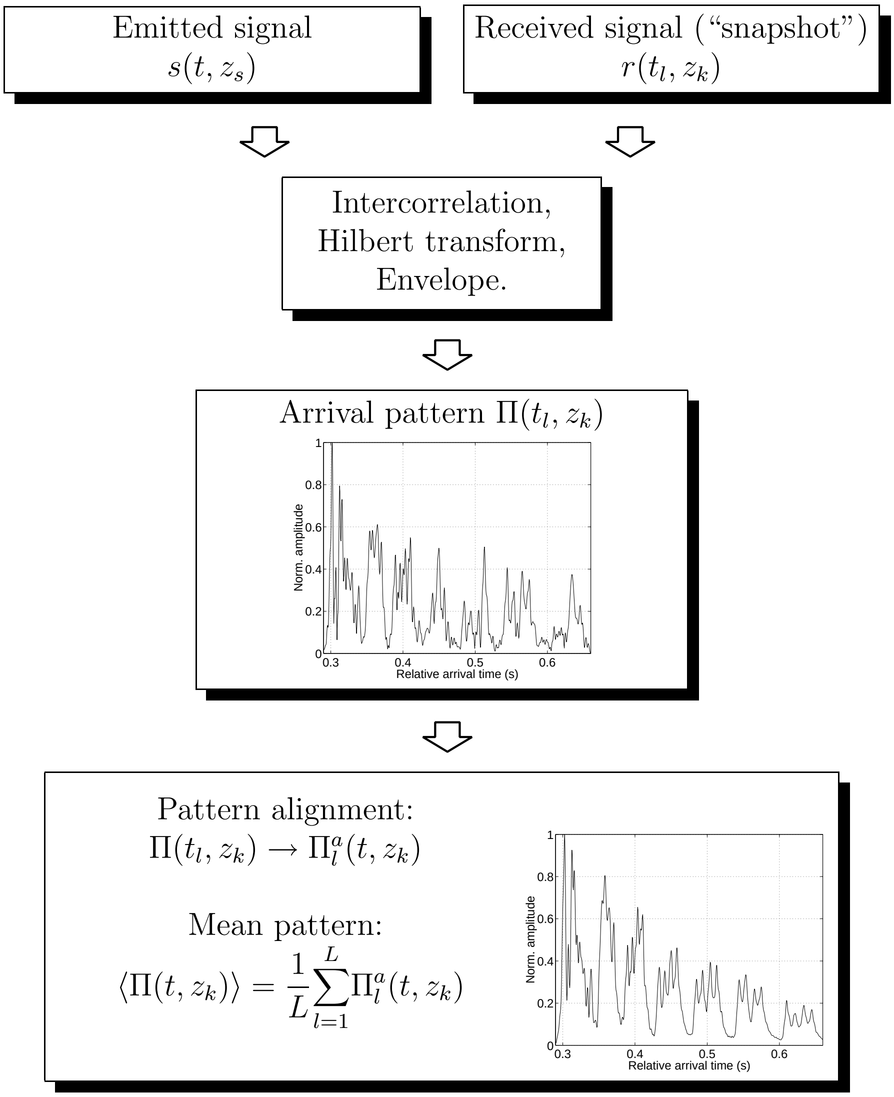

Figure 3.13: Calculation of mean arrival patterns.

described here. Due to the synchronization problems the patterns were self aligned by the leading edge. After the alignment one could calculate a mean pattern over L "snapshots":

$$\langle \Pi(t, z_k) \rangle = \frac{1}{L} \sum_{l=1}^{L} \Pi_l^a(t, z_k) \ . \tag{3.2}$$

The calculation of the mean arrival pattern enhanced the presence of the arrival times. The lack of synchronization with the emitted signal implies also that the arrival times are not distributed along an absolute time scale, but depend on the position of the alignment. In this sense those arrivals correspond to "relative" arrivals, τ_r.

The mean arrival patterns for the hydrophone at 115 meters, and $L = 10$ (see Eq.(3.2)), can be seen in Fig.3.14[8] (the arrival patterns of the hydrophones at 35 and 105 meters exhibit similar temporal variations). In general the temporal variations of the mean arrival patterns exhibit a complex and unstable behaviour in the temporal interval $\tau_r \in [\ 0.3\ ,\ 0.4\ ]$ s, and convey after that interval to a stable distribution of several vertical "stripes". Those "stripes" can better be seen in the cases of Events I and III. The "stripes" amplitude decays with the increase of τ_r. Moreover, the vertical "stripes" structure in Events I and III reveals the presence of four sub-stripes, which is the most remarkable feature of the mean arrival patterns. In fact, the stripes and sub-stripes of those patterns, for both Events I and III, indicate the clustering of "late" arrivals (here, "late" arrivals means those arrivals distributed after 0.4 s) in groups of *four* arrivals. Each group of four arrivals will be referenced, hereafter, as a "quadruplet", and to each set of arrivals, formed by sub-groups of fours arrivals, will be given the name of "set of quadruplets", or simply "quadruplets". In addition to the arrival clustering in groups of quadruplets one can notice that the vertical stripes of Events I and III exhibit a temporal modulation typically semidiurnal, to which should contribute, in different

[8]In each figure the vertical time scale, in hours, starts at the beginning of the corresponding Event (see the Events description, in the previous section).

degrees, both the internal and surface tides. Event II, which corresponded to a set of acoustic transmissions with simultaneous variations in the source horizontal distance and/or depth, exhibits significant variations in terms of the temporal dispersion of the arrivals, and of their number. The particularities of the Events will be discussed once more, with the help of ray-tracing simulations, in section 4.2.

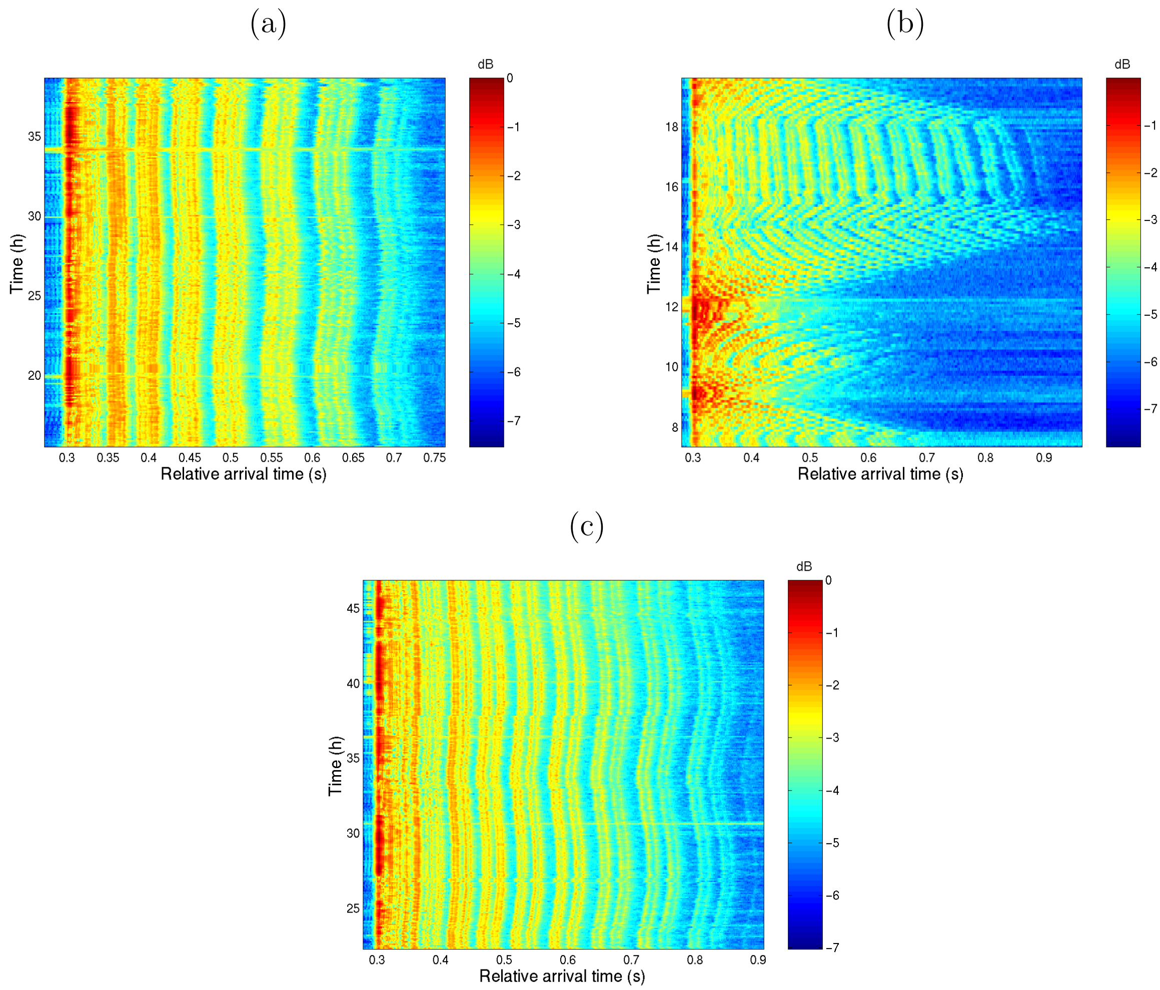

Figure 3.14: Arrival patterns of acoustic transmissions of the INTIMATE'96 sea trial (hydrophone at 115 m): (a) Event I, (b) Event II, and (c) Event III. The vertical color bars indicate the relative amplitude of the arrival patterns.

Chapter 4

The forward problem

As indicated in Chapter 1 tomographic inversion can not be developed independently of the forward problem. This principle implies that the theoretical model described in Chapter 2 should be explored intensively, in order to adapt the general method of acoustic tomography to the particular case of internal tides. That adaptation will be based, on one side, on a preliminary analysis of the oceanographic data of the INTIMATE'96 sea trial and, on the other side, on a set of simulations of acoustic propagation. The application of acoustic propagation models intends to take advantage of the comparison between the modeled and the observed arrival patterns. In fact, the calculation of the arrival pattern using the normal-mode model KRAKEN [48], for the specific configuration of Event I ($R = 5.6$ km, $D = 135$ m, $z_r = 115$ m, $c_0(z)$ corresponds to the mean sound speed profile illustrated in Fig.3.12), exhibits a structure of arrivals clustered in groups of quadruplets (see Fig.4.1, case (a)). The modeled arrival pattern not only reproduces the temporal distribution of the quadruplets, but exhibits also a variation of their amplitude that is close to the one shown by the arrival pattern calculated from acoustic data (see cases (a) and (b) of Fig.4.1). Nevertheless, the model fails significantly trying to reproduce the real arrival pattern in the proximity of the largest arrival (first 0.05 s). This failure indicates not only the limitations of the model, but it also indicates the instability of the first arrivals. The exploration of the theoretical model of tide propagation and the intensive comparison of the simulations with real data will be discussed in the following sections.

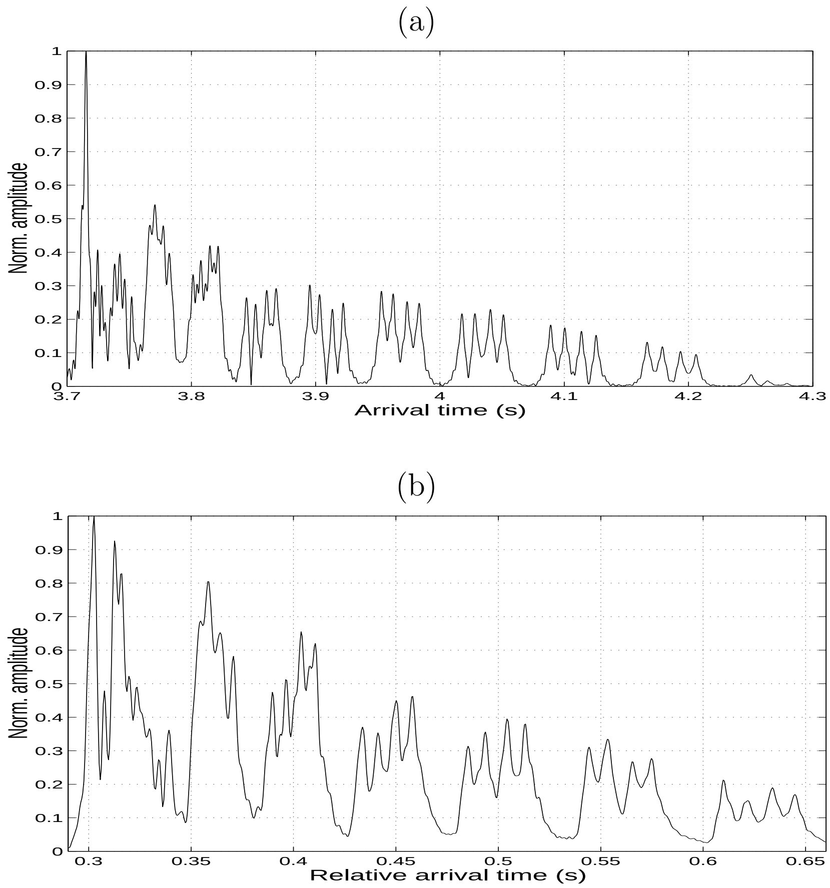

Figure 4.1: Modeled arrival pattern (case (a)) and arrival pattern calculated from acoustic data (case (b)).

4.1 Real data

4.1.1 Equivalence between EOFs and HNMs

The current and thermistor chain temperature data have a proper temporal resolution for the calculation of Empirical Orthogonal Functions, hereafter EOFs [61]. The EOFs (which will be referenced also as empirical modes) represent a powerful and robust tool for the parameterization of a general set of measured data, since each observation can be represented as an empirical expansion on the orthogonal basis of EOFs. In this way, EOFs have been used intensively in tomography problems to parametrize the variations of the sound speed profile in deep and shallow waters, and also to reduce the search space of the parameters under estimation [7, 62]. In the case of the INTIMATE'96 sea trial both records of ADCP and thermistor chain data make it possible to calculate the EOFs for the independent records of currents and temperature. The two bases of EOFs can be seen in Fig.4.2, cases (a) and (b).

On the other side, as previously discussed in section 2.3, the current and temperature fields can be represented as orthogonal expansions on the bases of normal –theoretical– modes. These modes can be calculated when the buoyancy profile, $N(z)$, is known (see Fig.4.2, case (c)). The existence of two different expansions for the same type of data rises the natural question of exploring the relationships between the two systems of orthogonal bases, i.e., how much of a given EOF can be represented as an expansion of theoretical modes, or vice-versa. Within the context of the tomography problem this is a fundamental question since the number of EOFs (and their representativity) depends on the number of observations. The theoretical (hydrostatic and non-hydrostatic) modes can be calculated numerically for a particular buoyancy profile, $N(z)$ (or, through Eq.(3.1), from the temperature), by transforming the SLP into a linear system of equations (see Appendix I). However, the calculation of theoretical modes, from T_0, requires a reduced amount of observations. The question regarding the representation of empirical modes in terms of theoretical modes (or vice-versa), for the case of the oceanographic data of the INTIMATE'96 sea trial, can be found in [63]. In that reference it is shown that each of the three first EOFs can be represented as a single non-hydrostatic normal mode. This result is very significant since it indicates an unique equivalence between each of the first three EOFs, and each of the

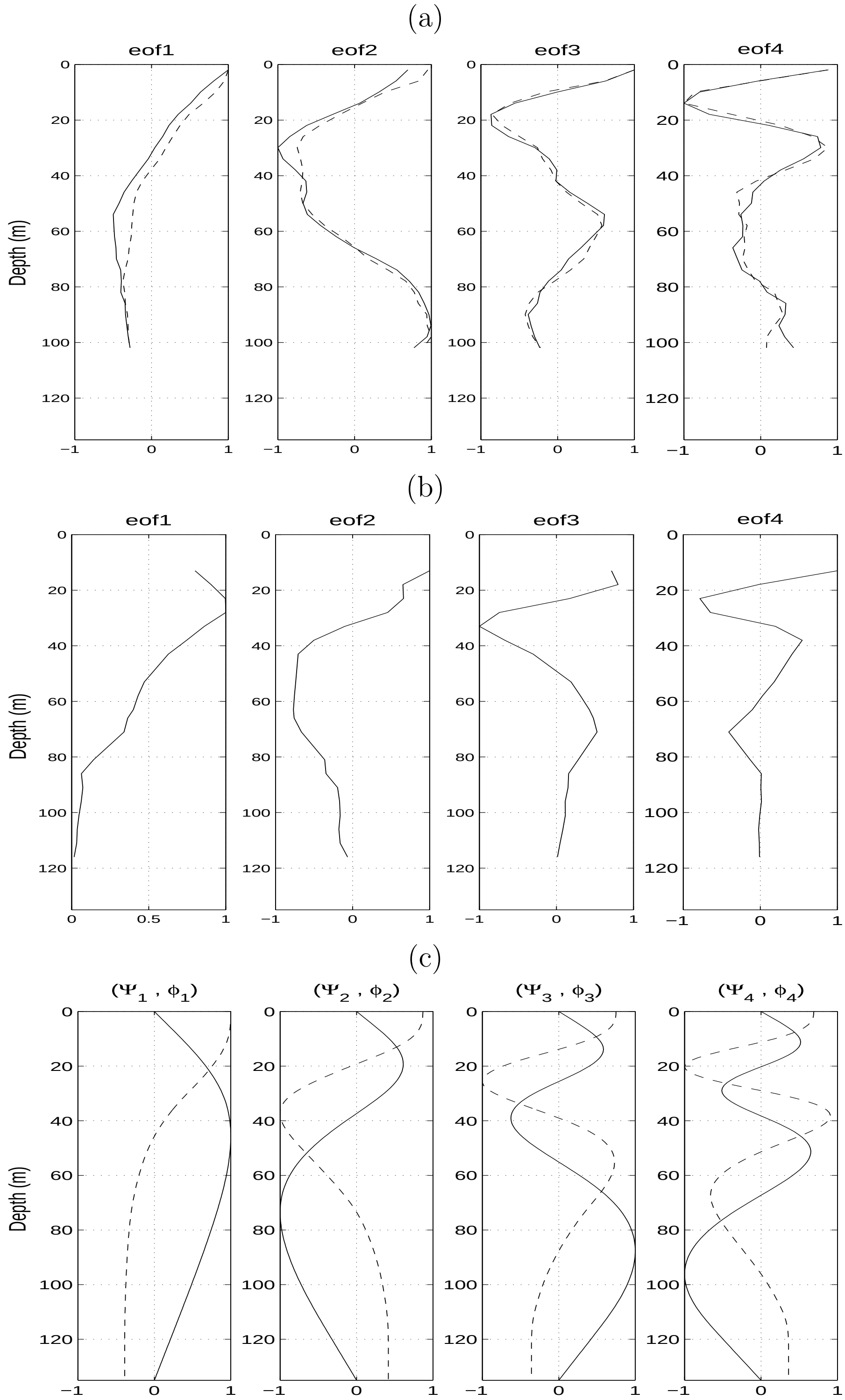

Figure 4.2: (a) EOFs for current data, the continuous line corresponds to u, the dashed line to v; (b) EOFs for temperature data; (c) HNMs calculated for the mean buoyancy profile.

first three theoretical modes. This result indicates also the predominance, *in average*, of the first three baroclinic modes in the environmental variations of the scenario monitorized during the INTIMATE'96 sea trial. Additional calculations, based on HNMs, revealed the same type of equivalence between EOFs and theoretical modes. These results indicate the validity of the rotationless and hydrostatic approximations in the environmental conditions of the INTIMATE'96 sea trial, with the additional theoretical advantage that the HNMs do not obey to a particular type of wave solutions. In this way, the main description of the theoretical modes will be based, hereafter, in the HNMs calculated through Eq.(3.1).

4.1.2 Direction of propagation of the internal tide

Another question discussed in [63] relates to the estimation of the direction of propagating of the internal tide within the area monitorized during the INTIMATE'96 sea trial. This estimation was based in the intercorrelation of modal amplitudes of the current components in order to estimate their temporal phase difference. From the theoretical point of view the amplitude of that phase difference depends on the direction of propagation, θ. The estimated value corresponded to a phase difference of 2.7 hours, which is equivalent to $\theta = 15°$. This value coincides with the orientation of the isobaths in the area of the continental slope (see Fig.3.3).

4.1.3 Weight of the HNMs in the variations of sound speed

The discussion presented in the previous section makes it evident the relevance of the first three HNMs, in the temporal variations of the temperature and sound-velocity fields. Furthermore, and taking into account the linear relationship between T and c (remarked during the discussion of Mackenzie's formula, Eq.(2.68), in section 2.4, and verified in the CTD observations), one can consider valid the following expansion of sound speed:

$$c(z,t) - c_0(z) = \frac{dc_0}{dz}\sum_m \alpha_m(t)\Psi_m \ . \tag{4.1}$$

Since one admits that the temperature and sound velocity fields share the same modal amplitudes it follows from the previous expansion that

$$\alpha_m(t) = \frac{\langle \frac{T(z,t) - T_0(z)}{dT_0/dz} \left| N^2(z) \right| \Psi_m \rangle}{\langle \Psi_m \left| N^2(z) \right| \Psi_m \rangle} \ , \tag{4.2}$$

i.e., the modal amplitudes of sound speed can be calculated using the temperature records. In particular, for the specific case of the INTIMATE'96 sea trial, the modal amplitudes of the first three HNMs can be calculated using the thermistor chain data. Those amplitudes reveal an oscillatory behaviour, with the presence of significant "peaks" in the case of the amplitude α_1 (see Fig.4.3).

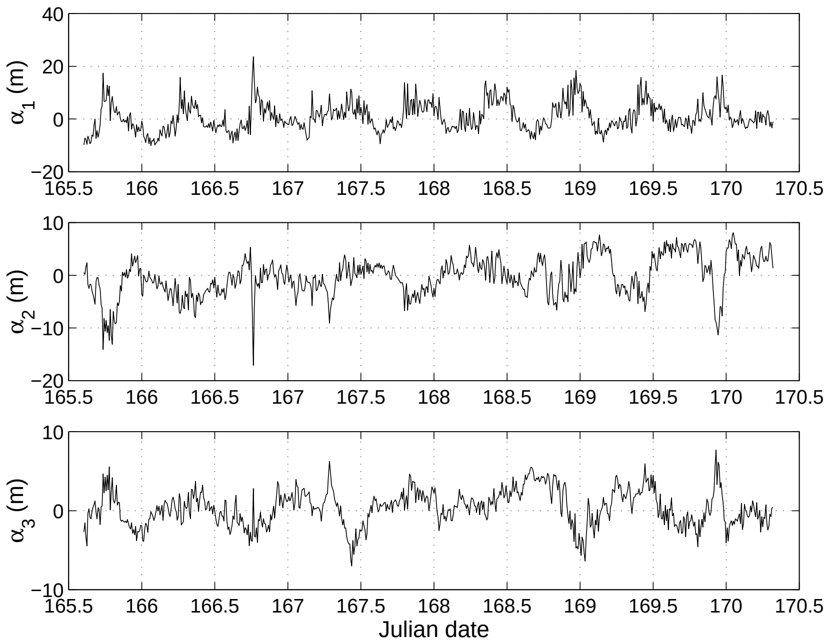

Figure 4.3: TERM-CMO, modal amplitudes of temperature.

The "weight" of each HNM in the variations of sound speed can be estimated as

$$P_m(t) = 100 \times \frac{1}{D}\int_0^D \frac{1}{\sum_{m=1}^{3} |V_m|} |V_m| \, dz \ , \tag{4.3}$$

where $V_m = \alpha_m \Psi_m dT_0/dz$. The temporal average would correspond to

$$\langle P_m \rangle = \frac{1}{t_f - t_i} \int_{t_i}^{t_f} P_m(t) dt \ . \tag{4.4}$$

The results of the application of the previous two formulas to the data illustrated in Fig.4.3 can be seen in Fig.4.4. Those results indicate that the first three HNMs represent, in average, 75% of the variations of the sound speed profile. Additionally, one verifies that the weight of each HNM decreases with the increase of its index.

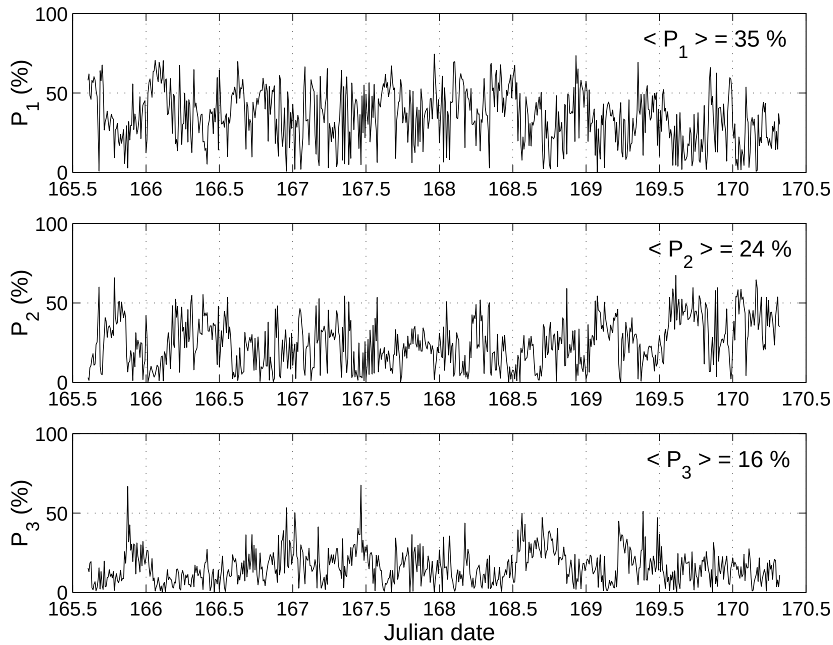

Figure 4.4: TERM-CMO, percents of the modal amplitudes and respective mean values.

4.2 Simulations

As previously indicated in section 3.3.3 the significant maxima of the arrival patterns indicate the acoustic arrival times, τ. On the other side, for the type of signal $s(t, z_s)$ used during the acoustic transmissions of the INTIMATE'96 sea trial, and for the minimal value of water column depth, one verifies the validity of Eq.(2.73), which suggests the application of a ray-tracing model. Instead of using a particular model, between the large number of ray-tracing programs developed specifically for applications of underwater acoustics[1], it was decided to write from scratch a ray-tracing program in MATLAB[2]. The simulations, developed in the following sections, will correspond to isotropic approximations of the Events I, II and III, i.e., they will correspond to cases when the acoustic signal propagates in an environment where the sound speed field, c, depends only on depth: $c = c(z)$.

Taking into account that the Events referenced previously clearly indicate the effects of the tides in the arrival times, so the modeling will be focused only in calculating the arrivals. The simulations will be developed in the following way: the first group of calculations will discuss the impact of the propagation geometry (which will reflect the barotropic tide impact) on the set of acoustic arrivals; the second group will simulate the influence of environmental variations (i.e., of the internal tide) on the arrivals. As will be shown in Chapter 6 the two groups of simulations will allow one to develop a robust tomography scheme to be applied to the acoustic data of the INTIMATE'96 experiment.

4.2.1 Variations in the propagation geometry

In the case of Event I the waveguide was characterized by a water column depth $D = 135$ m, and by a propagation distance $R = 5.6$ km. The eigenrays between the acoustic source, at the depth of 90 m, and the hydrophone 3, can be calculated using the mean sound speed profile $c_0(z)$ illustrated in Fig.3.12 (similar calculations can be developed for hydrophones 1 and 2). The propagation eigenrays (see Fig.4.5) can be classified in two groups: those which are refracted between the acoustic source and the surface (known as "RBR"[3] rays),

[1]For an extensive list of ray-tracing programs one can consult, for instance, the site *Ocean Acoustic Library* in *http://oalib.saic.com*.

[2]The *MATrix LABoratory*. The MATLAB is a programming environment, strongly oriented to the manipulation of vectors and matrices, that allow one to develop a simplified treatment of data and further visualization of the corresponding results.

[3]*Refracted and Bottom Reflected*.

and those which are reflected between the waveguide boundaries (known as "SRBR"[4] rays).

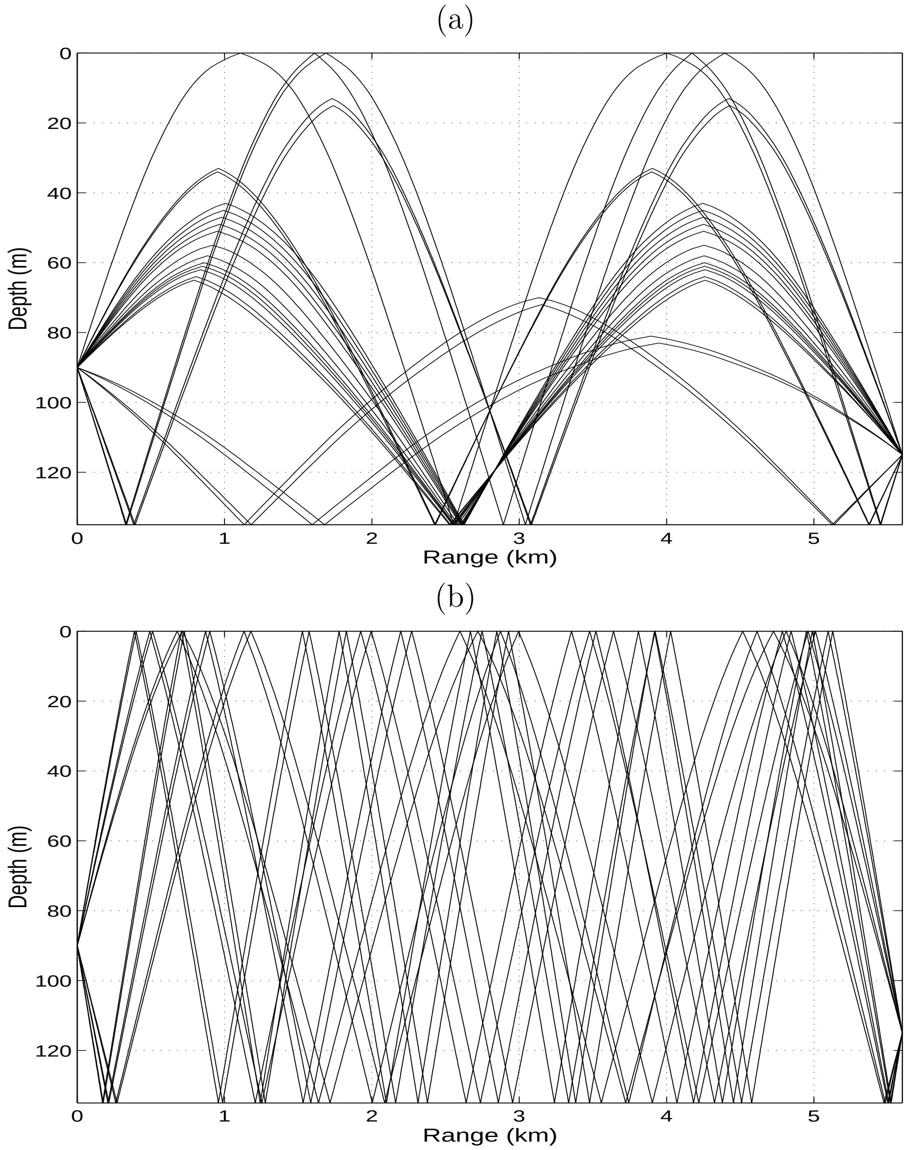

Figure 4.5: Types of propagation eigenrays: RBR (case (a)) and SRBR (case (b)).

The eigenrays of the RBR type correspond to a set of arrivals, distributed closely in the proximity of the first arrival, and spreading along a temporal window of about 14 ms. The group of SRBR eigenrays exhibits a series of arrivals spreading along a temporal window significatively larger (of about 260 ms), with a clustering of arrivals in "quadruplets". As will be discussed in section 5.4.4 the first group corresponds to *unstable* eigenrays and their arrivals can be classified as *unresolved*. Instead the second group corresponds to *stable* eigenrays,

[4] *Surface Reflected and Bottom Reflected.*

and can be associated to a group of *resolved* arrivals. The presence of the quadruplet groups is related to the assimetry of alignment between the acoustic source and the hydrophone, and can be derived analytically in the case of an isovelocity waveguide (c = constant) [64]. It will be shown in section 5.4.1 that the quadruplets are the only arrival groups to take into account within the context of the inverse problem.

In order to identify the effects of the surface tide on the groups of quadruplets the ray-tracing simulation described previously was repeated for several waveguide depths, D. Taking into account the geometry of the VLA, fixed to the bottom, it was considered realistic to introduce a correction $\delta D = D - D_{ref}$ to the depth of the hydrophone 3, where D_{ref} = 135 m. The amplitude of those variations was extended slightly beyond the surface tide predictions at the position of the VLA, which are illustrated in Fig.4.6. The values shown in that figure were calculated using the tide model RSC94, which was downloaded from the site indicated in section 2.1.

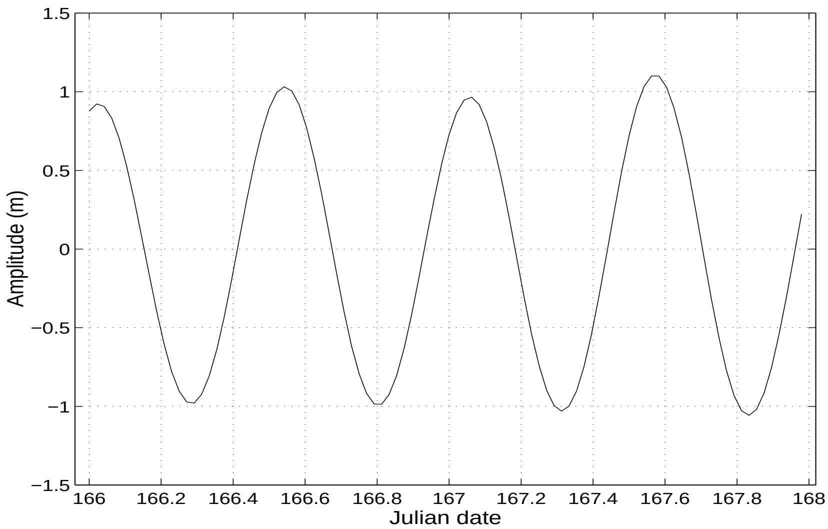

Figure 4.6: Surface tide predictions at the position of the VLA.

The modeling results, considering only the temporal variations of the quadruplets, are illustrated in Fig.4.7. As shown by the ray identifiers (the integer value indicates the total number of reflections and the positive/negative sign indicates whether the ray was launched towards the surface, "+", or towards the bottom, "–") the particular structure of each ray is not affected by the variations of depth, keeping constant the number of reflections and the "launching" angle. On the other hand the increase of depth leads to an increase of the temporal spreading of the quadruplets, and also to an increase of the temporal separation of the arrivals that constitute each quadruplet. However, the temporal perturbations induced by the variations in D are insufficient in order to obtain an "exchange" of arrivals between groups of different quadruplets. In the case of a periodical –semidiurnal– variation in D the corresponding modeling of arrival times should reproduce a pattern alike to the one observed in the arrival patterns of Events I and III.

The simulations of a variable transmission distance, R, for the hydrophone 3, are illustrated in Fig.4.8. The transmission distance had a variation between 3.8 and 5.6 km. The figure indicates the variations of the *relative* arrival times, $\tau_r(R) = \tau(R) - \tau_1(R)$, where $\tau_1(R)$ represents the first "absolute" arrival, to simplify the comparison with the arrival patterns of Event II. The waveguide has a constant depth $D = 135$ m, and the aperture of the acoustic source is constant and symmetric, with an amplitude of 30°. In contrast with the previous case one verifies a temporal increase between the arrivals of each quadruplet, when R *decreases.* As in the previous case the separation between the arrivals of the quadruplets leads to the increase of the temporal window occupied by the respective groups of quadruplets. On the other hand their number decreases when R decreases. The alignment of each sequence of relative arrivals, according to the different phases of acoustic transmissions of Event II, should reproduce a variation of relative arrivals reasonable close to the pattern exhibited by the arrival patterns of that Event.

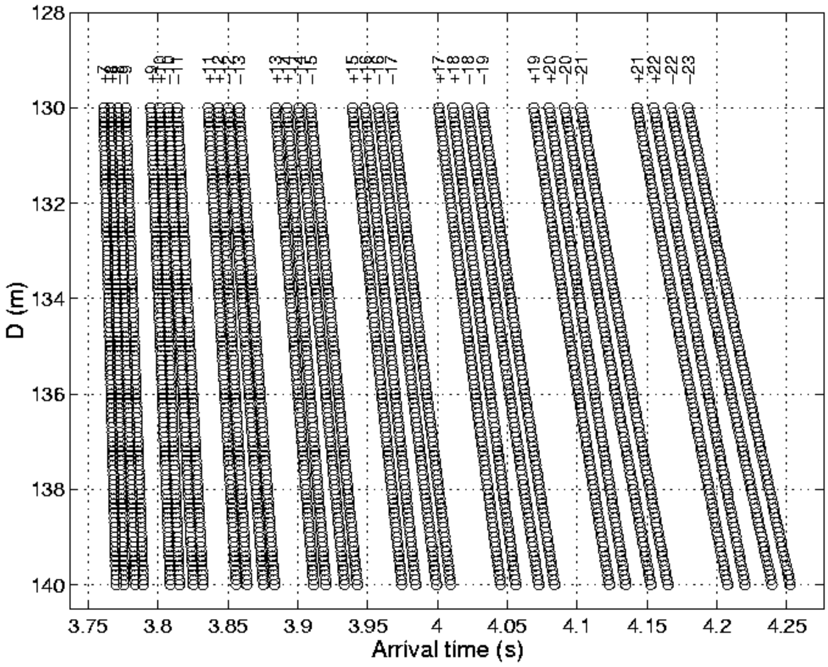

Figure 4.7: Dependence of the resolved acoustic arrivals (quadruplets) on bottom depth, D, (hydrophone 3).

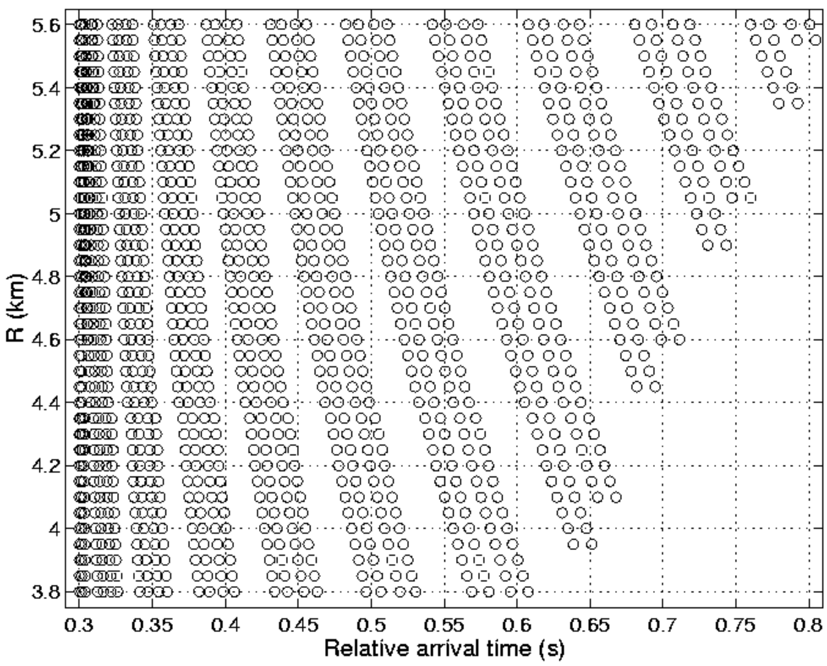

Figure 4.8: Dependence of the relative arrivals on transmission distance, R, (hydrophone 3).

4.2.2 Environmental variations

In a certain sense the set of previous simulations seem to "exhaust" the sources of perturbation that give rise to the temporal variations of the arrival patterns noticed in the Events I, II and III. Therefore, in order to identify the specific contribution of the internal tide to the acoustic data of those Events one needs to develop two additional groups of simulations, sharing the same waveguide geometry, but corresponding to two different realizations of the sound speed profile. The first profile should correspond to the mean –unperturbed– sound speed profile, $c_0(z)$; the second profile, $c(z)$, may correspond to a particular CTD-IH profile, considered as representative of a perturbed profile, and chosen in order to obtain a smooth variation along depth of the perturbation in sound speed. The two sound speed profiles, $c_0(z)$ and $c(z)$, and their difference, $\delta c(z) = c(z) - c_0(z)$, are illustrated in Fig.4.9. As discussed in [64] the RBR eigenrays change their structure from one profile to the other, while the SRBR eigenrays, corresponding to the groups of quadruplets, keep their structure. In this sense, the arrivals corresponding to the first group of eigenrays can be considered as unstable arrivals, while the arrivals corresponding to the second group of eigenrays can be considered as stable. In section 5.4.1 it will be shown that the only arrivals to be taken into account in the tomographic inversion scheme correspond to the stable arrivals.

The arrival sets illustrated in figures 4.7 and 4.8 correspond, in a certain sense, to particular cases of *temporal fronts*, where the horizontal axis of the figure corresponds to the temporal axis of arrival time. As indicated by *Munk et al.* ([5]) the temporal fronts (which are obtained by calculating the arrival times, τ, along the depth, z) provide a more complete perspective of the propagation problem than the usual diagrams of propagation rays.

In the case of the mean sound speed profile of Fig.4.9, and for a waveguide with the

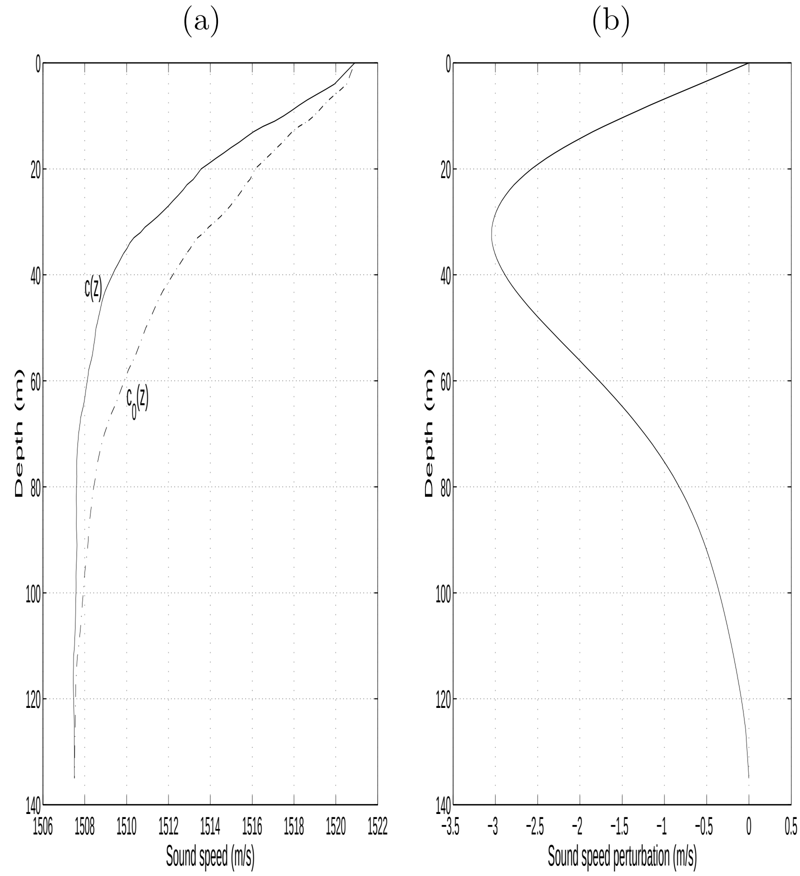

Figure 4.9: Environmental variations: (a) reference and perturbed profiles of sound speed, $c_0(z)$ and $c(z)$, respectively; (b) sound speed profile perturbation, $\delta c(z)$.

geometry of Event I, the corresponding temporal front reveals a complex linear arrival structure, in zigzag (see Fig.4.10, upper case). This structure linearly relates the quadruplets located at different depths, which implies that those arrivals are correlated. On the other hand the locations of the temporal front, where one can observe an intersection of the arrival structure, indicate situations of *ambiguity* in time and depth, since those intersections correspond to propagation geometries where different eigenrays can arrive simultaneously at the hydrophone.

By changing the reference profile, $c_0(z)$, with the perturbed profile $c(z)$, illustrated in Fig.4.9, and calculating the respective temporal front, one can find an arrival structure almost identical to the previous one (see Fig.4.10, lower case). In fact, excluding the unresolved

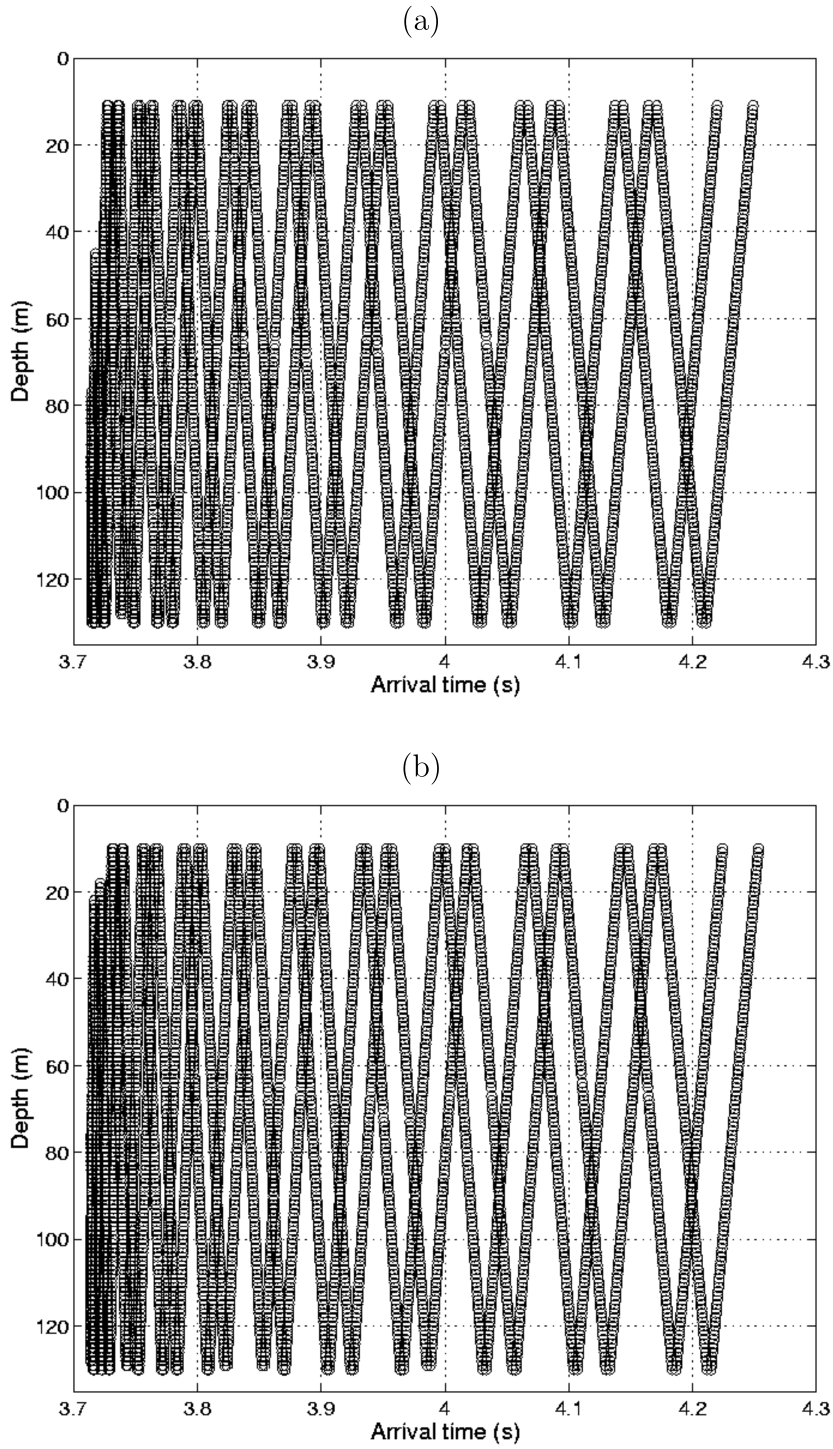

Figure 4.10: Temporal fronts for $c_0(z)$ (case (a)) and $c(z)$ (case (b)).

arrivals, one can verify that displacing "backwards" the second front along the temporal axis it would match perfectly the first front. In this way, one can ensure that the main impact of the internal tide on the acoustic arrivals will consist in "displacing" the temporal front of the reference profile. The amplitude of the temporal displacement, $\delta\tau$, although constant for all depths, should depend on the integral characteristics of the perturbation $\delta c(z) = c(z) - c_0(z)$. The *apriori* quantification of that displacement rises important theoretical and practical questions, which exceed the objectives of this dissertation. Therefore, those questions will not be discussed here. In particular, one of the main conclusions that one draws is that by considering only the quadruplet groups, and recalculating the two temporal fronts in terms of relative arrivals, $\tau_r = \tau - \tau_{ref}$, one can get the *same structure* in both cases. In this way, the relative arrival times, τ_r, do not contain *any type of information related to the environmental variations, δc, of the propagation scenario*, and, therefore, the relative arrival times do *not allow to solve the acoustic problem of internal tide tomography.* This conclusion eliminates the possibility of applying any inversion method, based on the relative arrival times, to the acoustic data of the INTIMATE'96 sea trial. In the best case such an application will just succeed in retrieving a tomography "image" of the progressive –semidiurnal– *alignment* of the arrivals, which in fact will be independent of the real environmental variations induced by the propagation of the internal tide.

Chapter 5

The inverse problem

The previous Chapter was dedicated to the modeling of the acoustic perturbations, induced by geometric and/or environmental variations of the water column, in the case of an horizontally isotropic waveguide. Within the context of the tomography problem one can now proceed with the discussion of the tomography inversion of the acoustic data of the INTIMATE'96 sea trial. That discussion would remain incomplete without a brief discussion of some of the results achieved within the context of the source localization problem, and of the modeling of acoustic propagation through an environment which is anisotropically perturbed (in time and horizontal distance) by the propagation of solitons. The discussion of these two issues will be developed in the following two sections.

5.1 Preliminary discussion

5.1.1 Soliton identification

It is known that the propagation of solitons in an acoustic waveguide can induce significant levels of attenuation in the energetic spectrum of the received signal. This type of observations has been the object of a large number of studies [28, 65, 66]. Despite the fact that those studies present many important results within the context of the forward and inverse problems they also present approximations which are not fully consistent from the mathematical point of view. For instance, it is frequently assumed that the soliton packets can be represented as a linear superposition of independent solutions, which is inconsistent with the non-linear character of Eq.(2.61), since it does not admit a linear superposition of independent solutions as another of its solutions.

The oceanographic observations of the INTIMATE'96 sea trial indicate that the first of the HNMs, is "allowed" to generate solitons. On the other hand the modal amplitudes of current components and temperature, associated with this theoretical mode, reveal significant variations in amplitude ("peaks"), which are repeated at the tidal frequency, and which are characteristic of the propagation of soliton packets [25, 41]; one of those peaks is temporally correlated with a significant perturbation of the acoustic signal, more specifically with a pattern of signal *focalization* [41, 42]. The sampling frequency of current and temperature data is insufficient to resolve the structure of the soliton packets including, in particular, the structure of the packet which would be correlated with the perturbation found in the acoustic data. The identification of that structure was discussed by using two different types of analytic solutions of Eq.(2.61), following the generation of packets with different structures. Each packet corresponds to a particular anisotropic configuration of the sound velocity field, and each configuration was used as input data to the normal mode model C-SNAP [67], to simulate the propagation of the acoustic signal through the respective soliton packet. The developed sets of narrowband [41] and broadband [42] simulations allowed to obtain, for a particular type of soliton packet, a focalization pattern reasonably close to the one observed. This result constitutes an important indicator of the sensitivity of the acoustic signal to the environmental –anisotropic– variations of the propagation channel, and also of the potential possibility of using that sensitivity to determine the corresponding –anisotropic– sound velocity field.

5.1.2 Source localization

As previously discussed in [68]–[70] the sensitivity of the arrival patterns to the propagation geometry can be explored in order to develop a particular approach to the problem of source localization during the three Events. The particular localization scheme discussed in those references is inspired on the methods of Matched-Field Processing (hereafter MFP) [71, 72], with the significant difference of matching the arrival patterns at a single hydrophone, more specifically of the hydrophone 3. A different perspective of the localization problem, based on the methods of sub-space decomposition [73]–[75], was also applied to the acoustic data of hydrophone 3 with equal success, in both range-independent [76] and range-dependent [77] environments. One of the most interesting results of the last two references is related to the estimation of the number of independent arrivals, which was based on statistical theoretical criteria [78]. In fact, the two studies indicate a *redundancy* of the acoustic arrivals at the hydrophone, i.e., the studies indicate that, within the total set of T arrivals, only a number $\mathsf{N} < \mathsf{T}$ contains independent information related to the acoustic waveguide. This fundamental result is extremely important for the acoustic tomography of the internal tide in the coastal zone, and will be discussed in detail in section 5.4.4.

5.2 The tomography problem

Ocean Acoustic Tomography, as initially proposed, was based in the usage of the perturbations of the arrival times, $\Delta\tau$, to calculate the perturbations of the sound speed profile $c(z)$ in relation to a reference profile $c_0(z)$: $\delta c(z) = c(z) - c_0(z)$, [4]. This perspective of the tomography problem, where the main characteristic of the signal to be analyzed corresponds to arrival times, is usually known as *Travel-Time Tomography*. Alternatively, it is possible to extend the methods of MFP (used often in the context of the source localization problem) to directly explore the sensitivity of the acoustic field, $\hat{p}$, to the geometrical and environmental parameters of the acoustic waveguide, to calculate directly the sound speed profile $c(z)$ [7, 79, 80]. This alternative is usually known as Matched-Field Tomography (hereafter MFT), and frequently takes advantage of the EOFs to parametrize the sound speed profile. In general it is difficult to understand *apriori* in which conditions one should use one of the techniques instead of the other. This question applies also to the tomography processing of acoustic data of the INTIMATE'96 sea trial. The following two sections will discuss this matter with the help of simulations.

5.3 Matched-Field Tomography (MFT)

5.3.1 Theoretical background

For a set of N vertical hydrophones the pressure field of the received signal can be characterized through a pressure vector, $\hat{\mathbf{p}}$, defined as

$$\hat{\mathbf{p}}(f) = [\ \hat{p}(f, z_1)\ ,\ \hat{p}(f, z_2)\ ,\ \ldots\ ,\ \hat{p}(f, z_{\mathsf{N}})\ ]^{\mathsf{t}}\ , \tag{5.1}$$

where $[\ldots]^{\mathsf{t}}$ indicates the transpose of $[\ldots]$, and each element $\hat{p}(f, z_j)$ $(j = 1, 2, \ldots\ \mathsf{N})$ of the column vector $\hat{\mathbf{p}}$ corresponds to the narrowband component of the Fourier transform of the respective received signal, $r(t, z_j)$. In order to further simplify the discussion of the methods of MFT the dependency on f will be omitted $(\hat{p}(f, z_j) = \hat{p}(z_j))$. Under the classic formulation of the source localization problem, based on MFP, one intends to determine the source location which is defined by an unknown depth, z_s, and an unknown horizontal distance of transmission, R. To achieve that goal one explores the information contained in a set of L signals $\hat{\mathbf{p}}$ (the "snapshots"). To determine the unknown vector of parameters (z_s, R) one compares the snapshots with a set of test vectors, $\hat{\mathbf{p}}_m(z, r)$, generated by a propagation model. This comparison is performed using a *cost function*, which achieves an optimal value (maximal or minimal) when $(z, r) \approx (z_s, R)$. A particular example of a cost function corresponds to the Bartlett estimator [71, 81]:

$$\hat{\mathcal{E}}(\boldsymbol{\theta}) = \hat{\mathbf{p}}_m^*(\boldsymbol{\theta})\hat{\mathbf{R}}(\boldsymbol{\theta}_0)\hat{\mathbf{p}}_m(\boldsymbol{\theta}) \ , \tag{5.2}$$

where $\boldsymbol{\theta}_0 = [z_s, R]^{\mathsf{t}}$, $\boldsymbol{\theta} = [z, r]^{\mathsf{t}}$, $\hat{\mathbf{p}}^*$ represents the conjugate transpose of vector $\hat{\mathbf{p}}$, and $\hat{\mathbf{R}}$ corresponds to the sampling covariance matrix:

$$\hat{\mathbf{R}} = \frac{1}{L}\sum_{l=1}^{L}\hat{\mathbf{p}}_l(\boldsymbol{\theta}_0)\hat{\mathbf{p}}_l^*(\boldsymbol{\theta}_0) \ . \tag{5.3}$$

In general, both $\hat{\mathbf{p}}$ and $\hat{\mathbf{p}}_m$ are normalized, which implies that

$$0 \leq \hat{\mathcal{E}}(\boldsymbol{\theta}) \leq 1 \ . \tag{5.4}$$

Sometimes the amplitude of the estimator is also calculated in dB. The Bartlett estimator previously described can be applied to narrowband MFP. For the broadband case one can apply the following incoherent estimator:

$$\hat{\mathcal{E}}_{inc}(\boldsymbol{\theta}) = \frac{1}{N_f}\sum_{j=1}^{N_f}\hat{\mathcal{E}}(f_j, \boldsymbol{\theta}) \ , \tag{5.5}$$

where N_f represents the number of processed frequencies, and each term of the sum corresponds to the estimator defined by Eq.(5.2), and calculated at frequency f_j. As in the case of the narrowband estimator the estimator defined by Eq.(5.5) is normalized:

$$0 \leq \hat{\mathcal{E}}_{inc}(\boldsymbol{\theta}) \leq 1 \ . \tag{5.6}$$

The parameterization of the sound speed profile can be developed, using EOFs, in the following way:

$$c(z) = c_0(z) + \sum_m \alpha_m EOF_m \ . \tag{5.7}$$

In this case the vector of parameters of the m-dimensional space corresponds to the vector $\boldsymbol{\theta} = (\ \alpha_1\ ,\ \alpha_2\ ,\ \dots\ , \alpha_m\ )$, and one expects that the cost function will achieve its optimal value at the position of the searched parameters, $\boldsymbol{\theta}_0 = (\ \alpha'_1\ ,\ \alpha'_2\ ,\ \dots\ , \alpha'_m\ )$. Most problems of practical interest involve optimization problems with a large number of dimensions, which makes practically impossible to develop a direct search of the unknown parameters. One of the methods that allow one to significantly reduce the search space corresponds to the "Genetic Algorithm" approach [82], which is based on evolutionary principles. Genetic Algorithms "explore" the cost function at different points of the search space, forming a "population" of "candidates", $\boldsymbol{\theta}_0$. Furthermore, using the rules of natural selection (crossings, mutations, etc.), the candidates are kept or renewed along several iterations (or "generations"), until one obtains a candidate $\boldsymbol{\theta} \approx \boldsymbol{\theta}_0$, such that

$$\boldsymbol{\theta}_0 = \arg \left\{ \max_{\boldsymbol{\theta}} \hat{\mathcal{E}}(\boldsymbol{\theta}) \right\} \ . \tag{5.8}$$

Genetic Algorithms have been applied efficiently in inverse problems of underwater acoustics as, for instance, in problems of source localization and geo-acoustic inversion [83]–[85]. Between the different models developed the "SAGA" model [86] deserves special attention, since it implements a method of Genetic Algorithms, tightly related to the usage of several models of acoustic propagation.

5.3.2 Narrowband MFT simulations

As previously discussed in section 4.1.1 the HNMs are equivalent to the EOFs of current and temperature data. In this way, using the expansion Eq.(4.1), one can parametrize the sound speed profile in terms of HNMs Ψ_m. The amplitudes of the three firsts HNMs, $\boldsymbol{\alpha}_0^{\mathsf{t}} = [\ \alpha_1\ \alpha_2\ \alpha_3\ ] = [\ -20\ 10\ 10\ ]$ m, consistent with the oscillation values of the amplitudes illustrated in Fig.4.3, allow one to generate the sound speed profile $c(z)$ illustrated in Fig.5.1. This profile was considered as representative of environmental variations being able to induce significant perturbations on the acoustic pressure.

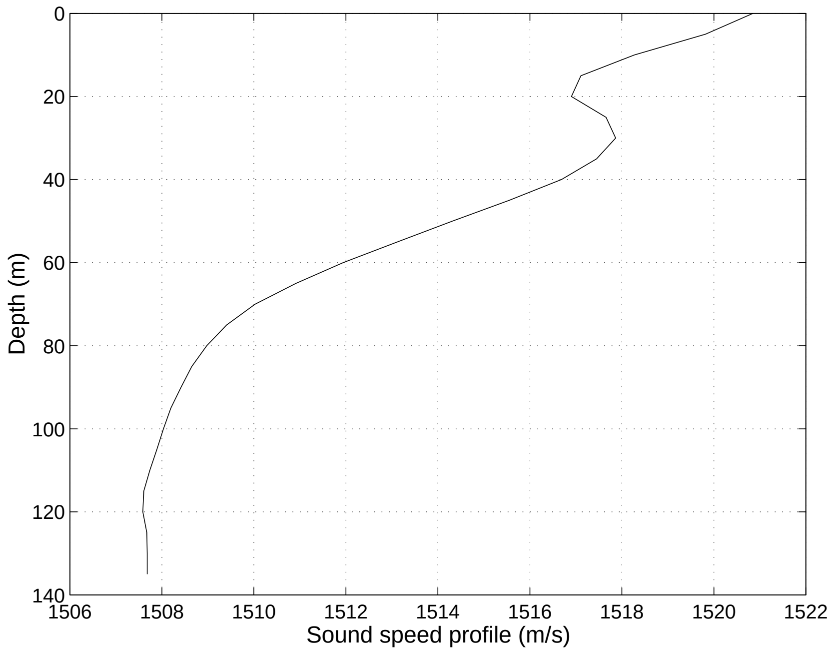

Figure 5.1: MFT simulation tests, "perturbed" sound speed profile.

The SNAP model [87] was used by SAGA to generate the acoustic pressure field, $\hat{\mathbf{p}}(\boldsymbol{\theta}_0)$, at the frequency $f = 550$ Hz, for the profile $c(z)$. Four hypothetical configurations of the reception system were considered (see Table 5.1). The fourth configuration corresponds to the configuration of the VLA of the INTIMATE'96 sea trial. Since the pressure field $\hat{\mathbf{p}}(\boldsymbol{\theta}_0)$ was not contaminated with noise the number of snapshots corresponded to $L = 1$.

Configuration	1	2	3	4
Number of hydrophones	11	6	3	3
Depth of 1st. hydrophone (m)	35	35	35	35
Depth of last hydrophone (m)	115	115	115	115
Separation between 1st. and 2nd. hydrophones (m)	8	16	40	70

Table 5.1: Narrowband MFT tests, idealized configurations of the reception system (the last configuration corresponds to the VLA of the INTIMATE'96 sea trial).

The SAGA model performance in the inversion of the parameters $\boldsymbol{\alpha}_0$ was tested for each configuration. The cost function corresponded to the estimator Eq.(5.2), which was calculated, from generation to generation, by modeling the acoustic pressure field, $\hat{\mathbf{p}}_m(\boldsymbol{\theta})$, using the parameterization of the sound speed profile given by Eq.(4.1). The search parameter space was discretized homogeneously, where each α was bounded between -25 e 25 m, with a discretization interval $\Delta\alpha = 0.25$ m.

The MFT tests showed that, in general, the calculation time increases with the decrease of the number of hydrophones. However, for configurations 1 and 2 the SAGA model calculated accurately the modal amplitudes of the profile $c(z)$, while in configurations 3 and 4, and independently of the number of times that SAGA tried to optimize the cost function, the inverted amplitudes were far away from expected values. The results of the tomography tests, for the different configurations, can be interpreted in a more direct way, by calculating the Bartlett estimator along the plane $\alpha_3 = 10$ m, as shown in Fig.5.2. The set of figures indicates that the decrease of the number of hydrophones, N, is followed by the appearing of secondary maxima, which start to be concurrent with the global maximum. In other words, one verifies that the ambiguity in the position of the global maximum increases when the number of hydrophones decreases, making more difficult to locate that maximum. One can expect that the contamination of the signal with noise should worsen the localization of the global maximum. In this way, the results of this set of simulations show the impossibility

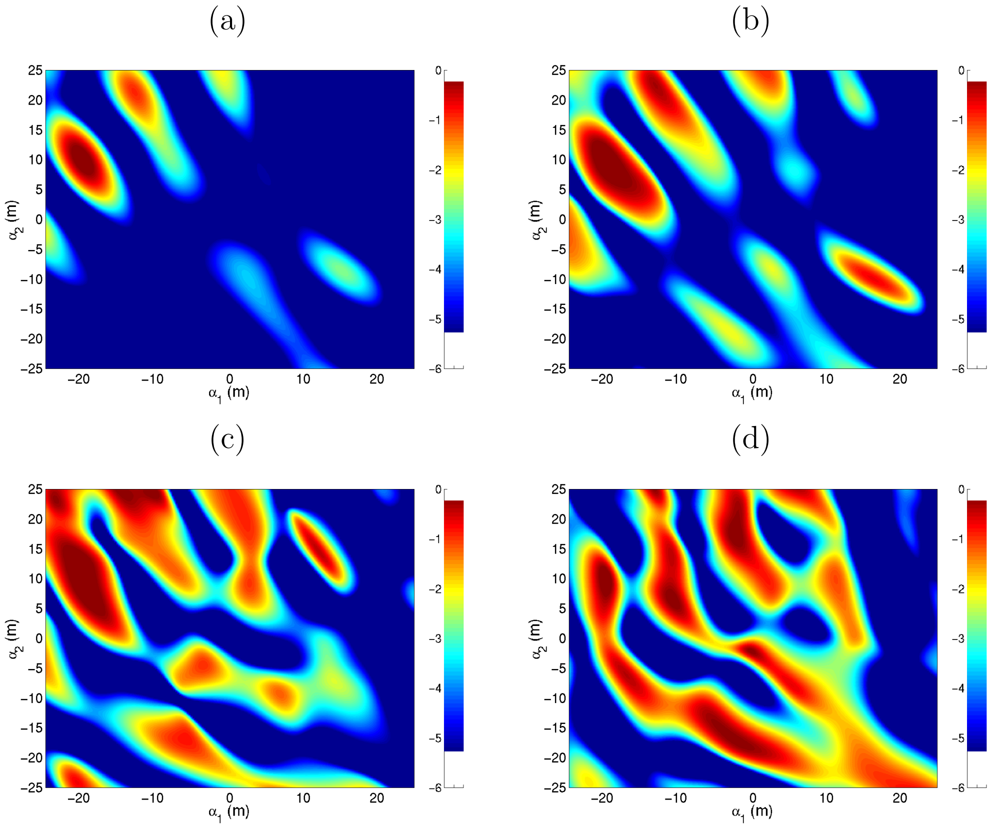

Figure 5.2: Evolution of the Bartlett estimator as the number of hydrophones (N) decreases: (a) $\mathsf{N} = 11$, (b) $\mathsf{N} = 6$ and (c) $\mathsf{N} = 3$; the case (d) corresponds to the VLA with 3 hydrophones of the INTIMATE'96 sea trial. The vertical color bars indicate the estimator amplitude in dB.

of tomographic inversion through the narrowband processing of the acoustic data of the INTIMATE'96 experiment.

5.3.3 Broadband MFT simulations

As previously discussed in [81] for the source localization problem, the broadband processing of the acoustic data can compensate some of the limitations of the narrowband processing. Based on this observation one can apply the incoherent estimator Eq.(5.5), to the tomography problem, to minimize the ambiguities of the narrowband Bartlett estimator, which were noticed in the previous section for the case of configuration 4. The tests, developed once more with the SAGA model (generating the acoustic field through the SNAP model), and for different numbers of frequencies N_f (from 300 to 800 Hz, $\Delta f = 500/N_f$), indicate that in the absence of noise, increasing N_f allow one to substantially improve the estimation of the amplitudes $\boldsymbol{\theta}$. Moreover, the direct calculation of the incoherent estimator, Eq.(5.5), in the plane $\alpha_3 = 10$ m (see Fig.5.3) shows that the ambiguity of the surface decreases when N_f increases.

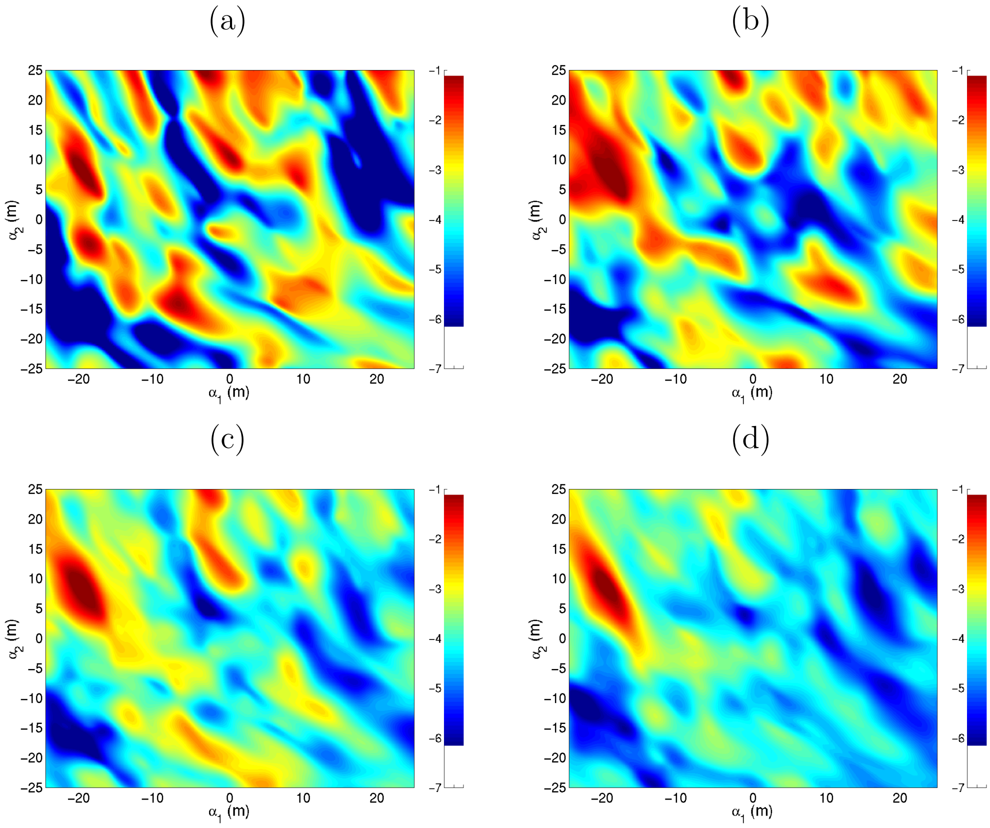

Figure 5.3: Evolution of the Bartlett estimator as the number of frequencies (N_f) increases: (a) $N_f = 3$, (b) $N_f = 6$, (c) $N_f = 11$ and (d) $N_f = 21$. For all cases $\mathsf{N} = 3$; the vertical color bars indicate the amplitude of the estimator in dB.

This set of results shows that the tomography broadband processing can be used to compensate the lack of tomography resolution of the narrowband processing. However, this recovering takes place at the cost of a substantial increase of the calculation time, which being of the order of several minutes in the narrowband case becomes to the order of many hours in the broadband case. It should be remarked also that additional tests indicated a significant sensitivity of the incoherent estimator to the contamination of data with noise. In this way, it can not be avoided to increase once more the number of frequencies in order to recover the tomography resolution, which implies again increasing the calculation time. This is a highly undesirable factor for the purposes of tomography monitoring.

5.4 Travel-Time Tomography

5.4.1 Theoretical background

It can be shown, on the basis of ray theory, that for an acoustic signal the perturbation of the arrival time, $\Delta\tau$, corresponds to [5]

$$\Delta\tau = \int_{\Gamma} \frac{ds}{c(z)} - \int_{\Gamma_0} \frac{ds}{c_0(z)} \ , \tag{5.9}$$

where Γ and Γ_0 represent the eigenrays corresponding to the perturbed and reference profiles, $c(z)$ and $c_0(z)$, respectively. In the case of small perturbations, $\delta c(z) = c(z) - c_0(z) \ll c_0(z)$, one can consider that $\Gamma \approx \Gamma_0$, so Eq.(5.9) can be rewritten as

$$\Delta\tau_j = \tau_j - \tau_j^0 = \int_{\Gamma_j} \frac{ds}{c(z)} - \int_{\Gamma_j} \frac{ds}{c_0(z)} \approx -\int_{\Gamma_j} \frac{\delta c(z)}{c_0^2(z)} ds \ . \tag{5.10}$$

In this expression the integral is taken along the non-perturbed eigenray Γ_j. Eq.(5.10) indicates that a first order perturbation on the sound speed profile leads to a first order perturbation on the arrival time. In this sense Γ_j corresponds to a *stable* eigenray and τ_j and τ_j^0 can be considered as resolved arrival times, (or, simply, resolved “arrivals”). By “collecting” a set of T perturbations in arrival times ($j = 1, 2, \ldots \mathsf{T}$), and representing the acoustic waveguide as a system composed by L layers, one can obtain the following system of linear equations [5, 8]:

$$\mathbf{y} = \mathbf{E}\mathbf{x} + \mathbf{n} \ , \tag{5.11}$$

where $\mathbf{y} = [\ \Delta\tau_1\ \Delta\tau_2\ \ldots\ \Delta\tau_{\mathsf{T}}\ ]^{\mathsf{t}}$, $\mathbf{x} = [\ \delta c_1\ \delta c_2\ \ldots\ \delta c_{\mathsf{L}}\ ]^{\mathsf{t}}$, and each δc_l corresponds to the mean of $\delta c(z)$, in the lth layer. Vector $\mathbf{y}$ is known as the *vector of temporal delays* or, simply, *vector of delays*. In Eq.(5.11) $\mathbf{n}$ represents the noise contribution to the set of observations $\mathbf{y}$. Matrix $\mathbf{E}$, of dimension $\mathsf{T} \times \mathsf{L}$, is known as the *Observation Matrix* [5]. The rows $\mathbf{e}_j$ of $\mathbf{E}$ have the following structure:

$$\mathbf{e}_j = \left[\frac{\Delta s_{j,1}}{c_{01}^2}\ \frac{\Delta s_{j,2}}{c_{02}^2}\ \ldots\ \frac{\Delta s_{j,\mathsf{L}}}{c_{0\mathsf{L}}^2} \right] , \tag{5.12}$$

where $\Delta s_{j,l}$ represents the length of the jth eigenray, within the layer l, with $j = 1, 2, \ldots, \mathsf{T}$ and $l = 1, 2, \ldots, \mathsf{L}$. Eq.(5.11) represents the starting point of the methods of Travel-Time Tomography.

The choice of the number of layers, L, can be done in many different ways. In general one chooses a large number of layers, as large as possible. In fact, in most cases of practical interest $\mathsf{L} \gg \mathsf{T}$. In this way, since $\mathsf{L} > \mathsf{T}$, Eq.(5.11) corresponds to a system with less equations than unknowns, i.e., corresponds to an undetermined system of equations. A system of this kind has an infinite number of solutions. In the absence of any *apriori* additional information an usual choice of the solution corresponds to the minimum norm solution [61]:

$$\mathbf{x}^{\#} = \mathbf{E}^{\#}\mathbf{y} , \tag{5.13}$$

where the pseudoinverse matrix, $\mathbf{E}^{\#}$, can be efficiently calculated through its Singular Value Decomposition (hereafter SVD) [5, 61]:

$$\mathbf{E} = \mathbf{U}\mathbf{S}\mathbf{V}^{\mathsf{t}} , \tag{5.14}$$

and then

$$\mathbf{E}^{\#} = \mathbf{V}_{\mathsf{r}}\mathbf{S}_{\mathsf{r}}^{-1}\mathbf{U}_{\mathsf{r}}^{\mathsf{t}} , \tag{5.15}$$

where the matrices $\mathbf{V}_\mathsf{r}$ and $\mathbf{U}_\mathsf{r}$ are formed by the first r columns of $\mathbf{V}$ and $\mathbf{U}$, respectively, and $\mathbf{S}_\mathsf{r}$ is a square diagonal matrix, with r non-zero elements. The index r corresponds to the rank of the observation matrix. The references related to Travel-Time Tomography studied within this dissertation (see, for instance, [4, 6, 8]) consider implicitly that the rank of the observation matrix corresponds to the number of arrivals T.

5.4.2 Array processing

In contrast with the methods of MFT, which deals in a natural way with array processing, the methods of Travel-Time Tomography deal with the information acquired on a single hydrophone. In this way, it arises naturally the issue about how to treat a set of equations of the form

$$\mathbf{y}_1 = \mathbf{E}_1\mathbf{x} + \mathbf{n}_1 \ , \ \mathbf{y}_2 = \mathbf{E}_2\mathbf{x} + \mathbf{n}_2 \ , \ \ldots \ \mathbf{y}_\mathsf{N} = \mathbf{E}_\mathsf{N}\mathbf{x} + \mathbf{n}_\mathsf{N} \ . \tag{5.16}$$

The equations (5.16), sharing the common factor $\mathbf{x}$, can be reduced to a single equation, identical to Eq.(5.11), by concatenating the system of equations (5.16) [5], i.e., by introducing the following array vectors and matrices:

$$\mathbf{y} = \begin{bmatrix} \mathbf{y}_1 \\ \mathbf{y}_2 \\ \vdots \\ \mathbf{y}_\mathsf{N} \end{bmatrix} \ , \ \mathbf{E} = \begin{bmatrix} \mathbf{E}_1 \\ \mathbf{E}_2 \\ \vdots \\ \mathbf{E}_\mathsf{N} \end{bmatrix} \ , \quad \text{and} \quad \mathbf{n} = \begin{bmatrix} \mathbf{n}_1 \\ \mathbf{n}_2 \\ \vdots \\ \mathbf{n}_\mathsf{N} \end{bmatrix} \ . \tag{5.17}$$

The concatenated system can be solved as indicated in section 5.4.1.

5.4.3 Regularization of the linear system of equations

The usage of a layer system to solve the inverse problem, Eq.(5.11), rises important questions. For instance, the discussion presented in [6] indicates that a proper choice of a layer system improves the accuracy of inversion. However, the same reference do not present any theoretical or practical discussion related to the criteria of choice of the most "accurate" layer system. A "reasonable" suggestion could be to increase the vertical resolution of the sound speed profile by increasing the number of layers. However, it is not difficult to discover that the increase of the number of layers leads to an undesirable increase of the number of discontinuities of the inverse solution. As commented in [5] the HNMs can be used to solve this problem by allowing the reparameterization of the system of equations, which decreases the degrees of freedom of the inverse solution. That reparameterization is described in this section. First, one can notice that the expansion Eq.(4.1) can be rewritten as

$$\delta c(z,t) = \left[\frac{dc_0}{dz}\Psi_1(z)\right]\alpha_1(t) + \left[\frac{dc_0}{dz}\Psi_2(z)\right]\alpha_2(t) + \left[\frac{dc_0}{dz}\Psi_3(z)\right]\alpha_3(t) \ . \tag{5.18}$$

Discretizing the previous equation on a vertical grid, $\{z_l\}$, one would have that

$$\begin{aligned}\delta c_l = \delta c(z_l,t) &= \frac{dc_0}{dz}\Psi_1\bigg|_{z=z_l}\alpha_1(t) + \frac{dc_0}{dz}\Psi_2\bigg|_{z=z_l}\alpha_2(t) + \frac{dc_0}{dz}\Psi_3\bigg|_{z=z_l}\alpha_3(t) = \\ &= \mathbf{\Psi}_l^{\mathsf{t}}\boldsymbol{\alpha}(t) \ ,\end{aligned} \tag{5.19}$$

where $\boldsymbol{\alpha}(t) = [\ \alpha_1(t)\ \alpha_2(t)\ \alpha_3(t)\ ]^{\mathsf{t}}$ and

$$\begin{aligned}\mathbf{\Psi}_l^{\mathsf{t}} &= \left[\ \frac{dc_0}{dz}\Psi_1\bigg|_{z=z_l}\ \ \frac{dc_0}{dz}\Psi_2\bigg|_{z=z_l}\ \ \frac{dc_0}{dz}\Psi_3\bigg|_{z=z_l}\ \right] = \\ &= \frac{dc_0}{dz}\bigg|_{z=z_l} \times [\ \Psi_1(z_l)\ \Psi_2(z_l)\ \Psi_3(z_l)\ ] = \beta_l \times [\ \Psi_1(z_l)\ \Psi_2(z_l)\ \Psi_3(z_l)\ ] \ .\end{aligned} \tag{5.20}$$

In the last equation

$$\beta_l = \frac{dc_0}{dz}\bigg|_{z=z_l} \ . \tag{5.21}$$

In this way the perturbation of the sound speed profile can be rewritten as

$$\mathbf{x} = \mathbf{\Psi}^{\mathsf{t}}\boldsymbol{\alpha} \ , \tag{5.22}$$

where

$$\mathbf{\Psi}^{\mathsf{t}} = \begin{bmatrix} \beta_1 \times (& \Psi_1(z_1) & \Psi_2(z_1) & \Psi_3(z_1) &) \\ \beta_2 \times (& \Psi_1(z_2) & \Psi_2(z_2) & \Psi_3(z_2) &) \\ \vdots & \vdots & \vdots & \vdots & \\ \beta_{\mathsf{L}} \times (& \Psi_1(z_{\mathsf{L}}) & \Psi_2(z_{\mathsf{L}}) & \Psi_3(z_{\mathsf{L}}) &) \end{bmatrix} . \tag{5.23}$$

Going back to the original problem one would have that

$$\mathbf{y} = \mathbf{E}\mathbf{x} + \mathbf{n} = \mathbf{E}\boldsymbol{\Psi}^{\mathsf{t}}\boldsymbol{\alpha} + \mathbf{n} = \mathbf{P}\boldsymbol{\alpha} + \mathbf{n} \ , \tag{5.24}$$

where

$$\mathbf{P} = \mathbf{E}\boldsymbol{\Psi}^{\mathsf{t}} \ . \tag{5.25}$$

Since the dimension of $\boldsymbol{\alpha}$ is 3, certainly inferior to the number of points in the vertical grid $\{z_l\}$, one can solve the system Eq.(5.24) by the least-squares method [61]:

$$\boldsymbol{\alpha}^{\#} = \left(\mathbf{P}^{\mathsf{t}}\mathbf{P}\right)^{-1}\mathbf{P}^{\mathsf{t}}\mathbf{y} \ . \tag{5.26}$$

Once the vector of amplitudes, $\boldsymbol{\alpha}$, is estimated, one can calculate the estimated vector of sound speed profile perturbations through the equation:

$$\mathbf{x}^{\#} = \boldsymbol{\Psi}^{\mathsf{t}}\boldsymbol{\alpha}^{\#} \ . \tag{5.27}$$

Since the HNMs are continuous functions of depth the regularization introduced in this section eliminates, in a natural way, all the issues related to a particular choice of a layer system. It should be remarked that a similar approach could be developed in terms of EOFs. However, as discussed in section 4.1.1, the calculation of EOFs demands the existence of a significant number of observations, while the calculation of HNMs can be performed using only the mean temperature profile.

5.4.4 Arrival redundancy

One of the most important conclusions of reference [76], based on the application of theoretical information criteria to the acoustic data of Event I, indicates that the estimated number of independent arrivals corresponds to 4. This results implies the redundancy of the arrival times. In terms of the observation matrix it follows that $\mathsf{r} = 4 < \mathsf{T}$, which implies important theoretical and practical questions, related to the inversion of matrix $\mathbf{E}$. The problem of redundancy is discussed in detail in [64], where it is shown that the estimated number of independent arrivals depends on the physical limitations of the propagation channel. In that reference it is shown that for the isovelocity case ($c =$ constant), and for a propagation scenario, where one avoids the symmetries between the source and hydrophone depths, it should take place a clustering of arrivals in groups of quadruplets. Furthermore, the analytic calculation of the corresponding observation matrix allows to show that any group of four rows of $\mathbf{E}$, corresponding to a particular quadruplet, depends linearly on the first group of four rows that correspond to the first quadruplet. This result implies that for the isovelocity case the rank of $\mathbf{E}$ is equal to 4. The rank deficiency of this observation matrix allows to infer the rank deficiency of $\mathbf{E}$ for the quadruplets of a general sound speed profile, $c(z)$. In this way, one can introduce an "effective" observation matrix, defined as:

$$\mathbf{E}_{eff} = \mathbf{U}_4 \mathbf{S}_4 \mathbf{V}_4^{\mathsf{t}} \; . \tag{5.28}$$

On the other side, the pseudo-inverse matrix would correspond to

$$\mathbf{E}^{\#} = \mathbf{V}_4 \mathbf{S}_4^{-1} \mathbf{U}_4^{\mathsf{t}} \; . \tag{5.29}$$

5.4.5 Tomography simulations

By analogy with the discussion presented in section 5.3 one can now proceed with the tests of the theoretical aspects of Travel-Time Tomography, on the basis of ray tracing simulations. Initially, one can calculate the matrix $\mathbf{\Psi}$ using the three firsts HNMs. Then, for each hydrophone, proceed according to the following scheme:

1. The ray-tracing model is used to simulate the eigenrays and arrival times for the

geometry of Event I, using both the reference and perturbed sound speed profiles, illustrated in Fig.4.9.

2. The stable eigenrays are used to calculate the observation matrix, $\mathbf{E}$, and, through its SVD, the effective observation matrix, $\mathbf{E}_{eff}$ (see Eq.(5.28)).

3. The regularization matrix, $\mathbf{P}$, is calculated through the product of Eq.(5.25).

4. The vector of amplitudes, $\boldsymbol{\alpha}$, is estimated applying the solution of Eq.(5.26).

5. The perturbation of the sound speed profile, $\mathbf{x}$, is estimated trough Eq.(5.22).

In the array processing case one calculates first the observation matrix of the concatenated system, calculates the corresponding effective observation matrix, and then continues the inversion scheme starting from item 3. The only source of "noise" in this set of simulations correspond to the the rounding errors, resulting from the transformation of the set of integral equations into a linear system of equations. The quality of the inversion was estimated by calculating in each case the mean depth error, defined as

$$\text{Mean depth error} \quad = \langle \left| \mathbf{x} - \mathbf{x}^{\#} \right| \rangle = \frac{1}{\mathsf{L}} \sum_{l=1}^{\mathsf{L}} \left| x_l - x_l^{\#} \right| \ . \tag{5.30}$$

The arrival times, used in the simulations, are illustrated in Fig.5.4.

The calculation time of travel-time inversion was of the order of some minutes, and all the inversion tests were performed much faster than any of the MFT simulations. As indicated by the inverse results for each hydrophone (see Fig.5.5, cases (a), (b) and (c)) the rounding errors increase with hydrophone depth. In the case of hydrophone 1 the match between the "real" and the inverted perturbations achieves a high degree of accuracy. That accuracy degrades progressively with the increase of hydrophone depth. The inverse solution of the

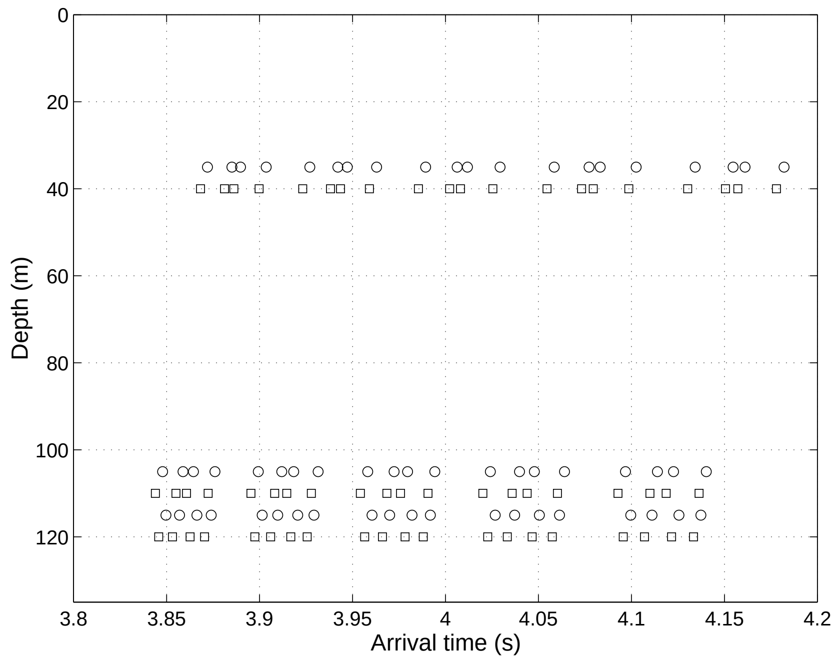

Figure 5.4: Travel-Time simulations, arrival times for $c_0(z)$ (squares) and $c(z)$ (circles).

concatenated system allows to improve the accuracy of the inverse solution relative to the hydrophones 2 and 3 (see Fig.5.5, case (d)). It is particularly interesting to notice that case (a) exhibits a more accurate solution than the one obtained in case (d), which in a certain sense indicates that the concatenation of the system deteriorates the tomographic resolution of hydrophone 1. However, one can develop a particular selection of the groups of arrivals, that provide a more accurate solution of the concatenated system than the one obtained for hydrophone 1. In this way, the issue of accuracy described previously seems to be related only to a question of numerical rounding. As will be shown in section 6.3, for the case of real data, the contamination of signal with noise significantly deteriorates the quality of the inversion, making the solution of the concatenated system definitely more accurate than any of the independent inverse solutions.

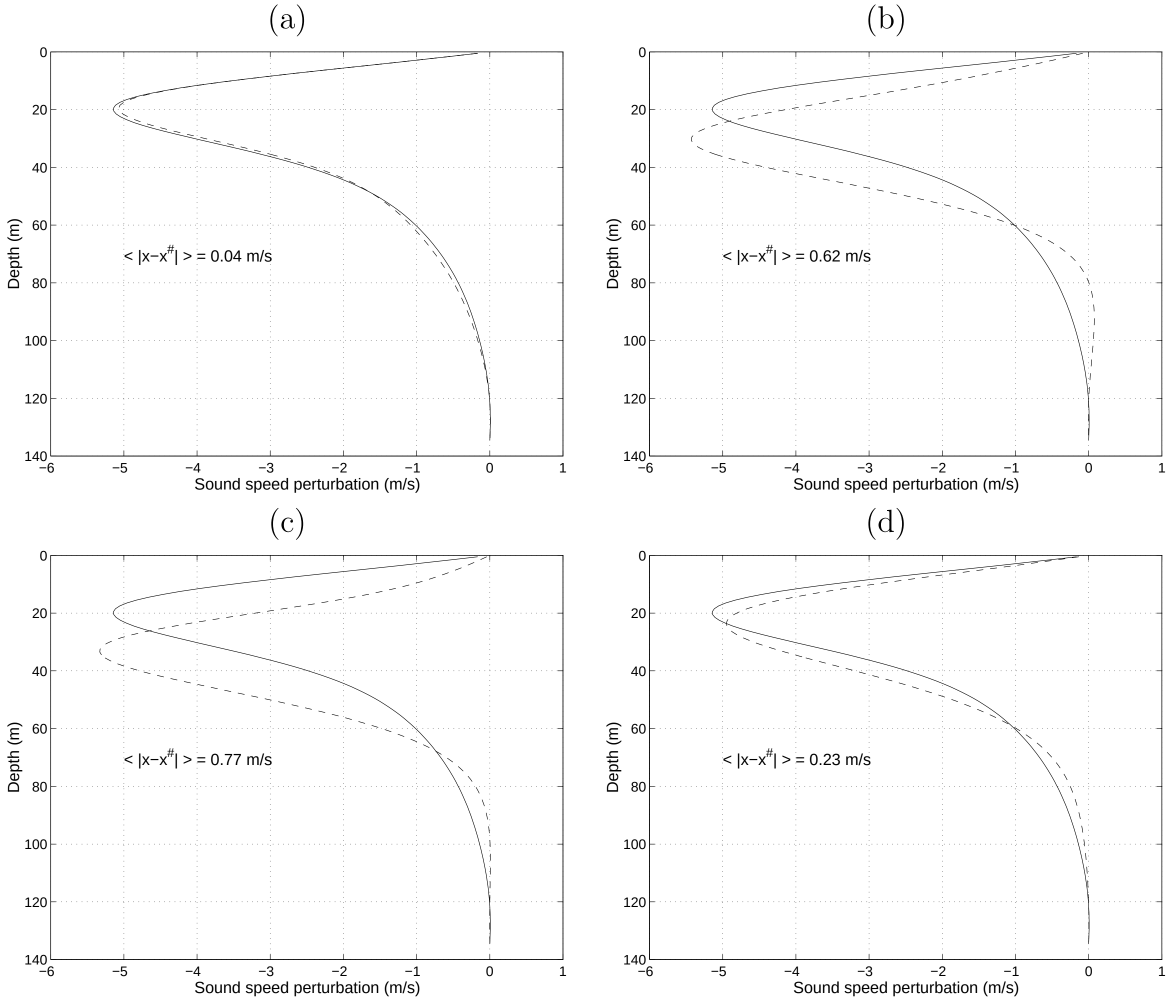

Figure 5.5: Inversion results: hydrophone 1 (a), hydrophone 2 (b), hydrophone 3 (c) and concatenated system (d). In all cases the continuous line indicates the “real” perturbation, while the dashed line indicates the corresponding inverse solution.

Chapter 6

Tomographic inversion: real data

The tomography simulations of the previous Chapter put in evidence the preference of the methods of Travel-Time Tomography over the methods of Matched-Field Tomography. Therefore, this Chapter will be dedicated to the discussion of the most important problems related to the tomography processing of the acoustic data of Event I, on the basis of the corresponding arrival times.

6.1 Extraction and comparison of acoustic arrivals

The first issue of practical interest is related to the extraction and further comparison of the acoustic arrivals[1]. Within the known literature these two questions are discussed at the level of two different problems: the problem of *identification* of the arrivals, and the problem of arrival *tracking* [5, 88, 89]. For a particular set of arrival patterns, Π_1, Π_2, $\ldots$ Π_L, the first problem can be solved by calculating the significant maxima (usually known as "peaks") of each arrival pattern, Π_l. Once the identification problem has been solved one can use a particular method of pattern recognition to "follow" the presence of the peaks along the acoustic transmissions. The peaks that do not appear in two consecutive transmissions are considered as unstable arrivals, and are eliminated from the tomography processing. Once

[1]Within this context by "arrivals" one should understand both the absolute and relative arrivals.

the identification and tracking problems have been solved, one can proceed with the travel-time based tomographic inversion. In reference [88] it is suggested to treat independently each problem. Therefore, one calculates the arrivals for each pattern, Π_l, and proceeds with the arrival comparison, using a least-squares criterion, according to all *possible configurations* of real and modeled arrivals. The configuration that optimizes the criterion allows to identify the stable arrivals, which are then used in the tomographic inversion.

In the particular case of the INTIMATE'96 dataset the arrivals of interest correspond to the quadruplet arrivals. Those arrivals are not extracted directly from each "ping" of acoustic data, but are extracted from a mean pattern, $\langle\Pi\rangle$, which is calculated according to the expression Eq.(3.2). The number of snapshots corresponds to $L = 37$ (i.e., it corresponds to an entire "run") which is equivalent to an observation horizon of 5 minutes. This value is small enough to allow the monitoring of the internal tide, and also to "compete" with the thermistor chain data in terms of temporal resolution. In this way, each run of the Tapes 4 to 10 was used to calculate the respective mean pattern, $\langle\Pi\rangle$. The extraction of the peaks from each mean pattern was developed by calculating all the "narrow" maxima of the pattern, and by excluding further the "narrow" maxima below a "threshold" amplitude. The criteria of "narrowness" and "threshold" amplitude were implemented heuristically, by trial and error and based, in particular, on the normalization of the temporal and amplitude axes of $\langle\Pi\rangle$. In contrast with the classical approach one of the advantages in applying the arrivals extraction heuristic is that it is *independent* of the problem of arrival comparison. In this way, the heuristic was applied only once to all mean arrival patterns of Event I, and the extracted peaks were stored in digital support for further tomography processing.

It should be remarked that the extraction criterion does not take into account the expected arrival structure, clustered in groups of quadruplets. Therefore, the heuristic of arrival extraction failed sometimes in the peak selection, and being unable to reproduce the expected clustering. This situation is worst in the cases when the reception system failed and the sets of quadruplets were no longer identifiable in the corresponding arrival pattern[2]. However, in many cases the "failure" in the arrival extraction was compensated significantly by the comparison of extracted and modeled arrivals, $\boldsymbol{\tau}_r$ and $\boldsymbol{\tau}_{0r}$, respectively.

The presence of the quadruplets can be recognized visually along the acoustic transmissions of Event I without any particular difficulties. However, implementing an algorithm that allows to solve the identification (and corresponding tracking) of the quadruplets is not a trivial task. In fact, in the mean patterns $\langle \Pi \rangle$ of Event I one can observe a significant number of arrivals, with situations where the groups of quadruplets are complete in a particular transmission, and appear incomplete in the transmission that follows. This behaviour induces a variety of situations which is very difficult to deal with in terms of the classical approach. This difficulty leaded to the separation of the identification and tracking problems. However, if one tries to apply the comparison method described in [88], to the acoustic data of Event I, the significant number of extracted arrivals would generate a large amount of possible configurations, including many cases totally inconsistent with the expected structure of quadruplets. The comparison of all configurations would increase tremendously the calculation time, and would compromise the monitoring objectives of tomographic inversion. The introduction of an additional comparison heuristic can allows to avoid an useless effort of long calculations. The heuristic revealed to be particularly efficient in the tomography processing and was simply based on the following principles:

[2]See, for instance, the Tape9/run13.

1. *Alignment:* in the comparison of two arrival sequences they are substituted by relative arrival sequences (which will be called simply as arrivals). These arrivals are aligned, along the time axis, through the temporal intervals that separate the quadruplet groups.

2. *Pairing match:* the previous alignment induces the formation of arrival pairs $\tau_{0r} \approx \tau_r$. If there is a "minimal" number of those pairs one can use the relative position of each modeled –non-paired– arrival, relative to the *closest* τ_{0r} of a matched pair, to predict the position of the corresponding real arrival. If the real arrival effectively close is "sufficiently close" to the predicted value the heuristic forms a new pair. In the opposite case the heuristic tests the following non-paired modeled arrival and repeats the comparison.

The more "similar" the modeled and real arrivals are, the more pairs the heuristic is able to match. In this way, the comparison heuristic allows to eliminate in most cases a significant amount of real arrivals that do not match the quadruplet structure.

6.2 Waveguide depth estimation

In order to test the robustness of the extraction and comparison heuristics of real arrivals both heuristics were applied to the problem of estimating the depth of the acoustic waveguide, D, along time. This estimation could take advantage of the simulations of the arrival sensitivity, to the geometric variations of the propagation channel (discussed in section 4.2.1). This estimation makes useless the usage of a tide prediction model and takes direct advantage of the acoustic data to perform that estimation.

In order to develop the estimation, the acoustic arrivals $\boldsymbol{\tau}_0\left(D, z_j\right)$ $(j = 1,2,3)$ were modeled for a waveguide depth $D \in [\ D_{min}\ ,\ D_{max}\ ]$, with $D_{min} = 130$ m and $D_{max} = 140$ m, and with a discretization interval $\Delta D = 0.1$ m. For each set of modeled arrivals, $\boldsymbol{\tau}_0\,(D, z_j)$, the respective set of relative arrivals was calculated:

$$\boldsymbol{\tau}_{0r}\,(D, z_j) = \boldsymbol{\tau}_0\,(D, z_j) - \boldsymbol{\tau}_{01}\ , \tag{6.1}$$

where $\boldsymbol{\tau}_{01} = \tau_{01}\mathbf{u}_1$, and $\mathbf{u}_1$ represents an "identity" vector:

$$\mathbf{u}_1 = [\ 1\ 1\ \ldots\ 1\ ]^{\mathsf{t}}\ . \tag{6.2}$$

The comparison heuristic was applied to each arrival set $\boldsymbol{\tau}_r\,(t, z_j)$ and $\boldsymbol{\tau}_{0r}\,(D, z_j)$, in order to form sets of matched pairs, $\boldsymbol{\tau}_r^p\,(t, z_j)$, and $\boldsymbol{\tau}_{0r}^p\,(D, z_j)$. For each set it was applied the following depth estimator:

$$\hat{\mathcal{T}}(t, D, z_j) = ||\boldsymbol{\tau}_r^p\,(t, z_j) - \boldsymbol{\tau}_{0r}^p(D, z_j)||\ . \tag{6.3}$$

In this way, the estimated depth value corresponds to

$$D_j^{\#}(t) = \arg\left\{\min_D \hat{\mathcal{T}}(t, D, z_j)\right\}\ . \tag{6.4}$$

The estimator Eq.(6.3) depends on the hydrophone depth z_j. An estimator that takes into account all the hydrophones (and which would provide a more consistent value of $D^{\#}(t)$) can be defined following the same principles that leaded to the expression (6.3), but substituting the vectors $\boldsymbol{\tau}_r\,(t, z_j)$ and $\boldsymbol{\tau}_{0r}(z_j, D)$ ($j = 1,\ 2,\ 3$), by the concatenated vectors of arrivals:

$$\boldsymbol{\tau}_r(t) = \begin{bmatrix} \boldsymbol{\tau}_r(t, z_1) \\ \boldsymbol{\tau}_r(t, z_2) \\ \boldsymbol{\tau}_r(t, z_3) \end{bmatrix}\ , \quad \text{and} \quad \boldsymbol{\tau}_{0r}(D) = \begin{bmatrix} \boldsymbol{\tau}_{0r}(D, z_1) \\ \boldsymbol{\tau}_{0r}(D, z_2) \\ \boldsymbol{\tau}_{0r}(D, z_3) \end{bmatrix}\ . \tag{6.5}$$

The estimation results are illustrated in Fig.6.1 and exhibit a clear semidiurnal variation of the waveguide depth, induced by the surface tide. The sudden variations of $D(t)$ correspond, probably, to environmental and geometric variations of unknown origin. It is

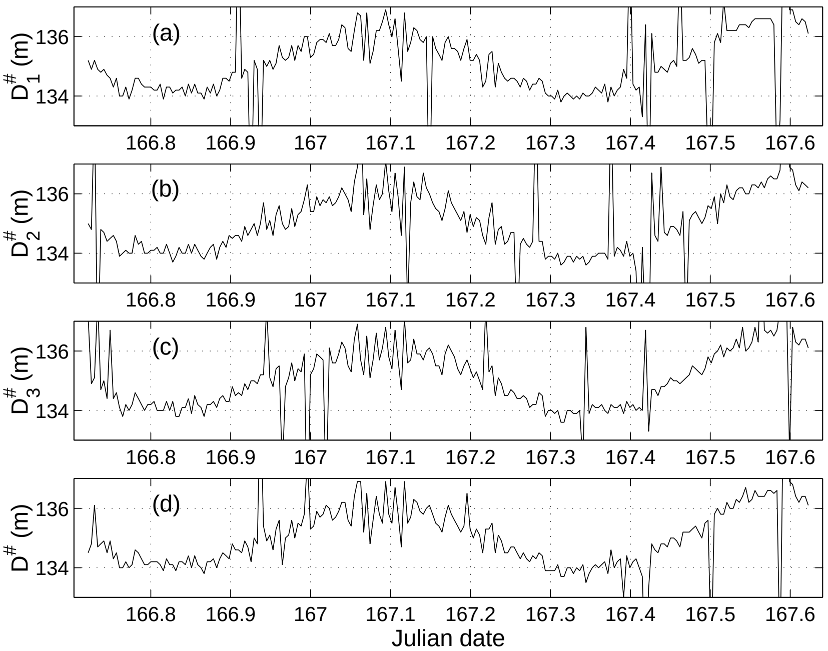

Figure 6.1: Waveguide depth estimation, D, using the arrivals of hydrophone 1 (case (a)), hydrophone 2 (case (b)), hydrophone 3 (case (c)), and concatenated arrivals (case (d)).

remarkable that the variations of the estimated waveguide depth reproduce the surface tide predictions illustrated in Fig.4.6. The superposition of the different curves indicates discrepancies of about 10 cm, which constitutes an important indication of the uncertainty in the estimation of D. As will be shown in the following section despite the apparently reduced value of uncertainty in $D^\#$ it can be able to introduce a significant uncertainty in the estimation of the inverse solution, $x^\#$.

6.3 Accuracy of tomographic inversion

The results of the previous section indicate the robustness of the heuristics of arrival selection and comparison. Moreover, the set of results provided a temporal estimation of the waveguide depth, $D^\#$. This estimation can be used to optimize the tomography processing of the acoustic data of Event I. Nevertheless, there are limitations to the tomography scheme which were not identified yet. The most important of those limitations consists in determining the accuracy of tomographic inversion, i.e., in determining the "proximity" between the estimated (inverse) and true solutions, $\mathbf{x}^{\#}$ and $\mathbf{x}$, respectively. That proximity can be calculated using the estimator:

$$\hat{\mathcal{X}} = \left|\left|\mathbf{x}^{\#} - \mathbf{x}\right|\right| \ , \tag{6.6}$$

which allows to measure the degree of "matching" between the estimated and true solutions. The estimator $\mathcal{X}$ can be calculated proceeding through the following stages:

1. Pick up a particular sound speed profile, $c(z, t)$, from the CTD-IH data.
2. Look up for the corresponding estimated depth, $D^{\#}(t)$, and introduce a vertical inversion grid $\{z_l\}$.
3. Calculate the true solution, $\mathbf{x}$.
4. Look up for the corresponding modeled arrivals, $\boldsymbol{\tau}_0(D^{\#}(t), z_j)$ (j = 1, 2, 3).
5. Look up for the corresponding real arrivals, $\boldsymbol{\tau}_r(t, z_j)$ (j = 1, 2, 3).
6. Compare and match pairs of arrivals:

$$\Big(\ \boldsymbol{\tau}_0(D^{\#}(t), z_j) \ , \ \boldsymbol{\tau}_r(t, z_j) \ \Big) \Rightarrow \Big(\ \boldsymbol{\tau}_0^p(D^{\#}(t), z_j) \ , \ \boldsymbol{\tau}_r^p(t, z_j) \ \Big) \quad \text{with} \quad j = 1, 2, 3 \ .$$

7. Calculate the inverse solution, $\mathbf{x}^{\#}$.

Unfortunately, one can not go directly from stage 6 to stage 7 because the matched real arrivals $\boldsymbol{\tau}_r^p(t, z_j)$ are *relative* (not absolute) arrivals. A preliminary attempt to solve this problem can consist in aligning the real arrivals by the modeled arrivals (which in fact reproduces the alignment of the temporal fronts for $c_0(z)$ and $c(z, t)$):

$$\boldsymbol{\tau}^p(t, z_j) = \boldsymbol{\tau}_r^p(t, z_j) - \boldsymbol{\tau}_{r1}^p(t, z_j) + \boldsymbol{\tau}_{01}^p(D^{\#}(t), z_j) \ , \tag{6.7}$$

where $\boldsymbol{\tau}^p_{r1}(t, z_j) = \tau^p_{r1}(t, z_j)\mathbf{u}_1$, and $\boldsymbol{\tau}^p_{01}(t, z_j) = \tau^p_{01}(D^{\#}(t), z_j)\mathbf{u}_1$, with $j = 1,\ 2,\ 3$. It is worthwhile to remark that in some cases the alignment could be performed using the last arrival, instead of the first one. The alignment introduced by Eq.(6.7) allows to generate "absolute" real arrivals and to calculate the respective concatenated vector of delays, $\mathbf{y}$. However, it is not difficult to find that the respective inverse solution, $\mathbf{x}^{\#}$, is far away from the true solution, $\mathbf{x}$. To find an inverse solution, closer to the true one, one has to "contaminate" several times the vector of delays with temporal perturbations:

$$\mathbf{y}' = \mathbf{y} + \boldsymbol{\delta}\mathbf{y} \ , \tag{6.8}$$

where $\boldsymbol{\delta}\mathbf{y} = \delta y \mathbf{u}_1$, and generate a "family" of solutions, $\mathbf{x}^{\#}(\mathbf{y}')$. Within that family one can select the solution that minimizes the proximity estimator, Eq.(6.6).

A preliminary test of this method consisted in selecting the CTD profile corresponding to the Tape4/run8 (the estimated depth value corresponded to 134.4 m). The matched pairs of aligned arrivals can be seen in Fig.6.2(a). The values of the temporal perturbation, δy, were generated within the interval

$$\delta y \in [\ -2\ ,\ 2\ ]\ \text{ms} \ . \tag{6.9}$$

Each hydrophone delay was compensated with the corresponding mean value in order to obtain a delay vector, $\mathbf{y}'$, with a mean value of 0 ms:

$$\mathbf{y}_j \Rightarrow \mathbf{y}_j - \langle \mathbf{y}_j \rangle \mathbf{u}_1 \ , \tag{6.10}$$

where

$$\langle \mathbf{y}_j \rangle = \frac{1}{\mathsf{T}_j} \sum_{j=1}^{\mathsf{T}_j} y_j \ . \tag{6.11}$$

Moreover, in order to minimize the presence of noise $\mathbf{n}$ in the delays $\mathbf{y}_j$, only the delays contained within the interval $[\ -0.2\ ,\ 0.2\ ]$ ms were included in the inversion scheme. This selection criterion was based in the simulation results, discussed in section 5.4.5. Fig.6.2(b) illustrates some of the solutions generated within the interval defined by Eq.(6.9). As shown by the figure the contamination of delays with temporal perturbations generates a family of solutions, which oscillate around apparently stable nodes. The existence of those nodes is an interesting feature of the family of inverse solutions, but its analysis exceeds the main objectives of this dissertation. Therefore, the existence of those nodes will not be discussed any further. Since the calculation of the inverse solution was developed through the regularization using HNMs (as discussed in section 5.4.3) each inverse solution $\mathbf{x}^{\#}$ corresponds to a vector of amplitudes $\boldsymbol{\alpha}^{\#}$ (see Fig.6.2(c)). The best inverse solution (i.e., the solution that minimizes Eq.(6.6) is illustrated in Fig.6.2(d).

The matching of the profiles shown in Fig.6.2(d) is not satisfactory. One can try additionally to minimize the estimator $\hat{\mathcal{X}}$ by generating the family of solutions using depths slightly different from the one estimated. In this way, after several attempts, the best match was achieved with $D^{\#} = 134.1$ m (see Fig.6.3(b)); Fig.6.3(a) indicates the corresponding paired and aligned arrivals.

The result illustrated in the figure shows that an uncertainty of the order of a few centimeters in the estimation of D can give rise to a significant uncertainty in the estimation of δc. Therefore, the estimation of the waveguide depth constitutes a fundamental factor in the tomography processing of acoustic data. In this sense the proximity estimator will depend on both temporal perturbations and variations of the estimated depth value:

$$\hat{\mathcal{X}} = \hat{\mathcal{X}}\left(\mathbf{y}', D\right) \ , \tag{6.12}$$

where $D \in \left[\ D^{\#} - \delta D \ ,\ D^{\#} + \delta D\ \right]$.

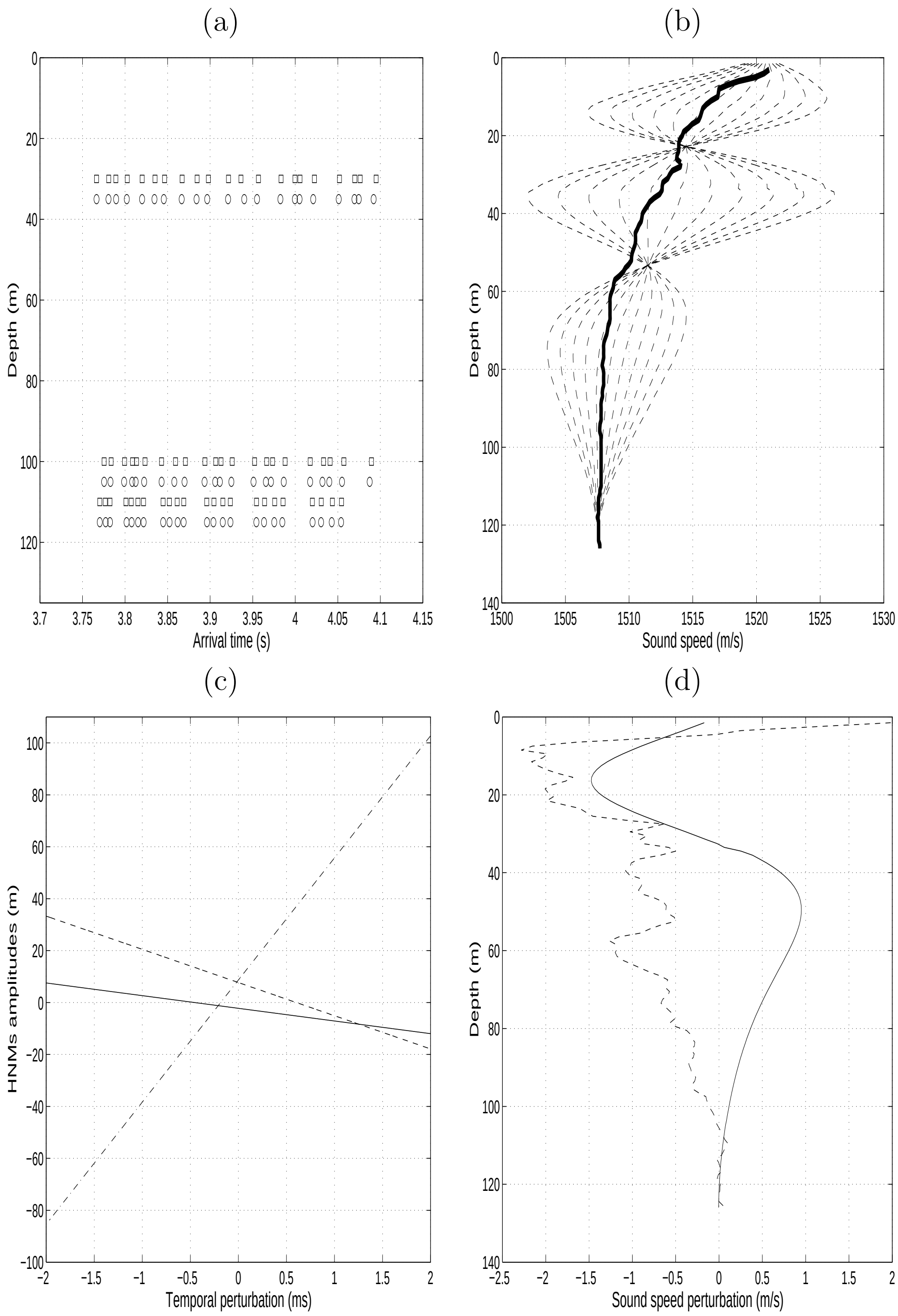

Figure 6.2: Matching of true and inverse solutions, Tape4/run8, $D^{\#} = 134.4$ m. (a) preliminary alignment of paired arrivals, the circles and squares correspond, respectively, to real and modeled arrivals; (b) family of generated solutions, the solid line corresponds to the searched profile; (c) amplitudes of HNMs, associated to the inverse solutions of case (a), α_1 (continuous line), α_2 (dashed line), and α_3 (dot-dash line); (d) solution $\mathbf{x}^{\#}(\mathbf{y}')$ that minimizes $\hat{\mathcal{X}}$ (continuous line), and true solution $\mathbf{x}$ (dashed line).

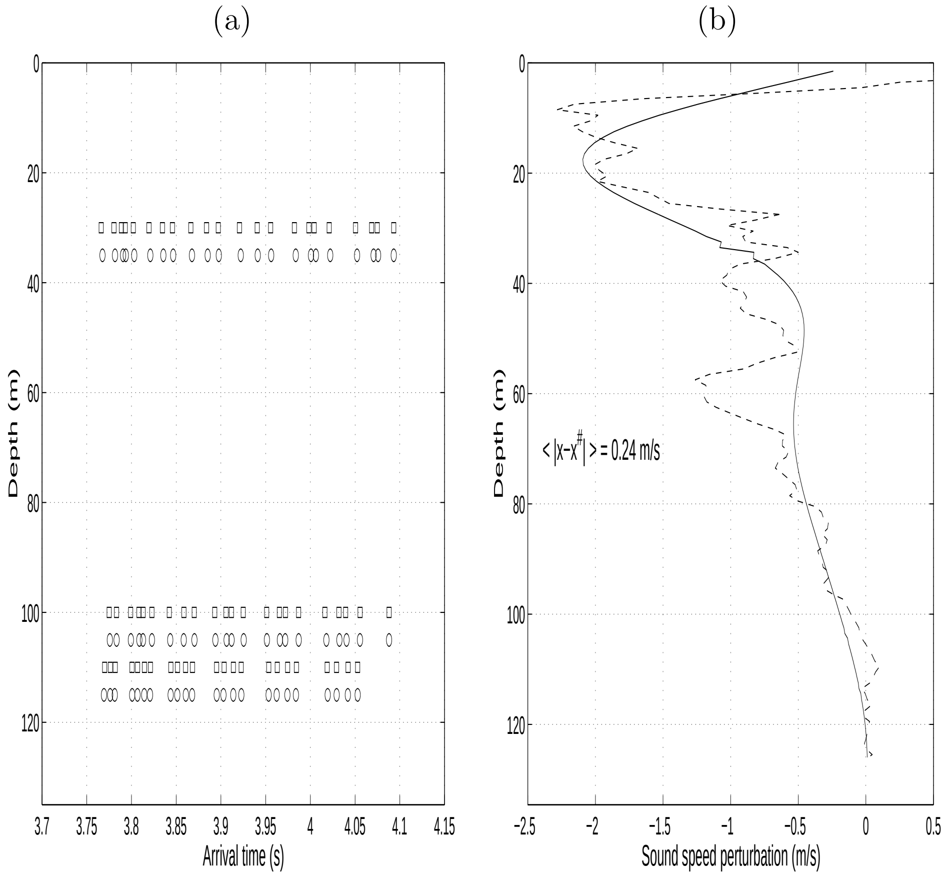

Figure 6.3: Matching of true and inverse solutions, Tape4/run8, $D^{\#} = 134.1$ m. (a) preliminary alignment of paired arrivals, the circles and squares correspond, respectively, to real and modeled arrivals; (d) solution $\mathbf{x}^{\#}(\mathbf{y}')$ that minimizes $\hat{\mathcal{X}}$ (continuous line), and true solution $\mathbf{x}$ (dashed line).

There are cases where the matching of profiles can not be accomplished, due either to transitory fails in the reception system, or on temporary contributions of higher-order baroclinic modes to δc, which will not be properly modeled by the regularization scheme described in section 5.4.3 (see Fig.6.4).

The matching of profiles was developed for the profiles of sound velocity, where one could find simultaneous records in both CTD-IH and acoustic data of Event I. After the matching by both temporal perturbations and variations of the estimated depth, one can verify that the matched field of sound speed reproduces in detail the profiles directly measured (see Fig.6.5, cases (a) and (b)). Moreover, the HNM amplitudes, for each matched profile, can be

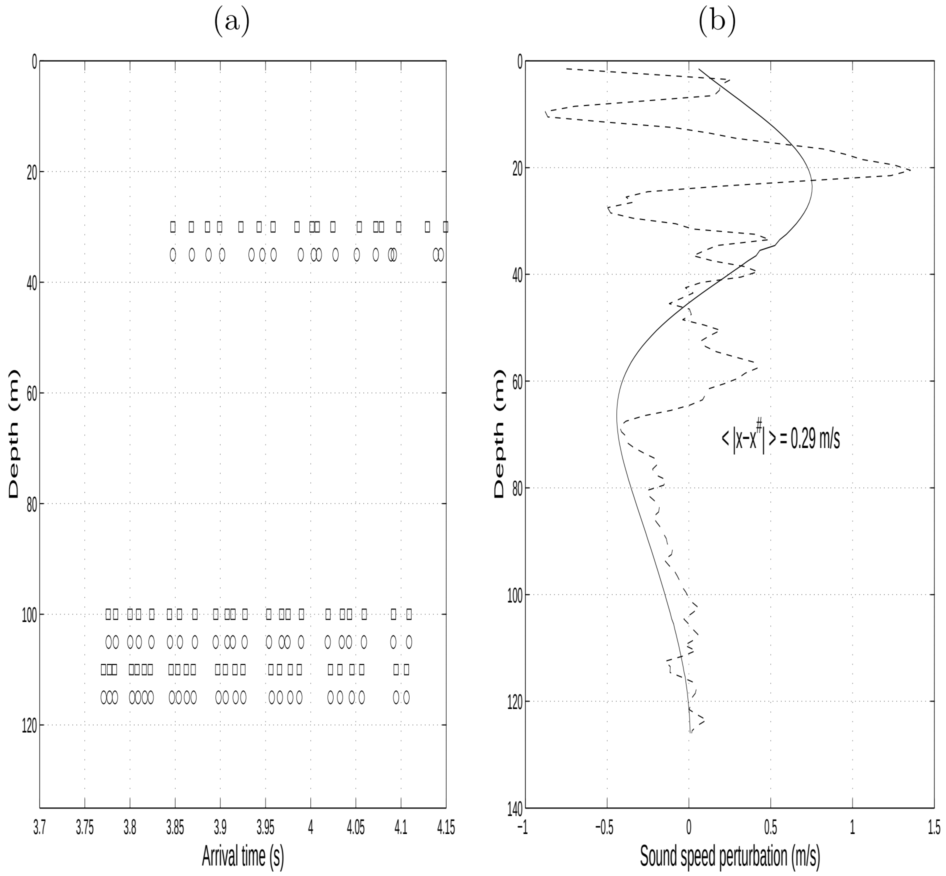

Figure 6.4: Matching of true and inverse solutions, Tape5/run15. (a) preliminary alignment of paired arrivals, the circles and squares correspond, respectively, to real and modeled arrivals; (d) solution $\mathbf{x}^{\#}(\mathbf{y}')$ that minimizes $\hat{\mathcal{X}}$ (continuous line), and true solution $\mathbf{x}$ (dashed line).

used to invert the temperature and salinity fields (see Fig.6.5, cases (c) and (d)) with a degree of accuracy that resembles in detail the direct observations. The entire set of tomography results confirms the high degree of resolution, that can be achieved through the application of acoustic tomography to the monitoring of internal tides.

6.4 Tomography processing for the entire data of Event I

The robustness of the tomographic inversion scheme, when applied to the processing of the entire acoustic data of Event I , is the last issue which remains opened. Since the absolute arrival times are unknown that inversion can be developed only at an approximated level.

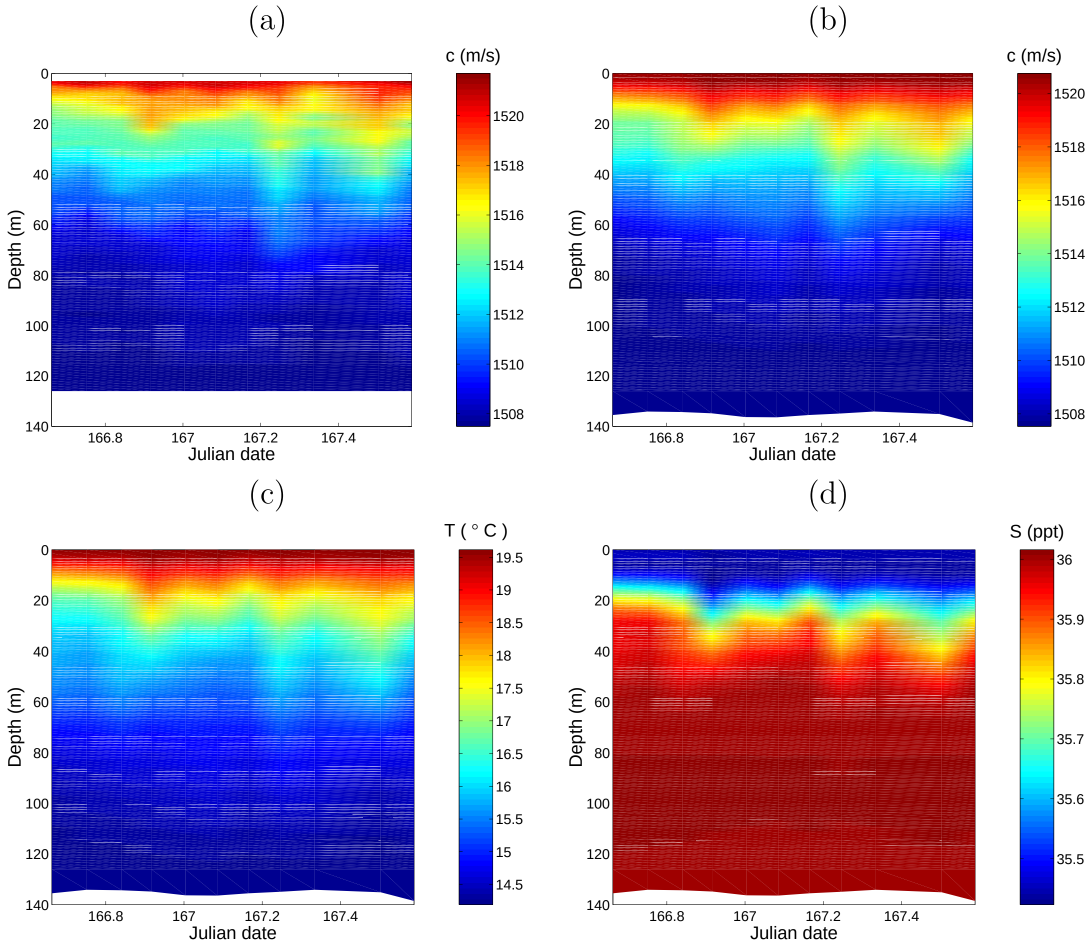

Figure 6.5: Tomography resolution of acoustic data of Event I: (a) test profiles (CTD-IH data), (b) matched profiles; inverted fields of temperature (c) and salinity (d).

In this sense one can take advantage of the amplitudes of the HNMs calculated already for the matched profiles. The tomographic inversion can be developed in a similar manner to the scheme described in the previous section, but introducing the estimator

$$\hat{\mathcal{A}}_j = \left|\left|\alpha_j^{\#} - \alpha_j^{ref}\right|\right| \ , \ j = 1, 2, 3 \ , \tag{6.13}$$

where the reference vector $\boldsymbol{\alpha}_{ref}(t) = \left[\ \alpha_1^{ref}(t) \ , \ \alpha_2^{ref}(t) \ , \ \alpha_3^{ref}(t) \ \right]^{\mathsf{t}}$ can be calculated by linear interpolation between the *matched* closest amplitudes:

$$\boldsymbol{\alpha}_{ref}(t) = \boldsymbol{\alpha}_1(t_1) + (t - t_1)\,\frac{\boldsymbol{\alpha}_2(t_2) - \boldsymbol{\alpha}_1(t_1)}{t_2 - t_1} \ , \ t_1 < t < t_2 \ . \tag{6.14}$$

As indicated by Eq.(6.13) the estimation of the components of $\boldsymbol{\alpha}^{\#}(t)$ is developed independently. In fact, a preliminary attempt to estimate directly $\boldsymbol{\alpha}^{\#}(t)$ minimizing the norm

$\left|\left|\boldsymbol{\alpha}^{\#} - \boldsymbol{\alpha}_{ref}\right|\right|$ completely failed.

The tomography scheme described in the previous section, in addition with the estimator $\hat{\mathcal{A}}_j$, was applied to all the 231 runs of acoustic data of Event I, and developing the tomographic inversion without interruptions. The corresponding results can be seen in figures Fig.6.6 and Fig.6.7. Those results, although approximated, reproduce a variation of the sound speed profile typically semidiurnal, with amplitudes which are consistent with the amplitudes found in the observations. Therefore, those results show the robustness of monitoring through the travel-time based acoustic tomography.

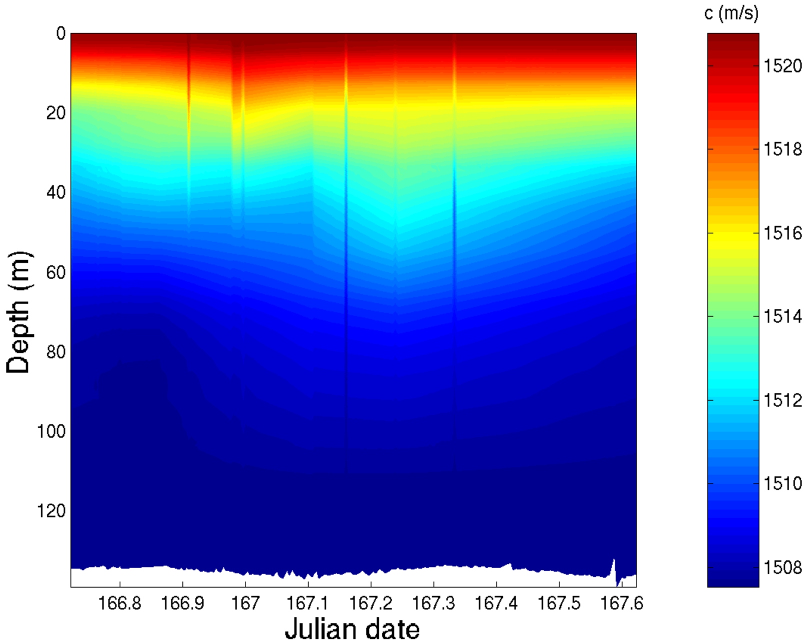

Figure 6.6: Tomography results based on reference profiles.

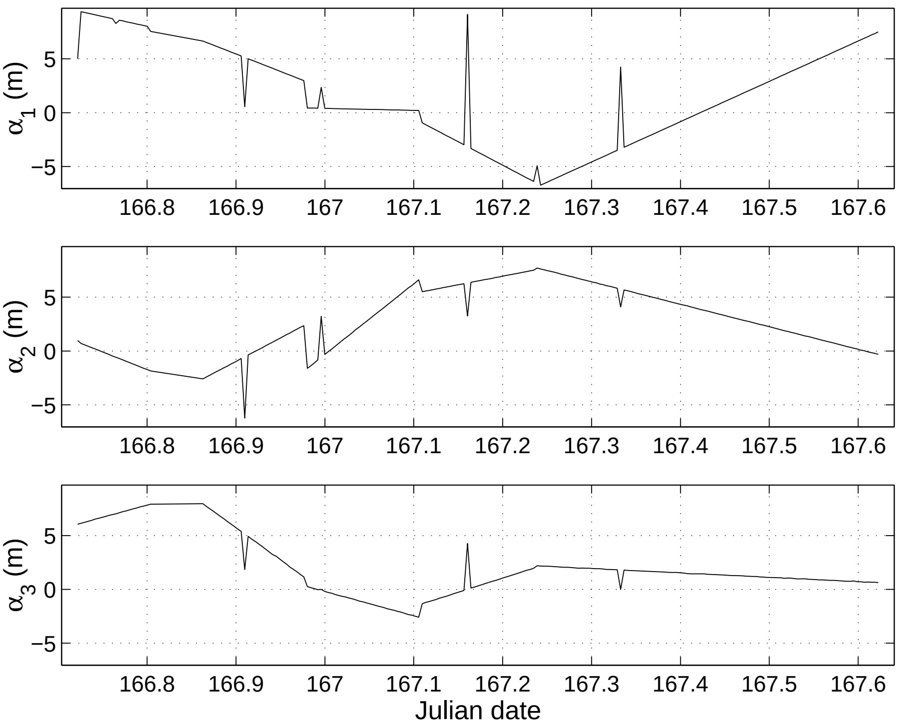

Figure 6.7: Estimated amplitudes of HNMs.

Chapter 7

Conclusions

The material of this thesis was dedicated initially to the detailed description of the physical model describing the propagation of internal tides, in the hydrostatic and non-hydrostatic cases, and also in the linear and non-linear cases. The theoretical background of that model allowed also to develop a simple description of the most important theoretical aspects related to the propagation of acoustic waves. In that sense the development of a logical structure, regarding acoustic waves, received a significant degree of attention in order to relate their propagation to the different acoustic propagation models, and also with some fundamental aspects of signal processing. That logical structure was progressively taken into account along the Chapters, during the discussion of the oceanographic and acoustic data of the INTIMATE'96 experiment, and also during the discussion of the simulations of the propagation problem, of tomographic inversion, and finally, during the discussion of tomographic inversion of the acoustic data of Event I of the INTIMATE'96 experiment. The discussion, presented along the different Chapters, allows one to remark a set of achievements which are described summarily in the following paragraphs.

First, the detailed analysis of the theoretical model of propagation of internal tides allows to introduce the concept of Hydrostatic Normal Modes (HNMs), which can be calculated from the mean temperature profile, $T_0(z)$. The theoretical discussion of the properties of HNMs suggests their choice as a robust alternative basis, to parametrize the sound velocity, temperature, salinity, and current fields. Furthermore, the comparison of HNMs with empirical modes (EOFs) of temperature data, shows the equivalence between the three first HNMs and the three first EOFs. This result is very significant in the sense that it confirms the usage of HNMs to take advantage of the mentioned parameterization. Additionally, one should remark the fact that the HNMs can be calculated using historical data, containing the mean temperature profile $T_0(z)$, without any particular restrictions to the frequency of sampling, or to the number of samples involved in the calculation of $T_0(z)$. In contrast, the calculation of EOFs demands temporal series properly spaced in time, implying the necessity of acquiring a significant amount of observations.

From the point of view of the forward problem, the simulations of acoustic propagation allow to clearly distinguish the effects of surface and internal tides on the acoustic arrivals. The ray-tracing simulations showed that the surface tide introduces significant variations in the structure of stable arrivals, which are clustered in groups of quadruplets, but without introducing significant perturbations in the initial groups of arrivals. In contrast, the internal tide introduces temporal perturbations to the entire set of arrivals. In this way, only an accurate measurement of the absolute arrival times can allow to identify in the received signal the perturbations induced by the propagation of the internal tide. The simulations of the inverse problem, developed in Chapter 5, clearly indicate the severe limitations of using a system of acoustic reception constituted by three hydrophones. In this sense the application of Matched-Field Tomography (MFT) to a configuration of acoustic reception, similar to the one of the INTIMATE'96 sea trial, will be insufficient when using narrowband tomography processing to develop an accurate estimation of the sound speed perturbations. The limitations of the narrowband processing can be compensated developing a broadband processing, but at the cost of significantly increasing the calculation time of tomographic inversion. An additional limitation of the broadband processing, detected during the simulations, corresponds to the large sensitivity of the broadband estimator to the contamination of signal with noise. The corresponding simulations, based on Travel-Time Tomography, showed calculation times significantly smaller, with the additional advantage of being possible to extend the Travel-Time Tomography method to an array processing scheme. Part of the tomography scheme, based on Travel-Time Tomography, took also advantage of HNMs to regularize the inverse problem. One of the most significant results of ray-tracing simulations consisted in the analysis of the issues related to the redundancy of arrival times. This redundancy was detected initially in real acoustic data within the context of the source localization problem. The adaptation of the methods discussed in Chapter 5, based on Travel-Time Tomography, to the acoustic data of Event I showed the significant level of accuracy that can be achieved in the inversion. In that Chapter it was shown additionally that the sound speed field inversion can be used also to invert the temperature and salinity fields when their mean profiles are known. This Chapter showed also the robustness of the application of the acoustic arrival selection, comparison and pairing heuristics, within the context of the application of Travel-Time Tomography to the monitoring of internal tides, and well suited to process efficiently the set of acoustic data of Event I. As a final conclusion it should be recommended to solve efficiently the technical problem of arrival synchronization (since this issue plays an important role within the tomography scheme based of Travel-Time Tomography), and also to use in the tomography experiments an array with four or more hydrophones. Additional information, like an accurate estimation of hydrophone depths, and/or data related to the array tilt, would certainly contribute to improve the accuracy of tomographic inversion.

Bibliography

[1] Stephen P. and Pickard G. *Introductory Dynamical Oceanography.* Pergamon Press, 2nd edition, Wiltshire, U.K., 1983.

[2] Knauss J.A. *Introduction to Physical Oceanography.* Prentice Hall, New Jersey, 2nd edition, 1997.

[3] Pickard G. and Emery W. *Descriptive Physical Oceanography.* Pergamon Press, 5th edition, Exeter, U.K., 1990.

[4] Munk W. and Wunsch C. Ocean acoustic tomography: A scheme for large scale monitoring. *Deep Sea Research*, 26(A):123–161, 1979.

[5] Munk W., Worcester P., and Wunsch C. *Ocean Acoustic Tomography.* Cambridge Monographs on Mechanics, Cambridge, University Press, 1995.

[6] Kumar P.S., Somayajulu Y.K., Murty T.V., Navelkar G.S., Saran A.K., Almeida A.M., and Murty C.S. Preliminary results of an acoustic tomography experiment (ate-93) in the eastern arabian sea. In *Proc. of the 3rd. European Conference on Underwater Acoustics*, pages 1081–1087, Copenhaguen, Denmark, 4-8 July 1996.

[7] Tolstoy A., Diachok O., and Frazer L.N. Acoustic tomography via matched field processing. *J. Acoust. Soc. America*, 89(3):1119–1127, March 1991.

[8] Stéphan Y. and Thiria S. Neural inversions for ocean acoustic tomography. In *Proc. of the 2nd. International Symposium on Inverse Problems*, pages 55–60, Paris, France, 2-4 November 1994.

[9] Ching-Sang Chiu, Miller J.H., and Lynch J.F. Inverse techniques for coastal acoustic tomography. In *Theoretical and Computational Acoustics*, editors D. Lee and H. Schultz, pages 917–931, World Scientific, Singapore, 1994.

[10] Ching-Sang Chiu, Miller J.H., Denner W., and Lynch J.F. Forward modeling of the barents sea tomography vertical line array data and inversion highlights. In *Full Field Inversion Methods in Ocean and Seismo-Acoustics*, editor O. Diaschok et al, pages 237–242, Kluwer Academic Publishers, Netherlands, 1995.

[11] Nathalie Jézéquiel. Observations de la marée interne sur le plateau continental par le tomographie acoustique. Rapport de stage, IFREMER-Centre Militaire d'Océanographie, Juin 1995.

[12] Pignot P. and Faure B. Marine media identification. In *Proc. of the 3rd. European Conference on Underwater Acoustics*, pages 809–813, Heraklion, Crete, Greece, 24-28 June 1996.

[13] Robinson I. S. *Satellite Oceanography.* Ellis Horwood, West Sussex, 1991.

[14] Apel J.R. *Principles of Ocean Physics*, volume 38. Academic Press, International Geophysics Series, London, 1987.

[15] Gerkema T. Generation of internal tides and solitary waves. *Journal of Physical Oceanography*, 25(6):1082–1094, June 1995.

[16] Kuryanov B. F. and Morozov A.K. Acoustic tomography of internal waves caused by tides near underwater mount in atlantic ocean. In *Proc. of the 3rd. European Conference on Underwater Acoustics*, Heraklion, Crete, Greece, 24-28 June 1996.

[17] Baines P.G. On internal tide generation models. *Deep-Sea Research*, 29(3A):307–338, 1982.

[18] Mazé R. Generation and propagation of non-linear internal waves induced by the tide over a continental slope. *Continental Shelf Research*, 7(9):1079–1104, 1987.

[19] Serpette A. and Mazé R. Internal tides in the bay of biscay: a two-dimensional model. *Continental Shelf Research*, 9(9):795–821, April 1989.

[20] Pichon A. and Mazé R. Internal tides over a shelf break: Analytical model and observations. *Journal of Physical Oceanography*, 20(5):657–671, April 1990.

[21] Sherwin T.J. Analysis of an internal tide observed on the malin shelf, north of ireland. *Journal of Physical Oceanography, Copyright by the Metereological Society*, 18(7):1035–1050, July 1988.

[22] Wunsch C. Internal tides in the ocean. *Reviews of Geophysical and Space Physics*, 13(1):167–182, February 1975.

[23] Baines P.G. Satellite observations of internal waves on the australian north-west shelf. *Australian J. Freshwater Mar. Res.*, 32, 1981.

[24] Ermakov S.A., da Silva J.C., and Robinson I.S. Ers sar imaging of long period internal (tidal) waves. In *Proc. of the 3rd. ERS Symp. on Space at the service of our Environment*, pages 1299–1304, Florence, Italy, 17-21 March 1997.

[25] Apel J.R. et al. An overview of the 1995 swarm shallow-water internal wave acoustic scattering experiment. *IEEE Journal of Oceanic Engineeering*, 22(3):465–500, July 1997.

[26] Jeans D.R.G. and Sherwin T.J. Solitary internal waves on the iberian shelf. Technical Report 44, Unit for Coastal and Estuarine Studies, University of Wales, Bangor, Anglesey LL59 5EY, November 1996. MORENA report.

[27] Small J., Hallock Z., and Scott J. Observations of large amplitude waves at the malin shelf edge during sesame 1995. *Continental Shelf Research*, 7(3):121–159, July 1996.

[28] Zhou J. and Zhang X. Resonant interaction fo sound wave with internal solitons in the coastal zone. *J. Acoust. Soc. America*, 90(4):2042–2054, October 1991.

[29] Korteweg D. and de Vries G. On the change of long waves advancing in a rectangular canal, and on a new type of long stationary waves. *Philosophical Magazine*, 39:422–443, January 1895.

[30] Gabov S. A. *Introduction to the theory of non-linear waves*. Ed. by the Moscow State University, Moscow (in russian), 1988.

[31] Ostrovsky L.A. Nonlinear internal waves in a rotating ocean. *Oceanology*, 18(2):119–125, 1978.

[32] Gerkema T. *Nonlinear dispersive internal tides: Generation models for a rotating ocean.* PhD. Thesis, Netherlands Institute for Sea Research (NIOZ), Texel, 1994.

[33] New A.L. Internal tidal mixing in the bay of biscay. *Deep Sea Research*, 35(5):691–709, 1988.

[34] Lamb K.G. Numerical experiments of internal wave generation by strong tidal flow across a finite amplitude bank edge. *Journal of Geophysical Research, Copyright by the American Geophysical Union*, 99(C1):843–864, January 1994.

[35] LeBlond P.H. and Mysak L.A. *Waves in the Ocean*. Elsevier Scientific Publishing Company, New York, 1989.

[36] Gill Adrian E. *Atmosphere-Ocean Dynamics*, volume 30. Academic Press, International Geophysics Series, London, 1982.

[37] Landau L.D. and Lifshitz A. *Hydrodynamics*. Nauka, Moscow (in russian), 1988.

[38] Butkov E. *Física Matemática*. Editora Guanabara, Rio de Janeiro, 1988.

[39] Apel J., Orr. M., Finette S., , and Lynch J. A new model for internal solitons and tides on the continental shelf. In *Shallow-Water Acoustics: Proceedings of the SWAC'97 Conference*, editors Zhang R. and Zhou J., pages 219–225, China Ocean Pres, Beijing, April, 1997.

[40] Jackson J.F. A brief review of internal waves in the ocean. UCES report U96-7, Unit for Coastal and Estuarine Studies, University of Wales, Bangor, August 1996.

[41] Rodríguez O.C., Jesus S., Stephan Y., Démoulin X., Porter M., and Coelho E. Nonlinear soliton interaction with acoustic signals: focusing effects. *Journal of Computational Acoustics*, 8(2):347–363, 2000.

[42] Rodríguez O.C., Jesus S., Stephan Y., Démoulin X., Porter M., and Coelho E. Dynamics of acoustic propagation through a soliton wave packet: observations from the intimate'96

experiment. In *Experimental Acoustic Inversion Metods for Exploration of the Shallow Water Environments*, pages 1–18, Carvoeiro, Portugal, March 1999.

[43] Chen P., Ingram R.G., and Gan J. A numerical study of hydraulic jump and mixing in a stratified channel with a sill. In *Proceedings of the 3rd International Conference on Estuarine and Coastal Modelling*, editor Oak Brook, pages 119–133, Illinois, 1993.

[44] Tikhonov A.N. and Samarski A.A. *Mathematical Physics.* Ed. Mir, Moscow, 1972 (in russian).

[45] Urick R.J. *Principles of Underwater Sound.* McGraw-Hill, New York, 1983.

[46] Jensen F.B., Kuperman W.A., Porter M.B., and Schmidt H. *Computational Ocean Acoustics.* AIP Series in Modern Acoustics and Signal Processing, New York, USA, 1994.

[47] Butikov E.I. *Optics.* Vyshaya Shkola, Moscow (in russian), 1986.

[48] Porter M. *The KRAKEN normal mode program.* SACLANT UNDERSEA RESEARCH (memorandum), San Bartolomeo, Italy, 1991.

[49] Tolstoy I. *Ocean Acoustics: Theory and Experiment in Underwater Sound.* Ed. by the Acoustical Society of America, New York, 1987.

[50] Weinberg N.L., Clark J.G., and Flanagan R.P. Internal tidal influence on deep-ocean acoustic-ray propagation. *J. Acoust. Soc. America*, 56(2):447–458, August 1974.

[51] Dushaw B.D., Chester D.B., and Worcester P.F. A review of ocean current and vorticity measurements using long-range reciprocal acoustic transmissions. *Oceans'93*, pages 298–305, 1993. Reprint.

[52] Martin Lauzer F.R., Stephan Y., and Evennou F. Analysis of tomographic signals to retrieve tidal parameters. In *Proceedings of the 2nd European Conference on Underwater Acoustics*, pages 1035–1050, Copenhague, Denmark, 1994.

[53] Colosi J.A., Flatté M., and Bracher B. Internal-wave effects on 1000-km oceanic acoustic pulse propagation: Simulation and comparison with experiment. *J. Acoust. Soc. America*, 96(1):452–468, July 1996.

[54] Book P. and Nolte L.W. Narrow-band source localization in the presence of internal waves for 1000-km range and 25-hz acoustic frequency. *J. Acoust. Soc. America*, 101(3):452–468, March 1997.

[55] Jackson D.J. and Ewart T.E. The effects of internal waves on matched-field processing. *J. Acoust. Soc. America*, 96(5):2945–2955, November 1994.

[56] Stephan Y., Démoulin X., Folegot T., Jesus S., Porter M., and Coelho E. Intimate'96 data report. Internal Report No. 27/EPSHOM/CMO/DE/NP, SHOM/CMO, Brest, France, June 1997.

[57] Hamilton E.L. Sound velocity and related properties of marine sediments, north-pacific. *Journal of Geophysical Research*, 75(23):4423–4446, August 1970.

[58] Hamilton E.L. Compressional-wave attenuation in marine sediments. *Geophysics*, 37(4):620–635, August 1972.

[59] Boles F.A. Observations on attenuation and shear-wave velocity in fine-grained, marine sediments. *J. Acoust. Soc. America*, 101(6):3385–3397, June 1997.

[60] Folegot T., Stephan Y., Démoulin X., Jesus S., Porter M., and Coelho E. Intimate'96: Problème direct. Internal Report AGLB.B.TF/TF.97.564, SHOM/CMO, Brest, France, June 1996.

[61] Menke W. *Geophysical Data Analysis: Discrete Inverse Theory.* Academic Press, Inc, San Diego, California, 1989.

[62] Collins M.D. and Kuperman W.A. Focalization: Environmental focusing and source localization. *J. Acoust. Soc. America*, 90(3):1410–1422, September 1991.

[63] Rodríguez O.C., Jesus S., Stephan Y., Démoulin X., Porter M., and Coelho E. Internal tide acoustic tomography: reliability of the normal modes expansion as a possible basis for solving the inverse problem. In *Proc. of the 4th. European Conference on Underwater Acoustics*, pages 587–592, Rome, Italy, 21-25 September 1998.

[64] Rodríguez O.C. and Jesus S. Physical limitations of travel-time-based shallow water tomography. *J. Acoust. Soc. Am*, 6(108), December 2000.

[65] Caille W. et al. Overview of the joint china-us yellow sea'96 experiment. In *Shallow-Water Acoustics: Proceedings of the SWAC'97 Conference*, editors Zhang R. and Zhou J., pages 17–22, China Ocean Pres, Beijing, April, 1997.

[66] Field R. et al. The sesame experiments - the effects of internal solitons on acoustic propagation at the malin shelf. In *Shallow-Water Acoustics: Proceedings of the SWAC'97 Conference*, editors Zhang R. and Zhou J., pages 227–232, China Ocean Pres, Beijing, April, 1997.

[67] Ferla C.M., Porter M.B., and Jensen F.B. *C-SNAP: Coupled SACLANTCEN normal mode propagation loss model.* SACLANT UNDERSEA RESEARCH CENTRE (SM-274), La Spezia, Italy, 1993.

[68] Porter M., Jesus S., Stephan Y., Démoulin X., and Coelho E. Exploiting reliable features of the ocean channel response. In *Shallow-Water Acoustics: Proceedings of the SWAC'97 Conference*, editors Zhang R. and Zhou J., pages 17–22, China Ocean Pres, Beijing, April, 1997.

[69] Porter M., Jesus S., Stephan Y., Démoulin X., and Coelho E. Shallow-water tracking in the sea of nazaré. In *Proc. of the 1998 Symposium on Undersea Technology*, pages 29–34, Tokyo, Japan, April 1998.

[70] Porter M., Jesus S., Stephan Y., Démoulin X., , and Coelho E. Single-phone source tracking in a variable environment. In *Proc. of the 4th. European Conference on Underwater Acoustics*, pages 575–580, Rome, Italy, 21-25 September 1998.

[71] Porter M. and Tolstoy A. The matched field processing benchmark problems. *Journal of Computational Acoustics*, 2(3):161–184, 1994.

[72] Jesus S. M. Normal-mode matching localization in shallow water: Environmental and system effects. *J. Acoust. Soc. America*, 4(90):2034–2041, October 1991.

[73] Bienvenu G. and Kopp L. Source power estimation method associated with high resolution bearing estimator. *IEEE*, CH1610:153–156, 1981.

[74] Mauuary D., Bozinoski S., and Graffouiliere P. High resolution methods for signal parameter estimations in ocean acoustic tomography. In *Proc. of the 3rd. European*

Conference on Underwater Acoustics, pages 815–820, Heraklion, Crete, Greece, 24-28 June 1996.

[75] Jesus S. M. A mode subspace approach for source localization in shallow water. *Signal Processing, Elsevier*, (28):117–122, 1992.

[76] Jesus S., Porter M., Stephan Y., Démoulin X., Rodríguez O.C., and Coelho E. Single hydrophone source localization. *IEEE Journal of Oceanic Engineering*, 25(3), July 2000.

[77] Jesus S., Porter M., Stephan Y., Coelho E., Rodríguez O.C., and Démoulin X. Single sensor localization in a range-dependent environment. In *Proceedings of the Oceans 2000 MTS/IEEE Conference and Exhibition*, Providence, Rhode Island, USA, September 11-14 2000.

[78] Wax M. and Kailath T. Detection of signals by information theoretic criteria. *IEEE Transactions on Acoustic Speech and Sigal Processing*, ASSP-33(2):387–392, April 1985.

[79] Diachok O. and Karangelen C. Experimental demonstration of sound-speed inversion with matched-field processing. *J. Acoust. Soc. America*, 93(5):2649–2655, May 1993.

[80] Baggeroer A.B., Kuperman W., and Mikhalevsky. An overview of matched field methods in ocean acoustics. *IEEE Journal of Oceanic Engineering*, 18(4):307–338, October 1993.

[81] Jesus S. M. Broadband matched-field processing of transient signals in shallow water. *J. Acoust. Soc. America*, 4(93):1841–1850, April 1993.

[82] Holland J. Adaptation in natural and artificial systems. Technical report, University of Michigan Press, 1975.

[83] Lotsberg O. and Jesus M. Matched field inversion of geoacoustic properties from towed array data in shallow water. In *Proc. of the 3rd. European Conference on Underwater Acoustics*, pages 601–606, Heraklion, Crete, Greece, 24-28 June 1996.

[84] Gingras D. and Gerstoft P. Inversion for geometric parameters in shallow water: Experimental results. *J. Acoust. Soc. America*, 97(6):3589–3598, June 1995.

[85] Soares C., Waldhorst A., and Jesus S. Matched field processing: Environmental focusing and source tracking with application to the north elba data set. In *Proc. of the Oceans'99 MTS/IEEE conference*, pages 1598–1602, Seattle, Washington, 13-16 September 1999.

[86] Gerstof P. *SAGA User Manual 3.0: An inversion software package.* SACLANT UNDERSEA RESEARCH CENTRE, La Spezia, Italy, 1999.

[87] Jensen F.B. and Ferla C.M. *SNAP: The SACLANTCEN normal-mode acoustic propagation model.* SACLANT UNDERSEA RESEARCH CENTRE (SM-121), La Spezia, Italy, 1979.

[88] Skarsoulis E.K, Athanassoulis, and U. Send. Ocean acoustic tomography based on peaks arrivals. *J. Acoust. Soc. America*, 100(2):797–813, August 1996.

[89] Skarsoulis E.K. A matched-peak inversion approach for ocean acoustic travel-time tomography. *J. Acoust. Soc. America*, 107(3):1324–1332, March 2000.

[90] Scheid F. *Análise Numérica.* McGraw-Hill, 2a. edição, Lisboa, Portugal, 1991.

Appendix I

Numerical solution of the Sturm-Liouville Problem

The particular cases of the Sturm-Liouville Problem discussed in sections 2.3.1 and 2.3.2 can be solved by substituting the respective differential equation, with a linear system of algebraic equations, leading to a classical (and simpler) problem of finding a set of eigenvectors and eigenvalues [90]. That substitution is described in this appendix.

First, by introducing the following notation:

$$\begin{array}{l} x = z \ , \quad y = \Psi_m \ , \\ a = 0 \ , \quad b = D \ , \end{array} \quad \lambda = \begin{cases} C_m^{-2} \\ \\ (k_h^2)_m \end{cases} , \ f(x) = \begin{cases} N^2 \\ \\ \dfrac{N^2 - \tilde{\omega}^2}{\tilde{\omega}^2 - f_c^2} \end{cases} , \tag{A.I.1}$$

one can rewrite any of the equations Eq.(2.14) or Eq.(2.24) in the form:

$$\frac{d^2 y}{dx^2} + \lambda f(x) y = 0 \ . \tag{A.I.2}$$

Furthermore, the boundary conditions can be written, in a general form, as

$$\alpha_1 y(a) + \beta_1 \left. \frac{dy}{dx} \right|_{x=a} = 0 \ , \quad \text{and} \quad \alpha_2 y(b) + \beta_2 \left. \frac{dy}{dx} \right|_{x=b} = 0 \ . \tag{A.I.3}$$

By discretizing the values of the independent variable:

$$x_j = jh + a \ , \ h = \frac{b-a}{N+1} \ , \quad \text{with} \quad j = 0, 1, 2, \ldots, N+1 \ , \tag{A.I.4}$$

approximating the second order derivative, within the grid $\{x_j\}$, using finite differences:

$$\left.\frac{d^2y}{dx^2}\right|_{x=x_j} \approx \frac{y_{j+1} - 2y_j + y_{j-1}}{h^2} \ , \tag{A.I.5}$$

discretizing the values of the linear term:

$$\lambda f(x)y|_{x=x_j} = \lambda f(x_j)y_j = \lambda f_j y_j \ , \tag{A.I.6}$$

and approximating the boundary conditions, Eq.(A.I.3), as

$$\alpha_1 y_0 + \beta_1 \frac{y_1 - y_0}{h} = 0 \ , \quad \text{and} \quad \alpha_2 y_{N+1} + \beta_2 \frac{y_{N+1} - y_N}{h} = 0 \ , \tag{A.I.7}$$

it is possible to obtain the following system of linear equations:

$$y_{j-1}\left(\frac{1}{h^2}\right) + y_j\left(-\frac{2}{h^2}\right) + y_{j+1}\left(\frac{1}{h^2}\right) = -y_j \lambda f_j \ . \tag{A.I.8}$$

For the particular cases $j = 1$ e $j = N + 1$, and taking into account the pair of equations Eq.(A.I.7) one can obtain that

$$y_1\left(\frac{1}{h^2}\right)\left(\frac{-\beta_1}{\alpha_1 h - \beta_1} - 2\right) + y_2\left(\frac{1}{h^2}\right) = -y_1 \lambda f_1 \ , \tag{A.I.9}$$

and

$$y_{N-1}\left(\frac{1}{h^2}\right) + y_N\left(\frac{1}{h^2}\right)\left(\frac{\beta_2}{\alpha_2 h + \beta_2} - 2\right) = -y_N \lambda f_N \ . \tag{A.I.10}$$

As one can see from the last pair of equations the particular choice of boundary conditions $\alpha_1 h - \beta_1 = 0$, or $\alpha_2 h + \beta_2 = 0$, will *apriori* make it impossible to find a numerical solution of Eq.(A.I.2). By introducing the vector $\mathbf{y} = [\ y_1\ y_2\ y_3\ \dots\ y_N\ ]^{\mathsf{t}}$ one can write the system of linear equations (A.I.8) in the following compact form:

$$\mathbf{Ay} = \lambda \mathbf{By} \ , \tag{A.I.11}$$

where the only non-zero elements of matrices $\mathbf{A}$ and $\mathbf{B}$ are

$$a_{11} = \frac{1}{h^2}\left(\frac{-\beta_1}{\alpha_1 h - \beta_1} - 2\right) \ , \ a_{12} = \frac{1}{h^2} \ ,$$

$$a_{j-1,j} = \frac{1}{h^2}\ ,\ a_{jj} = -\frac{2}{h^2}\ ,\ a_{j,j+1} = \frac{1}{h^2}\ , \tag{A.I.12}$$
$$a_{N-1,N} = \frac{1}{h^2}\ ,\ a_{NN} = \frac{1}{h^2}\left(\frac{\beta_2}{\alpha_2 h + \beta_2} - 2\right)\ ,$$

and

$$b_{jj} = -f_j\ . \tag{A.I.13}$$

The solution of Eq.(A.I.11) corresponds to a general case of finding the eigenvectors $\mathbf{y}$, and eigenvalues, λ, of the matrices $\mathbf{A}$ and $\mathbf{B}$. This problem can be efficiently solved using MATLAB built-in functions.

Appendix II

Publications

Proceedings of the Fourth European Conference on Underwater Acoustics
Edited by A. Alippi and G.B. Cannelli
Rome, 1998

INTERNAL TIDE ACOUSTIC TOMOGRAPHY: RELIABILITY OF THE NORMAL MODES EXPANSION AS A POSSIBLE BASIS FOR SOLVING THE INVERSE PROBLEM

O.C. Rodríguez[1], S. Jesus[1], Y. Stephan[2], X. Démoulin[2], M. Porter[3] and E. Coelho[4]

[1]UCEH-Universidade do Algarve (UALG), Campus de Gambelas, 8000, Faro, Portugal
[2]EPSHOM/CMO (SHOM), BP426, F-29275, Brest, France
[3]New Jersey Institute of Technology (NJIT), Newark, NJ 07102, USA
[4]Instituto Hidrográfico (IH), 1296, Lisbon, Portugal

Abstract: *Using hydrodynamic and thermodynamic equations appropriate for modelling internal tides, one can predict the current and temperature distributions associated with the ocean's dynamic modes. Comparing such predictions with observations from the INTIMATE'96 experiment, we find a high degree of correlation between the first 3 theoretically calculated dynamic modes and corresponding empirical orthogonal functions (EOF's) derived from an ensemble of temperature and current profiles. The implications are twofold. First, this implies that the dominant variability in the INTIMATE'96 experiment is indeed associated with internal tides. Secondly, it suggests that in future tidal experiments a theoretically generated basis may be used as effectively as an EOF basis (which requires more extensive oceanographic measurements). We have also used the set of dynamic modes to simulate the effect of the tides on acoustic propagation to understand the relative importance of the usual surface tide (barotropic) and the internal (baroclinic) tides.*

1 INTRODUCTION

Possible applications of OAT for inversion of the internal tide field have not been considered till the present time, despite the large amount of references related to the influence of internal tides on acoustic signals and simulations of underwater propagation through an internal wave field (see [1] for a particular analysis and a list of publications). Most of the studies consider as starting assumptions that: 1)the statistical distribution of the internal modes follows the GarrettMunk spectrum, and 2)the perturbations on sound velocity (and hence on temperature) can be represented as an orthogonal decomposition on the basis of dynamic normal modes (hereafter simply normal modes) of the internal wave. Both approximations simplify significantly the solution of the inverse problem and seem to offer a good description of acoustical propagation in deep water scenarios. However, the validity of those assumptions becomes dubious when applied to sound propagation in the continental shelf. A key complication is the affect of the tides which leads to an internal wave spectrum with strong peaks at the tidal frequencies. In addition, the internal waves are often of large amplitude leading to nonlinear effects and associated solitons or bores.

To understand these issues more completely an experiment called INTIMATE'96 (INternal Tide Investigation by Means of Acoustic Tomography Experiment) was conducted off the coast of Portugal. Oceanographic measurements conducted during the experiment have enabled us to perform a detailed analysis of hydrodynamic and thermodynamical equations governing the internal tides. As will be shown in the following sections the resulting current and temperature modes provide a detailed description of the internal tide and offer a reliable set of normal modes for oceanographic inversion.

2 THEORETICAL BACKGROUND

Internal tides are a particular case of internal waves of tidal frequency and generated by the interaction of the surface (barotropic) tide with bottom topography. The coupling mechanism remains poorly understood; however, the internal tides are generally most strongly excited at a sharp bathymetric feature such as as a sea mount or at the continental shelf-break. The main consequence of this interaction is the oscillation of the thermocline with the tidal period. However, the internal tides also have a surface manifestation. They cause very small displacements of the ocean level that can be measured by satellite altimeters. In addition they circulate organic surfactants disturbing the surface reflectivity at both optical and radio bands and revealing their banded structure.

The hydrodynamic equations for baroclinic currents [2], in the case of internal planewave propagation, can be solved by an eigenfunction expansion using a basis of functions, Ψj, and their derivatives, $\phi_j = d\Psi j/dz$, in the following way:

$$(u, v) = \sum_j (u_j, v_j)\phi_j \exp\left[i\left(k_x^j x + k_y^j y - \omega t\right)\right] \tag{1}$$

$$w = \sum_j wj\Psi_j \exp\left[i\left(k_x^j x + k_y^j y - \omega t\right)\right] \tag{2}$$

where ω corresponds to the tidal frequency. The eigenfunctions Ψ_j can be obtained by solving the standard differential equation for internal waves (see [2],p.223). Similar expansions can be used for pressure and density perturbations. From a 'geometrical' point of view the given set of expansions can be considered as projections of currents onto two different bases of eigenfunctions: w is projected onto the orthogonal basis formed by functions Ψ_j and (u, v) onto the corresponding basis of functions ϕ_j.

The wavenumber components are related to the direction of internal tide propagation θ through the relationships:

$$k_x^j = k_h^j \cos\theta \ , \ k_y^j = k_h^j \sin\theta \ ,$$

where k_h^j is the eigenvalue of the jth normal mode ($k_h^j < k_h^{j+1}$) and its inverse is proportional to the modal wavelength. Vertical stratification of the environment is represented in the differential equation for Ψ_j through the buoyancy frequency $N^2(z)$, which is normally related to mean density. For inversion it is better to use the alternative relationship

[2]

$$N^2 = g\left[a_T\frac{dT_0}{dz} + a_T^2\frac{gT_0}{C_{ps}} - a_s\frac{ds}{dz}\right] \ , \tag{3}$$

where $a_T = 2.4110^{-4}\,(°\mathrm{C})^{-1}$ and $C_{ps} = 3994\ \mathrm{J(kg°C)}^{-1}$. Usually the salinity depends weakly on depth so we can neglect the salinity term and develop a buoyancy profile that depends only on the temperature. Thus, the temperature profile provides a critical piece of information. It allows us to calculate the buoyancy profile and thereby the dynamical modes. The dynamical modes themselves are characterized in terms of their spatial and temporal scales and provide a suitable basis for expressing the ocean structure in terms of density, currents, and pressure. Nevertheless, from a tomographic point of view, the system of Eqs.(1)-(2) does not provide a dynamical basis for expanding the sound speed field. To address this, recall the thermodynamical equation [2]:

$$\frac{D}{Dt}\left(\rho c_v T\right) = \nabla\left(k_T \nabla T\right) + Q_T \tag{4}$$

where c_v denotes the specific heat at constant volume, k_T the thermal conductivity and Q_T represents all sources and sinks of heat. An approximate solution for temperature perturbations,

$$T - T_0(z) = \frac{dT_0}{dz}\sum_j T_j \Psi_j \exp\left[i\left(k_x^j x + k_y^j y - \omega t\right)\right] \tag{5}$$

can be obtained in the case of k_T, $Q_T = 0$ and assuming ρ and c_v are constant. This solution provides a physical relationship between the temperature field and the basis of normal modes; the orthogonal expansion for temperature (and hence for sound velocity) follows automatically from Eq.(5) when the temperature gradient depends weakly on depth.

3 COMPARISON WITH EXPERIMENTAL DATA

During the INTIMATE'96 experiment [3] an intensive survey of thermistor, CTD, XBT and ADCP data was conducted at the Vertical Array (VLA), and along two transmission legs, one due north and one due west of the array (see Fig.1(a)). Received signals were later correlated with an estimate of the transmitted waveform and then aligned and averaged over 10 transmissions (about 1 minute) to increase the signaltonoise ratio. The experiment was conducted near the shelf break were the internal tides tend to be strongest.

Both sets of normal modes and their derivatives (Fig.1(b)) were obtained from the mean profile of temperature at the VLA. The correlation between theoretical and empirical functions is shown in Fig.2(a) and Fig.2(b) for currents and temperature respectively. The correlation coefficients were estimated by expanding current and temperature EOF's onto corresponding bases of theoretical functions as follows:

$$EOF_l^{(u,v)} \approx \sum a_{lm}\phi_m \ , \ EOF_l^T \approx \frac{dT_0}{dz}\sum b_{lm}\Psi_m$$

where (u, v) is the horizontal current and T is the temperature. Since the basis is orthogonal, the coefficients in the above expansions are easily calculated by inner products. The results presented in Fig.2 reveal a strong correlation between empirical and corresponding theoretical eigenfunctions up to mode 3. This result is very significant since it indicates that every theoretical function from the given set is equivalent to the correspondent EOF. Furthermore, the quantity and resolution of empirical functions depends on the number and resolution of measured profiles, while all the theoretical functions can be obtained from a coarse estimate of the mean temperature distribution and still provide a detailed description of the internal tide.

In a simple model, the internal tides propagate like plane waves. Thus, we can also use the dynamical modes to estimate the direction of propagation of the internal tide by looking at how the modal amplitudes at two different locations are shifted with respect to each other. (A similar approach was applied in Ref.[4] using isotherms in the INTIMATE'96 experiment.) Calculated amplitudes of modal oscillations for u and v are shown in Fig.3(a). The time shift for every pair of modal oscillations was estimated by looking at maximizing the peak in crosscorrelations between coefficients at two different stations. The lags associated witht the first three modes were 2, 3, and 3 hours respectively giving a mean lag of 2.7 hours. Figure 3(b) allows us to convert this time lag to an angle of propagation yielding $\theta \approx 15°$. This is in close agreement with a theoretical prediction based on the orientation of the shelf break. These results are further supported in studies of the temperature coefficients at different stations.

4 ACOUSTIC SIMULATIONS AND REAL TRANSMISSIONS

The acoustic data taken in INTIMATE'96 shows a clear tidal cycle; however, since both the surface tide and the internal tides have the same temporal frequency it is not readily obvious which component is driving the acoustic perturbations. To study this further, we use the dynamical modes together with surface tide predictions, to calculate temperature and sound velocity distributions. We then simulate the impact of both barotropic and baroclinic tides on acoustic transmissions.

These simulations were performed with the KRAKEN model [5] for the lower hydrophone of the VLA located at 115 m depth, and suggest that the surface tide introduces periodic oscillations of the later groups of arrivals (Fig.4(a)) but not the early arrivals (Fig.4(c)). This situation changes when the internal tide is included in theoretical fields of temperature and sound speed as shown in Fig.4(d). Received transmissions from the INTIMATE'96 experiment show such oscillations of late arrivals (Fig.4(b)) and confirm the simulated effects of the surface tide on received signals [3]. Since the received transmissions are aligned by their leading edge, the analysis of initial arrivals did not support (or contradict) the prediction related to the internal tide. Nevertheless the given set of simulations provided a clear distinction of barotropic and internal tide perturbations on received signals.

5 CONCLUSIONS

On the basis of this analysis the following conclusions can be drawn: 1)the buoyancy profile (which characterizes the waveguide stratification) can be properly obtained from mean temperature distribution; 2)theoretical normal modes can be accurately calculated from above mentioned buoyancy profile; 3)both sets of normal modes and normal mode

(a) (b)

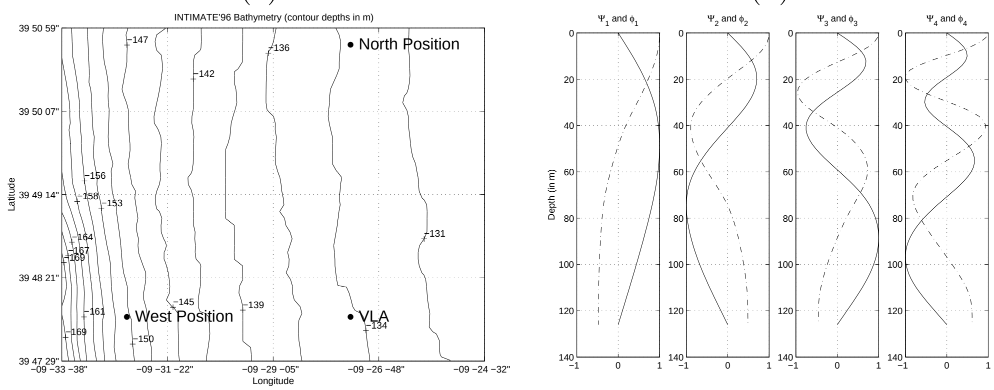

Figure 1: *(a)* Bathymetry of the INTIMATE'96 experiment; *(b)* temperature-derived normal modes (continuous line) and their derivatives (dott-dashed line).

(a) (b)

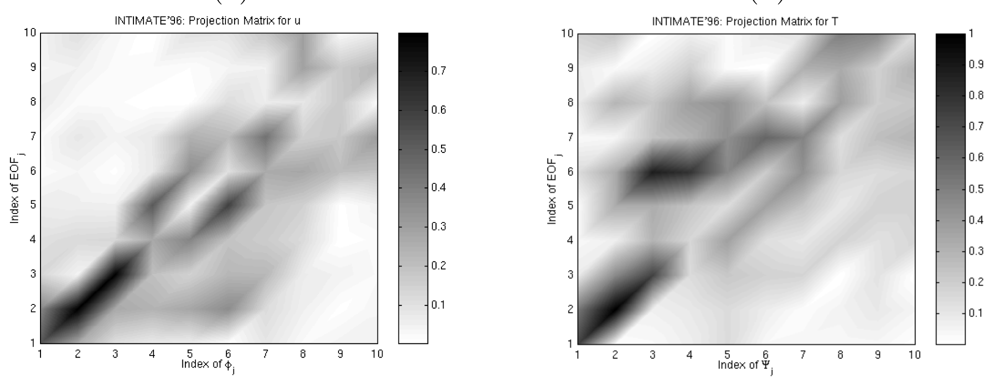

Figure 2: Correlation matrices for u *(a)* and temperature *(b)*.

(a) (b)

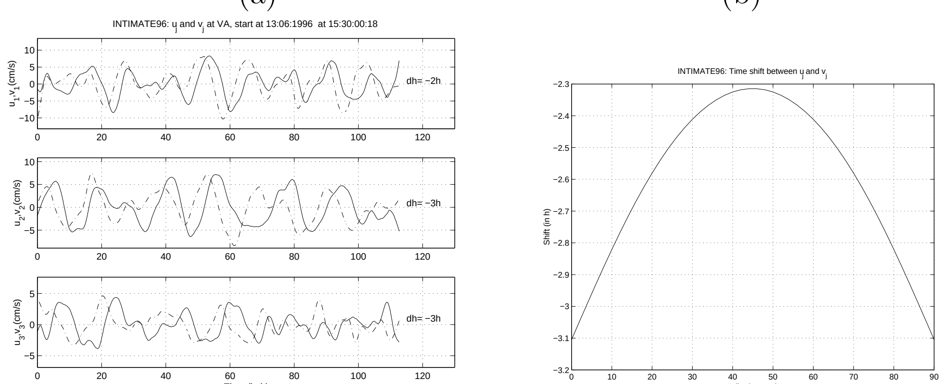

Figure 3: *(a)* Modal amplitudes for u (continuous line) and v (dott-dashed line); *(b)* theoretical dependence of phase shift on θ (note the time shift at $\theta = 15°$).

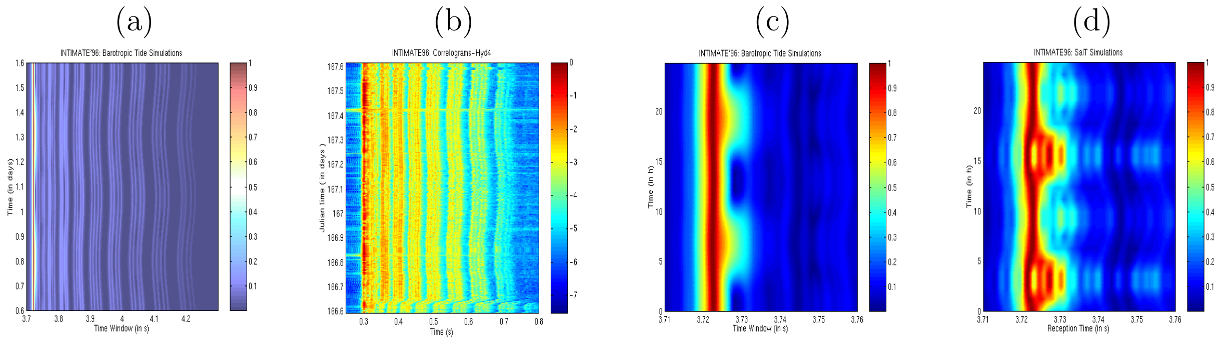

Figure 4: *(a)* Simulated arrival patterns for the surface tide and *(b)* real transmissions from the INTIMATE'96 experiment; zoom on initial peaks for surface tide *(c)* and both surface and internal tides *(d)*.

derivatives offer a detailed description of the internal tide, in particular through expansions of temperature and currents on corresponding basis of normal modes and normal mode derivatives, respectively; 4)the set of theoretical normal modes (and normal mode derivatives) is highly correlated with EOF's of temperature and current data, up to mode 3; 5)this set of normal modes can be used to generate physically consistent fields of temperature and sound velocity; 6)acoustic simulations based on such fields allow one to clearly distinguish the effects of both barotropic and internal tides on underwater acoustic transmissions by revealing oscillations of late and early arrivals; such oscillations can be seen for the case of the surface tide in real data from the INTIMATE'96 experiment.

REFERENCES

[1] Simmean J., Flatté S.M., and Wang G. Wavefront folding, chaos, and diffraction for sound propagation through ocean internal waves. *J. Acoust. Soc. America*, 102(1):239–255, July 1997.

[2] Apel J.R. *Principles of Ocean Physics*, volume 38. Academic Press, International Geophysics Series, London, 1987.

[3] Démoulin X., Stéphan Y., Jesus S., Coelho E., and Porter M. Intimate'96: A shallow water tomography experiment devoted to the study of internal tides. In Zhang R. and Zhou J., editors, *Proceedings of the Shallow Water Acoustics Conference (SWAC'97)*, pages 485–490, Beijing, April 1997.

[4] Folégot T. Intimate'96: Probl'eme direct. R'ef'erence aglb tf tf.97.564, Centre Militaire d'Oceanographie, Atlantide Grenat Logiciel, F29200 Brest, Juin 1997.

[5] Porter M. The kraken normal mode program. (sm245), SACLANT UNDERSEA RESEARCH CENTRE, La Spezia, Italy, 1991.

Journal of Computational Acoustics, Vol.8, No.2(2000) 347-363

NONLINEAR SOLITON INTERACTION WITH ACOUSTIC SIGNALS: FOCUSING EFFECTS

O.C. RODRÍGUEZ and S. JESUS
UCEH-Universidade do Algarve, Campus de Gambelas, 8000, Faro, Portugal

Y. STEPHAN and X. DEMOULIN
EPSHOM/CMO, BP426, F-29275, Brest, France

M. PORTER
Science Applications International Corp., San Diego, USA

E. COELHO
Instituto Hidrográfico, 1296, Lisboa, Portugal

Received 6 August 1999
Revised 11 January 2000

The problem of nonlinear interaction of solitary wave packets with acoustic signals has been intensively studied in recent years. A key goal is to explain the observed transmission loss of shallow-water propagating signals, which has been found to be strongly time-dependent, anisotropic, and sometimes exhibited unexpected attenuation vs. frequency. Much of the existing literature considers the problem of signal attenuation in a static environment, without considering additional effects arising from groups of solitons evolving both in range and time. Hydrographic and acoustic data from the INTIMATE'96 experiment clearly exhibit the effects of soliton packets. However, in contrast with reported observations of signal attenuation, the observed transmission loss shows a pronounced signal enhancement that behaves like a focusing effect. This focusing is correlated with peaks in current, temperature, and surface tide. That correlation suggests that the nonlinear interaction of solitary wave packets with acoustic signals can lead to a focusing of the signal. To clarify this issue, hydrographic data was used to generate physically consistent distributions of "soliton-like" fields of temperature and sound velocity. These distributions were then used as input for a range-dependent normal-mode model. The results strongly support the hypothesis that the soliton field causes the observed signal enhancement.

1. Introduction

Naturally generated solitons can often be observed in coastal zones as a result of nonlinear interaction of the surface tide with the continental shelf. Acoustic propagation through such Solitary Wave Packets (SWPs) has been intensively studied in recent years (see for instance Refs. 1 and 2). These SWPs have often been identified as the main cause of abnormal signal attenuations. Most of the studies analysed the problem of acoustic propagation through SWPs from a "static" point of view, since they did not consider the effects of SWPs that evolve in both range and time. A detailed analysis of current, thermistor, and acoustic data from the INTIMATE'96 experiment[3] reveals SWPs propagating across the experimental site. An interesting feature of the acoustic data, is an increase of signal amplitude which is clearly correlated with peaks in current, temperature, and surface tide. This increase of amplitude can be seen as a sort of focusing effect. To determine if this effect could be the result of acoustic propagation through a "dynamic" SWP, the hydrographic data from the experiment was used to develop physically consistent distributions of range-dependent "soliton-like" fields of temperature and sound speed. These were then given as input to an acoustic propagation model. The simulation results strongly support the assumption that a SWP was responsible for the observed signal focusing.

This paper is organized as follows: Sec. 2 presents a brief theoretical background of soliton propagation; this background simplifies the analysis of hydrographical data from the INTIMATE'96 experiment, which is described in Sec. 3. The acoustic data, correlated with hydrographic data from the previous section, is discussed in Sec. 4 and it is followed by corresponding acoustic simulations. The main conclusions of the paper are presented in Sec. 5.

2. Theoretical Background

The starting point for the analysis of soliton propagation in a rotationless environment with complex stratification is the so-called *Korteweg-de Vries* equation (hereafter simply KdV) for modal vertical displacement η_m[4,5] :

$$\frac{\partial \eta_m}{\partial t} + C_m \frac{\partial \eta_m}{\partial x} + \alpha_m \eta_m \frac{\partial \eta_m}{\partial x} + \beta_m \frac{\partial^3 \eta_m}{\partial x^3} = 0 \tag{2.1}$$

where

$$\alpha_m = \frac{3}{2} s \frac{C_m}{D} \quad , \quad \beta_m = \frac{1}{2} d D^2 C_m \quad , \tag{2.2}$$

$$s = D \frac{\langle \phi_m^3 \rangle}{\langle \phi_m^2 \rangle} \quad , \quad d = \frac{1}{D^2} \frac{\langle \Psi_m^2 \rangle}{\langle \phi_m^2 \rangle} \quad , \tag{2.3}$$

$$\frac{d^2 \Psi_m}{dz^2} + \frac{N^2}{C_m^2} \Psi_m = 0 \ , \ \phi_m = \frac{d\Psi_m}{dz} \ , \ \Psi_m(0) = \Psi(D) = 0 \ , \ \langle \phi_m \phi_n \rangle = \left\langle N^2 \Psi_m \Psi_n \right\rangle = 0 \ , \tag{2.4}$$

N is the buoyancy frequency, D is the water depth, x corresponds to the axis of propagation, $\langle \ \rangle$ is an "inner product" defined as

$$\langle \ \ldots \ \rangle = \int_0^D \ \ldots \ dz \ , \tag{2.5}$$

and Ψ_m and ϕ_m are the Hydrostatic Normal Modes (hereafter HNMs) of the corresponding linear rotationless form of the hydrodynamic equations. In contrast with the corresponding equation for a homogeneous fluid[6], which admits a single soliton generation, it follows from Eq.2.1 that by combining both nonlinear and stratification effects it is possible to obtain an entire set of "modal" solitons with characteristics that depend on HNMs. Whether or not this explains the observations of propagating SWPs depends on the properties of the HNMs.

2..1 *The "Sech" solution*

For displacements having large enough amplitudes and steepness, the KdV equation admits the well-known soliton solution[7]

$$\eta_m = \eta_m^0 \mathrm{sech}^2\left(\frac{x - \mathcal{C}_m t}{\Delta_m}\right) \ , \tag{2.6}$$

where η_m^0 represents the peak amplitude of the modal soliton, which has a nonlinear characteristic width

$$\Delta_m = \sqrt{\frac{12\beta_m}{\alpha_m \eta_m^0}} \ , \tag{2.7}$$

and propagates with a nonlinear phase speed given by

$$\mathcal{C}_m = C_m + \frac{\alpha_m \eta_m^0}{3} \ . \tag{2.8}$$

As seen from the above equations Δ_m is inversely proportional to the amplitude of the modal soliton, whereas $\mathcal{C}_m$ is linearly proportional to η_m^0; the implication is that the larger η_m^0, the faster the soliton propagates and the narrower or steeper the soliton is.

2..2 *The "Dnoidal" Solution*

Another solution to the KdV equation is[7]

$$\eta_m = \eta_m^0 \left[2\mathrm{dn}^2_{(m,\mathsf{S})}\left(\frac{x - \mathcal{C}_m t}{\Delta_m}\right) - (1 - \mathsf{S}^2)\right] \ , \tag{2.9}$$

where the index S is a function of the normalized variable $\tau = x/C_m t$ and $\mathrm{dn}_{\mathsf{S}}(\varphi)$ is the "dnoidal" Jacobi elliptic function. The shapes of the "dnoidal" solution agree well with the backscattered profiles measured from SAR images[5,8] . As $\mathsf{S} \to 1$ the above expression becomes the "sech" profile. From a dynamical point of view there are significant differences between this and the previous type of solutions: Eq.2.6 describes a SWP with a *single* modal soliton, which propagates in time and space without deforming its shape (see Fig. 1(a)). In contrast, Eq.2.9 describes a perturbation with an evolving profile (see Fig. 1(b)), resembling the evolution of soliton packets. The number of solitons within a packet depends on the values of τ and S. The importance of this point will be discussed in Sec. 4 when performing the acoustic simulations.

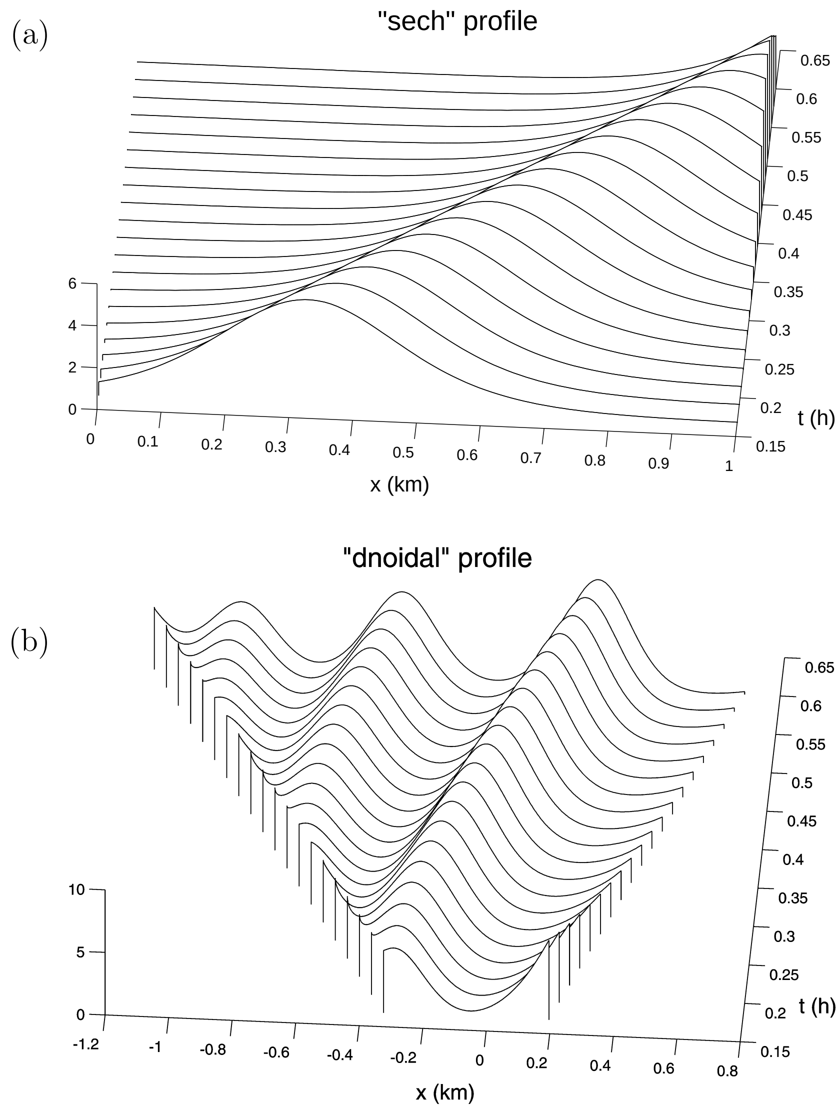

Fig. 1: Spatial and temporal evolution of soliton modal displacement η_1, for a "sech" profile (a), and for a "dnoidal" profile (b). Soliton parameters are $\eta_1^0 = 5$ m, $\Delta_1 = 196$ m and $\mathcal{C}_1 = 54.2$ cm/s (values taken from Ref.7).

2..3 *Temperature perturbations*

It follows from hydrodynamic coupled equations for horizontal currents and displacement[4] that the horizontal components of fluid velocity depend linearly on vertical soliton displacement. Nevertheless, from a tomographic point of view, the system of hydrodynamic equations does not provide a physical basis for expanding the temperature field, and thus the sound-speed field. To address the tomographic issue, let us recall the thermodynamic equation[9]

$$\frac{D}{Dt}\left(\rho C_v T\right) = \nabla\left(k_T \nabla T\right) + Q_T \ , \tag{2.10}$$

where C_v denotes the specific heat at constant volume, k_T is the thermal conductivity, and Q_T represents all sources and sinks of heat. Linearizing and solving this differential equation (see the appendix) one obtains:

$$T \approx T_0(z) + \frac{dT_0}{dz}\sum_m T_m \eta_m \Psi_m \ , \tag{2.11}$$

which shows that the vertical structure of temperature is related to the HNM Ψ_m (in contrast with horizontal currents, which depend only on ϕ_m). The horizontal dependence remains linearly related to the vertical displacement and this approximation becomes linear when $dT_0/dz \approx$constant.

The theoretical description of soliton propagation will be used in the following section to understand the current and temperature features found in hydrographic records from the INTIMATE'96 experiment.

3. Experimental Data

The INTIMATE'96 experiment[3,10] performed during June 1996, North of Lisbon (see Fig. 2) involved the collaboration of the following institutions: the Universidade do Algarve (UALG), Faro, the Instituto Hidrográfico (IH), Lisbon (both from Portugal), and the Centre Militaire Oceanographique (SHOM), Brest, France. The project team received also support from the Saclant Undersea Research Centre (SACLANTCEN), La Spezia, Italy, which lent the Vertical Linear Array (hereafter VLA). The experiment was conceived with the main goal of applying ocean acoustic tomography to the detection and inversion of the internal tide. The French oceanographic vessel BO'DENTRECASTEAUX towed an acoustic source at 90 m depth, which emitted linear frequency-modulated chirps sweeping from 300-800 Hz with a 2-second duration. The transmissions were repeated every 8 seconds, then received on the 4-hydrophone VLA and telemetered back to the Portuguese vessel NRP ANDROMEDA. The hydrophones were located at 35, 70, 105 and 115 m depth. Signal transmissions were performed from north and west positions (see Fig. 2), along range-independent and range-dependent acoustic tracks, respectively, with corresponding distances of approximately 5.6 and 6.4 kms. The bottom compressional speed and attenuation were estimated from coring measurements as 1750 m/s and 0.9 dB/wavelength, respectively. During the experiment an intensive survey of thermistor, CTD, XBT and ADCP data was performed near the position of the VLA and at the source location. This allowed for the calculation of Empirical Orthogonal Functions (hereafter EOFs, see Fig. 3) and HNMs (see Fig. 4), and a high degree of correlation was found between both sets of functions.[10]

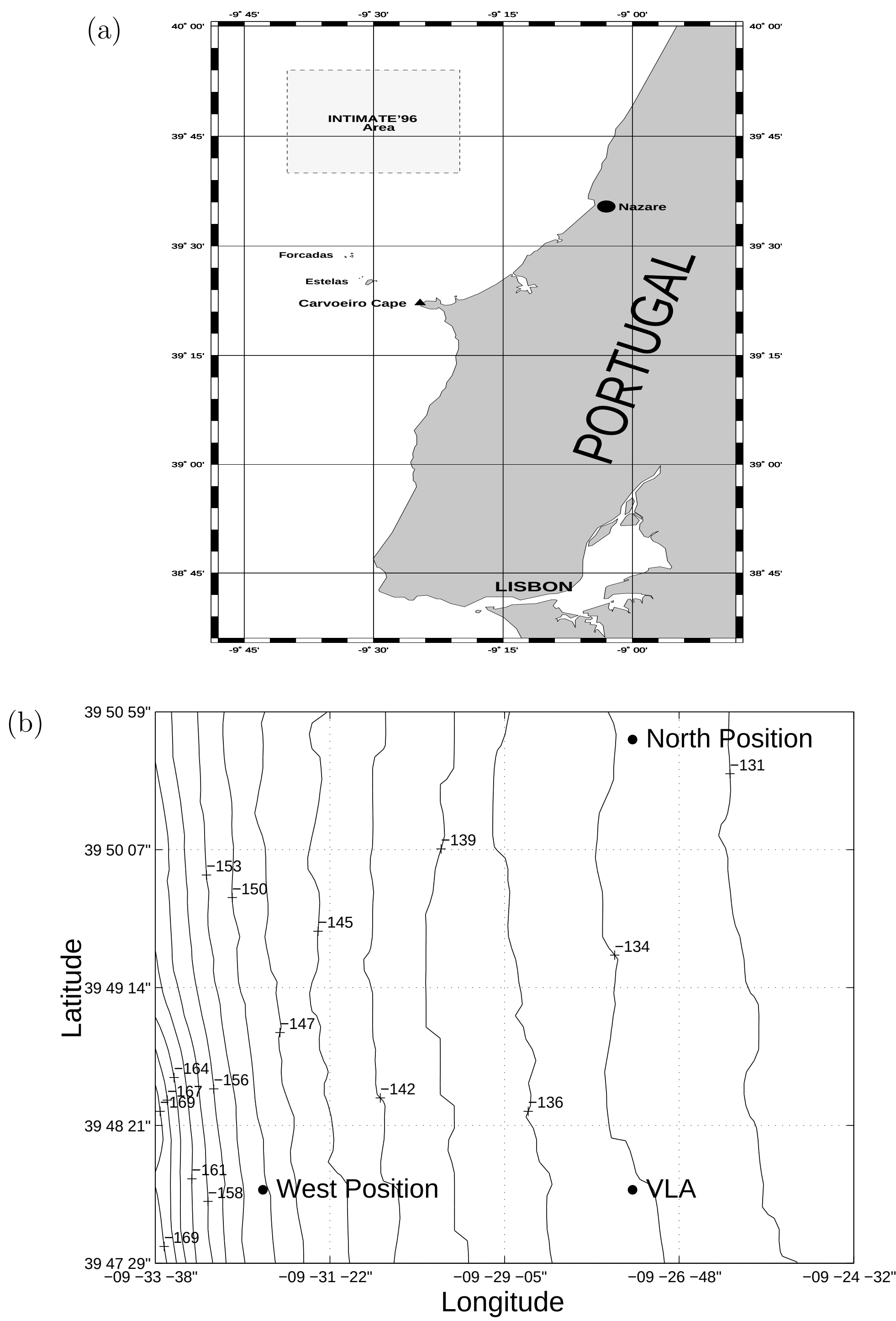

Fig. 2: Chosen area of the INTIMATE'96 experiment (a) and bathymetry of the experimental site (b) (contour depths in m).

(a)

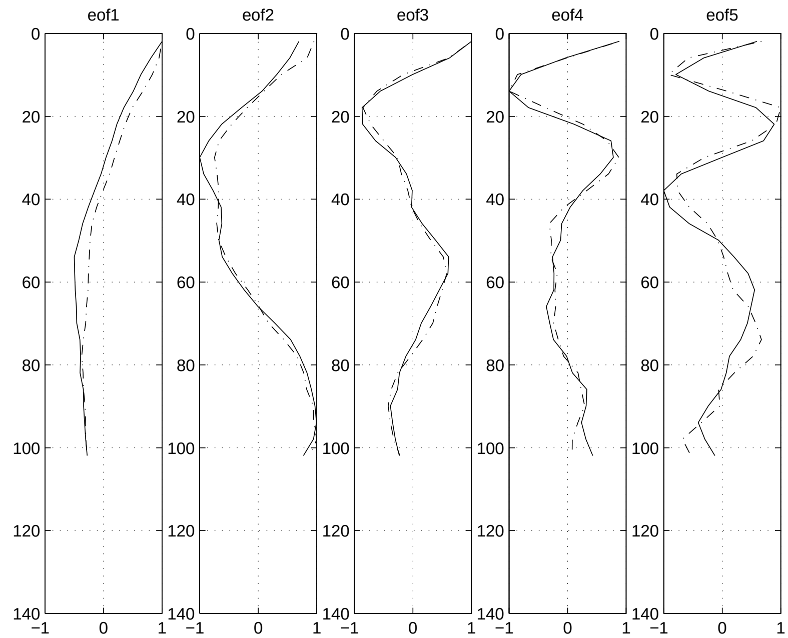

(b)

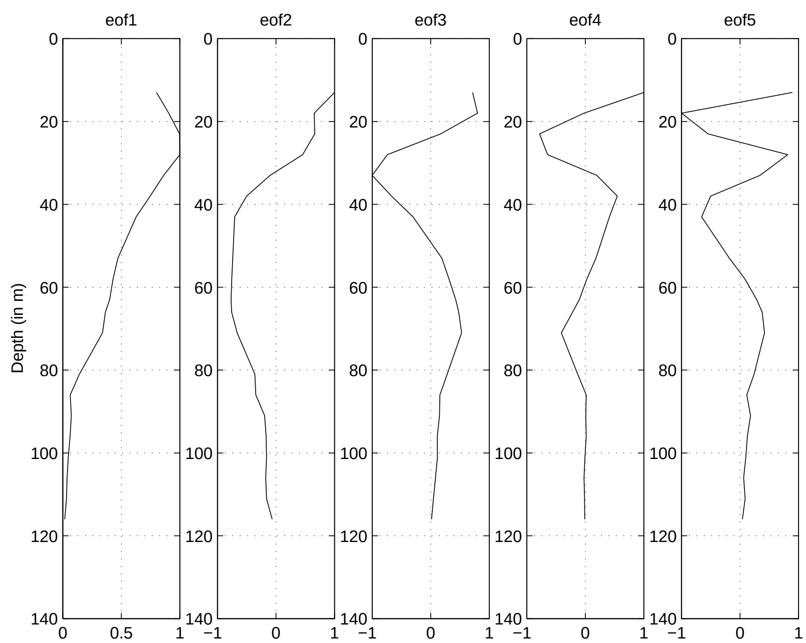

Fig. 3: EOFs for current comp. u (solid line) and v (dot-dash line) (a) and for temp. T (b).

In particular, the mean sound-speed profile exhibits a typical summer shallow-water profile which decreases with depth (see Fig. 5), the corresponding values of the discretized profile are shown in Table 1. The smooth downward refracting gradient of the profile contrasts significantly with usual schematic two-layer representations.

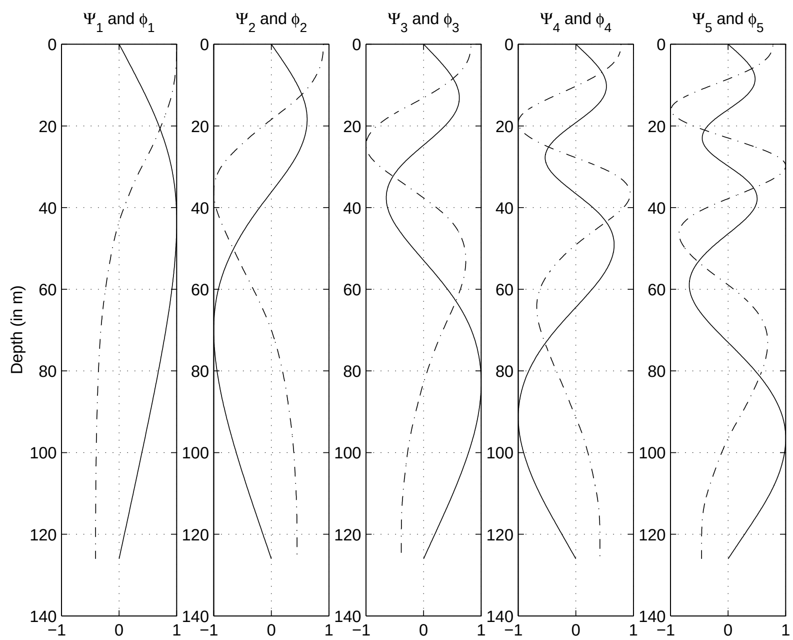

Fig. 4: Normalized HNMs Ψ_m (solid line) and $\phi_m = d\Psi_m/dz$ (dot-dash line).

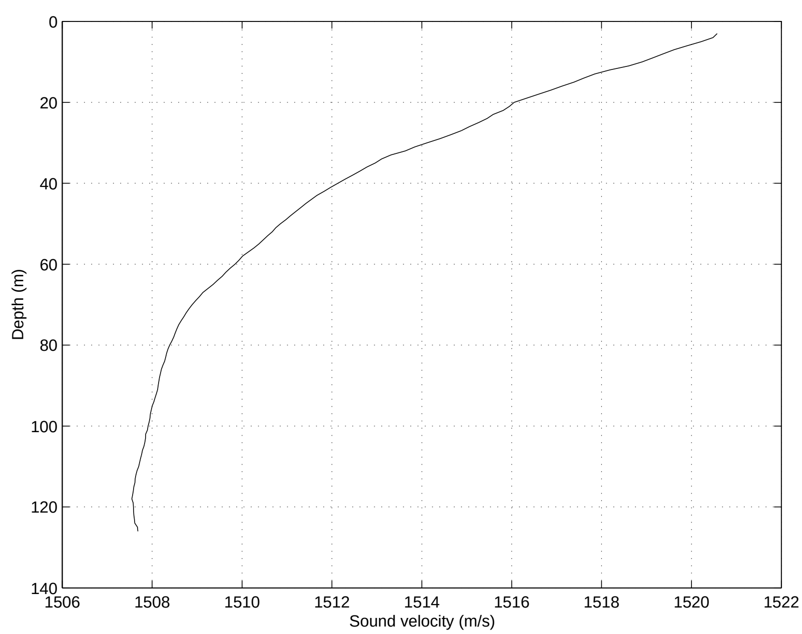

Fig. 5: Mean velocity profile from CTD-IH.

Table 1. Discretized values of the mean sound-speed profile.

Depth (m)	Sound Velocity (m/s)	Depth (m)	Sound Velocity (m/s)
3	1520.6	65	1509.4
5	1520.2	70	1508.9
10	1518.9	75	1508.6
15	1517.4	80	1508.4
20	1516.1	85	1508.2
25	1515.3	90	1508.1
30	1514.1	95	1508.0
35	1512.9	100	1507.9
40	1512.1	105	1507.8
45	1511.4	110	1507.7
50	1510.9	115	1507.6
55	1510.4	120	1507.6
60	1509.8	125	1507.7

A preliminary step in the analysis of current and temperature data consisted in calculating the dependence of Δ_m on η_m^0 for some of the HNMs (see Eq.2.7). Those calculations revealed that not every pair (Ψ_m, ϕ_m) is "allowed" to generate modal solitons. For $m > 1$, the characteristic soliton width Δ_m becomes complex, and this implies that the characteristics of the SWPs depend only on Ψ_1 and ϕ_1.

To detect the propagation of SWPs across the experimental site (and on the basis of the previous result) one can take advantage of the correlation between EOFs and HNMs, and calculate the empirical "modal" amplitudes of hydrographic data for the first EOF. Those amplitudes were separated with a Butterworth filter into low-pass and high-pass components with the cutoff frequency chosen in order to obtain a "tidal" band (with periods longer than 4h) and a "buoyancy" band (with shorter periods). Due to the low sampling frequency ($\sim 1/10$ minutes) the estimation of vertical displacement from thermistor data did not resolve the structure of SWPs. Nevertheless, it was expected to "capture" some of the solitons within a packet —if present— in the high-pass component. This data processing did not provide any physical information about the direction and phase velocity of SWPs since the measurements were taken at a single location. The results of filtering are shown in Fig. 6. In all cases —and particularly in the bottom plots of temperature records— there are significant "peaks" (the position of the first three peaks is denoted with arrows), which are not distributed randomly, but appear to be repeated at each tidal cycle. Those peaks are located slightly behind the maxima of the corresponding tidal component, which is shown by the vertical dashed lines starting at each peak's position and crossing the low-pass component of modal amplitude. The position of the second peak is "missing" in the high-pass modal amplitude of u, which might be due to the low temporal resolution of hydrographic data. However, its expected position is shown to enhance the general "alignment" between the

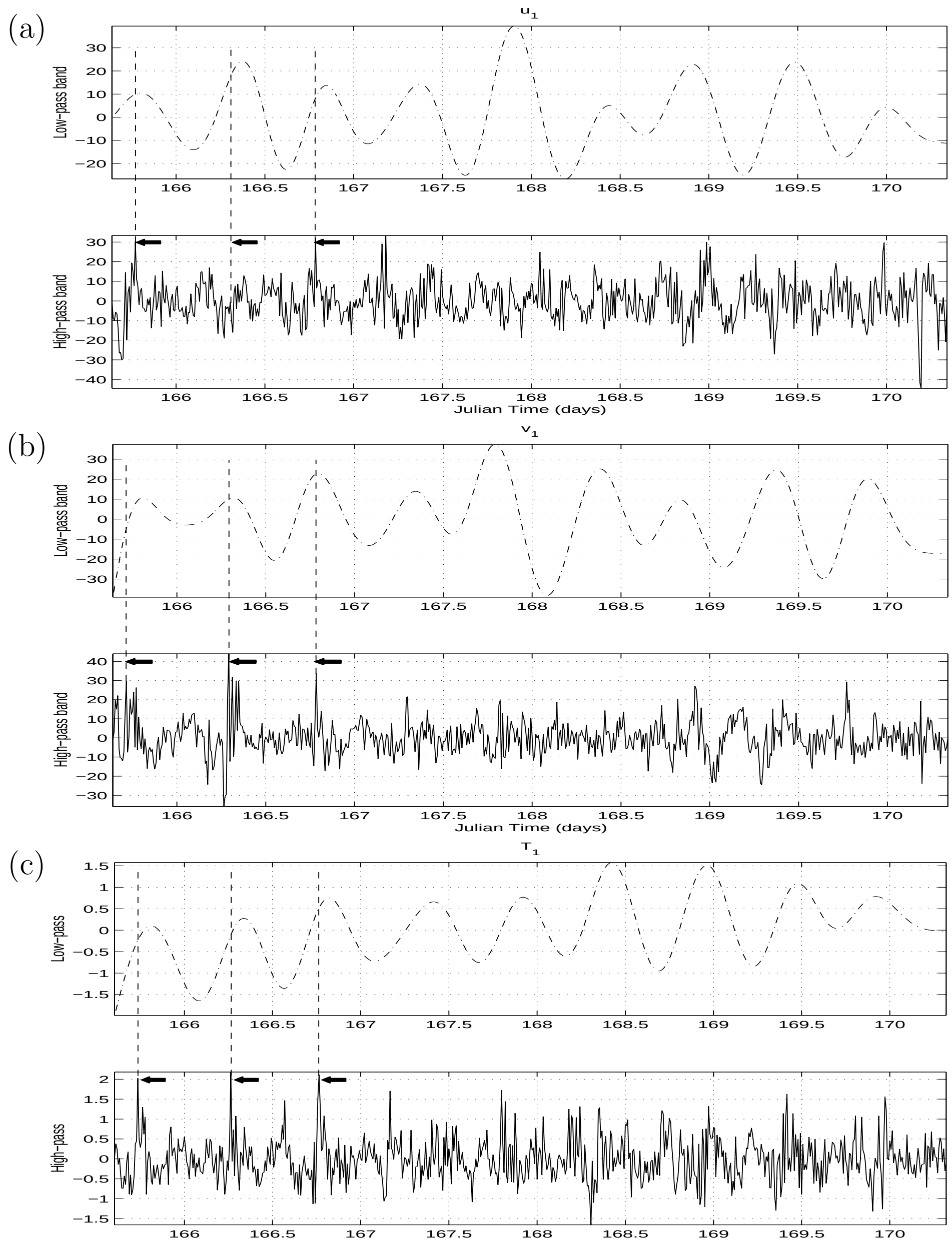

Fig. 6: Modal amplitudes of horizontal current components u (a), v (b) and temperature T (c); velocity is in cm/s and temperature in Celsius degrees. The second peak is missing in the modal amplitude of u but its expected position is shown to enhance the general comparison.

soliton peaks and the corresponding maxima of tidal components. Peaks in the current data reach amplitudes up to 40 cm/s, which is close to the corresponding maximal value reported by Apel *et al.*[5].

4. Acoustic Simulations and Comparison with Real Data

Based on the analysis of temperature records the first step consisted of searching for acoustic perturbations of the received signal, temporally correlated with any of the peaks of the high-pass component of temperature. To accomplish this task, part of the acoustic transmissions from the north source position to the VLA was processed, during a time interval of $\Delta t = 3$ h around the third temperature peak (near 166.75 d, see Fig. 6, on bottom). The processing consisted in calculating the following quantity:

$$-20\log_{10}|\hat{p}(f)| \ , \tag{4.1}$$

where $\hat{p}(f)$ corresponds to the monochromatic component at frequency f, of the Fourier transform of the received signal $p(t)$. The quantity defined by Eq.4.1 will be called as "relative transmission loss" (hereafter RTL). The processed acoustic data revealed a sharp pattern of acoustic perturbations (near 166.765 d, see Fig. 7, on top). The pattern is complex but it reveals an increase in signal amplitude across a wide band of frequencies. As observed earlier, this can be seen as a sort of focusing effect. At a single frequency the perturbation pattern appears to be poorly resolved, due to the superposition of noise on each frequency component. Therefore, some averaging was applied to different RTL curves over a temporal window of 200 seconds. The curves were further smoothed in time with a low-pass filter. The RTL curve at 430 Hz (see Fig. 7, on bottom), shows the focusing effect more clearly. The overall amplitude excursion of the RTL corresponds approximately to 9 dB. Besides the propagation of soliton packets across the experimental site it seems unlikely to find other physical mechanisms that can account for the RTL perturbation described above. In particular, for the INTIMATE'96 environment, the propagation of the surface tide does not affect the depth of the thermocline. Therefore, the tide can not lead to significant interactions of the acoustic signal with the bottom.

Unfortunately, the temporal correlation between the temperature peak commented on previously and the acoustic data is not evident. This might be due to the significant difference between the sampling rates of temperature records, one sample every 10 minutes, and acoustic transmissions, with one emission every 8 seconds. To clarify this issue one can exploit the theoretical knowledge on soliton propagation and generate "soliton-like" fields of temperature and sound velocity, which can be used as input for an acoustic propagation model. The primary goal of the simulations is to obtain a qualitative agreement between the modeled and the measured dependences of RTL along time.

An important theoretical question of soliton propagation is the choice of initial conditions that define the starting shape $\eta_m(x, 0)$ and starting amplitude η_m^0 of the SWP. A complete

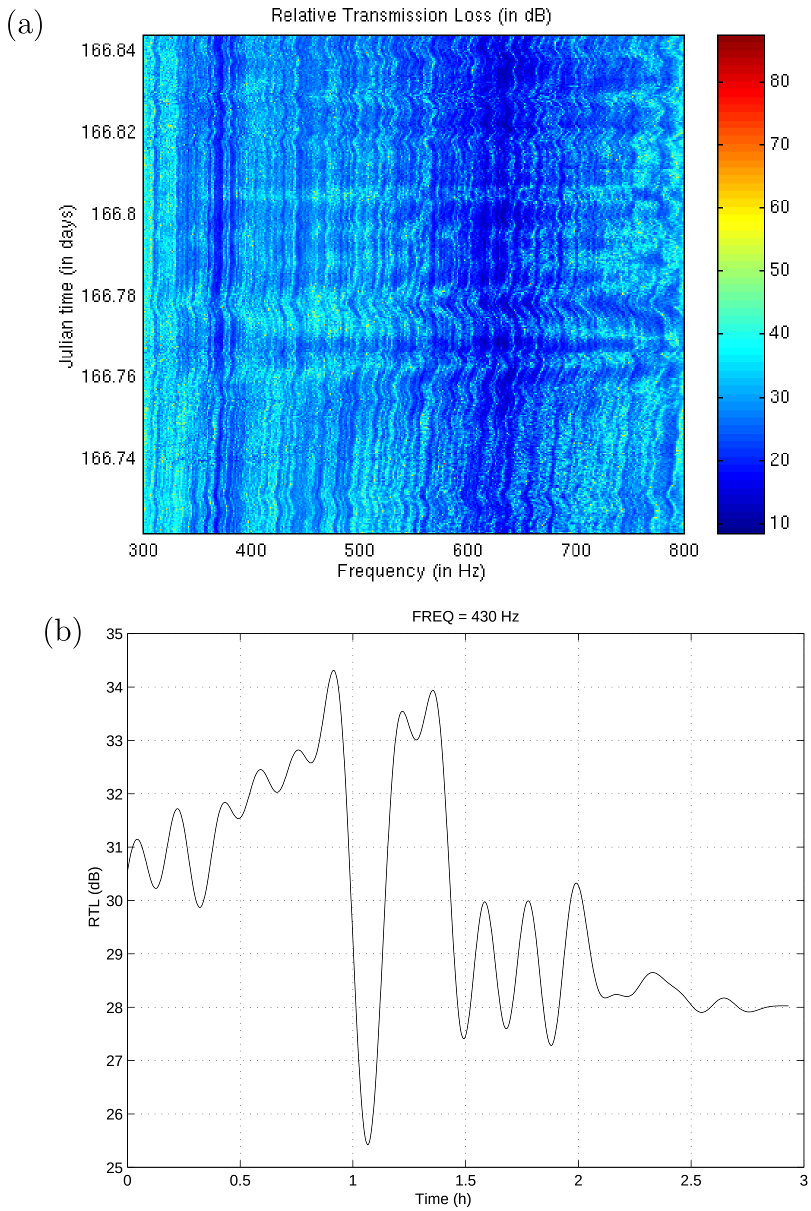

Fig. 7: Relative transmission loss over frequency (a) and averaged and smoothed relative transmission loss at 430 Hz (b).

discussion of this problem should handle the analysis of the forcing mechanisms of soliton generation, which is an issue beyond the scope of this paper. For this reason, and also because SWPs in our environment depend only on Ψ_1 and ϕ_1, η_1^0 was estimated from direct measurements, through the analysis of isotherms from thermistor data. To accomplish this task the mean depth of each isotherm was calculated, and the corresponding isotherm oscillations along time were corrected to the mean depth. This gave a distribution of corrected

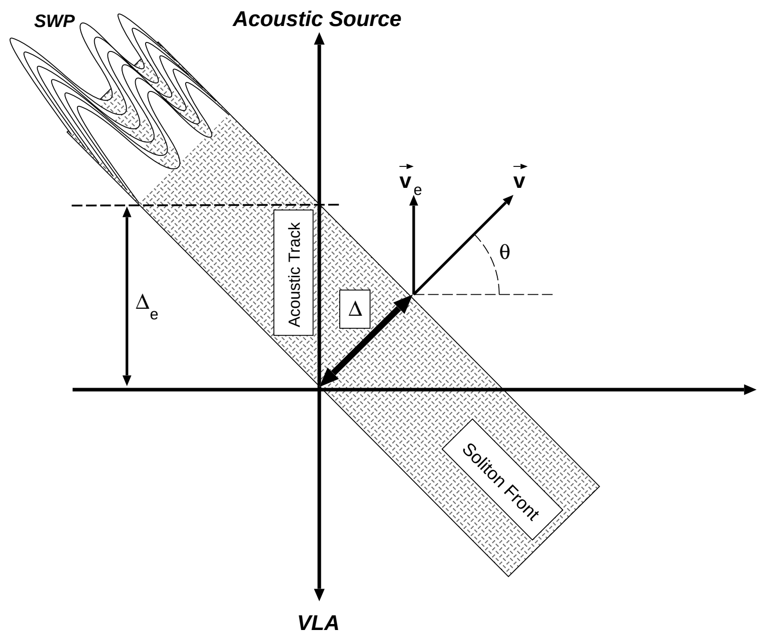

Fig. 8: Geometry of soliton propagation across the experimental site.

isotherms, from which the one that exhibited the narrowest peak of amplitude was selected. That one was considered to be representative of the initial soliton amplitude. That gave $\eta_1^0 \approx 25$ m. Furthermore, from Eqs. (2.2),(2.3),(2.4) and (2.7) one can predict that $C_1 =$ 44 cm/s, $\alpha_1 = 0.012$ s^{-1} and $\beta_1 = 300.4$ m^3/s, while from Eq.2.8 one predicts that $\mathcal{C}_1 = 54$ cm/s. This value of soliton speed is close to the measured values discussed in Ref.5.

The "solitonized" fields of temperature are calculated from Eq.2.11. Furthermore, each temperature profile is converted to sound-speed using the well-known Mackenzie's formula. Those transformations reflect the fact that the propagation of the SWP across the acoustic waveguide leads to time-dependent —and range-dependent— perturbations of the sound-speed profiles. Those perturbations of sound-speed affect dynamically the acoustic signal, mainly due to the dependence of refraction and surface/bottom interactions, on time and range. The expected geometry of soliton propagation is shown in Fig. 8, where θ represents the direction of propagation. Since the thermistor chains were located slightly to the east of the VLA, and because the temperature perturbation occurs *before* the acoustic perturbation, one can assume that the SWP "starts" propagating south-east from the VLA. According to the previous figure the effective width of the soliton front is $\Delta_e = \Delta/\sin\theta$, where Δ is the width of the front along the direction of propagation[1]. Moreover, the effective velocity of soliton propagation is $V_e = \mathcal{C}_1 \sin\theta$. In this way, one starts calculating the transmission loss (hereafter TL) using the mean sound-speed profile, "displaces" the SWP a distance $V_e \Delta t$

[1]Do not confuse this width with the characteristic soliton width Δ_m.

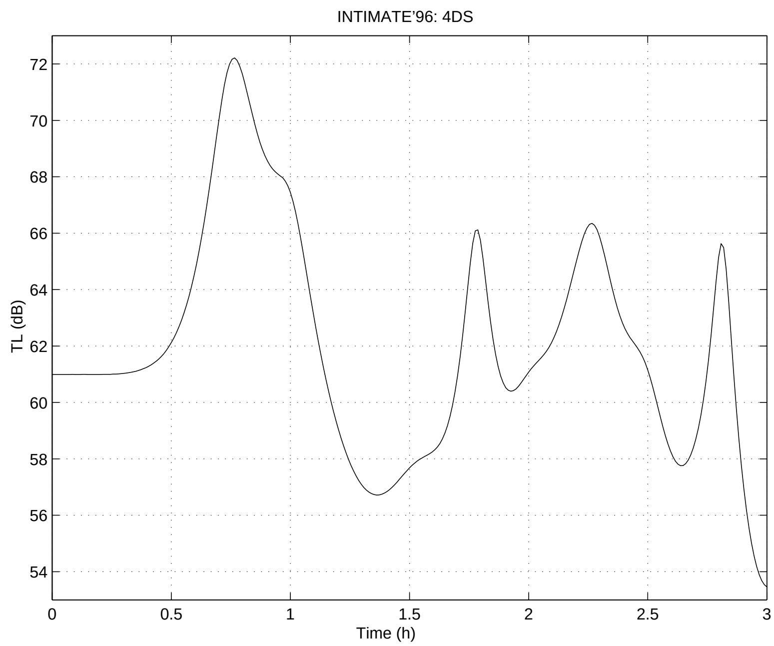

Fig. 9: Simulation result for a "dnoidal" SWP with 4 solitons.

(with $\Delta t = 2$ minutes) towards the north position of the acoustic source, and calculates the TL again. The displacement is repeated until the SWP covers a temporal window of 3 hours.

A preliminary set of simulations was performed with the acoustic model C-SNAP[11], by calculating the TL at $f = 430$ Hz, for a "sech" profile, and for a set of four "dnoidal" SWPs. Each "dnoidal" soliton packet contained an integer number of solitons, up to four. Those packets were calculated by modifying, through trial and error, the parameters S and τ. The angle of propagation was considered as $\theta = 15°$, which corresponds to the estimated direction of propagation of the internal tide[10]. The shape of the "dnoidal" packets did not change over time, which is an assumption based on observations[2]. The results showed a complex dependence of TL on time, where one can observe high levels of attenuation, but also levels of signal focussing. The result that resembles best the curve of RTL was obtained for the case of a "dnoidal" SWP with four solitons (see Fig. 9). The modeled dependence of TL on time exhibits the pattern of attenuation, focusing and attenuation again, as the SWP approaches and passes over the VLA. Further simulations with other values of θ, using both the "sech" and "dnoidal" soliton profiles, revealed an oscillating-like highly nonlinear dependence of TL on θ. These simulations gave further consistency to the soliton hypothesis, since the acoustic model predicted certain degrees of signal focusing at particular positions of the soliton packets. Nevertheless, none of the simulations reproduced a focusing effect in qualitative agreement with the one observed.

[2] For instance, the soliton packet described in Ref. 12, and observed at a few tens of miles from the INTIMATE'96 experimental site, propagated shoreward keeping a stable shape during almost 12 h.

5. Conclusions

On the basis of this analysis the following conclusions can be drawn: 1) nonlinear approximations to hydrodynamic equations for a rotationless environment admit the generation of “modal” solitons with characteristics that depend on HNMs; 2) the “sech” and “dnoidal” modal solutions of the KdV equation correspond to different dynamics of soliton propagation: the “sech” profile describes a single soliton, which propagates in time and space without changing its shape, while “dnoidal” profiles evolve both in time and space and for certain parameter choices can give a better description of SWPs; 3) current and temperature hydrodynamic fields depend linearly on vertical modal displacements, which can be obtained as solutions of the KdV equation; such solutions can be used to generate physically consistent fields of temperature and sound velocity; 4) separation of current and thermistor records of the INTIMATE’96 experiment into low-pass and high-pass components shows evidence of soliton groups propagating across the experimental site; 5) one of these groups is coincident with a strong perturbation of the acoustic signal which, when analysed in detail, reveals an increase of signal amplitude, i.e., an effect similar to signal focusing and 6) simulations of acoustic propagation through “soliton-like” fields of sound velocity show a similar effect of signal focusing and confirm the assumption that a SWP may be responsible for the observed acoustic perturbation.

Appendix

It can be shown[5] that the dynamic fields of currents (u, v, w) can be expanded in terms of HNMs Ψ_m and $\phi_m = d\Psi_m/dz$ as follows:

$$(u, v) = \sum_m (u_m, v_m)\, \eta_m \phi_m \ , \ \text{and}\ w = \sum_m w_m \Psi_m \frac{\partial \eta_m}{\partial t} \ , \tag{A.1}$$

where η_m represents modal displacement, and (u_m, v_m, w_m) are coefficients of modal amplitude for the current components u, v and w. For η_m being calculated in meters, and t in seconds, w_m will be a dimensionless parameter while u_m and v_m will have dimensions m/s. By taking $k_T = 0$ and constant $(c_v\ , \rho)$ Eq.2.10 becomes:

$$\frac{\partial T}{\partial t} + u\frac{\partial T}{\partial x} + v\frac{\partial T}{\partial y} + w\frac{\partial T}{\partial z} = 0 \ . \tag{A.2}$$

In the general case it is not clear which terms can be neglected and which ones can not. However, by neglecting coupling mechanisms and taking into account that an important feature of soliton propagation is the significant dynamics of the perturbation along the depth axis, one can neglect the second and third nonlinear terms, and rewrite Eq.A.2 as follows:

$$\frac{\partial T}{\partial t} + w\frac{\partial T}{\partial z} = 0 \ . \tag{A.3}$$

Now, recalling the general structure of expansions [Eqs. (A.1)] let us consider that

$$T(x,y,z,t) \approx T_0(z) + T' \ , \ \text{and} \ \ T' = \sum_m T_m \Psi_m \gamma_m \ . \tag{A.4}$$

In the last expression γ_m is an unknown function, while T_m corresponds to a dimensionless coefficient of modal amplitude for temperature. Both γ_m and T_m should be chosen in order to ensure the consistency of Eq.A.3. Using Eqs. (A.4) it can be obtained that:

$$\frac{\partial T}{\partial t} = \sum_m T_m \Psi_m \frac{\partial \gamma_m}{\partial t} \ . \tag{A.5}$$

Furthermore, neglecting again coupling mechanisms between modes, and through further linearization, the second term in Eq.A.3 can be approximated as:

$$w\frac{\partial T}{\partial z} \approx \frac{dT_0}{dz} \sum_m w_m \Psi_m \frac{\partial \eta_m}{\partial t} \ . \tag{A.6}$$

Substituting Eq.A.5 and Eq.A.6 into Eq.A.3 it follows automatically that

$$T_m = -w_m \text{ and } \gamma_m = \eta_m \frac{dT_0}{dz} \ .$$

The minus sign indicates that the time oscillations of w and T have a phase difference of π radians. The last pair of equations lead to Eq.2.11.

References

[1] Zhou J., Zhang X., and Rogers P. Resonant interaction of sound wave with internal solitons in the coastal zone. *J. Acoust. Soc. America*, 90(4):2042–2054, October 1991.

[2] Caille G.W. et al. Overview of the joint chine-u.s. yellow sea-96 experiment. In Zhang R. abd Zhou J., editor, *Shallow-Water Acoustics*, pp. 17–22, Beijing-China, April 1997. China Ocean Press. proceedings of the SWAC'97 Conference.

[3] Démoulin X., Stéphan Y., Jesus S., Coelho E., and Porter M. "Intimate'96: A shallow water tomography experiment devoted to the study of internal tides". In *Proceedings of SWAC'97*, pp. 485–490, Beijing, April 1997. China Ocean Press. Edited by Zhang R. and Zhou J.

[4] Ostrovsky L.A. Nonlinear internal waves in a rotating ocean. *Oceanology*, Vol. 18 No.2, pp. 119–125, 1978.

[5] Apel J.R. et al. An overview of the 1995 swarm shallow-water internal wave acoustic scattering experiment. *IEEE Journal of Oceanic Engineeering*, 22(3):465–500, July 1997.

[6] Gabov S. A. *Introduction to the theory of nonlinear waves.* Ed. by the Moscow State University, Moscow, 1988. (in russian).

[7] Apel J., Orr. M., Finette S., and Lynch J. A new model for internal solitons and tides on the continental shelf. In Zhang R. and Zhou J., editors, *Shallow-Water Acoustics*, pp. 219–225, Beijing, April 1997. China Ocean Press. Proceedings of the SWAC'97 Conference.

[8] Apel J. et al. The new jersey shelf shallow water acoustic random medium propagation experiment (swarm). In Zhang R. and Zhou J., editors, *Shallow-Water Acoustics*, pp. 213–218, Beijing, April 1997. China Ocean Press. Proceedings of the SWAC'97 Conference.

[9] LeBlond P.H. and Mysak L.A. *Waves in the Ocean.* Elsevier Scientific Publishing Company, New York, 1989.

[10] Rodríguez O.C., Jesus S., Stephan Y., Démoulin X., Porter M., and Coelho E. Internal tide acoustic tomography: Reliability of the normal modes expansion as a possible basis for solving the inverse problem. In Alippi A. and Cannelli G.B., editors, *Proc. of the 4th. European Conference on Underwater Acoustics*, pp. 587–592, Rome, Italy, 21-25 September 1998.

[11] Ferla C.M., Porter M.B., and Jensen F.B. *C-SNAP: Coupled SACLANTCEN normal mode propagation loss model.* SACLANT UNDERSEA RESEARCH CENTRE (SM-274), La Spezia, Italy, 1993.

[12] D.R.G. Jeans, and Sherwin T.J. *Solitary internal waves on the Iberian shelf.* MORENA scientific and technical report no.44, University of Wales, UK, 1996.

DYNAMICS OF ACOUSTIC PROPAGATION THROUGH A SOLITON WAVE PACKET: OBSERVATIONS FROM THE INTIMATE'96 EXPERIMENT

O.C. RODRÍGUEZ AND S.M. JESUS
UCEH-Universidade do Algarve
Campus de Gambelas,
Faro, Portugal

Y. STEPHAN AND X. DEMOULIN
Service Hydrographique et Océanographique
de la Marine
Brest, France

M.B. PORTER
Science Applications International Corp.
San Diego, USA

AND

E.F. COELHO
Instituto Hidrográfico
Lisbon, Portugal

Abstract. Experimental observations of acoustic propagation through a Soliton Wave Packet (SWP) show an abnormally large attenuation over some frequencies, that was found to be significantly time-dependent and anisotropic. Nevertheless, by considering the problem of signal attenuation, the approach used in most of the studies can be considered as "static" since no additional effects were taken into account as a SWP evolves in range and time. Hydrographic and acoustic data from the INTIMATE'96 experiment clearly exhibit traces of the presence of soliton packets, but in contrast with known observations of attenuation, its frequency response also reveals a sudden increase of signal amplitude, which may be due to a focusing effect. This signal increase coincides with a significant peak found in current and temperature records. However, the correlation of both acoustic and hydrographic features is difficult to support due to the different time scales between the rate of hydrographic data sampling and the rate

A. Caiti et al. (eds.), Experimental Acoustic Inversion Methods for Exploration of the Shallow Water Environment, 1-18.

of signal transmissions. To study the possibility that a SWP could be responsible for the observed signal increase, the INTIMATE'96 hydrographic data was used to generate physically consistent distributions of "soliton-like" fields of temperature and sound velocity, which were used as input for a range-dependent normal-mode model; it was found that for a particular soliton field, the set of "dynamic" (i.e., range-dependent and time-dependent) acoustic simulations reveals an acoustic signature similar to that observed in the data. These results contribute to a better understanding of underwater propagation in shallow-water coastal environments and therefore provide a potential basis for range-dependent temperature and sound-speed inversions.

1. Introduction

It is known that naturally generated solitons can often be observed in coastal zones, as a result of nonlinear interaction of the surface tide with the continental shelf; the generation mechanism remains however poorly understood. The significant circulation of organic surfactants caused by SWPs induces small displacements of the ocean level and leads to a modulation of the sea-surface roughness which can be clearly detected by satellite SAR images. Such surface signatures provide a detailed information about the propagation characteristics of SWPs (Small *et al.*, 1995). Soliton packets have been observed by satellite almost everywhere in coastal zones and in particular near Portugal. Observations of propagating solitons include also a considerable amount of current and temperature measurements. For instance during the summer of 1994 current and temperature data taken near Porto (Sherwin *et al.*, 1996) allowed for the observation of a wave packet, composed of three solitons, which could be tracked during their propagation towards the shore. The waves were characterized by sudden isotherm depressions of up to 45 m lasting 10–35 minutes, accompanied by current surges of up to 0.45 m/s and shears of up to 0.7 m/s (over 60 m). These SWPs propagated away from the shelf break towards the shore with an average speed of 0.56 m/s and appeared each tidal cycle, which confirms the important role of tides as a significant source for the generation of SWPs.

The problem of acoustic propagation through SWPs has been intensively studied in recent years, essentially To explain the anomalous frequency response of shallow-water propagating signals, which were found to be strongly time dependent, anisotropic and sometimes exhibiting an abnormally large attenuation over some frequency range (Zhou *et al.*, 1991),(Caille *et al.*, 1997). Most of the known reports noted the problem of signal attenuation, without regard to additional effects as a soliton packet evolves in time and range. Hydrographic and acoustic data from the INTIMATE'96 experiment clearly exhibit traces of soliton presence. However, in contrast with referenced observations of attenuation, the frequency response reveals also a “soliton-like” acoustic signature which corresponds to an increase of signal amplitude. Such an acoustic feature can be due to a focusing effect. To study the possibility that the signal increase could be caused by the presence of a SWP in the acoustic waveguide the hydrographic data was used to generate physically consistent distributions of “soliton-like” fields of temperature and sound velocity, which were used as input for a range-dependent acoustic propagation model. As will be shown in the following sections the results of acoustic “dynamic” (i.e., range-dependent and time-dependent) simulations strongly support the assumption that a particular SWP was responsible for the observed soliton-like acoustic signature.

2. Theoretical Background

2.1. THE KORTEWEG-DE VRIES “MODAL” EQUATION

The starting point for the analysis of soliton propagation in a rotationless environment with complex stratification is the so-called *Korteweg-de Vries* equation (hereafter simply KdV) for modal vertical displacement η_m (Ostrovsky, 1978),(Apel *et al.*, 1997):

$$\frac{\partial \eta_m}{\partial t} + C_m \frac{\partial \eta_m}{\partial x} + \alpha_m \eta_m \frac{\partial \eta_m}{\partial x} + \beta_m \frac{\partial^3 \eta_m}{\partial x^3} = 0 \tag{1}$$

where x corresponds to the axis of propagation, t represents the time coordinate, C_m corresponds to the modal phase speed of linear waves in a non-rotating fluid, α_m and β_m are coefficients of non-linearity which depend on Hydrostatic Normal Modes (hereafter HNMs) Ψ_m and $\phi_m = d\Psi_m/dz$ as follows:

$$\alpha_m = \frac{3}{2}\frac{\langle \phi_m^3 \rangle}{\langle \phi_m^2 \rangle} C_m \ , \ \beta_m = \frac{1}{2}\frac{\langle \Psi_m^2 \rangle}{\langle \phi_m^2 \rangle} C_m \quad . \tag{2}$$

The eigenfunctions Ψ_m can be calculated by solving a standard Sturm-Liouville problem:

$$\frac{d^2\Psi_m}{dz^2} + \frac{N^2}{C_m^2}\Psi_m = 0 \ , \ \Psi_m(0) = \Psi_m(D) = 0 \ , \tag{3}$$

where $N^2(z)$ represents the buoyancy frequency and D is the water depth. The complete derivation of Eq. (1) can be found in (Ostrovsky, 1978).

In contrast with the corresponding equation for a homogeneous fluid (Gabov, 1988), which admits a single soliton generation, it follows from Eq. (1) that by combining both nonlinear and stratification effects it is possible to obtain an entire set of “modal” solitons with characteristics that depend on HNMs. Whether or not this explains the observations of propagating SWPs depends on the properties of the HNMs.

2.2. THE "SECH" SOLUTION

It is well known that the KdV equation admits a "sech" solution of the following form (Apel *et al.*, 1997):

$$\eta_m = \eta_m^0 \operatorname{sech}^2 \left(\frac{x - \mathcal{V}_m t}{\Delta_m} \right) \tag{4}$$

where η_m^0 represents the peak amplitude of the modal soliton, which has a nonlinear characteristic width

$$\Delta_m = \sqrt{\frac{12\beta_m}{\alpha_m \eta_m^0}} \ , \tag{5}$$

and propagates with a nonlinear phase speed given by

$$\mathcal{V}_m = C_m + \frac{\alpha_m \eta_m^0}{3} \ . \tag{6}$$

As seen from the above equations Δ_m is inversely proportional to the amplitude of the modal soliton, whereas $\mathcal{V}_m$ is linearly proportional to η_m^0. The implication is that the larger η_m^0, the faster the soliton propagates and the narrower or steeper the soliton is. The solution given by Eq. (4) describes a *single* nonlinear perturbation, which propagates in both time and range without deforming its shape. In this way a single modal "sech" solution does not agree with observations, which show the propagation of SWPs exhibiting dispersive properties and made up of different "components". However, a reasonable explanation for this is that each component of the SWP corresponds to a particular "sech" profile and dispersion is a direct consequence of the different phase speeds of packet components.

2.3. THE "DNOIDAL" SOLUTION

Another solution to the KdV equation is (Apel *et al.*, 1997):

$$\eta_m = \eta_m^0 \left[2\mathrm{dn}^2_{(m,\mathsf{s})} \left(\frac{x - \mathcal{V}_m t}{\Delta_m} \right) - (1 - \mathsf{s}^2) \right] \tag{7}$$

where the index s is a complex function of the normalized variable $\tau = x/C_m t$ and $\mathrm{dn}_{\mathsf{s}}(\varphi)$ is the "dnoidal" Jacobi elliptic function. Shapes of the "dnoidal" solution agree well with backscattered profiles measured from SAR images (Apel *et al.*, 1997). As $\mathsf{s} \to 1$ the above expression becomes the "sech" profile. The dynamics of a "dnoidal" soliton are completely different from the one of the "sech" profile. The Eq. (7) describes not a single but an entire SWP which evolves in time and range. The number of solitons within the packet depends on s and τ. This implies that one can derive entire sets of "dnoidal" soliton packets from a single HNM.

For certain parameter choices the "dnoidal" profile resembles better the observations of SWPs. However, this leads to some ambiguity because if a single "dnoidal" solution resembles an entire packet it is not clear *which* of the modal solutions has to be considered, and there is also the possibility that the packet is made up of several "dnoidal" components. This matter is clearly related with the discussion of packet propagation in terms of "sech" components and will be recalled during the discussion of thermistor data.

2.4. CURRENT PERTURBATIONS

It can be shown within the theoretical context of soliton propagation that the non-linear fields of horizontal currents $\vec{U}_h = (u, v)$ can be expanded in terms of HNMs ϕ_m as follows (Ostrovsky, 1978):

$$\vec{U}_h = D \sum_m \vec{\mathcal{U}}_m \, \phi_m \tag{8}$$

where $\vec{\mathcal{U}}_m = (u_m, v_m) \sim \eta_m$ and D represents the water depth.

2.5. TEMPERATURE PERTURBATIONS

From the analysis of the coupled nonlinear and rotationless form of Hydrodynamic Equations it follows that modal amplitudes of horizontal current components depend linearly on modal vertical displacement $(\mathcal{U}_m, \mathcal{V}_m) \sim \eta_m$. Nevertheless, from a tomographic point of view, the system of Hydrodynamic Equations does not provide a physical basis for expanding the sound speed field. To address the tomographic issue let us recall the thermodynamic equation (LeBlond *et al.*, 1989)

$$\frac{D}{Dt} \left(\rho C_v T \right) = \nabla \left(k_T \nabla T \right) + Q_T \tag{9}$$

where C_v denotes the specific heat at constant volume, k_T is the thermal conductivity and Q_T represents all sources and sinks of heat. Linearizing and solving this differential equation (Rodríguez *et al.*, 1998) one can obtain that:

$$T \approx T_0(z) + \frac{dT_0}{dz} \sum_m T_m \Psi_m \ , \tag{10}$$

where $T_m \sim \eta_m$. The approximation becomes linear when $dT_0/dz \approx$ constant.

3. Hydrographic and Acoustic Data

The INTIMATE'96 experiment, performed during the summer 1996, north of Lisbon (see Fig. 1), was the first experiment on underwater acoustics to be performed in Portuguese waters. The experiment was conceived with the main goal of applying the methods of ocean acoustic tomography to the detection and inversion of the internal tide. The area of the experimental site was chosen because of the potential presence of internal tides and internal waves. Some characteristics of the experimental site were known from previous surveys performed by the Instituto Hidrográfico.

The general strategy of the INTIMATE'96 experiment was the following (see Fig. 2): the French vessel BO'DENTRECASTEAUX carried the acoustic source which emitted a 2 second-long LFM chirp with a bandwidth of 500 Hz between 300 and 800 Hz, repeated every 8 seconds. The signal was received on a vertical linear array (hereafter VLA) with four hydrophones, and then transmitted by radio to the Portuguese vessel NRP ANDROMEDA, for online monitoring and backup.

Signal transmissions were performed from North and West positions (see Fig. 3), along range-independent and range-dependent acoustic tracks, respectively, with corresponding distances of 5.6 and 6.4 km. During the experiment an intensive survey of thermistor, CTD, XBT and ADCP data near the VLA was conducted. This allowed for the calculations of empirical orthogonal functions (hereafter EOFs) of currents and temperature, and also for the calculations of HNMs (see Fig. 4). It should be noted that the analysis of ADCP and thermistor data could be used only to retrieve detailed information of the environmental dynamics at that location. An important result of the analysis of hydrographic data is that a high degree of correlation was found between EOFs and HNMs, up to mode 3 (Rodríguez *et al.*, 1998). This is very significant since it indicates that every HNM is equivalent to the corresponding EOF. Furthermore, the quantity and resolution of EOFs depends on the number and resolution of measured profiles, while HNMs can be obtained from a coarse estimate of mean temperature and still provide a detailed description of the environmental dynamics. Once the HNMs were determined, the relationship of Eq. (5) was used to calculate the characteristic soliton width Δ_m as a function of peak amplitude η_m^0 (see Fig. 5). An important result of these calculations is that Δ_m is complex except for HNMs 1, 5, 11, 15 and 19. This simplifies significantly the analysis of propagating SWPs since together with the degree of correlation between HNMs and EOFs mentioned previously, the ambiguity related to the structure of soliton packets is eliminated: only the first modal solution of the KdV equation will be responsible for the generation of SWPs. Whether the packet corresponds to a "sech" profile or a "dnoidal" profile

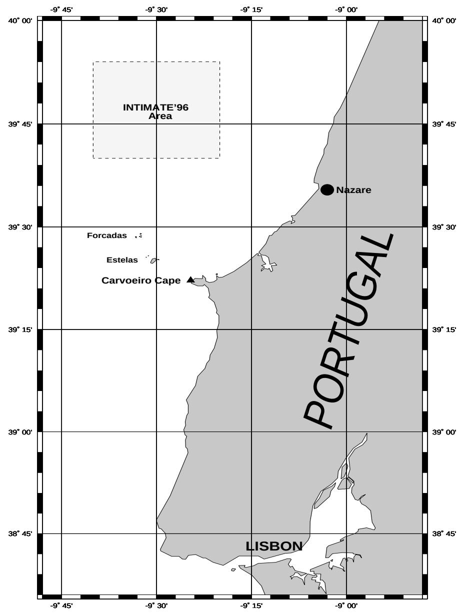

Figure 1. The INTIMATE'96 experimental site.

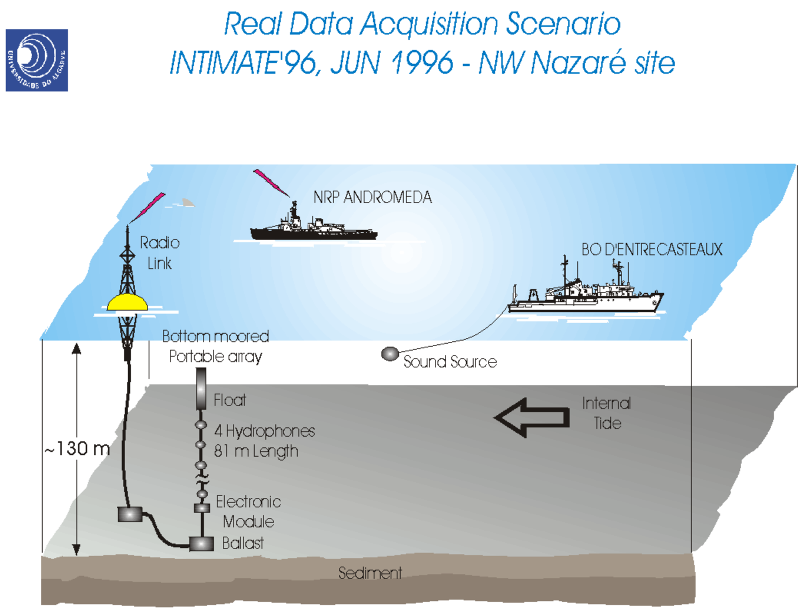

Figure 2. General strategy of the INTIMATE'96 experiment.

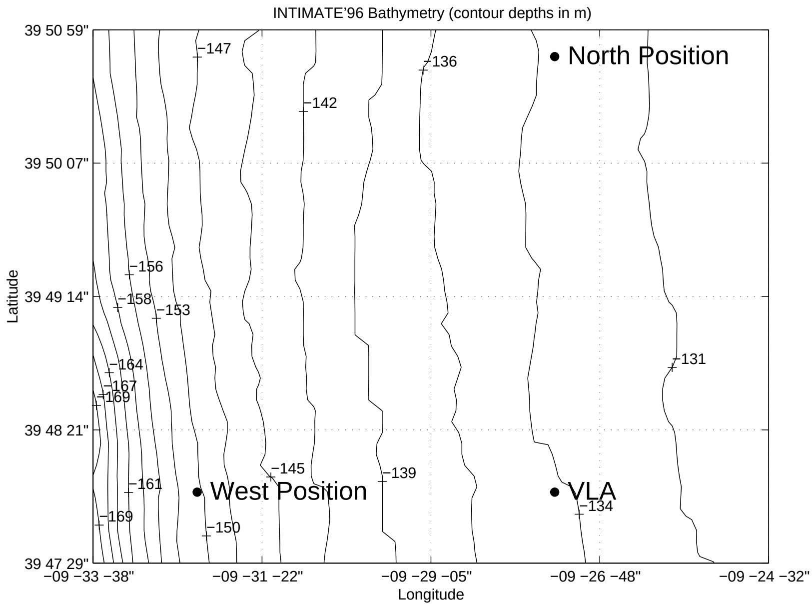

Figure 3. General bathymetry of the INTIMATE'96 experiment.

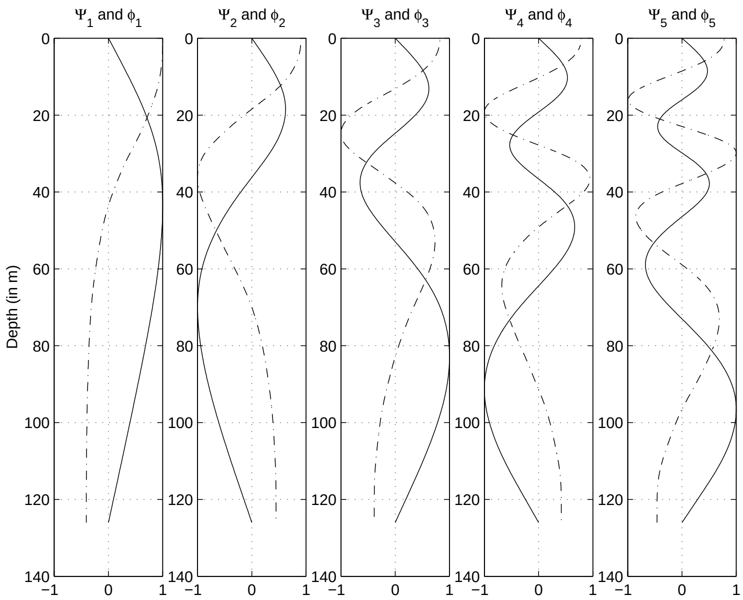

Figure 4. Normalized Hydrodynamic Normal Modes Ψ_m (continuous line) and their derivatives ϕ_m (dot-dash line) calculated from CTD data near the VLA.

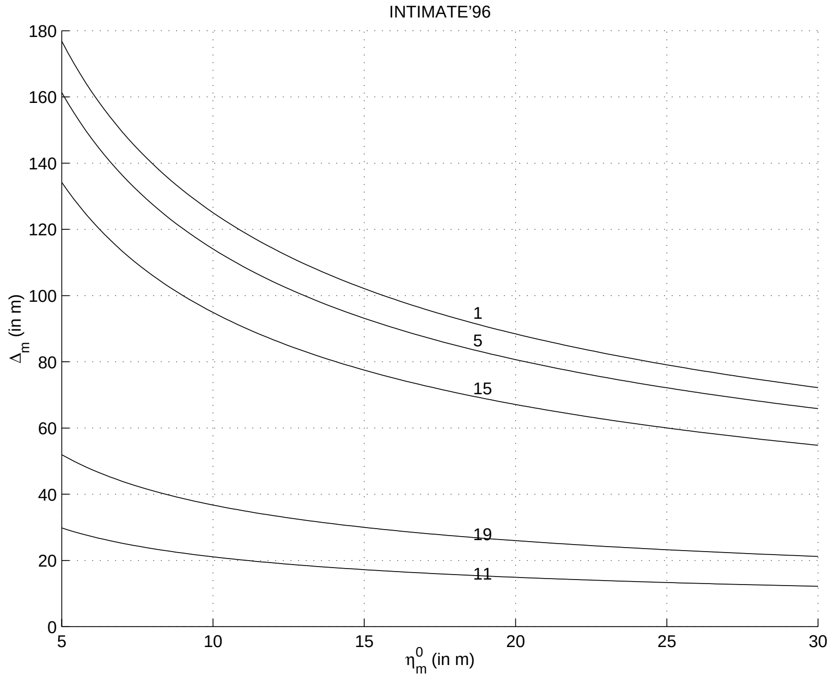

Figure 5. Characteristic modal soliton width Δ_m as a function of their peak amplitude η_m^0, with numbers indicated the corresponding indexes of the Hydrodynamic Normal Mode.

depends on the particular conditions of soliton generation, which is beyond the scope of this study.

Following the same type of analysis presented in (Apel *et al.*, 1997), and taking advantage of the correlation between EOFs and HNMs, the empirical "modal" amplitudes of hydrographic data were filtered into low-pass and high-pass frequency components; the cutoff frequency for separation was chosen to obtain a "tidal" band which will cover all the processes with periods longer than 4 h (and in particular should enhance the tidal component with a period of 12.42 h) and a "buoyancy" band, with shorter periods. Due to the low sampling frequency ($\sim 1/10$ minutes) the estimation of vertical displacement from thermistor data did not resolve the structure of soliton packets. Nevertheless it was expected to "capture" some of the solitons within a packet —if present— in the high-pass frequency component; they could be recognized as being part of a SWP due to the correlation of such peaks with the maxima of the low-pass frequency component. However, the processing of data did not provide any physical information about the direction and phase velocity of SWPs due to the lack of information at other locations.

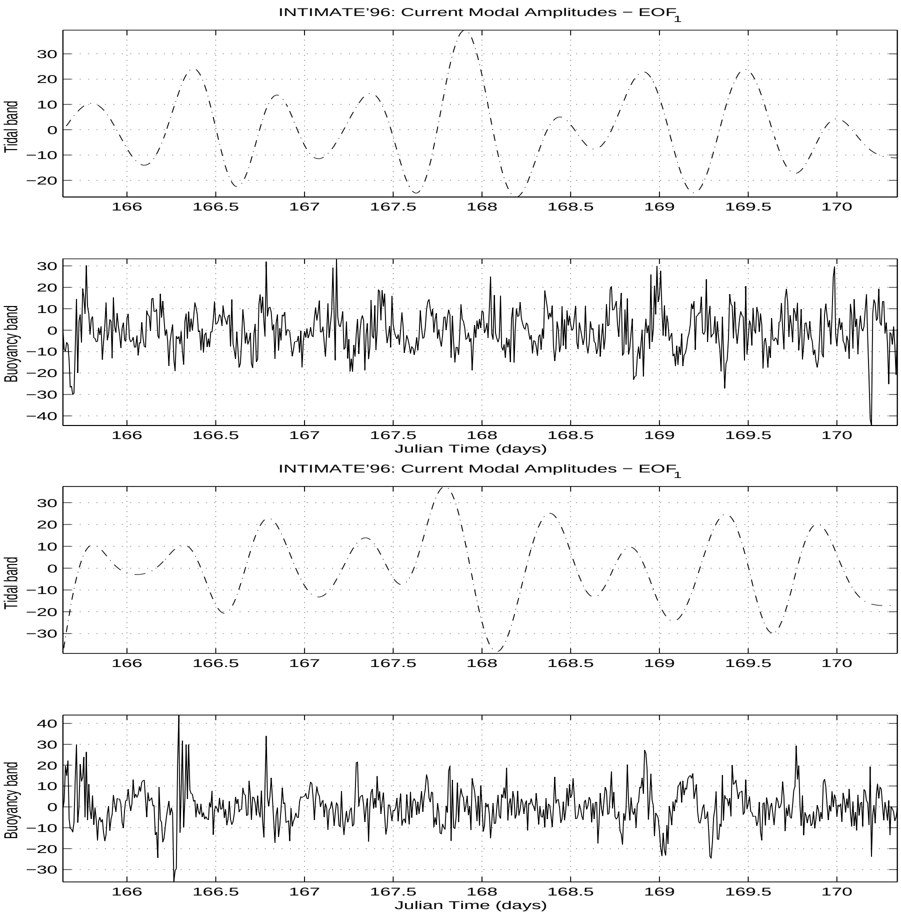

Figure 6. Filtered modal amplitudes of horizontal current components u (top) and v (bottom); units are given in cm/s.

The results of filtering are shown in Figs.6 and 7. There are two common features that can be seen in both figures: the first is the tidal oscillation of the low-frequency components, which is related to the process of propagation of the internal tide; the second is the presence of significant "peaks" in all high-frequency components. For the case of currents (see Fig. 6) peaks reach amplitudes up to 40 cm/s, which agrees with observations from (Apel *et al.*, 1997) and (Sherwin *et al.*, 1996). The distribution of peaks is not arbitrary. By looking at their positions (see for instance Fig. 7) it becomes clear that peaks are "aligned" with the maxima of the low-frequency component, indicating propagation of tidal solitons. Peaks are located slightly behind the maxima. A reasonable explanation for this is that the phase speeds of the internal tide and SWPs are different, leading to a difference in travel times as the internal tide and the SWPs propagate away from the shelf break towards the shore.

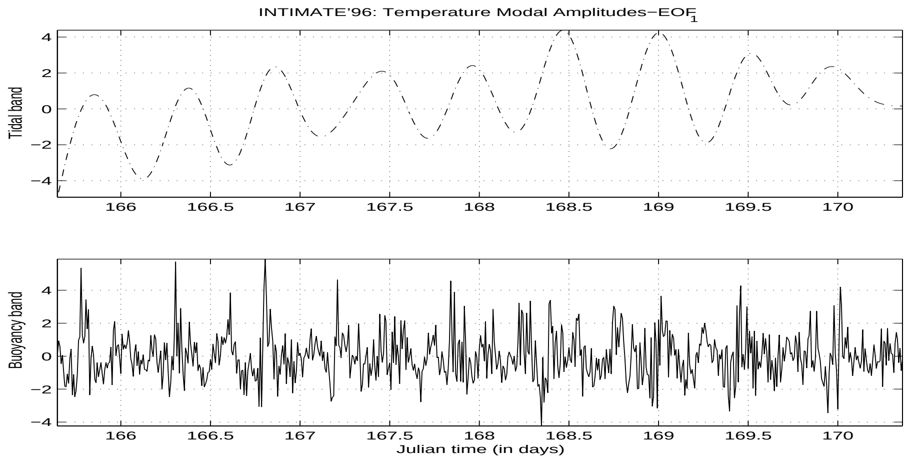

Figure 7. Filtered modal amplitude of temperature; units are given in degrees Celsius.

4. Acoustic Data and Simulations

From an acoustic point of view the third peak found in the high-pass filtered thermistor data of Fig. 7 was of particular interest, since part of the acoustic transmissions from the North position to the VLA, separated by a distance of 5.6 km, covered a temporal window of 3 hours around that peak. The corresponding calculation of relative transmission loss (see Fig. 8), with source and receiver depths of 90 and 115 m, respectively, revealed two bright symmetric "stripes" for which TL increases with frequency. This is an effect compatible with that expected from acoustic propagation through a SWP. However, the most interesting feature is a "soliton-like" signature between the "stripes". It corresponds to an increase of signal amplitude lasting over 15 minutes and can be due to a sort of focusing effect. This particular behaviour of TL with time is not described in any of the consulted referencies. The increase in signal is significantly enhanced in the curve of TL at 430 Hz (see Fig. 9) and shows also that after the second stripe the transmission loss appears to be shifted irreversibly to a level around 28 dB, versus the initial level of approximately 31 dB.

The soliton hypothesis seems the most reasonable one to explain the observed perturbations of TL essentially due to the temporal correlation between the peak discussed in the beginning of this section and the presence of the acoustic perturbation in TL. Other phenomena (like the passage of a wave front driven by the tide) seem less likely mainly because there is no experimental evidence of their presence (in contrast with the presence of solitons in the current and the temperature data) and therefore they do not seem to be concurrent with the propagation of SWPs. Unfortunately the temporal correlation between the considered peak in the thermistor data and the "soliton-like" signature of acoustic data is difficult to support due

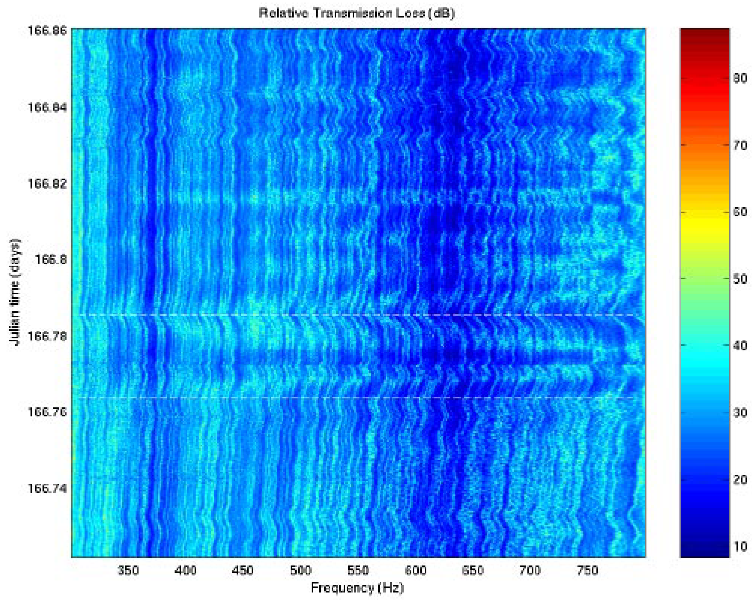

Figure 8. Relative transmission loss in dB with frequency, with dashed lines indicating the temporal interval where the signal perturbation occurs.

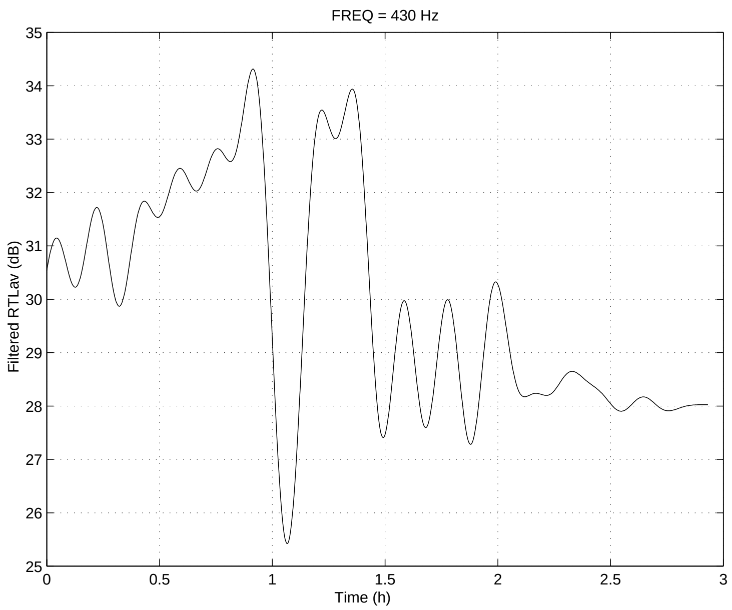

Figure 9. Averaged and smoothed transmission loss at 430 Hz.

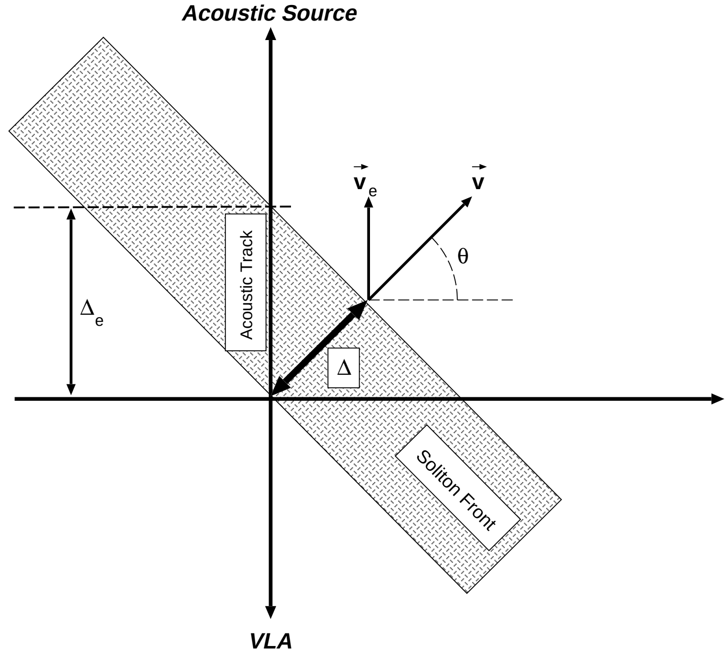

Figure 10. Considered geometry of SWP propagation.

to the significant differences between the sampling rate of hydrographic data (1 sample every 10 minutes) and the rate of acoustic transmissions (1 transmission every 8 seconds). To clarify this issue we exploited the theoretical knowledge of soliton propagation to generate "soliton-like" fields of temperature and sound velocity and used them as input for the acoustic model C-SNAP (Ferla *et al.*, 1993). From a previous estimation of internal tide propagation (Rodríguez *et al.*, 1998) the angle of propagation of SWP was estimated as $\theta \approx 15°$ (see Fig. 10). The solutions Eqs. (4) and (7) were used to derive a single "sech" profile and several "dnoidal" profiles, with the number of solitons within each packet being controlled by s and τ.

Acoustic simulations were performed with C-SNAP at 430 Hz and for several realization of such fields, as if SWPs were propagating from the VLA to the North Position. For each soliton profile one finds a complex dependence of TL on the particular characteristics and position of the SWP. The best result of simulations was obtained for a "dnoidal" packet with four solitons (see Fig. 11). The simulated TL reproduces the behaviour of attenuation, signal increase and attenuation again, and also shows an irreversible shift from around 61 dB to a level around 54 dB. However the pattern is not symmetric around the attenuation maxima and the signal increase lasts twice as long as in the experimental data. Calculations of TL

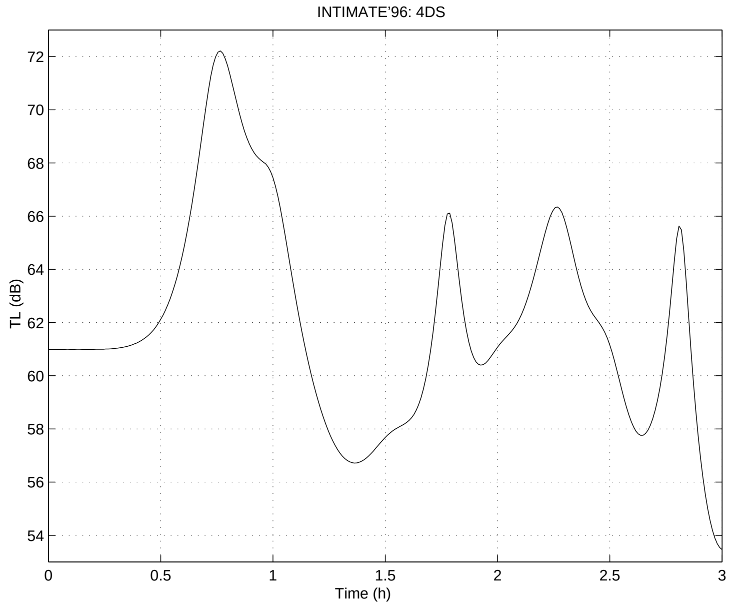

Figure 11. Simulated transmission loss at 430 Hz.

at additional frequencies (see Fig. 12) reveal the effect of signal increase if the constraint of keeping only 10 propagating modes is applied. Again in simulations the effect of signal increase is broader than that observed, and it holds only for some frequencies. It should be noted that according to the simulations the complex distribution of TL presented in Fig. 11 is the result of propagation of the acoustic signal through a part of the "dnoidal" SWP as it starts to pass over the VLA. Furthermore, progressive propagation of the soliton packet will lead to an irreversible shift in TL but it will not be followed by a perturbation pattern like the one shown in Fig. 9 exhibiting signal attenuation, signal focusing and attenuation again.

The simulations described above concerned propagation from the point of view of normal modes. However, it was also important to obtain some support with the help of ray tracing. To accomplish this task a preliminary range-independent ray tracing for a narrow beam of rays was performed (see Fig. 13), using the sound speed profile of the INTIMATE'96 experiment and assuming a geometry of propagation like the one described in the discussion of acoustic transmissions. The main goal of these simulations was to determine if the refraction of rays due to their propagation through the SWP can be consistent with the simulation results. To simplify this task the ray-tracing was performed by calculating only a part of all the

This is twice more than the number of propagating modes considered in (Zhou *et al.*, 1991).

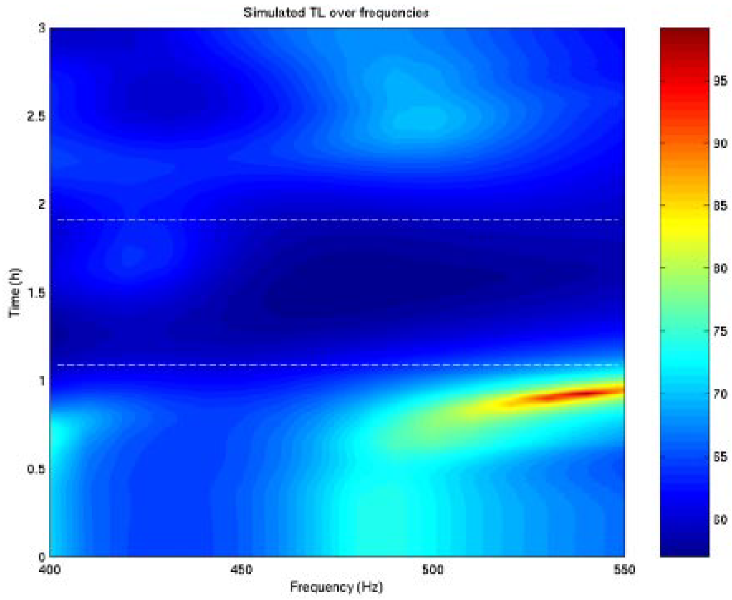

Figure 12. Dynamic simulations over frequency, with dashed lines indicating the temporal interval where the focusing occurs.

possible rays and within a small aperture of the acoustic source. From the figure it can be seen that the beam width increases monotonically with range. Two cases of range-dependent ray-tracing were considered: the first for the position of the "dnoidal" SWP where signal attenuation was found (see Fig. 14, on top), and the second, were the SWP leads to signal increase (see Fig. 14, on bottom). From the ray-tracing it can be seen that the SWP leads to additional refraction of rays at the end of the ray beam. However, the refraction acts in different ways depending on the position of the SWP: when compared with the range-independent case, the beam becomes wider in the first case and narrower (or "focussed") in the second. This indicates that one can expect a decrease of signal amplitude followed by an increase as the SWP propagates towards the source. These ray tracing simulations agree qualitatively with the results that were obtained with C-SNAP.

The quantitative differences between real data and simulations indicate that the soliton profile which provided the best results does not give the closest estimate to the real soliton perturbation. However, the qualitative agreement achieved confirms the assumption of propagating SWPs providing the appropriate conditions for the observation of the signal increase.

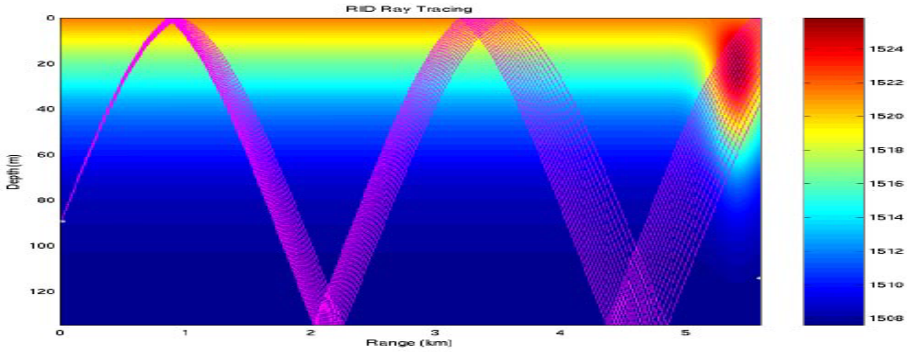

Figure 13. Range-independent ray-tracing; for the sake of simplicity only a part of all the possible rays is plotted. Part of the “dnoidal” SWP is plotted for comparison with the range-dependent cases (see below). The hydrophone is considered to be near 30 m depth.

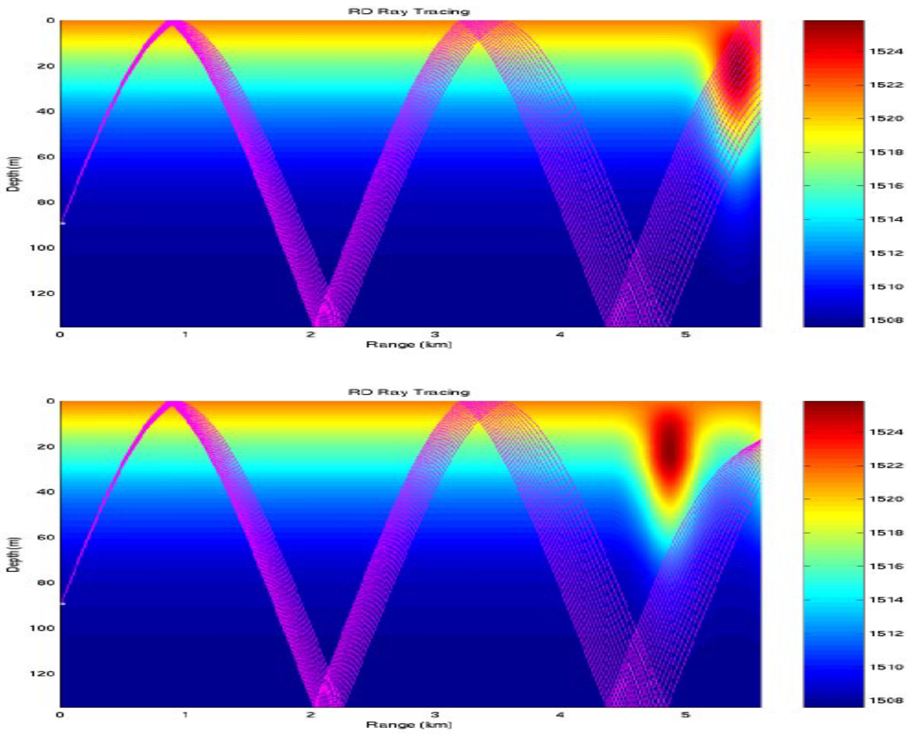

Figure 14. Range-dependent ray-tracing showing beam spreading *(on top)* and focusing *(on bottom)*.

5. Conclusions

On the basis of this analysis the following conclusions can be drawn: from the nonlinear rotationless form of the hydrodynamic equations it can be shown that a stratified environment admits the generation of "modal" solitons, with characteristics that depend on Hydrodynamic Normal Modes (HNMs). The "sech" solution of the KdV equation describes a single modal nonlinear perturbation, which propagates in range and time without changing its shape, while the "dnoidal" modal solution of the same equation describes a dynamically evolving SWP, where the number of solitons inside the packet varies in range and time. Further analysis of the nonlinear rotationless form of Hydrodynamic Equations indicates that modal amplitudes of current and temperature will be proportional to modal vertical displacement, i.e., will exhibit a similar "soliton-like" shape; this can be exploited to generate physically consistent "soliton-like" distributions of temperature and sound velocity. The filtering of modal amplitudes of current and thermistor records from the INTIMATE'96 experiment into low-pass and high-pass frequency components reveals possible propagation of SWPs across the experimental site; one of the SWPs is coincident with an increase of signal amplitude, which can be due to a focusing effect. The set of acoustic range-dependent and time-dependent simulations through "soliton-like" fields of sound velocity agree with observations when a particular "dnoidal" profile is considered; the results of normal-mode calculations are qualitatively supported with range-dependent ray tracing tests for the positions of the SWP where the normal mode results indicate successive signal attenuation and signal increase.

References

Small, J., Hallock, Z., Pavey, G. and Scott, J. (1995), Observations of large amplitude internal waves at the Malin Shelf edge during SESAME 1995, *Continental Shelf Research*

Jeans, D.R.G. and Sherwin, T.J. (1996) Solitary Internal Waves on the Iberian Shelf, *MORENA Scientific and Technical Report No.44* Project MAST II MAS2-CT93-0065

Zhou, J., Zhang, X. and Rogers, P. (1991) Resonant interaction of sound wave with internal solitons in the coastal zone, *J. Acoust. Soc. America* Vol. **90** no. 4, pp. 2042–2054

Caille, G.W., Dahl, P.H., Gan, Z., Jin, G., Lei, L., Rogers, P.H., Spindel, R.C., Sun, Z. Zhang, R. and Zhou, J. (1997) Overview of the Joint Chine-U.S. Yellow Sea-96 Experiment, *Proceedings of the SWAC'97 Conference in Beijing* pp. 17–22

Apel J.R.(1987), *Principles of Ocean Physics*

Ostrovsky, L.A. (1978) Nonlinear Internal Waves in a rotating ocean, *Oceanology* Vol. **18** no. 2, pp. 119–125

Apel, J.R., Badiey, M., Chiu, C., Finette, S. , Headrick, R., Kemp, J., Lynch, J.F., Newhall, A., Orr, H., Pasewark, B.H., Tielburger, D., Turgut, A., Heydt, K. and Wolf, S. (1997) An Overview of the 1995 SWARM Shallow-Water Internal Wave Acoustic Scattering Experiment, *IEEE Journal of Oceanic Engineering* Vol. **22** no. 3, pp. 465–500

Gabov S.A. (1988) *Introduction to the theory of nonlinear waves (in russian)*

Apel, J., Orr, M., Finette, S. and Lynch, J. (1997) A new model for internal solitons and tides on the continental shelf, *Proceedings of the SWAC'97 Conference in Beijing* pp. 219–225

LeBlond, P.H. and Mysak, L.A. (1989) *Waves in the Ocean*

Rodríguez, O.C., Jesus, S., Stephan, Y., Demoulin, X., Porter, M. and Coelho, E. (1998) Internal Tide Acoustic Tomography: Reliability of the normal modes expansion as a possible basis for solving the inverse problem, *Proceedings of the 4th. European Conference on Underwater Acoustics in Rome* pp. 587–592

Ferla, C.M., Porter, M.B. and Jensen, F.B. (1993) C-SNAP: Coupled SACLANTCEN normal mode propagation loss model, *SACLANT UNDERSEA RESEARCH CENTRE (SM-274)*, La Spezia, Italy

Single hydrophone source localization

S.M. Jesus, M.B. Porter, Y. Stéphan, X. Démoulin, O. Rodriguez and E. Coelho

Abstract— **The method presented in this paper assumes that the received signal is a linear combination of delayed and attenuated uncorrelated replicas of the source emitted waveform. The set of delays and attenuations, together with the channel environmental conditions, provide sufficient information for determining the source location. If the transmission channel is assumed known, the source location can be estimated by matching the data with the acoustic field predicted by the model conditioned on the estimated delay set. This paper presents alternative techniques, that do not directly attempt to estimate time delays from the data but, instead, estimate the subspace spanned by the delayed source signal paths. Source localization is then done using a family of measures of the distance between that subspace and the subspace spanned by the replicas provided by the model. Results obtained on the INTIMATE'96 data set, in a shallow water acoustic channel off the coast of Portugal, show that a sound source emitting a 300-800 Hz LFM sweep could effectively be localized in range or depth over an entire day .**

Keywords—**Source localization, subspace methods, shallow water, broadband.**

I. Introduction

The aim of single hydrophone broadband source localization is to provide a range/depth localization approach for coherently using the information contained in the time series received by a single hydrophone.

Classical matched-field processing (MFP) methods mostly use vertical or horizontal hydrophone arrays with significant apertures in order to obtain sufficient source location spatial discrimination. The reader is referred to the pioneering work of Hinich [1] and Bucker [2] and to Baggeroer *et al.* [3] and references therein, for a full overview of the classical work done in MFP. Although many studies used MFP with single frequency data (tones), some do combine information at different frequencies. Both incoherent and coherent forms have been studied providing what are effectively broadband MFP (BBMFP) estimators [4], [5],[6].

Source localization in the time domain was first clearly suggested by Clay [7][1] who used a time reversal of the channel impulse response to reduce transmission distortion and (in simulation) localize a source. Li *et al.* [9] used the same technique for localizing a source in a laboratory waveguide using air as the medium of propagation. Single hydrophone localization in particular, was studied by Frazer [10] who introduced several Clay-like estimators and tested them on simulated data. In 1992, Miller *et al.*[11] showed, using computer simulations, that it is possible to localize short duration acoustic signals in a realistic range-dependent environment, while, the same method was applied for range and bearing estimation using bottom moored sensors in [12]. Time domain source localization was actually achieved by Brienzo *et al.*[13] using data received on a vertical array in a deep water area on the Monterey fan. In this case, a generalized conventional beamformer was used for recombining the received data in time domain (matched-filter), and then between sensors in space domain (beamformer).

In shallow water, arrival time estimation is in many practical situations compromised due to the low signal-to-noise ratio (SNR) and/or to the difficulty in resolving individual paths[14]. Furthermore, because of such factors as bottom interaction and ocean variability, shallow water presents many challenges for accurate acoustic modeling. Nevertheless, in a more recent study, it has been demonstrated that with suitably robust processors, received and model-predicted waveforms could be correlated at a single array sensor yielding practical schemes for source tracking [15],[16]. In this case, the lack of spatial information was "compensated" by coherent broadband processing.

Difficulties associated with single hydrophone localization are obviously related with the lack of spatial diversity. Thus, a key point of interest, is to understand the degree to which spatial aperture can be compensated for using broadband information. The method proposed in this paper goes along the lines of those being used in ocean tomography, where the features of interest for ocean characterization are the time delays associated with the different acoustic paths (or rays)[17]. Our approach does not directly attempt to estimate time delays from the data but, instead, searches for the source location for which the time delay set maximizes a mean least squares criteria. In that sense it gives a mean least squares solution constrained to the given acoustic model.

Making the further assumption that there are features (clusters of acoustic arrivals) that are decorrelated, allows us to extend this approach to signal-noise subspace splitting. In that case estimating source location is equivalent to measuring the distance between the estimated signal subspace and the subspace spanned by the delayed source signal paths given by the acoustic model. Such subspace-based distance measures are shown to yield good source

This work was partially supported under PRAXIS, FCT, Portugal and by the Office of Naval Research.

S.M. Jesus and O. Rodriguez are with UCEH - Universidade do Algarve, Campus de Gambelas, PT-8000 Faro, Portugal. E-mail: sjesus@ualg.pt .

M.B. Porter is with the Center for Communications and Signal Processing Research and Dept. of Mathematical Sciences, NJIT, Newark, NJ, USA. E-mail: porter@oalib.njit.edu.

Y. Stéphan and X. Démoulin are with CMO-Service Hydrográphique et Oceanográphique de la Marine, F-29275 Brest Cedex, France. E-mail: stephan@shom.fr

E. Coelho is with Instituto Hidrográfico, Rua das Trinas 49, PT-1296 Lisboa, Portugal.

[1]although source localization feasibility had been mentioned 10 years earlier by Parvulescu [8].

location estimates on real data.

This paper is organized as follows: Section 2 presents the linear data model and the assumptions that underline the methods being developed. Section 3 presents the classical time-delay estimation (TDE) problem. Section 4 extends TDE methods to source localization by including the environmental information. The resulting algorithm is then tested, with simulated data, in section 5. Section 6 shows the results obtained on a data set recorded in a shallow water area off the west coast of Portugal, during the INTIMATE'96 experiment in June 1996 and finally, section 7, discusses the results and draws some conclusions.

II. Linear data model

According to the linear data model, the received acoustic signal due to a source at location $\theta_s = (r_s, z_s)$ is given by

$$y_n(t, \theta_s) = z_n(t, \theta_s) + \epsilon_n(t), \tag{1}$$

where ϵ is the noise sequence, assumed spatially and temporally white, zero-mean and uncorrelated with the signal, $t = 1, \ldots, T$ is the discrete-time index within each n-index time snapshot and z is the noise-free signal given by

$$z_n(t, \theta_s) = p_n(t, \theta_s) * s_0(t). \tag{2}$$

Here, s_0 is the source emitted waveform and p is the channel impulse response. Under the assumption that the medium between the source and the receiver behaves as a multiple time delay-attenuation channel, its impulse response can be written

$$p_n(t, \theta_s) = \sum_{m=1}^{M} a_{n,m}(\theta_s)\delta[t - \tau_{n,m}(\theta_s)], \tag{3}$$

where the $\{a_{n,m}(\theta_s), \tau_{n,m}(\theta_s); n = 1, \ldots, N; m = 1, \ldots, M\}$ are respectively the signal attenuations and time delays along the M acoustic paths at time snapshots $n = 1, \ldots, N$.

To proceed with the estimation of the $\tau_{n,m}; m = 1, \ldots, M; n = 1, \ldots, N$ time delays, it is necessary to assume that the variation in time delays is small within each N snapshot data set, i.e., that $\tau_{n,m} = \tau_m + \delta\tau_{n,m}$ where $\delta\tau_{n,m} \ll \tau_m$ and $\delta\tau_{n,m} \ll T_0$ where T_0 is the observation time($T_0 = NT\Delta t$, where Δt is the sampling interval). That additional assumption allows one to write

$$z_n(t, \theta_s) = \sum_{m=1}^{M} a_{n,m}(\theta_s)s_0[t - \tau_m(\theta_s)], \tag{4}$$

where $\tau_m(\theta_s)$ is the mean arrival time of path m within the observation time T_0. With the assumptions made in (4) one can now rewrite (1) as

$$\mathbf{y}_n(\theta_s) = \mathbf{S}[\boldsymbol{\tau}(\theta_s)]\mathbf{a}_n(\theta_s) + \boldsymbol{\epsilon}_n, \tag{5}$$

with the following matrix notations,

$$\mathbf{y}_n(\theta_s) = [y_n(1, \theta_s), y_n(2, \theta_s), \ldots, y_n(T, \theta_s)]^t, \quad \dim T \times 1 \tag{6a}$$

$$\boldsymbol{\tau}(\theta_s) = [\tau_1(\theta_s), \ldots, \tau_M(\theta_s)]^t, \quad \dim M \times 1 \tag{6b}$$

$$\mathbf{s}_0(\tau) = [s_0(-\tau), \ldots, s_0((T-1)\Delta t - \tau)]^t, \quad \dim T \times 1 \tag{6c}$$

$$\mathbf{S}[\boldsymbol{\tau}(\theta_s)] = [\mathbf{s}_0(\tau_1), \ldots, \mathbf{s}_0(\tau_M)], \quad \dim T \times M \tag{6d}$$

and

$$\mathbf{a}_n(\theta_s) = [a_{n,1}(\theta_s), \ldots, a_{n,M}(\theta_s)]^t, \quad \dim M \times 1 \tag{6e}$$

where T is the number of time samples on each snapshot and M is the number of signal replicas at the receiver. Equation (5) forms a linear model on the amplitude vector $\mathbf{a}$, where further assumptions on the relative dimensions and rank of matrix $\mathbf{S}$ and noise distributions allow for different solutions for the estimation of $\boldsymbol{\tau}$. For simplicity the dependence of $\boldsymbol{\tau}$ and $\mathbf{a}$ on the source location parameter θ_s will be omitted in the next two sections.

III. Time delay and amplitude estimators

In model (5) both the amplitude and the time delay vectors are unknown. However, as discussed in the introduction, we prefer to focus on the time delay vector for localization which should be a more stable feature and therefore yield a more robust processor. There are two possible approaches for solving this problem: the first is to consider that the amplitude vector is deterministic and therefore both $\mathbf{a}$ and $\boldsymbol{\tau}$ are to be estimated; the second considers that $\mathbf{a}$ can also be random and then one has to resort to second order statistics for estimating the time-delay vector $\boldsymbol{\tau}$. These two approaches will be formulated in the next subsections.

A. Deterministic amplitudes

To begin one needs some estimate of the amplitude vector $\mathbf{a}$. This is a sort of classical problem and may be easily addressed using least squares(LS), or under the Gaussian white noise assumption, as a generalized maximum likelihood (ML) problem. In either case, one obtains the following:

$$\hat{\mathbf{a}} = \arg\{\min_{\mathbf{a}} e(\boldsymbol{\tau}, \mathbf{a}) = \parallel \mathbf{y} - \mathbf{S}(\boldsymbol{\tau})\mathbf{a} \parallel^2\}, \tag{7}$$

whose solution is well-known to be

$$\hat{\mathbf{a}} = (\mathbf{S}^H\mathbf{S})^{-1}\mathbf{S}^H\mathbf{y}, \tag{8}$$

where ^{H} indicates complex conjugate transpose. Inserting $\hat{\mathbf{a}}$, of (8), in (5) the problem now becomes that of estimating a known signal in white noise (for each assumed $\boldsymbol{\tau}$). The optimal solution is given by the well known matched-filter. That can be seen by plugging (8) into (7) to obtain a new function to be maximized,

$$e(\boldsymbol{\tau}) = \parallel \mathbf{y}^H\mathbf{S}(\boldsymbol{\tau}) \parallel^2, \tag{9}$$

which is now only a function of delay vector $\boldsymbol{\tau}$. Passing from (7) to (9), requires the additional assumption that the matrix $\mathbf{S}$ is orthogonal, *i.e.*, that $\mathbf{S}^H\mathbf{S} = \mathbf{I}$. In terms of propagation, that assumption is equivalent to assuming that signals travelling along different paths suffer uncorrelated perturbations. Whether this occurs in practice depends on a variety of factors.

The description above assumes that only a single measurement $\mathbf{y}$ is available. If instead there are N randomly distributed vectors inserted in a matrix as $\mathbf{Y} = [\mathbf{y}_1, \ldots, \mathbf{y}_N]$, of dimension $T \times N$, the problem is formulated as the minimization of

$$\| \mathbf{Y} - \mathbf{S}(\boldsymbol{\tau})\mathbf{A} \|^2, \tag{10}$$

where $\mathbf{A}$ is now a $M \times N$ matrix containing the M signal amplitudes at N times. In this case the solution for $\mathbf{A}$ is analogous to (8),

$$\hat{\mathbf{A}} = (\mathbf{S}^H\mathbf{S})^{-1}\mathbf{S}^H\mathbf{Y}. \tag{11}$$

Substituting (11) into (10) gives the new function for $\boldsymbol{\tau}$

$$e(\boldsymbol{\tau}) = \frac{1}{N}\sum_{n=1}^{N} \| \mathbf{y}_n^H \mathbf{S}(\boldsymbol{\tau}) \|^2 . \tag{12}$$

In this case, and for an infinite observation time, one can estimate the M time delays from the M highest peaks of function (12), *i.e.*,

$$\{\hat{\tau}_m^{\mathrm{LS}}; m = 1, \ldots, M\} = \arg\{\max_{\tau} \sum_{n=1}^{N} \| \mathbf{y}_n^H \mathbf{s}_0(\tau) \|^2\}, \tag{13}$$

and then replace the time delay estimates obtained from (13) into matrix $\mathbf{S}$ of the amplitude estimator (11) and iterate. In practice, for a finite observation time, (12) may not exhibit M clear peaks and a complex M-dimensional search may be required to solve (13). As it will be seen below, such complex search procedure is not needed here since only the value of the functional (12), at model predicted values of $\boldsymbol{\tau}$, is necessary for source localization.

B. Random amplitudes

Once model (5) has been adopted, an additional assumption on the mutual decorrelation of the multipath amplitudes (assumed now as random and zero mean), allows one to extend the least squares or maximum likelihood (LS/ML) method above, to subspace separation based methods[2]. In fact, the linear model (5) allows one to characterize the signal part as covering a $K(< M)$-dimensional subspace where K is the number of uncorrelated paths (or groups of paths) in the received signal— this is the signal subspace.

In general, a number $N \geq M$ of uncorrelated time snapshots are available which is a requirement for estimating the signal subspace. Let us consider the data matrix $\mathbf{Y}$ and its SVD $\mathbf{Y} = \mathbf{U}\boldsymbol{\Sigma}\mathbf{V}^H$. Since $T > N$, $\mathbf{Y}$ has a maximum rank of N. Taking into account the linear model (5) with the assumptions made on the decorrelation of noise, signal and amplitude components, it can be shown [18] that the M eigenvectors $\{\mathbf{u}_1, \ldots, \mathbf{u}_M\}$ associated with the M largest singular values $\sigma_1 \geq \sigma_2 \geq \ldots, \geq \sigma_M$ provide the optimal estimate (in the sense of least squares and maximum likelihood) of the signal subspace. Indeed the vectors $\mathbf{u}_m; m = 1, \ldots, M$ span the same (signal) subspace as the M signal replicas $\mathbf{s}_0(\tau_1), \ldots, \mathbf{s}_0(\tau_M)$. Therefore, considered as a function of search delay τ, the projection of the signal replicas onto the subspace spanned by the first M eigenvectors will be a maximum for $\tau = \tau_m; m = 1, \ldots, M$. Thus we seek the maxima of the functional

$$e(\tau) = \| \mathbf{U}_M^H \mathbf{s}_0(\tau) \|^2, \tag{14}$$

where $\mathbf{U}_M = [\mathbf{u}_1, \ldots, \mathbf{u}_M]$. Using (14), the associated signal subspace (SS) based time delay τ_m estimator can be written

$$\{\hat{\tau}_m^{\mathrm{SS}}; m = 1, \ldots, M\} = \arg\{\max_{\tau} \ \| \mathbf{U}_M^H \mathbf{s}_0(\tau) \|^2\}. \tag{15}$$

Similarly, knowing that $\mathbf{U}_M$ and its complement $\mathbf{U}_{T-M} = \mathbf{U}_M^{\perp}$ split the whole space $\Re^T$ into two orthogonal subspaces, the projection of the signal replicas onto the $\mathbf{U}_M$ signal subspace complement (denoted $\mathrm{SS}^{\perp}$ in the sequel) will tend to zero for the same true values of τ. Therefore, the noise subspace based time delay τ_m estimator is given by

$$\{\hat{\tau}_m^{\mathrm{SS}^{\perp}}; m = 1, \ldots, M\} = \arg\{\max_{\tau} [\| \mathbf{U}_{T-M}^H \mathbf{s}_0(\tau) \|^2]^{-1}\}, \tag{16}$$

where the matrix $\mathbf{U}_{T-M} = [\mathbf{u}_{M+1}, \ldots, \mathbf{u}_T]$ is formed from the data eigenvectors associated with the $M+1$ to T smallest singular values. These eigenvectors span the subspace containing the non-signal components, so the estimator is generally called the noise subspace or signal subspace orthogonal estimator.

IV. Source localization

The source localization problem can be readily deduced from the last sections both for the LS/ML and the subspace separation based methods. Until now only the received signal was used for analysis but source localization requires data inversion for source properties. That means, in particular, that the medium where the signal is propagating has to be taken into account using a specific propagation model to solve the forward problem. The propagation model determines a set of time delays at the receiver for the given environment and for each hypothetical source location.

Let us define $\boldsymbol{\tau}(\theta)$ as the model-calculated time delay vector for source location θ, conditioned on a given environmental scenario. For all possible values of θ in a set Θ, the vector $\boldsymbol{\tau}(\theta)$ will cover a continuum on an M-dimensional space as does the source replica vector. In other words, the source replica vectors span a subspace $S(\theta)$ that has dimension M under the assumption of uncorrelated paths

$$S(\theta) = \mathrm{range}(\mathbf{S}[\boldsymbol{\tau}(\theta)]) = \mathrm{range}\{\mathbf{s}_0[\boldsymbol{\tau}(\theta)]; \theta \in \Theta\}. \tag{17}$$

As explained in the previous section, an estimate of the actual $S(\theta_s)$ subspace associated with the true source location can be obtained as the span of the M eigenvectors contained in $\mathbf{U}_M$:

$$\hat{S}(\theta_s) = \mathrm{range}(\mathbf{U}_M). \tag{18}$$

[2]subspace methods do not require random amplitudes that can be either random or deterministic

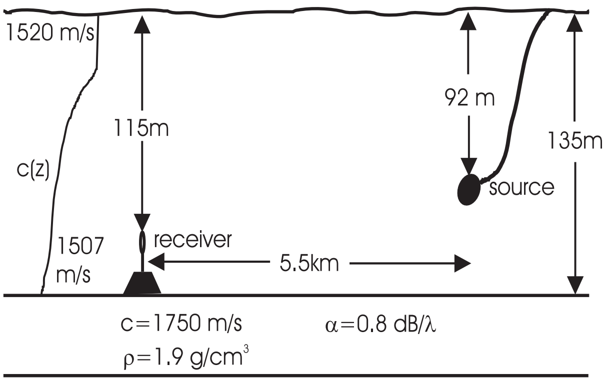

Fig. 1. INTIMATE'96 environmental scenario used for simulation.

Those two subspaces share the same dimension M. An estimator $\hat{\theta}_s$ of θ_s could, in principle, be derived from the notion of distance between subspaces. This is usually based on respective projections but alternatively one may use the CS decomposition theorem [19] and define the distance measure

$$d(\theta) = \sqrt{1 - \sigma^2_{min}(\mathbf{U}_M^H \mathbf{S}[\boldsymbol{\tau}(\theta)])}, \qquad \theta \in \Theta \qquad (19)$$

where $\sigma_{min}(\bullet)$ is the minimum singular value of matrix $\bullet$. The distance measure (19) has poor performance for estimating the source location parameter θ_s, since it mainly depends on the estimation of the smallest eigenvalue of a matrix that is itself highly dependent on the SNR. In practice, M is not known and varies with θ which introduces further sensitivity into $d(\theta)$.

Alternatively, a constrained LS/ML based estimate $\hat{\theta}_{\mathrm{LS}}$ of source location θ_s will be, according to (12)-(13), given by the value of θ that satisfies

$$\max_{\boldsymbol{\tau}(\theta)} \frac{1}{N} \sum_{n=1}^{N} \parallel \mathbf{S}[\boldsymbol{\tau}(\theta)]^H \mathbf{y}_n \parallel^2, \qquad \theta \in \Theta. \qquad (20)$$

The resulting source location estimator can therefore be written as

$$\hat{\theta}_{\mathrm{LS}} = \arg\{\max_{\boldsymbol{\tau}(\theta)} \frac{1}{N} \sum_{n=1}^{N} \sum_{m=1}^{M} \parallel \mathbf{s}_0[\tau_m(\theta)]^H \mathbf{y}_n \parallel^2\}, \qquad \theta \in \Theta. \qquad (21)$$

Similarly, using (15) and (21) for the SS approach, the source location estimate corresponds to the maximum of the sum over paths of the projections of the replica signal for each time delay set onto the estimated signal subspace,

$$\hat{\theta}_{\mathrm{SS}} = \arg\{\max_{\boldsymbol{\tau}(\theta)} \sum_{m=1}^{M} \parallel \mathbf{U}_M^H \mathbf{s}_0[\tau_m(\theta)] \parallel^2\}, \qquad \theta \in \Theta. \quad (22)$$

Finally, for the $\mathrm{SS}^\perp$ approach, the function is searched for the minimum of the sum over paths of the projections onto the noise subspace estimate,

$$\hat{\theta}_{\mathrm{SS}^\perp} = \arg\{\min_{\boldsymbol{\tau}(\theta)} \sum_{m=1}^{M} \parallel \mathbf{U}_{T-M}^H \mathbf{s}_0[\tau_m(\theta)] \parallel^2\}, \qquad \theta \in \Theta. \qquad (23)$$

Depth (m)	**Sound speed** (m/s)
0.0	1520
5.0	1520
11.3	1518
21.3	1516
32.0	1512
42.7	1510
72.8	1508
94.6	1507
135.0	1507

TABLE I

MEASURED SOUND SPEED PROFILE USED IN THE SIMULATION EXAMPLE.

V. Simulation Results

In order to test the methods presented in the previous section, and to have a feeling of their performance on real data, the environmental and geometry scenario used for simulation was the same as that of the real data of next section. Let us consider the case of an LFM sweep with a duration $D_t = 1s$ and a frequency band from 200 to 400 Hz. The signal is transmitted in a 135 m depth waveguide with a slightly downward refracting sound speed profile (table 1) over a sandy bottom characterized by a 1750 m/s sound speed, a density of 1.9 g/cm^3 and a compressional attenuation of 0.8 dB/λ (figure 1).

The ray-arrival times and amplitudes predicted with Bellhop [20] for a sound source and a receiver at 92 and 115 m depth respectively and at 5.6 km range from each other, are shown in figure 2. The arrivals are arbitrarily ordered in accordance with their take-off angle at the source. The intermediate angles correspond to rays which are launched nearly horizontally, therefore with smaller amplitude loss as seen in figure 2(a). Their path lengths are shorted yielding a sort of bowl-shaped arrival time pattern seen in figure 2(b).

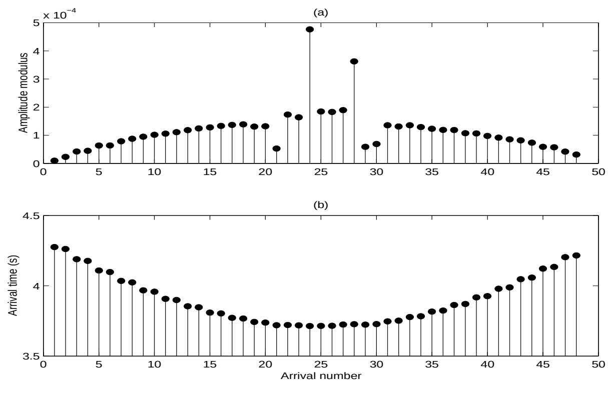

Fig. 2. Ray-model predicted arrival amplitudes (a) and times (b).

A number of $N = 100$ snapshots was generated according to model (5) with a high SNR (>20 dB) and the decorrelation between multipath amplitudes was simulated by generating a Gaussian vector with its mean equal to the value given by the model (figure 2(a)), and its standard deviation $\sigma_a = 0.5 \parallel \mathbf{a} \parallel$. The corresponding arrival pattern, based on (13), is shown in figure 3. Note that there are many more arrivals in figure 2 than we see as peaks in figure 3. This indicates that there are many unresolved paths. (With increased bandwidth, these paths would be resolved.)

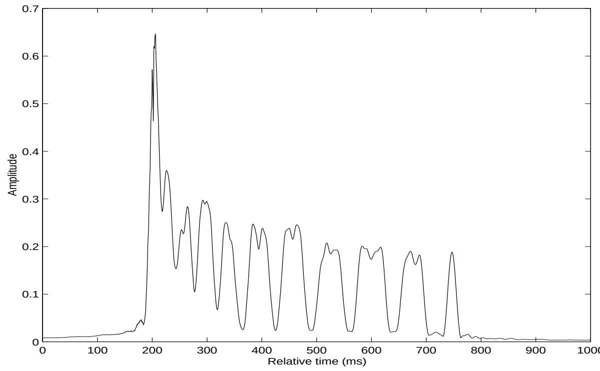

Fig. 3. Arrival pattern with LS/ML estimator [eq.(13)].

Figure 4 shows the arrival pattern for the same data set but using the signal subspace estimator (15) with the number of arrivals set to the true number, *i.e.*, $M = 48$. Notice that the higher resolution allows to distinguish many more arrivals. The amplitudes are not proportional to the received signal correlation since no eigenvalue weighting was used to project the source signal onto the signal subspace. Figure 5 shows the arrival pattern obtained with the noise subspace estimator (16). The path resolution is the same as that of the signal subspace method. However, it is much less sensitive to the actual subspace dimensionality since an underestimation of M would result in a mis-projection onto the signal subspace. Numerically, this is a large number and therefore a small contribution to the inverse function in the noise subspace estimator. On the other hand, an over estimation of M would result in a few unobserved directions among several thousand (depending on the value of T) which in practice has little effect on the result. The main practical difficulty is simply the computational cost of manipulating matrices of high dimension. For that reason the estimators were implemented in the frequency domain for the real data analysis of the next section.

VI. Real data analysis

The INTIMATE'96 sea trial was primarily designed as an acoustic tomography experiment to observe internal tides and details of the experimental setup has appeared elsewhere [21]. However, for the sake of completeness, a brief description of the experiment follows. The experiment was conducted in the continental platform near the town of Nazaré, off the west coast of Portugal, during June 1996 and consisted of several phases during which the acoustic

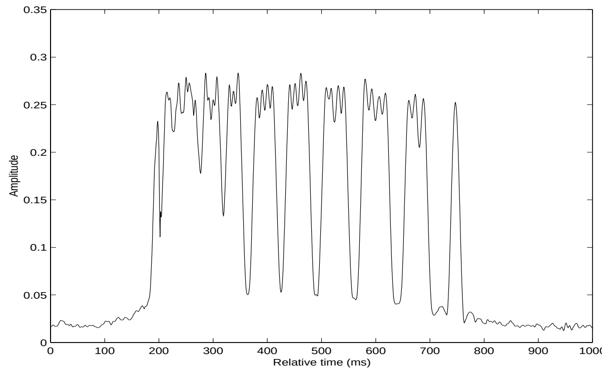

Fig. 4. Arrival pattern with SS estimator [eq.(15)] and M=48.

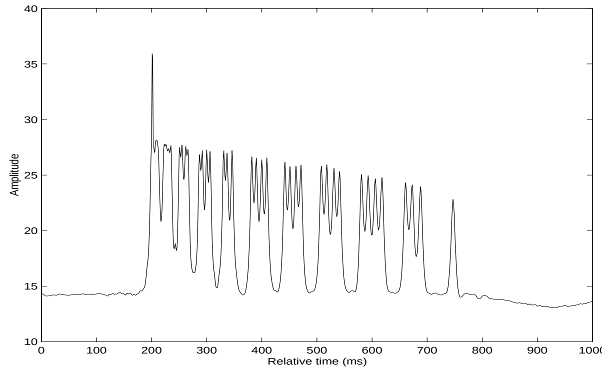

Fig. 5. Arrival pattern with $SS^{\perp}$ estimator [eq.(16)] and M=48.

source was either stationnary or being towed along predetermined paths. This paper is concerned with the data acquired in phase 1 during which the scenario is shown in figure 1 and is identical to that used for the simulations in chapter 5. The only difference is that the source signal used during INTIMATE'96 was a 300-800 Hz LFM sweep with 2 s duration repeated every 8 s. The signal received at 5.5 km range on the 115 m depth hydrophone is shown in figure 6. At that range the time-frequency source signature could be clearly seen (figure 6(a)), while the time-series shows a strong multipath effect (figure 6(b)).

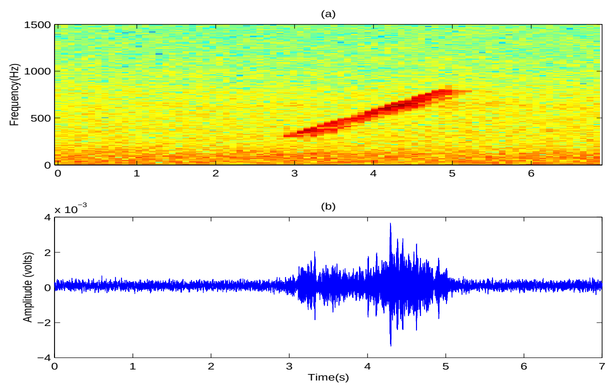

Fig. 6. Received signal at 115 m depth and 5.5 km range: time-frequency plot(a) and time-series (b).

The SNR has been estimated to be approximately 10 dB within the frequency band of interest. As a first test of the match between the predicted arrival times and the estimated arrival patterns, figure 7 shows an example of a received data arrival pattern, using (13). The corresponding predicted arrival times are represented by the vertical lines on the time axis. The agreement between the two patterns is almost perfect for this case. In order to establish a localization statistic, the algorithms described above were used to estimate the source range at a given correct source depth. Separately, we have estimated source depth using a given (correct) range during a 20 hour long run (phase 1) where the source was held at approximately constant range and depth and the environment was nearly range independent with a 135 m depth channel and a slightly downward refracting sound speed (as explained in section 5 and in detail in [21]).

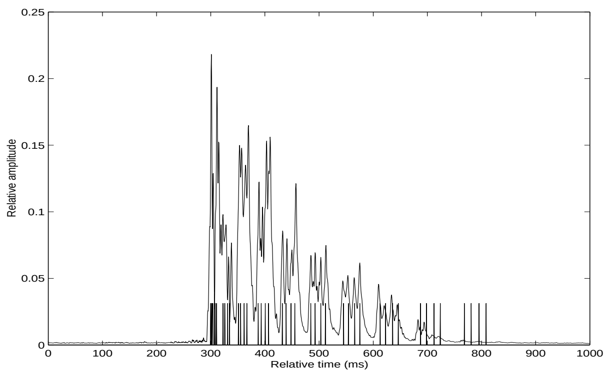

Fig. 7. Arrival pattern using the LS estimator for a sound source at 5.5 km range and 92 m depth received on a sensor at 115 m depth. Vertical lines on time axis represent Bellhop predicted arrival times.

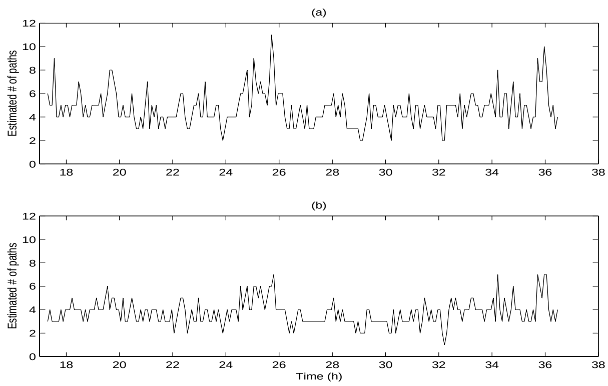

Fig. 8. Estimated number of uncorrelated paths: with Akaike's (AIC) criterion (a) and with the Minimum Description Length (MDL) criterion (b). The start time is 17:20 June 14, 1996.

The first problem encountered when processing the real data using the subspace based methods was the estimation of the number of existing paths, M, in equations (22) and (23). In principle, M can be predicted by the acoustic model for each source range and should be equal to the rank of matrix $\mathbf{S}$. However, in practice, it was found that the matrix $\mathbf{S}$ was largely rank deficient, and the number of estimated uncorrelated paths (or path groups) was much smaller than the number of predicted paths M. Figure 8 shows the number of estimated paths for a 20 hour long run using the classical Akaike Information Criterion (AIC) and Minimum Description Length (MDL) [22]. It can be seen in figure 8 that the estimated number of paths varies from 4 to 5 for AIC and from 3 to 4 for MDL (while the model predicted number of paths is $M = 48$).

It is known that AIC tends to give higher estimates than MDL and in many practical situations to overestimate the model order so these results are anticipated. In our case, the AIC and MDL order estimates inserted in (22) and (23) yield approximately the same results and so we will only present the former. In figure 9 we estimated source range and in figure 10 we estimated source depth. In these figures the three estimators (21), (22) and (23) are respectively shown in ambiguity plots (a), (b) and (c). Taking the peak locations from those plots yields corresponding subplots (d),(e) and (f) showing the estimated location (either range or depth) vs. time. A statistic of the estimated mean and MSE of the proposed estimators is summarized in table 2. The data singular-value decomposition was performed on 35 consecutive data snapshots every 5 minutes - each snapshot containing a single received source waveform. Therefore the data shown has 231 samples along the time axis and, since samples are 5 min apart, the whole data set represents 19.25 hours worth of data.

Figures 9(a) and 9(b), given by the LS/ML and SS estimators, are very similar and show a relatively stable and well defined estimate with a mean source range of 5.48 km (figures 9(d), 9(e) and table 2) which coincides with the mean DGPS range estimate recorded during the cruise. The waving effect seen in time is mainly due to the surface tide (figure 11). The phase coincidence between tide height and the range estimate is striking and simply shows the influence of water depth variation on the multipath time delays structure between the source and the receiver. Figure 9(c), obtained with the signal subspace orthogonal projector, shows a more ambiguous surface - larger mean square error (MSE) - with, however, the same mean source range estimate than for the other estimators (figure 9(f) and table 2). This poorer result is possibly due to the signal subspace rank deficiency mentioned above. The first impression from figure 10, when compared to figure 9, is that the results are poorer for source depth than for source range. This is mainly a function of the axis scales since we localize in range over a wide sweep while depths of interest are limited to the channel depth.

There is also a dependence on the basic variation of the acoustic field; however, in terms of intensity the characteristic scale is a few wavelengths in both range and depth. Among the three estimators shown in figures 10(a), 10(b) and 10(c), is the signal subspace that provided the best mean result with 92 m, very close to the true nominal value and also the lowest estimated MSE. However, all the methods perform well and there is little practical basis for choosing one over the other. The authors also believe that if a broadband random source signal was used the results would be similar as those obtained with the LFM deter-

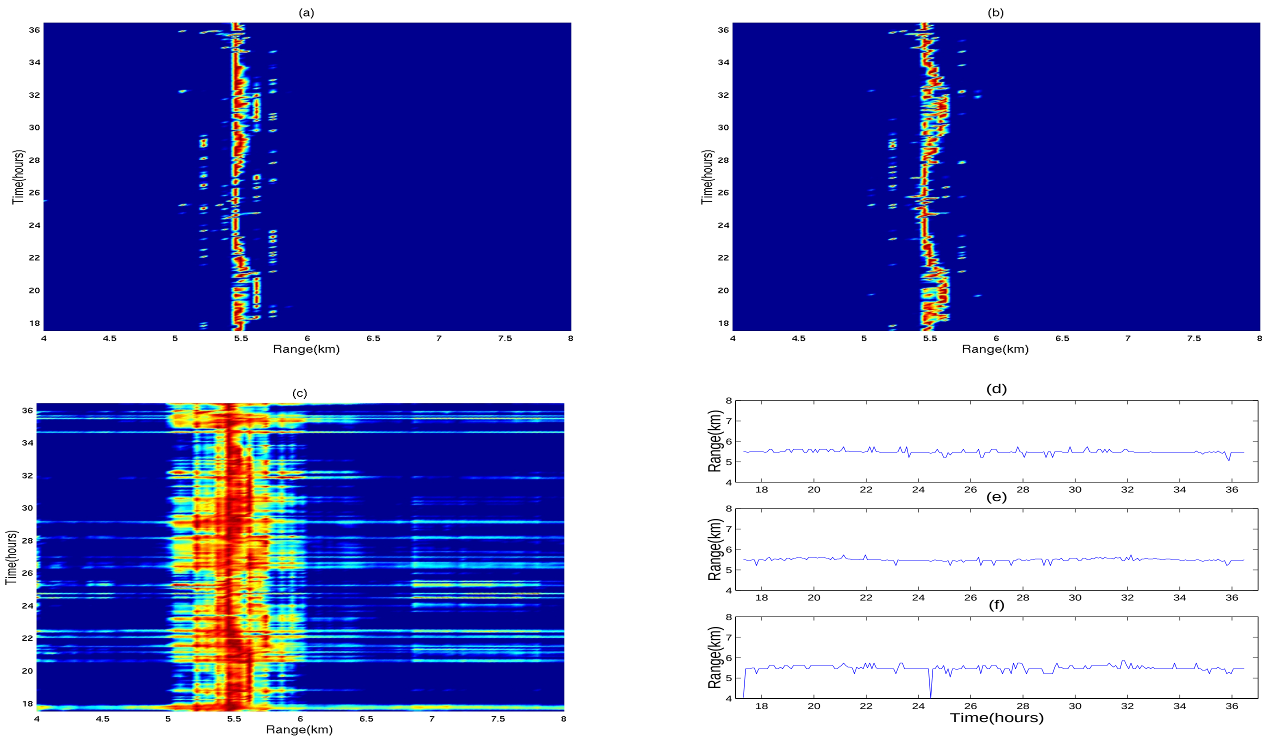

Fig. 9. Time-depth localization plots for INTIMATE'96 phase 1 data set with LS/ML method (a), signal subspace (b) and noise subspace projection (c). Figures (d), (e) and (f) show the depth estimate obtained as the max on each surface (a), (b) and (c) respectively. The start time is 17:20 June 14, 1996.

ministic signals provided that the emitted signal replicas were known at the receiver and that the frequency band was identical.

	Range (m)		**Depth** (m)	
	mean	mse	mean	mse
LS/ML	5.48	9.3	85	348
SS	5.49	7.1	92	259
$SS^{\perp}$	5.48	34.7	80	363

TABLE II
Source localization in range and depth: estimated mean and mean sqare error (MSE) for the three methods: LS/ML, SS and $SS^{\perp}$.

VII. Discussion and conclusions

The discussion of the results can be separated into two distinct aspects: one is the estimation of the arrival times - which is a question of time-delay estimation - and the other is the usage of the estimated pattern to match the predicted arrival times and its impact on source localization. Time-delay estimation has been intensively studied in the underwater acoustic multipath context, see for example [23] - [26], and references therein. Three different methods were presented here only to emphasize the importance of high-resolution of time-delays in presence of limited bandwidth signals. The source localization aspect is much more central to the paper and, in that respect, the results shown should be compared with those obtained in Porter, *et al.* [15],[16], in which a method similar to (21) is used but the correlation is made between the log of the received signal and the log of the predicted arrival signal. The output is the peak of the correlation function. The motivation for that processor is discussed more extensively in those papers. Briefly, the log processor brings into balance the strong early arrivals with the weak late arrivals. The resulting estimator accentuates the basic arrival pattern (in terms of arrival times) rather than the arrival amplitude. However, as the processor is based on a correlation of the complete time-series it is sensitive to both the peaks and valleys of the data. In the present study, even greater emphasis is placed on the arrival-times of the individual paths. In fact, the match function given by (21) is made only *for the predicted arrival times*. In other words, only the peaks of the arrival pattern (assuming the correct prediction of time delays) are used. Obviously, the result will be optimal if the peak locations are correctly predicted and resolved, and this is why subspace methods have been introduced for time-delay resolution enhancement. Conversely, errors on the prediction of arrival times would directly impact on the quality of the localization. In terms of the required computation effort, the methods presented here generally take approximately 5 times the computation time than that required by Porter's method in the same conditions.

This paper has presented a comprehensive method for source localization using broadband signals received on a

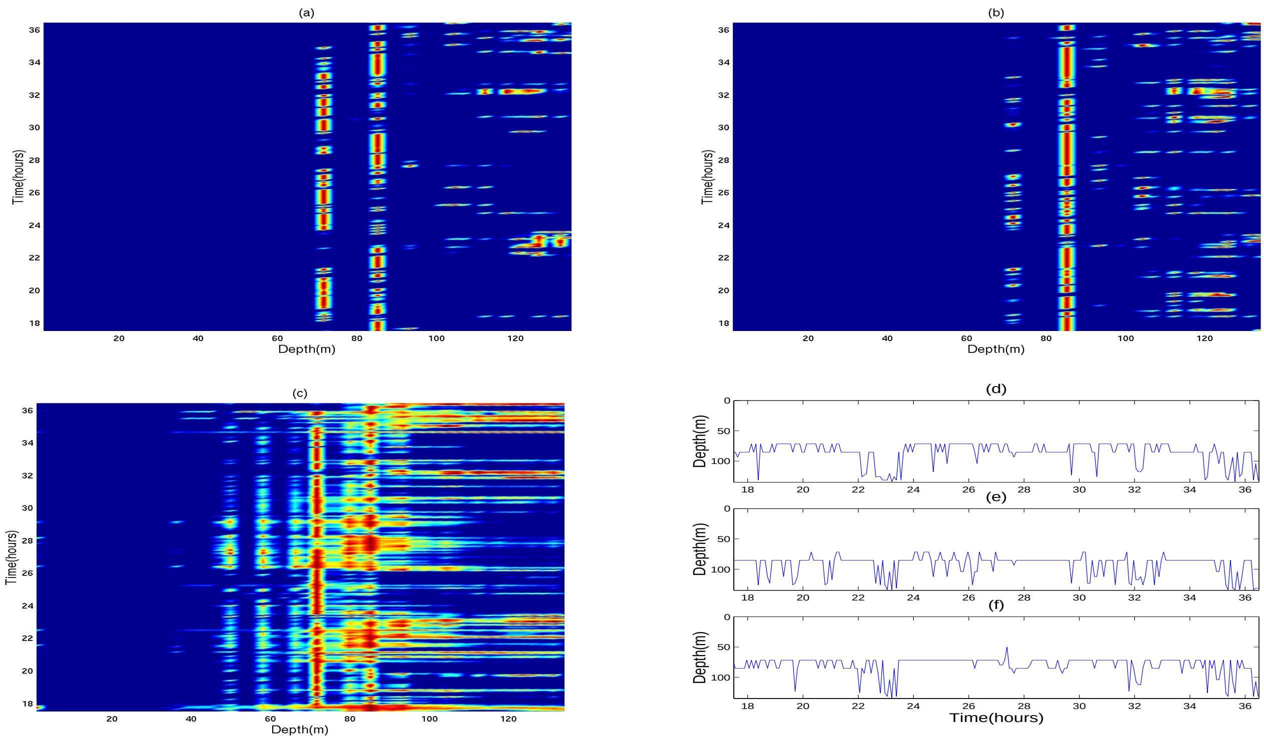

Fig. 10. Time-depth localization plots for INTIMATE'96 phase 1 data set with LS/ML method (a), signal subspace (b) and noise subspace projection (c). Figures (d), (e) and (f) show the depth estimate obtained as the max on each surface (a), (b) and (c) respectively. The start time is 17:20 June 14, 1996.

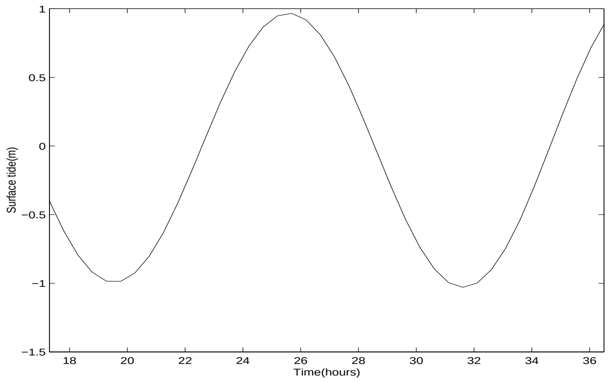

Fig. 11. Surface tide prediction for the receiver location. The start time is 17:20 June 14, 1996.

single hydrophone. The method assumes a classical model of the received data as a linear combination of time delayed replicas of the emitted waveform with unknown but uncorrelated random amplitudes. The received signal is assumed to be corrupted by white Gaussian noise and in all cases the emitted signal is supposed to be known at the receiver. First, classical TDE methods for estimating the time delay set are presented and tested on simulated data. Then subspace based methods are obtained, in a classical way, for estimating the signal subspace spanned by the received paths and its orthogonal complement. It is shown that time delays can be derived from the intersection of the signal subspace estimate and the subspace spanned by the replica signals. For computing the replica signals there are now a variety of well-developed acoustic models suitable for this application including normal mode, PE, wavenumber integration and ray models. Ray models have a clear speed advantage for these broadband applications since the ray approximation produces broadband information (arrival times and amplitudes) for no additional cost. Of course, ray models are also generally the least accurate but they were found fully adequate for our application.

The source location estimators are then computed as the sum of the contributions of the match between the received and replica signals at the predicted arrival times. The match itself is performed in three different ways using, one, the full received signal, two, the projection of the received signal onto the signal subspace and, three, its complement projection onto the noise subspace.

These source location estimators have been applied to localize a sound source emitting a 300-800 Hz, 2 seconds long LFM sweep recorded in a shallow water area off the coast of Portugal. The source range or depth have been successfully tracked during a 20 hours time period. The results obtained show the feasibility of single sensor source localization at known depth or at known range: source range can be estimated within a few meters from the true range of 5.5 km, while for source depth the results show some persistent biais and estimation errors varying between a few meters up to several tens of meters from the expected true source depth of 92 m. Comparison of the methods presented here with the results obtained in the same data set in Porter *et al.* [15],[16] show that rather different approaches gave very similar results with, however, a significant advantage in terms of computer time requirements for the later. The methods presented here, in particular those subspace based, should have an advantage relative to that of Porter when the signal has a narrower band that only allows for a few paths to be resolved at the receiver. The results obtained with real data show that the correlation and interaction between acoustic paths plays an important role in source localization giving new insights into the understanding of how their combination and (re)combination forms complex arrival patterns.

Acknowledgements

The authors acknowledge the support of SACLANTCEN for lending the acoustic receiving system and the dedicated collaboration of P. Felisberto in the real data acquisition and processing during INTIMATE'96. This work was partially supported under PRAXIS XXI, FCT, Portugal and by the Office of Naval Research.

References

[1] M.J. Hinich, "Maximum-likelihood signal processing for a vertical array", *J. Acoust. Soc. Am.*, vol. 54, pp.499-503, 1973.
[2] H.P. Bucker, "Use of calculated sound fields and matched-field detection to locate sound sources in shallow water", *J. Acoust. Soc. Am.*, vol. 59, pp.368-373, 1976.
[3] A.B. Baggeroer and W.A. Kuperman, "Matched field processing in underwater acoustics", *Proc. NATO ASI Conf. on Acoustic Signal Processing for Ocean Exploration*, pp. 83-122, Madeira, Portugal, 1992.
[4] A.B. Baggeroer, W.A. Kuperman and H. Schmidt, "Matched-field processing: source localization in correlated noise as an optimum parameter estimation problem", *J. Acoust. Soc. Am.*, vol. 83, pp.571-587, 1988.
[5] S.M. Jesus, "Broadband matched-field processing of transient signals in shallow water", *J. of Acoust. Soc. Am.*, vol. 93(4), Pt. 1, pp.1841-1850, 1993.
[6] S.P. Czenszak and J.L. Krolik, "Robust wideband matched-field processing with a short vertical array", *J. Acoust. Soc. Am.*, vol. 101(2), pp.749-759, 1997.
[7] C.S. Clay, "Optimum time domain signal transmission and source location in a waveguide", *J. Acoust. Soc. Am.*, vol. 81, pp.660-664, 1987.
[8] A. Parvulescu and C.S. Clay, "Reproducibility of signal transmissions in the ocean", *Radio Eng. Electron.*, vol. 29, pp.223-228, 1965.
[9] S. Li and C.S. Clay, "Optimum time domain signal transmission and source location in a waveguide: Experiments in an ideal wedge waveguide", *J. Acoust. Soc. Am.*, vol. 82(4), pp.1409-1417, 1987.
[10] L.Neil Frazer and P.I. Pecholcs, "Single-hydrophone localization", *J. Acoust. Soc. Am.*, vol. 88(2), pp.995-1002, 1990.
[11] J.H. Miller and C.S. Chiu, "Localization of the sources of short duration acoustic signals", *J. Acoust. Soc. Am.*, vol. 92(5), pp.2997-2999, 1992.
[12] D.P. Knobles and S.K. Mitchell, "Broadband localization by matched fields in range and bearing in shallow water", *J. Acoust. Soc. Am.*, vol. 96(3), pp.1813-1820, 1994.
[13] R.K. Brienzo and W. Hodgkiss, "Broadband matched-field processing", *J. Acoust. Soc. Am.*, vol. 94(5), pp.2821-2831, 1993.
[14] G.C. Carter, "Variance bounds for passively locating an acoustic source with a symmetric line array", *J. Acoust. Soc. Am.*, vol. 62(4), pp. 922-926, 1977.
[15] M.B. Porter, S. Jesus, Y. Stéphan, X. Démoulin and E. Coelho, "Exploting reliable features of the ocean channel response", *Proc. of SWAC'97*, Beijing, April 1997.
[16] M.B. Porter, Y. Stéphan, X. Démoulin, S. Jesus and E. Coelho, "Shallow-water tracking in the sea of Nazaré", *Proc. Underwater Technologies'98*, IEEE Oceanic Engineering Society, Tokyo, Japan, 1998.
[17] W. Munk, P. Worcester and C. Wunsch, *Ocean Acoustic Tomography*, Cambridge University Press, 1995.
[18] O.R. Schmidt *A Signal Subspace Approach to Multiple Emitter Location and Spectral Estimation*, PhD Thesis, Stanford University, 1982.
[19] Theorem 2.6.1, pp. 77-78 in G.Golub and C.Van Loan, *Matrix Computations*, Sec.Ed. The John Hopkins Univ. Press, 1989.
[20] M.B.Porter and Y.C. Liu, "Finite-Element Ray Tracing", *Proc. Int. Conf. on Theoretical Comp. Acoust.*, Vol.2, pp.947-956, ed. D. Lee & M.H. Schultz, World Scientific, 1993.
[21] X. Démoulin, Y.Stéphan, S. Jesus, E.Coelho and M.B. Porter, "INTIMATE96: a shallow water tomography experiment devoted to the study of internal tides", *Proc. of SWAC'97*, Beijing, April 1997.
[22] M. Wax and T. Kailath, "Detection of signals by information theoretic criteria", *IEEE Trans. on Acoust. Speech and Signal Processing*, Vol. ASSP-33, no.2, pp.387-392, 1985.
[23] C.H. Knapp and G.C. Carter, "The Generalized Correlation Method for Estimation of Time Delay", IEEE Trans. on ASSP, Vol. 24, No. 4, pp.320-327, 1976.
[24] Y.T. Chan, R.V. Hattin and J.B. Plant, "The Least Squares Estimation of Time Delay and Its Use in Signal Detection", IEEE Tran. on ASSP, Vol. 26, No. 3, pp.217-222, 1978.
[25] J.P. Ianniello, "Time Delay Estimation Via Cross-Correlation in the Presence of Large Estimation Errors", IEEE Trans. on ASSP, Vol. 30, pp.998-1003, 1982.
[26] J.C. Rosenberger, "Passive localization", Proc. of NATO ASI on Underwater Acoustics Data Processing, Ed. Y.T.Chan, pp.511-524, Kluwer, 1989.

Sérgio M. Jesus received his "Doctorat Es-Sciences" in Engineering Sciences from the Université de Nice, France in 1986. From 1986 to 1992 he was a staff scientist at the SACLANT Undersea Research Centre, La Spezia, Italy, in the Ambient Noise and Signal Processing Groups. During that period he was involved with underwater acoustic field noise directionality and early studies on target detection using matched field processing. In 1992 he joined the Electrical Engineering and Computer Department at the University of Algarve, Faro, Portugal where he is currently associate professor. His interests are underwater acoustics signal processing, model-based inversion, ocean and seafloor tomography and underwater communications. He is member of IEEE, EURASIP and of the Acoustical Society of America.

Michael B. Porter Michael B. Porter was born in Quebec, Canada, on September 19, 1958. He received the B.S. degree in Applied Mathematics from the California Institute of Technology (Pasadena, CA) in 1979. In 1984 he received a Ph.D. in Engineering Science and Applied Mathematics from Northwestern University (Evanston, IL). From 1983 to 1985 Dr. Porter was a scientist at the Naval Ocean Systems Center, San Diego, CA, where he performed research in numerical modeling of antennas, optical fibers, sonar transducers, and ocean acoustics problems. From 1985 to 1987 he was employed as a research physicist at the Naval Research Laboratory in Washington, D.C.. At NRL his interest included matched-field processing and computational acoustics. From 1987-1991 he continued research in these areas as a Senior Scientist at the SACLANT Undersea Research Centre (NATO) in La Spezia, Italy. For the last 9 years he has been with the Department of Mathematical Sciences at the New Jersey Institute of Technology as Associate then Full Professor. During this time he also held visiting positions at the University of Algarve and the Scripps Institution of Oceanography. He is presently on leave from NJIT at SAIC where he is an Assistant Vice President with the Ocean Sciences Division. Dr. Porter is the recipient of the A.B. Wood Medal from the Institute of Acoustics and an Innovators Award from the Naval Research Laboratory. He is a fellow of the Acoustical Society of America.

Yann Stephan was born in Lannion, France, in 1966. He received the Engineer diploma in electrical engineering from ENSIEG in Grenoble, France, in 1990 and the Ph.D. degree in computer sciences in 1996 from CNAM, Paris, France. Since 1992, he has worked with the Service Hydrographique et Ocanographique de la Marine (SHOM) within the Center for Military Oceanography, Brest, France, first as a Research Engineer in ocean acoustic tomography. Since 1997, he has been the Head of the Ocean Acoustics Group. His current topics include inverse methods,internal waves tomography, and tactical use of the environment.

Xavier Demoulin received the Magistere of matter sciences from ENSL, Lyon, and the DEA in physical methods in remote sensing, Paris, France, in 1990. After receiving his degree, he was employed as a physicist for several companies. Since 1995, he has been working as an engineer with the Service Hydrographique et Ocanographique de la Marine, Brest, France. His current work is focused on geoacoustics and shallow water underwater acoustics.

Orlando C. Rodríguez has got an Engineer degree in Physics at the Lomonosov State University, Moscow, Russia, in 1992. Since 1992 he was hired as teaching assistant at the Physics Department, University of Algarve, Faro, Portugal. In 1995 he obtained an Msc at the University of Algarve, Faro, Portugal. At present he is preparing his PhD on Acoustic Tomography, applied to the detection and inversion of internal tides. His main interests are acoustic modelling through ray-tracing techniques, internal tides, internal solitary waves and travel-time based tomography.

Emanuel M.M. Ferreira Coelho was born in March 1961. He is an Hydrographic Engineer at the Portuguese Navy and an associate professor at the University Lusófona, Lisboa, Portugal. He obtained his Msc (1991) and Ph.D. (1994) both in Physical Oceanography, with a minor in Digital Signal Processing at the Naval Postgraduate School, California, USA. He is now a researcher and the Head of the Oceanography Division at the Instituto Hidrográfico, Lisboa, Portugal. His past and present topics of research have covered: coordination and participation in several oceanographic campaigns and studies dedicated to mesoscale and sub-mesoscale processes, mainly related with submarine canyons dynamics, quasi-inertial internal waves and the occurrence of internal dynamical instabilities; development of software for the processing of acoustic data for ocean turbulance measurements in prototype instrumentation; coordination and participation in cruises using both ship based observations and ROV data for the evaluation of diffusive processes in the upper ocean and for testing of acoustic methods for sea observation, namely acoustic tomography; analysis of near-inertial internal wave propagation over irregular (finite) topography and non-linear internal waves generation and propagation.

Single sensor source localization in a range-dependent environment

S.M. Jesus[1], M.B. Porter[2], Y. Stéphan[3], E. Coelho[4], O.C. Rodríguez[1] and X. Démoulin[3]
[1] Universidade do Algarve, PT-8000 Faro, Portugal.
[2] Science Applications Int. Corp., La Jolla, CA 92037, USA.
[3] CMO-SHOM, F-29275 Brest Cedex, France.
[4] Instituto Hidrográfico, PT-1296 Lisboa, Portugal.

Abstract— **Source localization with a single sensor explores the time spread of the received signal as it travels from the emitter to the receiver. In shallow water, and for ranges larger than a few times the water depth, the received signal typically exhibits a large number of closely spaced arrivals. However, not all the arrivals are equally important for estimating the source position since a number of them convey redundant information. Theoreticaly, identifying the non-redundant arrivals is feasible in a isovelocity range independent waveguide. In previous work, the number of non-redundant arrivals and the dimension of the data sample signal subspace have been related in a range-independent case. This paper addresses the problem of determining the number of significant arrivals for localizing a sound source over a range-dependent environment off the West coast of Portugal during the INTIMATE'96 sea trial.**

Keywords— **Source localization, subspace methods, shallow water, broadband signals.**

I. Introduction

Source localization with a single hydrophone is known to be a difficult problem in underwater acoustics, due to the reduced amount of spatial information. The lack of spatial information is to be compensated by the time spread of the emitted signal as it travels from the source to the receiver. Whether that time spread is sufficiently correlated to the medium of propagation to uniquely pinpoint the source position depends on a variety of factors such as the source range, water depth, sea bottom acoustic impedance, sea surface roughness, depths of source and receiver relative to the sound speed profile, etc... Previous work has shown that the correlation between the predicted and the estimated channel impulse responses was sufficient to track an acoustic source over various shallow water propagation environments [1],[2]. Alternatively, classical eigen analysis of the received time series allows to decompose the data set into two orthogonal subspaces that were used for source localization in a range independent environment [3]. A crucial step in time series analysis is to determine the order of the underlying signal model, that is to say, the dimension of the signal subspace. This paper attempts to shows how the signal subspace dimension can be interpreted in physical means by associating the identified eigenvectors with uncorrelated acoustic rays. In a range-dependent environment ray propagation is significantly altered and the number of eigenrays participating to the signal subspace should generally increase translating, in some sense, a higher degree of diversity and therefore an increased potential for localization. The real data that serves as illustration was obtained during the INTIMATE'96 experiment, off the west coast of Portugal, in a mild range-dependent environment (130 to 160 m water depth) for source ranges varying from 1 to 12 km. The emitted signal was a 300-800 Hz linear FM, with a 2 second duration.

This work was supported under contract 2./2.1/MAR/1698/95, PRAXIS, FCT, Portugal and by the Office of Naval Research.

II. Background

A. Data model

A widely accepted model for the time series received at one acoustic sensor due to a sound source emitting a signal $s_0(t)$ at location $\theta_s = (r_s, z_s)$ is

$$y_n(t, \theta_s) = \sum_{m=1}^{M} a_{n,m}(\theta_s) s_0[t - \tau_m(\theta_s)] + \epsilon_n(t), \tag{1}$$

where $\epsilon_n(t)$ is the observation noise, assumed spatially and temporally white, zero-mean and uncorrelated with the signal and $a_{n,m}$ and τ_m are the replica amplitudes and time delays respectively. M is the number of signal replicas due to successive signal reflections between the source and the receiver. An implicit assumption in model (1) is that the M replicas observed at the receiver are stable within the data window, *i.e.*, that the variation in time delays $\tau_{n,m}$ with snapshot n is negligeable and therefore can be approximated by a single mean value τ_m.

A compact form for (1) is

$$\mathbf{y}_n(\theta_s) = \mathbf{S}[\boldsymbol{\tau}(\theta_s)]\mathbf{a}_n(\theta_s) + \boldsymbol{\epsilon}_n, \tag{2}$$

with the following matrix notations,

$$\mathbf{y}_n(\theta_s) = [y_n(1, \theta_s), y_n(2, \theta_s), \ldots, y_n(T, \theta_s)]^t, \quad \dim T \times 1 \tag{3a}$$

$$\boldsymbol{\tau}(\theta_s) = [\tau_1(\theta_s), \ldots, \tau_M(\theta_s)]^t, \quad \dim M \times 1 \tag{3b}$$

$$\mathbf{s}_0(\tau) = [s_0(-\tau), \ldots, s_0((T-1)\Delta t - \tau)]^t, \quad \dim T \times 1 \tag{3c}$$

$$\mathbf{S}[\boldsymbol{\tau}(\theta_s)] = [\mathbf{s}_0(\tau_1), \ldots, \mathbf{s}_0(\tau_M)], \quad \dim T \times M \tag{3d}$$

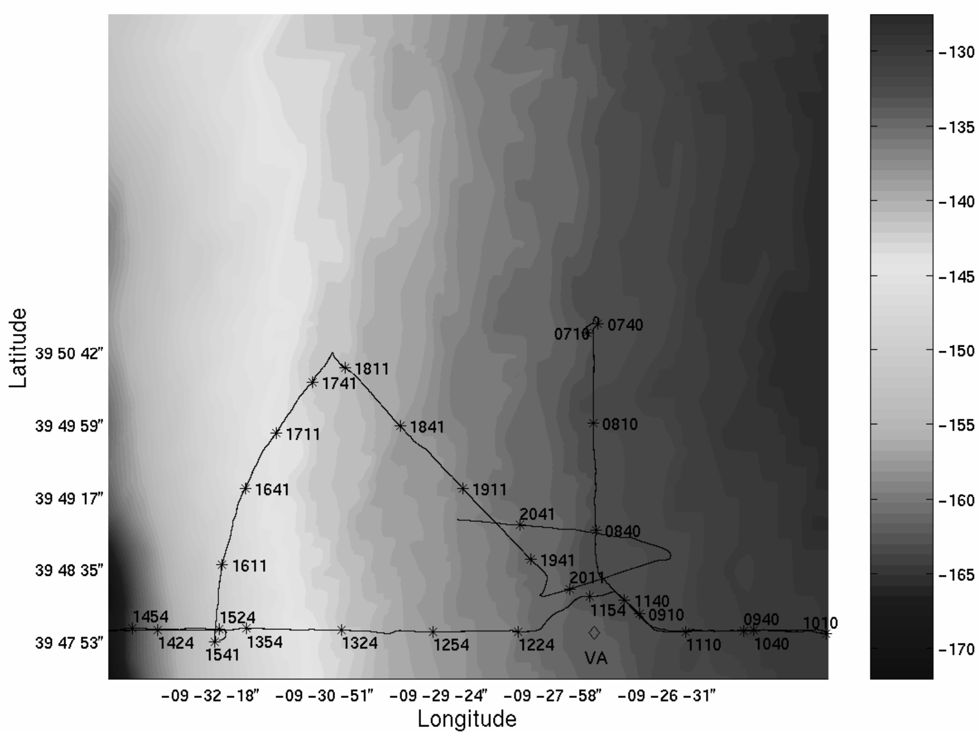

Fig. 1. INTIMATE'96: bathymetry map, source track and vertical array position (◇ VA) during Event II, on June 16, 1996.

and

$$\mathbf{a}_n(\theta_s) = [a_{n,1}(\theta_s), \ldots, a_{n,M}(\theta_s)]^t, \quad \dim M \times 1 \qquad (3e)$$

where T is the number of time samples on each snapshot n.

B. Time delays and source localization

A classical objective in source localization as well as in travel-time tomography is to estimate the set of arrival times $\boldsymbol{\tau}$. Matching that set of arrivals with the model predicted values is the basis for the source localization process and of tomography inversion. A common procedure is to correlate the received time series with the source emitted signal to obtain the so-called pulse-compressed arrival pattern.That arrival pattern is an estimate of the channel impulse response that would be an exact image for a source signal with an infinite bandwith. It is well known that the maxima of the arrival pattern provide an optimum estimate of the arrival times $\tau_m; m = 1, \ldots, M$ in the maximum likelihood (ML) sens and under the assumption that the arrivals are uncorrelated, thus

$$\{\hat{\tau}_m^{\mathrm{ML}}; m = 1, \ldots, M\} = \arg\{\max_{\tau} \sum_{n=1}^{N} \| \mathbf{y}_n^H \mathbf{s}_0(\tau) \|^2\}. \quad (4)$$

Assuming zero-mean random amplitudes, (2) becomes a linear random observation model and one may ressort to second order statistics for estimating $\boldsymbol{\tau}$. Decomposition of the data matrix $\mathbf{Y} = [\mathbf{y}_1, \mathbf{y}_2, \ldots, \mathbf{y}_N]$ allows for determining the principal components associated with the highest singular values that span the same subspace as the columns of matrix $\mathbf{S}$. Therefore an alternative estimator for the arrival times is given by

$$\{\hat{\tau}_m^{\mathrm{SS}}; m = 1, \ldots, M\} = \arg\{\max_{\tau} \| \mathbf{U}_M^H \mathbf{s}_0(\tau) \|^2\}, \quad (5)$$

where the superscript ^{SS} denotes that the estimator is based on the signal subspace. A geometrical interpretation of (5) is that the arrival estimates are given by the intersection of the emitted signal continuum $\mathbf{s}_0(\tau)$, for all possible values of τ, and the subspace spanned by the columns of $\mathbf{U}_M$. As a matter of completeness one could as well determine the arrival estimates as the inverse of the projections onto the $\mathbf{U}_M$ orthogonal complement - the so-called noise subspace [4].

Source location can be readily deduced from the above estimators as the sum of the arrival amplitudes for the model predicted arrival set for each tentative source location. Two estimators will be compared in this paper, one based in (4)

$$\hat{\theta}_{\mathrm{ML}} = \arg\{\max_{\boldsymbol{\tau}(\theta)} \frac{1}{NM} \sum_{n=1}^{N} \sum_{m=1}^{M} \| \frac{\mathbf{s}_0[\tau_m(\theta)]^H \mathbf{y}_n}{a_m(\theta)} \|^2\}, \quad \theta \in \Theta. \quad (6)$$

and one based in (5)

$$\hat{\theta}_{\mathrm{SS}} = \arg\{\max_{\boldsymbol{\tau}(\theta)} \sum_{m=1}^{M} \| \frac{\mathbf{U}_M^H \mathbf{s}_0[\tau_m(\theta)]}{a_m(\theta)} \|^2\}, \qquad \theta \in \Theta. \quad (7)$$

Estimators (6) and (7) are very similar to those used in [4] for a range-independent data set. In the present work normalization by the predicted amplitude $a_m(\theta)$ of each arrival was introduced to account for a 12 km wide range-dependent search interval for. Without that normalization the source location estimate was biased for the most energetic (first) arrivals and the source was consistently located at the beginning of the search interval.

C. Redundant arrivals and subspace dimension

In (5) and (7) $\mathbf{U}_M$ is a matrix whose columns are the vectors associated with the M highest singular vectors of data matrix $\mathbf{Y}$. In practice, and in presence of noise, a number of low-amplitude arrivals may be undetectable at the receiver and one problem is that of estimating the dimension of the data underlying signal subspace. In this paper, we used the minimum description length (MDL), which is a likelihood-based criterium proposed by Wax et all. [5] for estimating signal subspace dimension in a linear observation Gaussian model. Recent work has shown that, for a range-dependent isovelocity propagation channel and a generic geometry with source and receiver at diferent depths, the non-redundant arrivals were included in a single quadruplet[6]. Under some mild approximations this result could be generalized to non-isovelocity channels and compared to the results obtained in a range-independent event of the INTIMATE'96 data set where the MDL estimated signal subspace dimension was found to be in average equal to four [4].

Similar theoretical analysis is cumbersome, if not impossible, for a range-dependent environment. However, it is well known, that in such environment, the quadruplet structure of the arrival pattern is destroyed, and therefore a higher number of non-redundant arrivals may be expected, possibly leading to a higher discrimination and therefore a better potential for source localization.

III. The Intimate'96 range-dependent data set

The Intimate'96 sea trial took place off the west coast of Portugal during June 1996. Results obtained in that data set have been reported elsewhere so the reader is referred to Demoulin *et al.* [7] for a complete description of the area and environmental conditions of the sea trial. The results presented here address the data gathered during Event II, from 07:10 to 20:41 of June 16, 1996. The bathymetry map, the source track and vertical receiving array position are shown in Fig. 1. The portion of the track until approximately 12:00 is nearly range-independent therefore we will concentrate in the remaining portion when the source ship goes off to the west until 14:30 and then in a arc-shaped track to the NE and finally back to the vertical array (VA). Water depth at source location during Event II is shown in Fig. 2.

During the same period of time CTD's were continuously made at the VA location and XBT's have been performed at the source position. Fig. 3 shows the sound speed profile calculated from XBT48 (14:03) that was used to initialize ray model TRIMAIN [8] to compute the predicted arrival times and amplitudes for each tentative source range. The bottom was characterized by a 1750 m/s compressional speed sandy layer with a density of 1.9 g/cm^3 and a com-

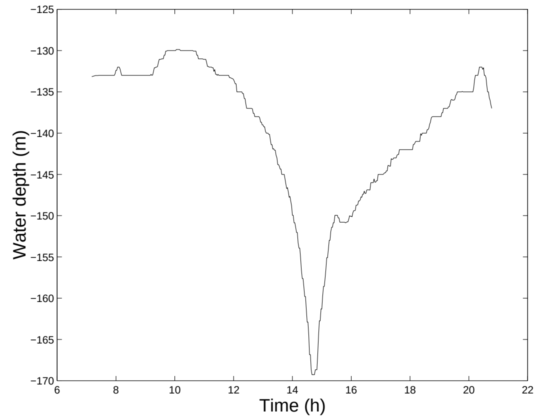

Fig. 2. Water depth at the source during Event II.

pressional attenuation of 0.8 dB/λ [4]. Bottom impedance characterization was found to be important for predicting late arrival amplitudes. Since these amplitudes were used for data balancing in (6) and (7) their estimation was critical for source localization over this environment.

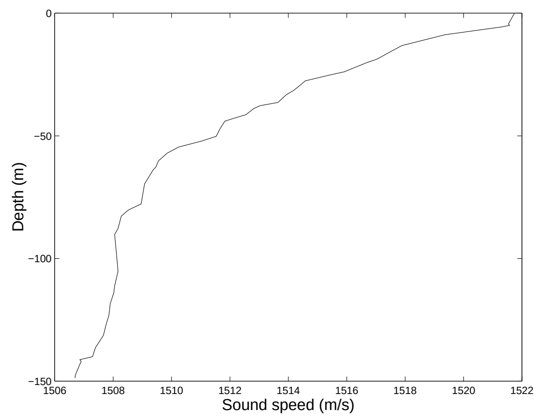

Fig. 3. Sound speed profile from XBT 48 (14:03).

The VA was composed of 4 hydrophones at nominal depths of 35, 70, 105 and 115 m. The emitted signal was an 300-800 Hz LFM sweep with 2 second duration and a repetition rate of 8 seconds. The source measured transfer function was used to filter the signal s_0 used for pulse compression at the receiver. Fig. 4 shows the source range estimation results at nominal depths obtained using only the hydrophone located at 115 m depth with both the ML and the SS methods (equations (6) and (7) respectively).

It can be remarked that despite the use of a range-independent ray model the source range (at correct depth) was correctly estimated at all times except for the largest ranges (approx. for $r > 9$ km) corresponding to the strongest water depth variation of the run (Fig. 2). Attempts with range-dependent ray-tracing profiles were unsuccessful at the present time.

The source range and depth along track are shown in Fig. 5, where it can be seen that an evolution of the source towards or away from the VA contributes to an increase or a decrease of the dimensionality of the signal subspace

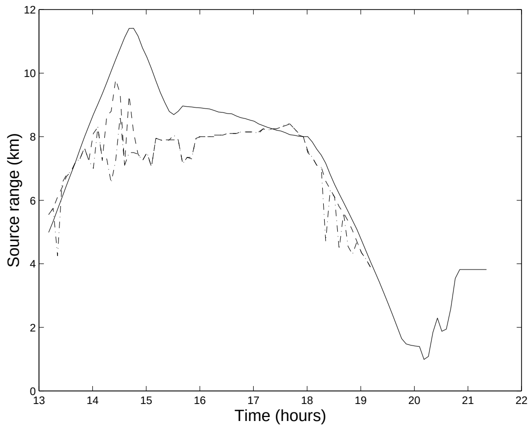

Fig. 4. Source range estimation during the range-dependent part of event II: GPS measured (—), ML estimated (-.-) and SS estimated (- - -).

that varies from a mean value of 4 at constant ranges and a value of up to 15 at ranges of less than, say, 5-6 km.

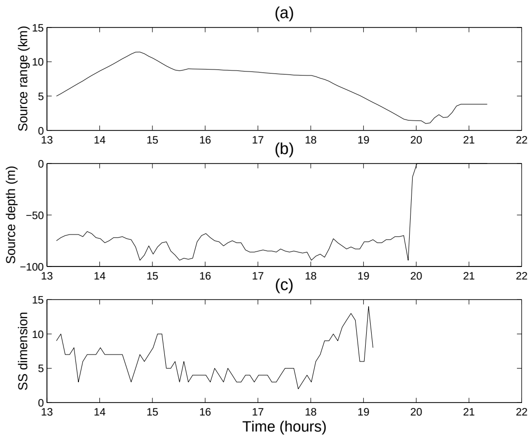

Fig. 5. INTIMATE'96: source range relative to vertical array (a), source depth (b) and estimated signal subspace dimension with MDL criteria (c), during the range-dependent part of event II, on June 16, 1996.

These results are in desagreement with the expectations. What is noted here is that somehow is the source range variation that has an impact on the dimensionality of the signal subspace and therefore seems to contribute to decorrelate the signal arrivals. It can be also noted that during these portions of the run (approximately 2.5 hours, from 13:00 to 14:00 and from 17:30 to 19:00) the SS method gave very accurate source range estimations and outperformed the ML estimator. Various tests keeping a constant subspace dimension throughout the run destroyed the localization.

IV. Conclusion

Source localization results in the INTIMATE'96 range-dependent data set have been reported by Porter et al. [2] using a direct correlation between the predicted and the estimated arrival paterns. To some extent these results are superior to those present in the present paper, specially at longer ranges. In this paper the goal was to understand the role of the uncorrelation between arrivals in a source tracking run over a range-dependent environment. In particular, from the analysis of over 6 hours of source range tracking in a 130 - 160 m water depth range-dependent environment, it was found that the number of independent arrivals varies significantly with the source range either outwards or towards the receiving array. At a constant range of 8 km, over an arc-shaped track, the number of uncorrelated arrivals defaults to approx. 4 or 5, despite the range-dependent nature of the propagation line. The source range estimation results given by the ML and the SS estimators are equivalent, except for the portions with stronger range variation where a correct tracking of the subspace dimension gave some advantage to the SS method. In conclusion one may ask what could be the advantages of using the SS method over the ML or the correlation based method of Porter et al. At this point only two advantages can be pointed out: one is theoretical and deals with the analysis of the principal components of the data and the understanding of their connection with the physical behaviour of ray-propagation. The other is practical and relates to the higher resolution of the SS method when compared to the ML method in cases of limited source signal bandwith (see simulated examples in [4]). Unfortunately there are also some drawbacks which are: a higher computational burden and a lower accuracy when compared to the direct correlation method of Porter et al..

Acknowledgment

The authors acknowledge the support of SACLANTCEN for lending the acoustic receiving system.

References

[1] M.B. Porter, S. Jesus, Y. Stéphan, X. Démoulin and E. Coelho, "Exploting reliable features of the ocean channel response", *Proc. of SWAC'97*, Beijing, April 1997.

[2] M.B. Porter, Y. Stéphan, X. Démoulin, S. Jesus and E. Coelho, "Shallow-water tracking in the sea of Nazaré", *Proc. Underwater Technologies'98*, IEEE Oceanic Engineering Society, Tokyo, Japan, 1998.

[3] S.M. Jesus, M.B. Porter, Y. Stephan, E. Coelho and X. Demoulin, "Broadband localization with a single hydrophone", Proc. of MTS/IEEE OCEANS'98, Nice, France, September 1998.

[4] S.M. Jesus, M.B. Porter, Y. Stephan, X. Demoulin, O.C. Rodríguez and E. Coelho, "Single hydrophone source localization", IEEE J. of Oceanic Eng., to appear July 2000.

[5] M. Wax and T. Kailath, "Detection of signals by information theoretic criteria", *IEEE Trans. on Acoust. Speech and Signal Processing*, Vol. ASSP-33, no.2, pp.387-392, 1985.

[6] O.C. Rodríguez and S.M. Jesus, "Physical limitations of travel time based shallow water tomography", submitted to J. Acoust. Soc. Am., Dec. 1999.

[7] X. Démoulin, Y.Stéphan, S. Jesus, E.Coelho and M.B. Porter, "INTIMATE96: a shallow water tomography experiment devoted to the study of internal tides", *Proc. of SWAC'97*, Beijing, April 1997.

[8] TRIMAIN-83: A variable-Bottom, Multiprofile Raytrace Program, E.L. Wright, B.G. Roberts Jr. et all., NRL, 1970 (downloaded from oalib.njit.edu).

Physical limitations of travel-time-based shallow water tomography

Orlando C. Rodríguez[a] and Sérgio M. Jesus
Unidade de Ciências Exactas e Humanas, Universidade do Algarve, Campus de Gambelas, 8000—Faro, Portugal

(Received 22 November 1999; revised 23 May 2000; accepted 6 September 2000)

Travel-time-based tomography is a classical method for inverting sound-speed perturbations in an arbitrary environment. A linearization procedure enables relating travel-time perturbations to sound-speed perturbations through a kernel matrix. Thus travel-time-based tomography essentially relies on the inversion of the kernel matrix and is commonly called ''linear inversion.'' In practice, its spatial resolution is limited by the number of resolved and independent arrivals, which is a basic linear algebra requirement for linear inversion performance. Physically, arrival independency is much more difficult to determine since it is closely related to the sound propagating channel characteristics. This paper presents a brief review of linear inversion and shows that, in deep water, the number of resolved arrivals is equal to the number of independent arrivals, while in shallow water the number of independent arrivals can be much smaller than the number of resolved arrivals. This implies that in shallow water there are physical limitations to the number of independent travel times. Furthermore, those limitations are explained through the analysis of an equivalent environment with a constant sound speed. The results of this paper are of central importance for the understanding of travel-time-based shallow water tomography. © *2000 Acoustical Society of America.* [S0001-4966(00)01212-1]

PACS numbers: 43.30.Pc, 43.60.Rw [DLB]

I. INTRODUCTION

Ocean acoustic tomography has been suggested in the last two decades as a powerful tool for large-scale ocean temperature monitoring. In contrast with standard ''local'' and ''direct'' methods, ocean acoustic tomography can be used to remotely determine mean current and temperature evolution through time in an ocean volume bounded by a system of acoustic sources and receivers.[1,2] Travel-time-based tomography has been widely used in the context of ocean acoustic tomography to invert for sound-speed perturbations of a background (reference) profile.[1–5] For instance, tomographic inversion can be performed by linearizing the integral relationship between perturbations in travel time and continuous perturbations in sound speed. After linearization, the perturbations in travel time are related to a set of discrete perturbations in sound speed through a kernel matrix, which depends on stable eigenrays of propagation. Sound-speed perturbations can be estimated by calculating a generalized inverse of the kernel matrix and relating back the set of sound-speed perturbations to travel-time perturbations. This technique is sometimes called ''linear inversion'' and its spatial resolution (i.e., the number of depths at which sound-speed perturbations can be reliably estimated) is fundamentally limited by the number of resolved—and as we will see independent—arrivals.

Despite the significant number of references related to linear inversion most studies are limited to its application in deep water, where the effects of sound reflection on the ocean boundaries can be, to a certain extent, neglected, and acoustic arrivals can be easily resolved for long-range propagation. In shallow water the interaction of sound with the ocean boundaries plays an important role and time resolution of closely spaced arrivals is generally an important practical issue. As an example, Fig. 1 shows a typical shallow water channel impulse response estimate. It is clear from that figure that initial arrivals are unresolved, while late arrivals are well resolved and ''clustered'' in quadruplets. From ray-tracing predictions it can be shown that most of the initial unresolved arrivals correspond to refracted and bottom reflected eigenrays, while the quadruplets correspond to surface and bottom reflected eigenrays. An important feature in this example is the significant number of resolved arrivals. In the context of travel-time-based shallow water tomography, and through linear inversion, it seems reasonable that those arrivals should be used to achieve a high spatial resolution of sound-speed estimates. This would be the case providing that all the resolved arrivals are independent, i.e., that all the acoustic arrivals that can be identified from one transmission to another correspond to ''pieces'' of information independently related to the perturbation of sound speed. This assumption seems to be implicitly accepted in some of the studies concerning linear inversion.[1,3,4] Nevertheless, it is shown in this paper that for shallow water the number of independent arrivals is in fact smaller, and in some cases much smaller, than the number of actually measured—resolved—arrivals. This result implies that in shallow water part of the acoustic arrivals carry redundant information and therefore there are fundamental physical limitations to the number of independent arrivals. Furthermore, and most importantly, this paper shows that the redundancy of shallow water stable arrivals can be explained through the compari-

[a]Electronic mail: orodrig@ualg.pt

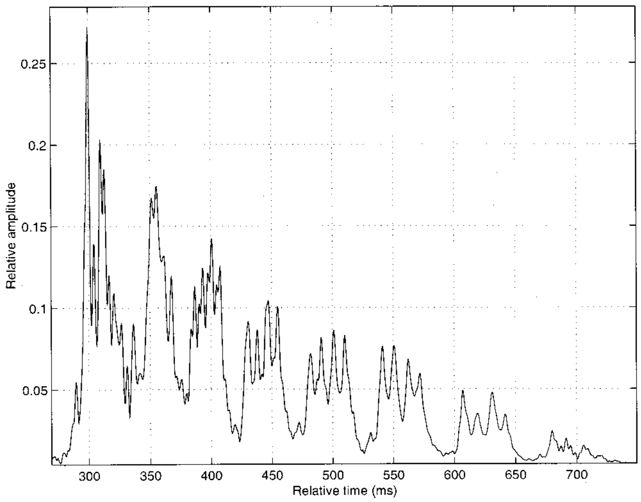

FIG. 1. Typical shallow water short-range arrival pattern showing unresolved (initial) and resolved (late) arrivals; resolved arrivals are ''clustered'' in groups of quadruplets [real data, taken from Jesus *et al.* (Ref. 6)].

son of the original waveguide with an isovelocity equivalent. Therefore, as a contribution to the general problem of acoustic tomography this paper presents the set of fundamental requirements for successful tomographic inversion of acoustic data in the context of travel-time-based shallow water tomography. This paper is organized as follows: Sec. II presents a brief theoretical review of linear inversion. This review is used in Sec. III to show, through simulations, that for deep water the number of independent arrivals is equal to the number of measured resolved travel times, while in shallow water the number of independent arrivals is much smaller than the number of actually measured resolved arrivals. The results of shallow water simulations are explained in Sec. IV through the comparison of the original acoustic waveguide with an isovelocity equivalent, and conclusions are drawn in Sec. V.

II. LINEAR INVERSION: THEORETICAL BACKGROUND

It can be shown on the basis of ray theory that the perturbation in travel time of an acoustic pulse can be written as[1,2]

$$\Delta\tau=\int_{\Gamma}\frac{ds}{c(z)}-\int_{\Gamma_0}\frac{ds}{c_0(z)}, \tag{1}$$

where Γ and Γ_0 represent the eigenrays corresponding, respectively, to the perturbed and background sound-speed profiles $c(z)$ and $c_0(z)$. The background sound-speed profile $c_0(z)$ is considered to be known, for instance, from historical data. For small perturbations of sound speed $\delta c(z)=c(z)-c_0(z)\ll c_0(z)$ one can take $\Gamma\approx\Gamma_0$, so the previous equation becomes

$$\Delta\tau_i=\tau_i-\tau_i^0=\int_{\Gamma_i}\frac{ds}{c(z)}-\int_{\Gamma_i}\frac{ds}{c_0(z)}\approx-\int_{\Gamma_i}\frac{\delta c(z)}{c_0^2(z)}ds, \tag{2}$$

where the integral is taken along the unperturbed eigenray Γ_i. The fundamental statement of this relationship is that a first-order perturbation in sound speed leads only to a first-order perturbation in travel time, while the path of the eigenray is not affected by this perturbation. In this sense Γ_i corresponds to a stable eigenray and τ_i and τ_i^0 can be considered as resolved travel times (or resolved arrivals). It is clear that the number of perturbations in travel time should be equal to the number of resolved eigenrays or, correspondingly, to the number of resolved arrivals. By ''collecting'' a set of T perturbations in travel time and representing the acoustic waveguide as a system composed of L layers, one obtains the following linear system:[2]

$$\mathbf{y}=\mathbf{E}\mathbf{x}+\mathbf{n}, \tag{3}$$

where $\mathbf{y}=[\Delta\tau_1\Delta\tau_2\ldots\Delta\tau_{\mathsf{T}}]^t$, $\mathbf{x}=[\delta c_1\delta c_2\ldots\delta c_{\mathsf{L}}]^t$, each δc_j is an average of $\delta c(z)$ in the jth layer, and $\mathbf{n}$ represents the contribution of noise to the set of observations $\mathbf{y}$. Since the linear inversion will be tested with simulated data it will be considered in the following that there is a perfect match between both sides of the equation and the observations are fully deterministic (i.e., $\mathbf{n}=0$).

Matrix $\mathbf{E}$, dimension $\mathsf{T}\times\mathsf{L}$, is called the ''kernel matrix,'' the $\mathbf{e}_i$ of which have the following structure:

$$\mathbf{e}_i=\left[\frac{\Delta s_{i1}}{c_{01}^2}\,\frac{\Delta s_{i2}}{c_{02}^2}\ldots\frac{\Delta s_{i\mathsf{L}}}{c_{0\mathsf{L}}^2}\right], \tag{4}$$

where Δs_{ij} stands for the length of ray i inside layer j with $i=1,2,\ldots,\mathsf{T}$ and $j=1,2,\ldots,\mathsf{L}$. The choice of the number of layers L can be done in many different ways. In general L is made as large as possible and in practice it is often larger than T. Under this assumption of $\mathsf{L}>\mathsf{T}$, Eq. (3) consists of an underdetermined system of equations that has more unknowns than equations, and therefore has an infinite number of solutions. Formally, the columns of matrix $\mathbf{E}$ form a dependent set and, in practice, there is also no guarantee that T rows of $\mathbf{E}$ are linearly independent, which is equivalent to saying that $\mathbf{E}$ may be rank deficient. In terms of the underlying problem of time delays and sound-speed perturbations, rank deficiency means that not all resolved arrivals carry independent sound-speed information. Straight linear algebra tells us that such a system of equations has a solution $\mathbf{x}$, but that solution is not unique; that is to say that further information is needed to pick one among the possible solutions. The set of possible solutions are those that satisfy the system of equations

$$\mathbf{E}\hat{\mathbf{x}}=\mathbf{p}, \tag{5}$$

where $\hat{\mathbf{x}}=[\mathbf{E}^t\mathbf{E}]^{-1}\mathbf{E}^t\mathbf{y}$ and therefore $\mathbf{p}$ is the projection of $\mathbf{y}$ onto the column space of $\mathbf{E}$. If such additional information is not available, the solution of Eq. (5) is the one that has minimum length. That solution is generally called the minimum norm solution and is given by the pseudoinverse

$$\mathbf{x}^{\#}=\mathbf{E}^{\#}\mathbf{y}. \tag{6}$$

The pseudoinverse $\mathbf{E}^{\#}$ is efficiently computed through the singular value decomposition[7] (SVD) of matrix $\mathbf{E}$, $\mathbf{E}=\mathbf{U}\mathbf{S}\mathbf{V}^t$, which provides a way of dealing with the rank of $\mathbf{E}$ by analysis of the singular spectra, $\sigma_1,\sigma_2,\ldots,\sigma_{\mathsf{T}}$, diagonal entries of $\mathbf{S}$, and further selection of the significant σ_i in the SVD. However, such selection can not be done in a unique manner since it generally depends on the particular charac-

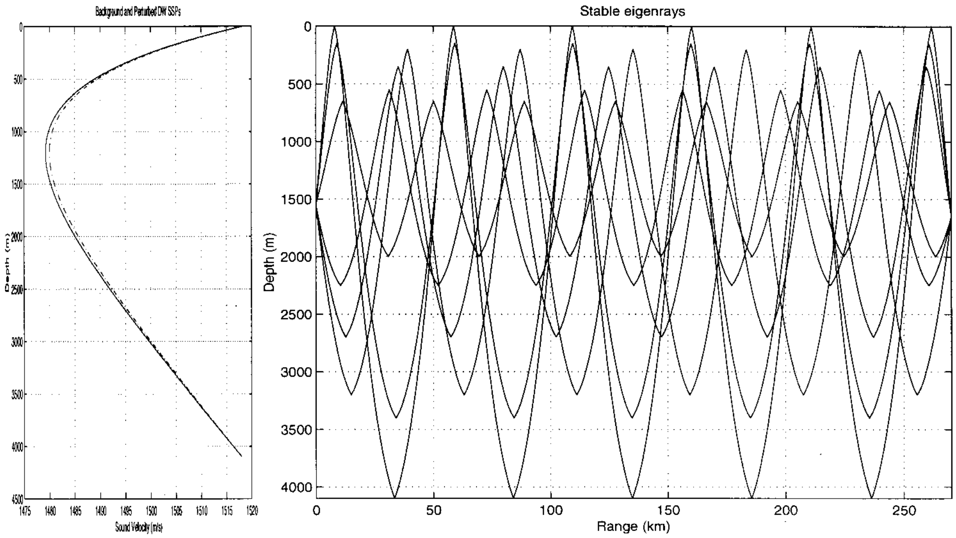

FIG. 2. Deep water test: Background $c_0(z)$ (dotted-dashed line) and perturbed $c(z)$ (continuous line) SSPs (left); stable eigenrays (right).

teristics of the problem. And even with the SVD solution being a minimum norm solution, nothing guarantees that such solution will be close to the searched solution, which is to say that minimizing $\|\mathbf{x}^{\#}\|$ does not imply the minimization of $\|\mathbf{x}^{\#}-\mathbf{x}\|$.

Finally, once the rank of the kernel matrix has been calculated, the minimum norm solution can be written as

$$\mathbf{x}^{\#}=\mathbf{V}_r\mathbf{S}_r^{-1}\mathbf{U}_r^t\mathbf{y}, \tag{7}$$

where subscript $r=\text{rank}$ ($\mathbf{E}$), and denotes that matrices $\mathbf{V}$ and $\mathbf{U}$ are formed by their r first singular vectors, and matrix $\mathbf{S}_r$ is square with its first (highest) singular values along the diagonal.

III. SIMULATION TESTS

Using the theoretical background presented in the previous section, travel-time-based tomographic inversion through ray-tracing simulations is tested to determine the number of independent arrivals in both deep and shallow water scenarios. For each scenario a background and a perturbed sound-speed profile (SSP) are chosen in order to obtain a negative perturbation of sound speed, which corresponds to positive perturbations in travel time. For each SSP a set of eigenrays is calculated and the set of stable eigenrays, resolved arrivals, and corresponding perturbations in travel time are determined. The kernel matrix, $\mathbf{E}$, is constructed with the stable eigenrays and then the inverse solution is calculated from its SVD. When dealing with real data the number of independent eigenrays N (which is the same as the number of independent arrivals) can be estimated by using statistical criteria.[6,8] Since the test case presented here is fully deterministic, an alternative method for estimating the rank of matrix $\mathbf{E}$ is proposed. That method takes advantage of the structure of the inverse solution based on the SVD of the kernel matrix, which was discussed in the previous section, and introduces the following functional:

$$E(i)=\frac{\|\mathbf{x}_i^{\#}-\mathbf{x}\|^2}{\|\mathbf{x}_i^{\#}\|^2}, \tag{8}$$

where $\mathbf{x}_i^{\#}$ is the inverse solution obtained from Eq. (7) and calculated with the first i singular values. The ''real'' perturbation $\mathbf{x}$ is calculated from $\delta c(z)$ (which is known in our simulated case) according to the adopted depth discretization. Using the functional $E(i)$ one can obtain the following estimator of the number of independent arrivals N:

$$\hat{N}=\arg\{\min_i E(i)\}. \tag{9}$$

The minimum of $E(i)$ does not have to be a minimum in the conventional sense since solutions with $N=1$ or $N=\mathsf{T}$ will also be admitted. If $N=\mathsf{T}$ (which should not be surprising) the natural conclusion is that all resolved arrivals are independent and therefore they all contribute with independent information to the tomographic inversion. However, if $N<\mathsf{T}$ (and from ray tracing there is no apparent reason for this to be so), then the unexpected conclusion is that only N of T resolved arrivals are independent, and the remaining $N-\mathsf{T}$ convey redundant information. Those redundant arrivals will not contribute with additional information to the tomographic inversion. It will be shown in the following subsections that in deep water one obtains the ''expected'' conclusion ($N=\mathsf{T}$), while in shallow water part of the resolved arrivals are redundant, i.e., $N<\mathsf{T}$.

A. Deep water test

The well-known analytical expression for the Munk velocity profile was used to generate the SSPs (see left panel of Fig. 2). Following the geometry of a real experiment[4] the acoustic source and the receiver depths are $z_s=1500$ and $z_r=1650\,\text{m}$, respectively, the depth of the acoustic waveguide is $D=4100\,\text{m}$, and the distance separating the source and the receiver is $R=270\,\text{km}$. The asymmetry $z_s\neq z_r$ is intentional. In fact, as discussed by Munk *et al.*,[2] by locating both source and receiver at the same depth one gets symmetric eigenrays, with turning points at the same depths. Therefore, those eigenrays sample the ocean in the same way and constitute a preliminary source of redundancy in the kernel matrix, which should be avoided. After eigenray ray tracing for the background and the perturbed SSPs, a set of five RR stable eigen-

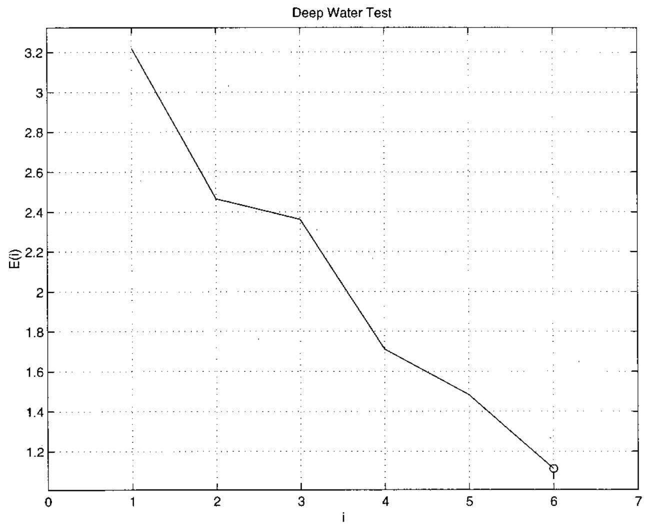

FIG. 3. Deep water test: Estimation of independent arrivals; the projection of the minimum [Eq. (8)] onto the horizontal axis indicates the number of independent arrivals N.

rays and one surface-reflected–bottom-reflected (SRBR) stable eigenray were found (see right panel of Fig. 2). The reflected eigenray should be considered in a somehow formal way (in fact this is the only eigenray that spans the entire water column) since in real conditions the amplitude of SRBR eigenrays is difficult to detect over the level of environmental noise.[9] Using Eq. (8) it can be found that $N=6$ (see Fig. 3). From this result it can be concluded that all the resolved arrivals are independent and this is the ''expected'' conclusion.

B. Shallow water test

The shallow water background SSP for this test corresponds to the mean profile from conductivity, temperature, depth (CTD) data used in Jesus *et al.*;[6] a particular profile from the same data was considered to be representative of the perturbed SSP (see left panel of Fig. 4). The geometry of propagation was taken also from that reference, with the acoustic source at depth $z_s = 90$ m, the hydrophone at depth $z_r = 115$ m and range $R = 5.6$ km, and the total depth of the waveguide being $D = 135$ m. As in the deep water test, the asymmetry $z_s \neq z_r$ avoids the redundancy of symmetric eigenrays with equal turning depths. From ray tracing it can be found that all eigenrays are of RBR or SRBR types (see Fig. 5). The RBR eigenrays [Fig. 5(a)] are not stable (see left box of right panel of Fig. 4) and therefore they can not be used in the tomographic inversion. The SRBR eigenrays [Fig. 5(b)] are stable and ''clustered'' in quadruplets and are, therefore, suitable for inversion purposes (see right box on right panel of Fig. 4). In general, the clustering of arrivals depends on the particular characteristics of the waveguide geometry and associated SSP. For the shallow water environment and SSP of this test one can remark that each quadruplet contains the arrival times τ, ordered according to the general sequence,

$$(\tau^{+}_{2m-1}, \tau^{+}_{2m}, \tau^{-}_{2m}, \tau^{-}_{2m+1}), \tag{10}$$

where the index of each τ represents the number of reflections on the surface or bottom of the corresponding eigenray, a ''+'' or a ''−'' sign indicates whether that eigenray was launched toward the surface or toward the bottom, respectively. To calculate the kernel matrix an homogeneous layer grid was introduced. Each layer has a thickness $\Delta z = 4$ m, which is four times more than the spatial resolution of the discretized sound-speed profile. The depth of every layer interface was coincident with every fourth depth of the discretized sound speed. To simplify the calculations, additional interfaces were added at depths z_s, z_r, and D, which were not included in the homogeneous grid. Thus a total of 36 layers was used to calculate the kernel matrix. The sound speed for each layer was the average of the discretized sound speeds contained within the layer. The functional $E(i)$ was calculated considering a total of 20 resolved arrivals. However, its minimum is reached at $N=4$ (see Fig. 6), which indicates that only 4 of the 20 resolved arrivals are independent, while the other 16 are redundant. It should be remarked that this result is in agreement with a statistical estimation of uncorrelated paths presented in Jesus *et al.*[6] It is clear that

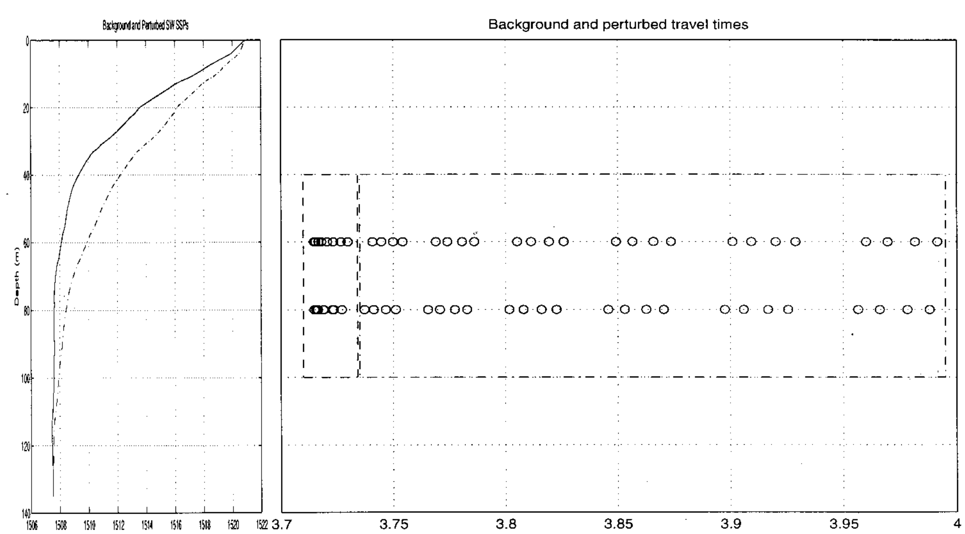

FIG. 4. Shallow water test: Background $c_0(z)$ (dotted-dashed line) and perturbed $c(z)$ (continuous line) SSPs (left); background τ_0 (lower sequence) and τ (upper sequence) travel times (right), left box indicates unstable arrivals, right box indicates resolved arrivals.

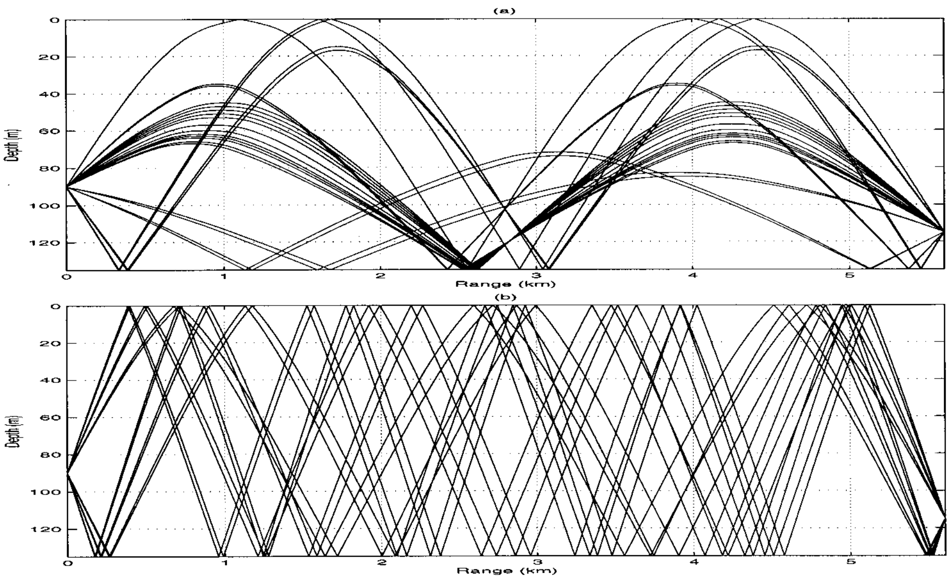

FIG. 5. Rays of propagation for unstable arrivals (a) and stable arrivals (b). (For simplicity only the first three quadruplets are shown.)

the result depends deeply on the particular structure of the kernel matrix, which will be discussed in the following section.

IV. DISCUSSION

The simulation results obtained in the previous section show that the number of independent arrivals (and therefore, of independent eigenrays) can be much lower than the number of resolved arrivals. It follows from those results that there are fundamental physical limitations to the number of independent parameters available for travel-time tomography. However, the general understanding of the simulation results still remains incomplete because those results only say *how many* of the eigenrays are independent, but they do not say *which* are the independent eigenrays and the reason for being so. Intuitively it seems reasonable to admit that each set of eigenrays, corresponding to a particular quadruplet, are independent, and therefore, that each of those eigenrays contains a ''piece'' of independent information. In mathematical terms this assumption states not only that rank $(\mathbf{E})=4$, but also that for a given quadruplet q the corresponding four rows in $\mathbf{E}$ are linearly independent, and can be used to calculate the four rows of any other quadruplet. However, within the context of ray theory there is not a clear explanation to support this assumption. In part this is due to the fact that, for a generic sound-speed profile $c_0(z)$, one can not derive explicit analytic expressions for each row $\mathbf{e}_i$ of the kernel matrix, thus ''hiding'' any possible dependence between different sets of rows. In general, for a shallow water waveguide, one can expect that most of the SRBR eigenrays are characterized by steep launching angles and by a significant number of reflections on both surface and bottom. As the number of reflections increases, the shape of the SRBR eigenrays tends to be closer to straight lines. Therefore, for a waveguide geometry like the one discussed in the shallow water test, but with an equivalent—constant—sound-speed profile, the isovelocity kernel matrix can provide a reasonable approximation to the original matrix $\mathbf{E}$. Moreover, for a constant c_0, each row of E can be explicitly calculated, making it possible to understand which eigenrays are the independent ones. Those results can provide fundamental knowledge related to the structure of the original kernel matrix, and thus provide an answer to the questions discussed in the beginning of this section.

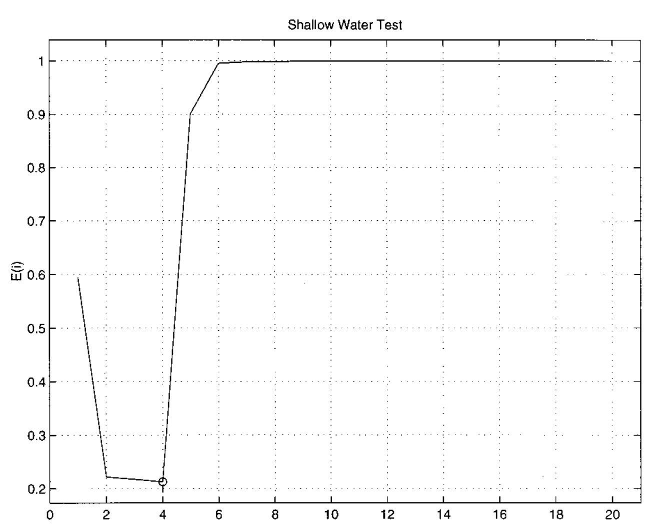

FIG. 6. Shallow water test: Estimation of independent arrivals; the projection of the minimum [Eq. (8)] onto the horizontal axis indicates the number of independent arrivals N.

In general, an SRBR eigenray launched to the surface can arrive at the hydrophone after being reflected an odd number of times $2m-1$, or after being reflected an even number of times $2m$, where m can take the values $1,2,\ldots$. The same kind of reasoning can be applied to an SRBR eigenray being launched to the bottom. Thus for a fixed m, there are four types of eigenrays connecting source and receiver. In the isovelocity case the launching angles of these four eigenrays can be derived by inspection and are given by

$$\tan \theta^{+}_{2m-1} = \frac{(2m-2)D+z_s+z_r}{R},$$

$$\tan\theta^{+}_{2m}=\frac{2mD+z_s-z_r}{R},$$
$$\tan\theta^{-}_{2m-1}=\frac{2mD-z_s-z_r}{R}, \tag{11}$$
$$\tan\theta^{-}_{2m}=\frac{2mD-z_s+z_r}{R},$$

where the convention of the ''+'' or a ''−'' sign was already introduced in the discussion of the shallow water test. The number of total reflections is given by the index of each θ. There is no practical sense in calculating the θ_m for large values of m because the contribution of a particular eigenray to the pressure field decreases as the number of reflections increases. Furthermore, the arrival times correspond to

$$\tau_m^{+/-}=\frac{R}{c_0\cos\theta_m^{+/-}}. \tag{12}$$

For an isovelocity SSP the clustering of arrivals depends mainly on the particular values of z_s, z_r, D, and R. However, by taking the values used in the shallow water test, and taking $c_0=1510\,\text{m/s}$, it can be found that the set of four arrivals will be ordered again according to the general sequence Eq. (10). For the sake of simplicity let us consider further that the linear inversion is performed with a set of q quadruplets, so $\mathsf{T}=4q$. A simple choice of the layer system consists in selecting a homogeneous grid composed of L layers, each with a thickness $\Delta z=D/\mathsf{L}$. The layer thickness will be taken sufficiently small to separate the source and the receiver with at least a single layer, i.e., the layer indexes will obey the following order:

$$j=1,2,...,\mathsf{L}=1,2,...,\mathsf{S},\mathsf{S}+1,...,\mathsf{R},\mathsf{R}+1,...,\mathsf{L}. \tag{13}$$

The indexes S and R correspond to the integer parts of $z_s/\Delta z$ and $z_r/\Delta z$, respectively. Furthermore, for the travel-time sequence given by Eq. (10) the isovelocity kernel matrix can be written as

$$\mathbf{E}=\begin{bmatrix}\mathbf{e}_1\\ \mathbf{e}_2\\ \mathbf{e}_3\\ \mathbf{e}_4\\ \mathbf{e}_5\\ \vdots\\ \mathbf{e}_\mathsf{T}\end{bmatrix}=\begin{bmatrix}[\Delta s_{11}\Delta s_{12}\cdots\Delta s_{1\mathsf{L}}]/c_0^2\\ [\Delta s_{21}\Delta s_{22}\cdots\Delta s_{2\mathsf{L}}]/c_0^2\\ [\Delta s_{31}\Delta s_{32}\cdots\Delta s_{3\mathsf{L}}]/c_0^2\\ [\Delta s_{41}\Delta s_{42}\cdots\Delta s_{4\mathsf{L}}]/c_0^2\\ [\Delta s_{51}\Delta s_{52}\cdots\Delta s_{5\mathsf{L}}]/c_0^2\\ \vdots\\ [\Delta s_{\mathsf{T}1}\Delta s_{\mathsf{T}2}\cdots\Delta s_{\mathsf{TL}}]/c_0^2\end{bmatrix}$$
$$=\begin{bmatrix}\alpha^{+}_{2\mathsf{M}-1}\times\mathbf{e}^{+}_{2\mathsf{M}-1}\\ \alpha^{+}_{2\mathsf{M}}\times\mathbf{e}^{+}_{2\mathsf{M}}\\ \alpha^{-}_{2\mathsf{M}}\times\mathbf{e}^{-}_{2\mathsf{M}}\\ \alpha^{-}_{2\mathsf{M}+1}\times\mathbf{e}^{-}_{2\mathsf{M}+1}\\ \alpha^{+}_{2\mathsf{M}+1}\times\mathbf{e}^{+}_{2\mathsf{M}+1}\\ \vdots\\ \alpha^{-}_{2\mathsf{M}+2q-1}\times\mathbf{e}^{-}_{2\mathsf{M}+2q-1}\end{bmatrix}, \tag{14}$$

where $\alpha_m^{+/-}=(c_0^2\sin\theta_m^{+/-})^{-1}$, and the index $2\mathsf{M}-1$ represents the number of even reflections of the first eigenray within the first quadruplet. The rows $\mathbf{e}_m^{+/-}$ are given by

$$\begin{aligned}
\mathbf{e}^{+}_{2m-1}=[&2m\Delta z\, 2m\Delta z\ldots(2m-\mathsf{S})\Delta z\\
&+z_s(2m-1)\Delta z\ldots(2m-1-\mathsf{R})\Delta z\\
&+z_r(2m-2)\Delta z\ldots(2m-2)\Delta z],\\
\mathbf{e}^{+}_{2m}=[&2m\Delta z\, 2m\Delta z\ldots(2m-\mathsf{S})\Delta z+z_s(2m-1)\Delta z\ldots\\
&(2m-1+\mathsf{R})\Delta z-z_r2m\Delta z\ldots 2m\Delta z],\\
\mathbf{e}^{-}_{2m}=[&2m\Delta z\, 2m\Delta z\ldots(2m+\mathsf{S})\Delta z\\
&-z_s(2m+1)\Delta z\ldots(2m+1-\mathsf{R})\Delta z\\
&+z_r2m\Delta z\ldots 2m\Delta z],\\
\mathbf{e}^{-}_{2m+1}=[&2m\Delta z\, 2m\Delta z\ldots(2m+\mathsf{S})\Delta z\\
&-z_s(2m+1)\Delta z\ldots(2m+1+\mathsf{R})\Delta z\\
&-z_r(2m+2)\Delta z\ldots(2m+2)\Delta z].
\end{aligned} \tag{15}$$

It follows from the previous set of equations that the rows $\mathbf{e}_m^{+/-}$ can be calculated recursively, through the relationship

$$\mathbf{e}^{+/-}_{2m+1}-\mathbf{e}^{+/-}_{2m-1}=\mathbf{e}^{+/-}_{2m+2}-\mathbf{e}^{+/-}_{2m}=[2\Delta z\, 2\Delta z\ldots 2\Delta z]. \tag{16}$$

As shown by Eqs. (15), every four rows $\mathbf{e}_i$ corresponding to a given quadruplet are independent. Furthermore, since α_i is a common factor to all the components of each row $\mathbf{e}_i$, the set Eqs. (16) indicates the linear dependence between each pair of rows $\mathbf{e}_i$ and $\mathbf{e}_{i+4}$. In this way, the previous analysis of the isovelocity kernel matrix indicates not only *how many* of the eigenrays are independent [since the analysis shows that rank ($\mathbf{E}$)=4], but indicates also in detail *which* are the independent eigenrays. For the case of a more generic sound-speed profile $c_0(z)$, as the number of reflections increases, one notes that the slope of each SRBR eigenray approaches a constant, given by the slope of the launching angle $\tan\theta$. Also significant is that the length of a single eigenray crossing a particular layer approaches the ratio $\Delta z/\sin\theta$. In this way, the general structure of Eqs. (15) suggests that, for the shallow water test, each row of $\mathbf{E}$ can be approximated as

$$\mathbf{e}_i\approx\alpha_i\times\left[\mathsf{M}_{i1}\frac{\Delta z}{c_{01}^2}\mathsf{M}_{i2}\frac{\Delta z}{c_{02}^2}\cdots\mathsf{M}_{i\mathsf{L}}\frac{\Delta z}{c_{0\mathsf{L}}^2}\right], \tag{17}$$

where $\alpha_i=(\sin\theta_i)^{-1}$ and M_{ij} represents the number of times that the eigenray i crosses the layer j. Through further analogy the set Eqs. (15) guarantees that there are at least four different types of row components (since the layer thickness is not a common factor), and that guarantees the linear independence of those four rows $\mathbf{e}_i$, corresponding to a particular quadruplet. The analogy to Eqs. (15) allows one to note also that

$$\mathbf{e}_{i+4}\approx\alpha_{i+4}\times\left[(\mathsf{M}_{i1}+2)\frac{\Delta z}{c_{01}^2}(\mathsf{M}_{i2}+2)\frac{\Delta z}{c_{02}^2}\cdots(\mathsf{M}_{i\mathsf{L}}+2)\frac{\Delta z}{c_{0\mathsf{L}}^2}\right], \tag{18}$$

which brings back the linear dependence between each pair of rows $\mathbf{e}_i$ and $\mathbf{e}_{i+4}$. Thus the analysis of the isovelocity kernel matrix, and its analogy to the kernel matrix of the original shallow water waveguide, provide a full understanding of the results of the shallow water test.

V. CONCLUSIONS

On the basis of this analysis the following conclusions can be drawn: (1) in the context of travel-time-based shallow water tomography it is of fundamental importance to determine the number of independent resolved arrivals; (2) with real data the estimation of independent arrivals can be done through statistical tests, while in simulations the estimation can be performed by comparison of the inverse and expected solution; (3) it can be shown through ray-tracing simulation and under the condition of placing the source and the receiver at different depths, that in deep water the number of independent arrivals is equal to the number of resolved arrivals; corresponding simulations in shallow water reveal that the number of independent arrivals is much smaller than the number of actually measured—resolved—arrivals; (4) finally, the problem of travel-time redundancy in the shallow water waveguide is fully explained through the detailed analysis of the kernel matrix of an equivalent isovelocity waveguide, where the rows of the isovelocity matrix show a fundamental rank deficiency of the kernel matrix associated with the original shallow water waveguide.

ACKNOWLEDGMENTS

The authors deeply want to thank the reviewers for the interest they have shown in the discussion of the material presented in this publication. Their detailed remarks concerning some incomplete aspects of the material presented in the first version of the manuscript undoubtedly guided the authors to develop a fundamental improvement of that material.

[1] W. Munk and C. Wunsch, ''Ocean acoustic tomography: A scheme for large scale monitoring,'' Deep-Sea Res., Part A **26**, 123–161 (1979).
[2] W. Munk, P. Worcester, and C. Wunsch, ''Ocean acoustic tomography,'' Cambridge Monographs on Mechanics, New York, 1995.
[3] Y. Stéphan and S. Thiria, ''Neural inversions for ocean acoustic tomography,'' in *Inverse Problems in Engineering Mechanics*, edited by Bui Tanaka *et al.* (Balkema, 1994).
[4] S. Prasanna, Y. K. Somayajulu, T. V. Ramana, G. S. Navelkar, A. K. Saran, A. M. Almeida, and C. S. Murty, ''Preliminary results of an acoustic tomography experiment (ATE-93) in the eastern Arabian Sea,'' Proceedings of the 2nd European Conference on Underwater Acoustics, edited by L. Bjorno, 1994.
[5] C-S. Chiu, J. H. Miller, and J. F. Lynch, ''Inverse techniques for coastal acoustic tomography,'' in *Environmental Acoustics*, edited by D. Lee and M. Schultz (World Scientific, Singapore, 1994).
[6] S. M. Jesus, M. B. Porter, Y. Stephan, X. Démoulin, O. Rodríguez, and E. Coelho, ''Single hydrophone source localization,'' IEEE J. Ocean Eng. **25**(3), 337–346 (2000).
[7] W. Menke, *Geophysical Data Analysis: Discrete Inverse Theory* (Academic, San Diego, 1989).
[8] M. Wax and T. Kailath, ''Detection of signals by information theoretic criteria,'' IEEE Trans. Acoust., Speech, Signal Process. **33**, No. 2, 387–392 (1985).
[9] I. Tolstoy and C. S. Clay, *Ocean Acoustics, Theory and Experiment in Underwater Sound* (AIP, New York, 1987).